
UNIVERSITY OF BIRMINGHAM

# Selective extraction and upcycling of $LiMn_2O_4$ cathode material from first-generation lithium-ion batteries

by

**Beatrice Browning**

Supervisors: Dr Phoebe Allan and Prof. Paul Anderson

A thesis submitted to The University of Birmingham

for the degree of Doctor of Philosophy

The School of Chemistry,

College of Engineering and Physical Sciences

The University of Birmingham

March 2024

# Abstract

The lithium-ion battery scrap pool is set to grow extensively in volume as first-generation electric vehicles reach their end-of-life in upcoming years. There are many key environmental and socioeconomic drivers for the recycling of lithium-ion batteries (Li-ion batteries, or LIBs) and methods to extract and process solid-state electrode materials are an essential part of the recycling process.

Some electrode materials from first-generation cells, such as lithium manganese oxide spinel, or $LiMn_2O_4$ (LMO), are no longer extensively used in current-generation vehicle cells. Therefore, in this thesis, experiments investigating the “upcycling” of LMO from lithium-ion battery cathode material are outlined, from quality control-rejected and end-of-life cathodes, in an array of experiments.

In the first results chapter LMO is selectively extracted from quality control-rejected (QCR) and end-of-life (EOL) cathode material followed by interconversion into an array of upcycling products. The experiments outlined highlighted the effectiveness of a selective leaching process for the extraction of LMO from spent cathode material and the success of the interconversion explored. The LMO, Mn oxalate dihydrate, $Mn_2O_3$ and $Mn_3O_4$ products formed with structures $Fd\bar{3}m$, C12/c1, Pcab and $I4_1/amd$ respectively, across the pristine and leached QCR and EOL samples in all cases, with minimal contamination that did not jeopardise the material structure, indicating this success.

In the second results chapter, upcycling experiments are conducted with QCR and EOL-derived Mn oxalate to generate MnO—C nanocomposite conversion anodes. In the first section synthetic conditions are investigated to manufacture nanosized MnO

suspended in a carbon matrix to ensure that intrinsic issues seen for conversion electrodes, that lead to poor capacity retention, are minimised for optimal electrochemical performance. The conditions chosen for this synthesis involved a mechanochemical route followed by an inert atmosphere heat treatment step, whereby the mechanochemical product was heated to 600 °C and held at this temperature for 4 hours under nitrogen. These conditions gave rise to the desired $_{nano}$MnO─C composite for subsequent electrochemical analysis, which was then applied to generated nanosized carbon composite Mn (II) oxide electrodes from lithium-ion battery-derived Mn-based precursors. The electrochemical performance of these leached nanocomposites highlights the upcycling opportunity for redundant LMO leached from QCR and EOL cathodes, with capacities of 777 (±12), and 916 (±37) $mAhg^{-1}$ reached after 15 cycles, respectively. These capacities exceed the theoretical capacity for MnO, at 755 $mAhg^{-1}$, significantly in the EOL case, highlighting the potential for upcycled products from leached cathode materials.

In the final chapter Mn oxalate, generated from pristine and leached material in the first chapter, is studied as a conversion anode. Though this anode material has been investigated in the literature, this chapter outlines innovative experiments to develop an electrochemical understanding of Mn oxalate anodes and to determine whether upcycled QCR and EOL Mn oxalate exhibit enhanced electrochemical behaviour when compared to the performance of pristine material. Firstly, electrochemical conditions are tailored to probe the anode material's fascinating capacity behaviour, by cycling the anode to a 2 V and 3 V voltage maximum. By the $100^{th}$ cycle, the discharge capacity of the 2 V max cells averaged out at 160 (± 7) $mAhg^{-1}$ and the 3 V max cells averaged out at 723 (±8) $mAhg^{-1}$ at 14% and 70% of their first discharge

capacity, respectively, indicating the effect of the 3 V maximum voltage on capacity retention. Furthermore, redox activity was much more significant out to 100 cycles for the 3 V max than the 2 V max anode, as exhibited in differential capacity analysis, which indicates that the 3 V max cell undergoes additional redox activity through increased oxidation state of Mn, or even through anionic redox of the oxalate group within the polyanion. In-situ pair distribution function (PDF) analysis gave additional insights into the origin of the interesting electrochemical behaviour, indicating that the conversion product at the end of the first cycle does not resemble Mn oxalate. This structure at the end of charge has been hypothesised to match with a zincblende-structured MnO with space group $F\bar{4}3m$, countering the reports of the reversible conversion reaction outlined extensively in the literature for Mn oxalate, but providing more insights into the electrochemical deviation between the 2 V and 3 V max half-cells. Finally, the electrochemical behaviour of Mn oxalate derived from pristine and leached QCR and EOL $LiMn_2O_4$ has been explored to determine the success of upcycling LMO into Mn oxalate conversion anodes. After 100 cycles the capacity recovery of the 3 V max cycled half-cells remained as high as 650 $mAhg^{-1}$ for the QCR and 475 $mAhg^{-1}$ for the EOL sample, proving to be highly successful in upcycling the interconverted $LiMn_2O_4$ into Mn oxalate material. Though the capacity retention after 100 cycles was lower with an increased degree of contamination from the leached samples, the capacity still outperforms the expected capacity based on the theoretical calculation, at 375 $mAhg^{-1}$.

# Acknowledgements

I would firstly like to thank Dr Phoebe Allan and Prof. Paul Anderson for their support and supervision during my PhD, and for allowing me to join the Faraday Institution's second cohort of PhD researchers. I cannot thank them enough for all the direction during my PhD, it has been such a pleasure to work with them over the last 5 years. Special thanks to Fran Long, Matt Howard and Dominic Grantley-Smith from the Faraday institution for their continued unwavering support.

Thank you to all of floor 5 at the University of Birmingham for the endless laughs, office antics, and never-ending entertainment during my time at Birmingham. I truly could not have asked for a better group of people to do a PhD alongside.

For all the support with experiments conducted in this thesis, I would like to thank Javier Castells-Gil, Abbey Jarvis, Joshua Stratford, Harry Fell, Jacob Williams and Rosie Madge. You not only have been incremental in helping my PhD progress but have also managed to make the never-ending experiments at Diamond / Argonne / in Birmingham entertaining.

I would finally like to thank my family and friends for their constant support and advice throughout my PhD. Their unwavering encouragement has given me the confidence to pursue so many opportunities and without them, I don't know where I'd be. Specifically, I want to thank Mum, Dad, Lucy, and Harry. I truly could not have done this without their backing, so I am thankful they have always had confidence in my ability and have spurred me on to jump at every opportunity that has come my way.

# Table of Contents

# 1 Introduction

## 1.1 Table of Figures

## 1.2 Why do we need lithium-ion batteries?

Worldwide, fossil fuels are used in abundance, both domestically and industrially, for various applications including for vehicles and heating. Unfortunately, the use of non-renewable fossil fuels is having a detrimental effect on the environment due to the emission of greenhouse gases; principally carbon dioxide.[1] One way in which the transition away from these non-renewable fuels has been achieved is by use of energy storage materials, such as batteries, which enable energy to be held in reserve for periods of high demand. In a report published by the United Nations Department of Economic and Social Affairs in 2021, it was stated that the largest contributor to greenhouse gas emissions worldwide was the electricity and heat sector, which, between 2011 and 2016, emitted ~15 billion GHG emissions ($CO_2$ equivalent) per year alone.[2] Looking domestically: the main findings from the UK government's 'Transport and environment statistics 2022', highlighted that the transport industry contributed to just under a quarter of total greenhouse gas emissions in 2020.[3] This has been the case for numerous years, and there has been increased pressure inflicted by climate change, alongside relevant policy alterations and tax incentives, to electrify this industry within the UK and worldwide. To make steps towards reduction in GHG emissions, the UK Government announced in 2020 that sales for new petrol/ diesel cars and vans will be banned by 2030, and all sales of other emitting vehicles will be eradicated by the end of the proceeding decade. In 2020 there was a > 50% decline in diesel car registrations in Great Britain compared to the previous year, highlighting public understanding that full road-vehicle electrification is looming.[4] These commercialised electric vehicles (EVs) use lithium-ion batteries (Li-ion batteries) which run via a 'rocking-chair' mechanism. The 'rocking chair' Li-ion battery, initially

composed of a $LiCoO_2$ (LCO) cathode and a graphite anode, was first made commercially available for use in mobile phones and laptops in the early 90's by Sony.[5] In subsequent years, there have been an array of modifications on this basic battery design to increase properties including cycle-life and capacity. The improvement of Li-ion battery cycle-life is of utmost importance to EV manufacturers, as it is necessitated that they achieve a lifetime comparable to petrol/diesel vehicles, before their battery cycle-life reaches 80% capacity (which is considered end-of-life (EOL) within an electric vehicle).[6]

## 1.3 Rocking-chair lithium-ion batteries and their composition

The rocking-chair Li-ion battery is composed of five principle components: the cathode, anode, current collectors, electrolyte and separator, The name 'rocking-chair' is due to the reversible intercalation of lithium ions between the anode and cathode, shown in Fig. 1.1.[7] In the vast majority of current commercialised Li-ion batteries, the anode is coated onto a copper foil current collector, and the cathode onto aluminium foil.[8] Each electrode must exhibit effective conduction of ions and electrons, respectable capacity retention, reversible insertion and extraction ions from its structure, and stability with respect to the other battery components - all while being inexpensive.[9] A binder material, such as polyvinylidene fluoride (PVDF), adheres the electrode material to the current collector, and the addition of carbon black into the electrode coating enables the electrode to establish a substantial electronic conduction network.[10,11] The

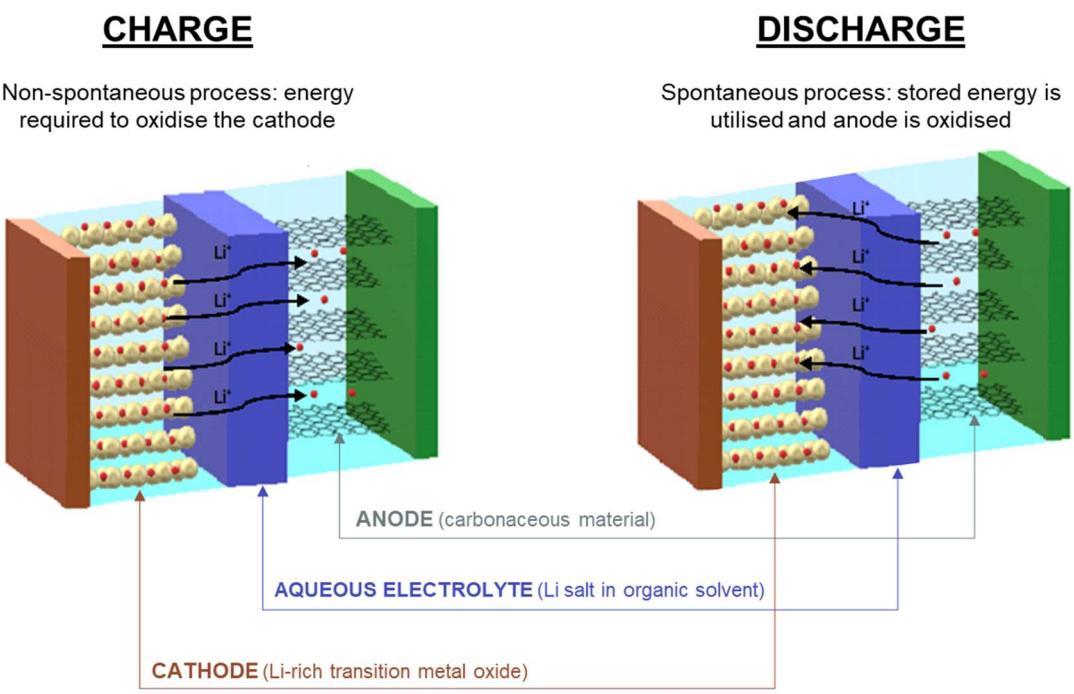


*Figure 1.1. The rocking chair motion of Li ions in a Li-ion battery, with 'rocking chair' referring to the motion of the lithium ions between the anode and cathode within the battery format.*

separator provides protection between electrodes and the liquid electrolyte, while hindering the likelihood of a short circuit.[12] The electrolyte facilitates the transport of ions between electrodes and has an array of compositions. To ensure electrolyte-electrode compatibility, the energy of each electrode material must fall within the 'electrolyte stability window', depicted in Fig. 1.2, to prevent unfavourable electrode-electrolyte redox reactions which lead to loss of valuable materials within the battery. In many cases the electrode will sit outside this electrolyte stability window and react with the electrolyte to form a solid electrolyte interphase (SEI) layer. The formation of the SEI layer is irreversible and uses the finite Li and electrolyte within the cell initially but once formed it acts as a protective layer which inhibits the propagation of more side reactions. This SEI layer was first recognised by A.N. Dey et al. as a vital protective

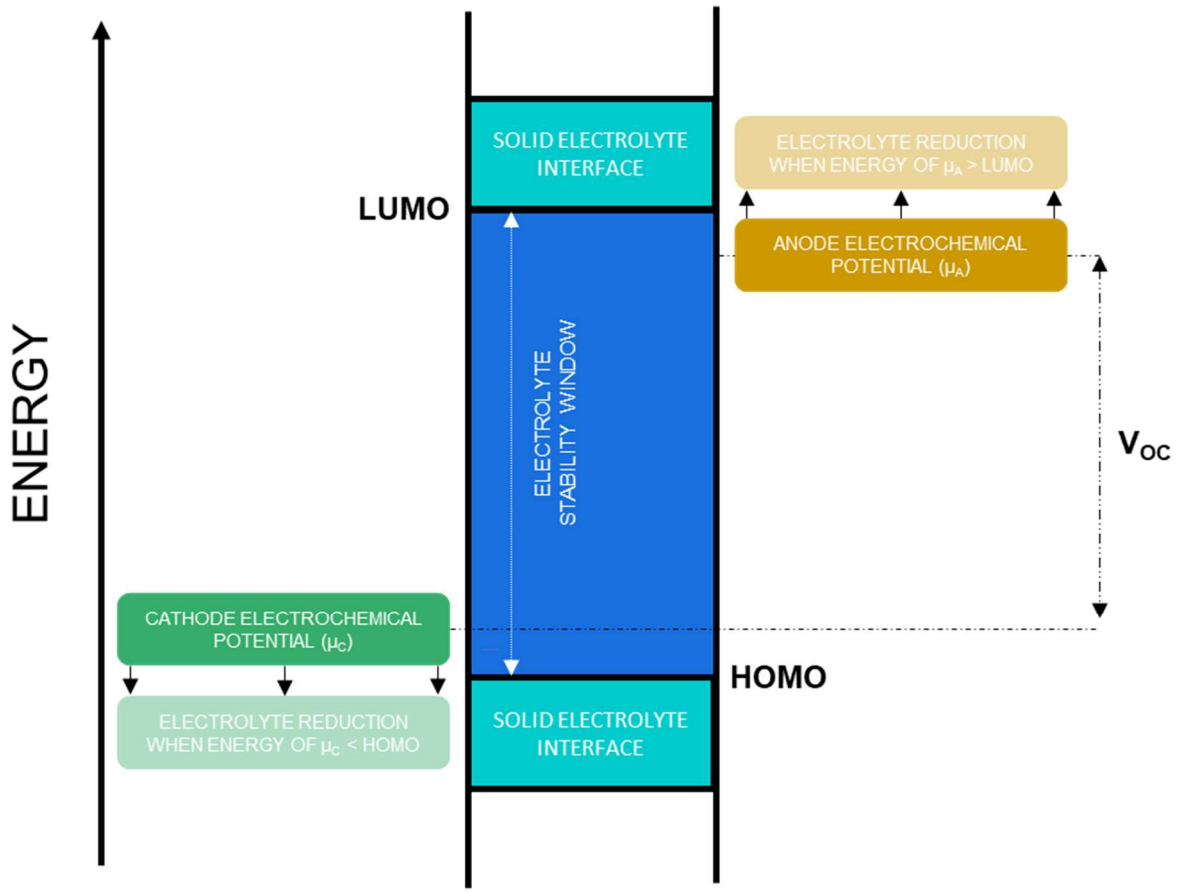


*Figure 1.2. The electrolyte stability window. The stability of the electrolyte to redox reaction is dependent on the electrochemical potentials of each electrode, as indicated in the energy difference between the lowest unoccupied molecular orbital (LUMO) and the highest occupied molecular orbital (HOMO) of the anode and cathode, respectively.*

film for primary lithium-ion batteries in the late 70s, whereby they emphasised the importance of characterisation of this film, and since then many experimentalists have studied its formation at length. Over the years, experimentalists have found that the SEI layer is ionically conductive but electronically insulating, and that the most desirable characteristics for this passive layer is that it is thin, uniform, stable and mechanically flexible.[13,14] The anode donates electrons during discharge and is typically composed of graphite, which has a layered structure for Li-ion

insertion/extraction during battery cycling, and has limited adverse mechanical and electrical effects.[15] The cathode accepts electrons during discharge and should have redox-active transition metals in the structure, alongside lithium (in LiBs) for Li-ion intercalation. In first-generation commercial LiBs, the cathode material was the layered transition metal oxide (TMO) LCO. However, due to safety and stability issues of cobalt, alternative transition metals compositions including metals such as nickel, cobalt, and manganese, were investigated. For electric vehicle batteries characteristics such as energy density, cell safety, fast charging – to ensure EVs have comparable charge times to that of refuelling an internal combustion engine vehicle – are all in demand for EV application. These requirements mean investigation into high energy density Ni-rich batteries, with chemistries such as $LiNi_{0.8}Mn_{0.1}Co_{0.1}O_2$ (NMC 811) have recently been prioritised. In a stationary energy storage application, however, fast charging is far less of a priority for consumers and safety/ stability is prioritised, meaning $LiFePO_4$ (LFP) batteries and lower-Ni NMC chemistries are generally being favoured. Although LFP traditionally has a lower energy density than the aforementioned Ni-rich chemistries, this material is now being favoured for usage in EV applications due to its long lifetime, low cost and intrinsic safety – in fact, in Tesla's Q1 2022 update, it was confirmed that almost half of their EVs produced that quarter used LFP batteries.[16] In China, where the EV revolution is highly advanced, the majority of heavy-duty (HD) vehicles use LFP chemistries. HD EVs in China are the most advanced in the world, in 2021 the Chinese produced over > 90% of electric buses globally.[17]

## 1.4 Li-ion battery recycling

### 1.4.1 Why do we need to recycle lithium-ion batteries?

As EV demand increases across the globe (with just under 7 million EV sales worldwide in 2021) the requirement for effective LiB recycling does too, as the materials found in LiBs (specifically the cathode) are not all readily available, nor are they inexpensive. By the beginning of the next decade, the amount of end of life lithium-ion batteries is set to reach > 100 GWh/ year.[18] Lithium (due to its growing demand and unbalanced world distribution, illustrated in Fig. 1.3) and cobalt (due to its value) are two elements of concern for recovery, with world total reserves of approximately 22 and 7.6 million tonnes of Li and Co metal existing worldwide in total in 2022, respectively.[19] The reduction of landfilled LiBs is also essential due to the fact that unattended battery debris with remaining charge in the battery may result in an elevated internal cell temperature, causing exothermic reactions with the electrolyte resulting in fire or explosions (or both).[20] As mainstream commercialised LiBs consist of an electrolyte in which an organic solvent is mixed with a $LiPF_6$ salt, upon exposure to moisture from the air at such elevated temperatures, hydrofluoric acid may also be produced, which is extremely toxic. The presence of the heavy metals, electrolyte components and alkaline metals also pose pollutant issues, since the vast majority do not readily degrade, and therefore can contaminate the surrounding ecosystem: by means of the earth, water or vegetation. [21,22]

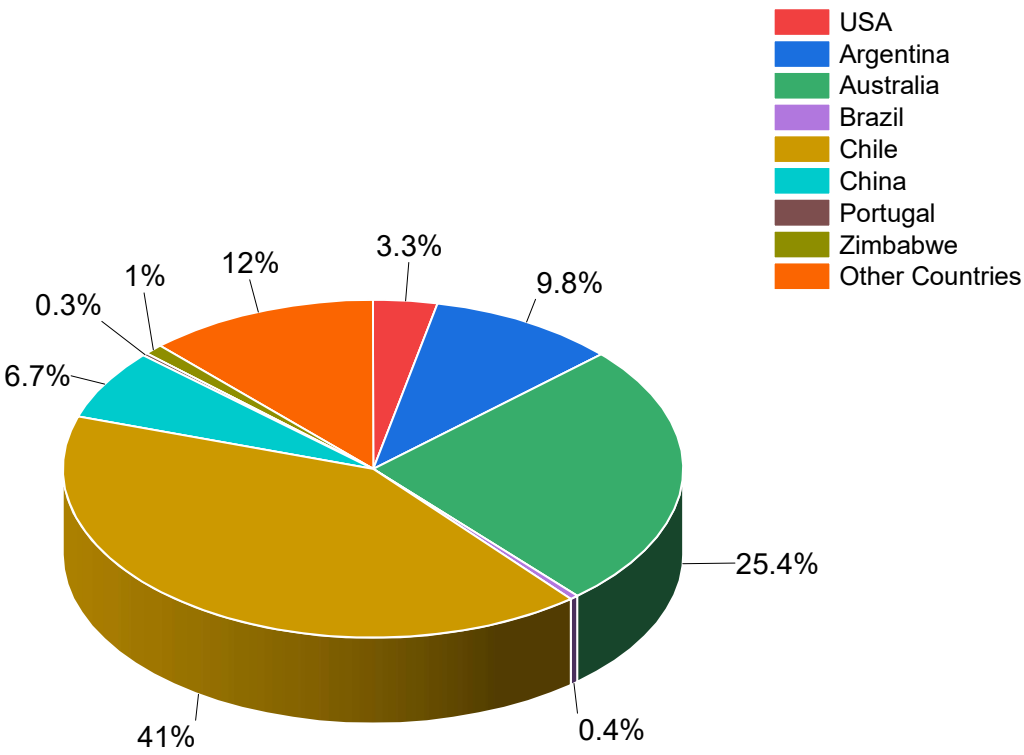


*Figure 1.3. Distribution of Li reserves recorded by the USGS in 2022 – 'other countries' with recorded Li reserves corresponds to (Austria, Canada, Congo (Kinshasa), Czechia, Finland, Germany, Mali, Mexico, and Serbia).*

## 1.4.2 Battery recycling worldwide – scrap pool considerations

The Li-ion battery scrap pool is composed of two sources of scrap: manufacturing (or process) scrap and end-of-life (EOL) batteries. Process scrap refers to inevitable battery material losses that come from battery manufacture, for which there are three main stages – electrode manufacture, cell assembly and cell finishing, outlined in Fig. 1.4.[23] The volume of end-of-life lithium-ion batteries available for recycling is growing year-on-year however there is a significant delay between the beginning and the end of a LiB's usable life which – depending on the battery application – can be anywhere

between 3 and 15 years. Such a lag in this supply of end-of-life scrap material therefore means that most of the current lithium-ion battery recycling scrap pool is composed of process scrap rather than on end-of-life material, which will remain the case in the short-term. For battery manufacturers in their start-up stages manufacturing losses are far more prevalent while the battery plant is in its pilot stage and, while these losses can be limited, there are always inevitable material losses that hold value for LiB recyclers. When considering composition of the process scrap pool worldwide, the chemistry mixture of this scrap will reflect the chemistry of the batteries being sold (and therefore manufactured) at the time, therefore application and battery requirement demand will determine the process scrap pool chemistry mix.[24] In 2021, over 3 million EVs were sold in China, which was greater than the *total* global EV sales in 2020.[25] With the huge demand for the electrification of the transport sector worldwide, EV sales – and therefore the global process scrap pool composition – are profoundly influenced by the Chinese EV market. This heavy influence highlights that, in 2021, the global manufacturing scrap pool will have been heavily influenced by Chinese EV chemistries. As there is a delay in the number of LiBs coming reaching end of life, the volume of the EOL scrap pool will take several years to overtake the contribution from the process scrap pool, as global EV demand remains high in upcoming years. In the long-term, the volume of the process scrap pool will remain significant, as many battery producers will be operational with streamlined manufacturing processes to diminish process losses, but the EOL scrap pool will dominate; due to the huge volume of portable, EV and stationary energy storage batteries set to reach end of life.[24] With all these contributions taken into consideration, the volume of the global scrap pool is set

to be excessive in upcoming years, and a promising opportunity for LiB material recovery is presented to battery recyclers worldwide.

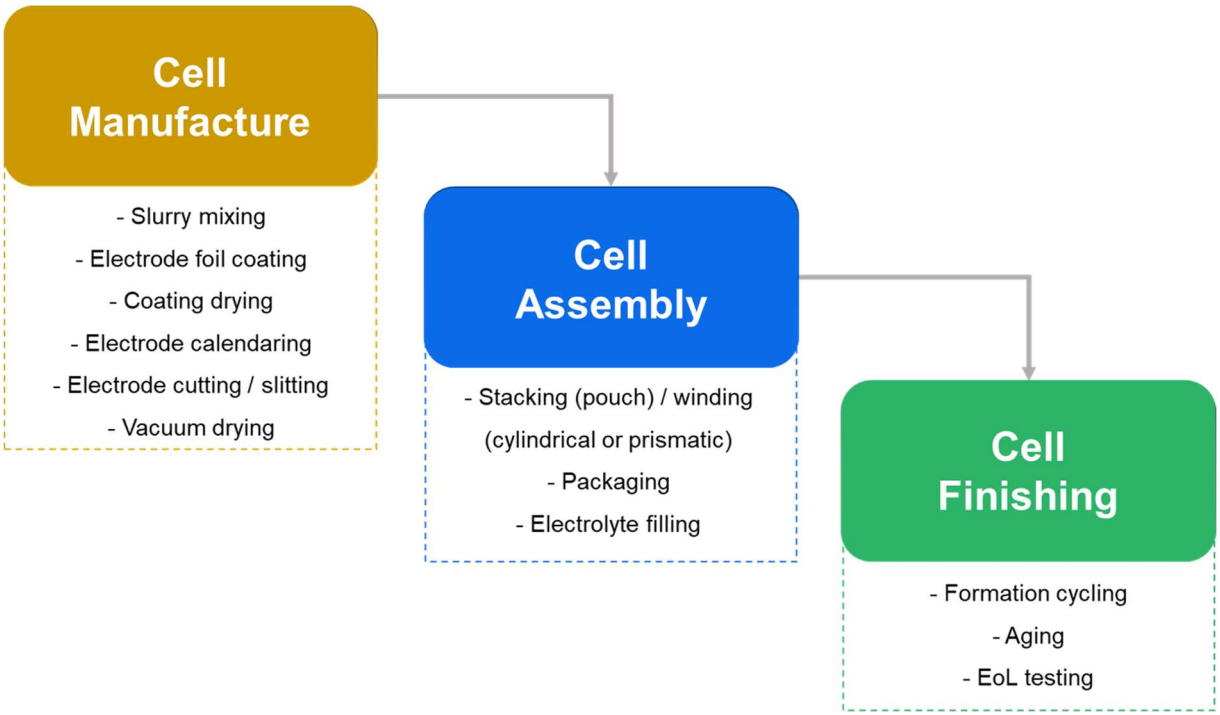


*Figure 1.4. The three key stages cell manufacture, and crucial assembly steps within each stage whereby process scrap losses may occur.*

### 1.4.3 Commercialised lithium-ion battery recycling procedures

In the UK, the LiB recycling industry is extremely nascent. Not only are there very few process scrap sources within the UK, but there is also an improved understanding of the management of spent batteries required. This requirement, however, is hindered by complications surrounding the quantity and timing of batteries reaching EOL, their

ultimate composition, and the economic viability of recovering valuable material from the EOL battery waste stream. Within the UK, the 'UK Battery Strategy' outlines key investments that are being allocated to advance understanding into Li-ion battery recycling and technological advancement, including funding from initiatives such as the Faraday Battery Challenge – which is focussed on driving the expansion of a robust supply chain for Li-ion batteries in the UK, encapsulating recycling within this. [26]

Due to its significant cost, the cathode currently drives economic practicality for LiB recycling, though anode recovery must not be completely overlooked, as finite resources are also still being depleted in order to meet consumer demand.[27] There are generally two overarching stages to battery recycling – pre-treatment and processing. The main processes used in industry include pyrometallurgy, hydrometallurgy and closed-loop (or direct) recycling, however commercialisation of direct recycling is still currently gaining traction compared to pyro- and hydrometallurgical techniques.[28] These techniques are outlined in the subsequent discussion.

### 1.4.4 Battery pre-treatment

There are a vast number of battery pre-treatment stages, which include collection, sorting, deactivation/discharge, disassembly, crushing and filtration/ separation, to name a few.[28] Depending on the sector, battery collection has specific issues. Within the battery industry – and particularly the portable battery industry – collection rates are typically low, due to a previous lack of incentivisation for recycling and recovery by governing bodies. In Europe in late 2022, however, members of the European parliament declared their highest collection targets for portable batteries yet, at 70%

by 2025 and 80% by the end of the decade. Alongside these targets, obligation for collection of all EOL automotive, EV and industrial batteries was also addressed.[29] It is worth mentioning that post-collection, not all batteries are pre-treated in the same way prior to processing – it is specific to each treatment process. For pyrometallurgical treatment, for example, complex disassembly and shredding of the battery packs and modules is not always necessary – whereas for hydrometallurgical processing it is (both metallurgical treatment methods are outlined in sections 1.4.5 and 1.4.6). Generally, most end-of-life lithium-ion batteries are discharged prior to treatment to eliminate hazards from handling batteries with residual stored energy – this also means that unused energy may also be harvested. After discharging, one method that many hydrometallurgical commercial processes have in common involves a sequence of mechanical processing stages including shredding and drying, separation, sieving and crushing.[28] These mechanical steps eventually lead to the separation of electrode foils and a recovered powder intermediate material that can be sold/ recycled, known as black mass. Black mass is a valuable powder intermediate which contains valuable cathode active transition metals such as Li, Co, and Ni. Due to the great mixture of battery chemistries in the LiB waste stream the composition of these elements found within black mass can vary greatly.[30] Within Europe and across the globe, all battery recyclers that intend to use hydrometallurgical processing will do so via this black mass intermediate. Once formed, the black mass will either be:

- Sold onto other companies.
- Sent to recycling companies with whom they have pre-determined offtake agreements in place.

- Sent to another one of the company's plants for processing – pre-treatment and processing of battery materials by the same company is considered an 'integrated' process.

There are many recycling plants that produce black mass intermediates, such as BASF (at their Schwarzheide plant), EcoBat Solutions Germany, all of Li-Cycle's existing and planned spoke facilities (in North America and Europe), and the Poland Legnica Sourcing Centre (PLSC). [31–34] These facilities handle their black mass as follows:

- BASF – Have plans to build a hydrometallurgical treatment centre to make this an integrated recycling process for the company. In the meantime, it is likely this black mass will be sold to trusted partners.[31]
- Ecobat Solutions Germany – This company has formed partnerships with offtake agreements for materials extraction once their black mass has been produced. It appears that their 'trusted partners' will be using hydrometallurgical treatment to produce battery materials for subsequent LiB manufacture.[32]
- Li-Cycle – This company has a 'spoke and hub' model for LiB recycling. At Li-Cycle's spoke facilities, black mass is produced. The black mass from the spoke will then be transported to Li-Cycle's planned hub facility in order to extract metal sulphate and carbonate products, meaning Li-Cycle operate using an integrated process.[33]
- PLSC – POSCO Holdings built PLSC as a battery recycling subsidiary in September 2022. The black mass generated at the PLSC plant in Poland will be shipped to POSCO Hy Clean metal (a South Korean joint recycling venture

between the companies Posco and Huayou Cobalt) in order to integrate the recycling process and extract battery grade Ni/Co/Li/Mn powders for subsequent LiB manufacture.[34,35]

### 1.4.5 Pyrometallurgy

Pyrometallurgy is a developed and straightforward physical recovery process which involves heating of the battery material at high temperatures. The high temperatures are used to drive redox reactions in which the transition metal oxides present in the cells are reduced to metals for subsequent recovery from mixed metal alloys, as outlined in Fig. 1.5. The constituent metals can then be separated using hydrometallurgical techniques, for use in succeeding cathode materials, or the alloy itself can be used in an alternative application. Advantages for the pyrometallurgical process include simple pre-treatment and simplicity for scaling-up. Disadvantages of pyrometallurgy include high energy consumption, hazardous gas emission, and the loss of lithium and aluminium in the slag. This waste stream containing Al and Li may be leached for recovery, however this is expensive and energy intensive, so is generally avoided.[36,37]

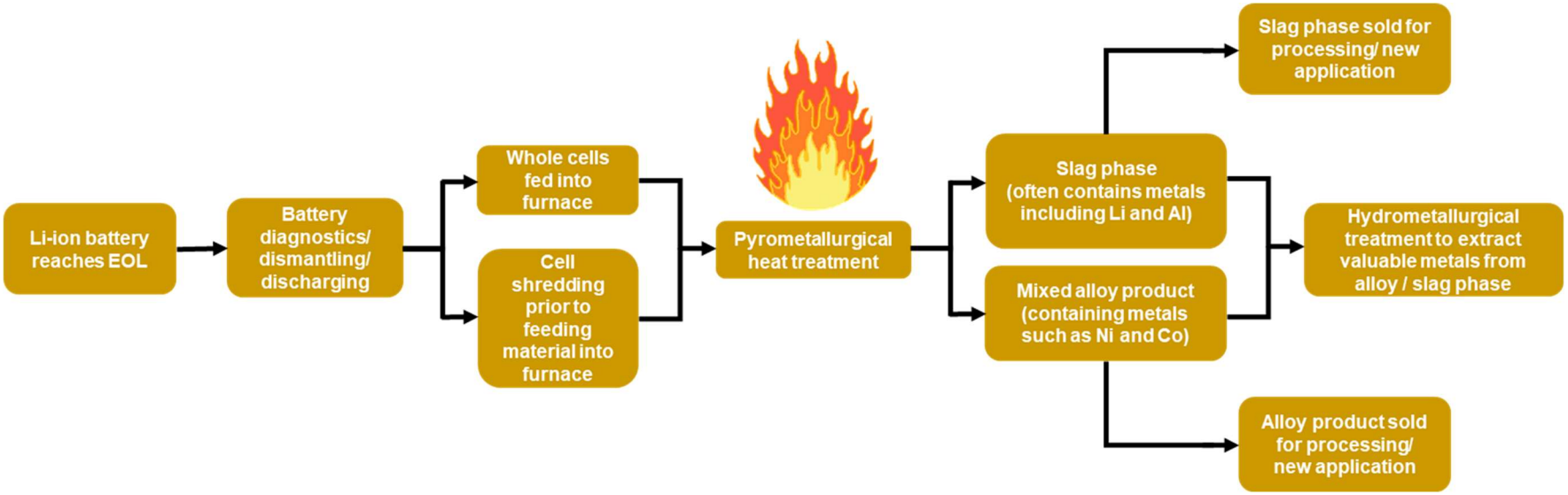


*Figure 1.5. General process flow of pyrometallurgical treatment, from lithium ion battery input all the way through to alloy production and potential hydrometallurgical treatment.*

### 1.4.6 Hydrometallurgy

Hydrometallurgy is a highly exploited chemical recovery process which involves recovery of metal salts or precursor cathode active material (PCAM) from mechanically pre-treated battery material, or black mass, using aqueous chemistry.[38] The main process involved in hydrometallurgy is leaching, outlined in Fig. 1.6, whereby inorganic or organic acids are employed. Inorganic acids, such as hydrochloric (HCl) or sulfuric acid, are effective in the recovery of Li and Co from spent batteries, with HCl proving to have the highest efficiency of Co recovery when used alone.[39] One common way of increasing Co recovery is through the use of a reducing agent in conjunction with the acid. Hydrogen peroxide reagent is used with sulphuric acid, to further convert $Co^{3+} \rightarrow Co^{2+}$ from the evolution of oxygen through $H_2O_2$ decomposition.[40] Unfortunately the residues from inorganic acid-based leaching can be polluting, and hazardous gas may sometimes be emitted (e.g. $Cl_2$ from leaching using HCl). As a resolution to some of the environmental issues, organic acids have been explored for metal recovery using hydrometallurgy. Advantages of hydrometallurgical leaching include a high metal recovery rate, reduced energy consumption and a decrease in wastewater. Disadvantages include the uncertain efficiency of the process, and the expense of the chemical reagents required.[38,39,41]

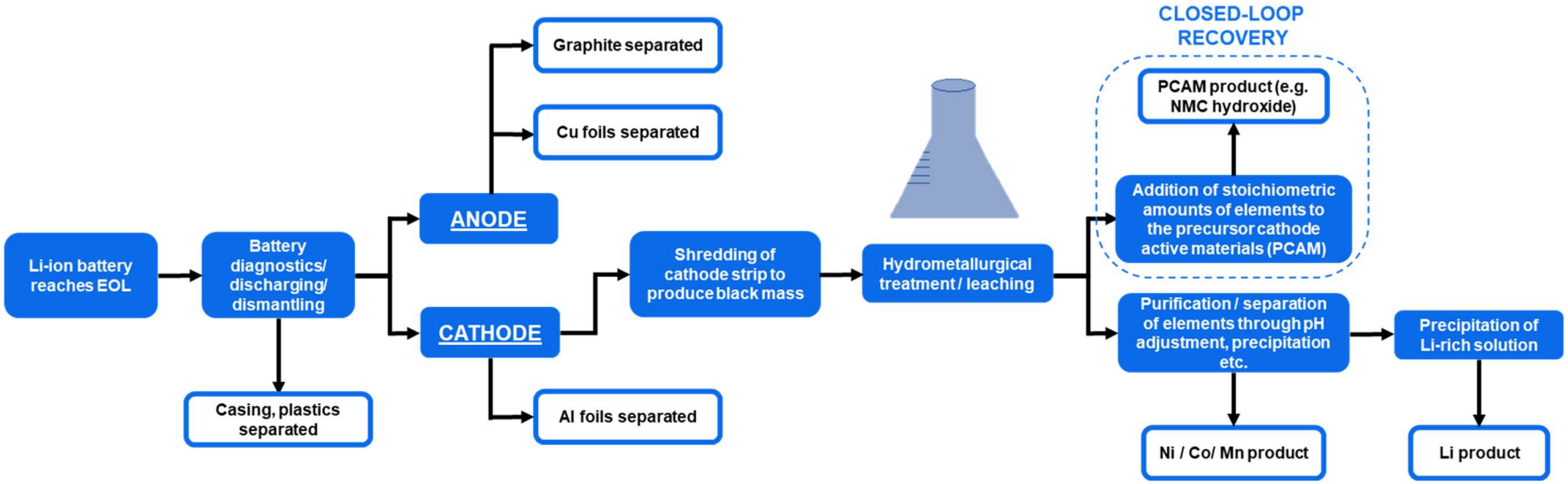


*Figure 1.6. General process flow of hydrometallurgical treatment – with closed-loop recovery route indicated and potential chemical products outlined.*

### 1.4.7 Closed-loop recycling

#### *Using hydrometallurgy to regenerate precursor material*

Closed-loop LiB recycling is gaining attention commercially as involves the direct reuse of spent LiB materials for application in new LiBs through regeneration of cathode active material, avoiding the mineral processing step. A commonly used closed-loop recycling method involves hydrometallurgical treatment and succeeding co-precipitation to form PCAM, as highlighted in the left-hand flow chart shown in Fig. 1.7. Closed-loop recycling is deemed preferable to reagent recovery for some battery recyclers, as it eliminates the need for separation of Co, Mn and Ni from recycling waste streams, and reduces depletion of natural metal resources.[42]

A range of closed-loop recycling practices have been analysed over the years, and a general hydrometallurgical route is shown on the left-hand side flow chart in Fig. 1.7 with the following discussion. In 2013 Wang et al. conducted a study in which $LiNi_{1/3}Mn_{1/3}Co_{1/3}O_2$ (or NMC 111) was recycled from a mixture of cathode materials, including LMO, NMC 111 and $LiFePO_4$ (or LFP). After leaching using sulphuric acid and hydrogen peroxide, the ratio of Co, Ni and Mn sulphates were adjusted to a 1:1:1 ratio in preparation for the objective NMC 111 product. Using NaOH, the alkalinity of the solution was increased to induce co-precipitation of the transition metals as hydroxides. $Li_2CO_3$ was precipitated out using $Na_2CO_3$ and was then ground with the transition metal co-precipitates. The ground precipitates were then pelletized and then sintered to produce NMC 111, which was synthesised into a cathode for electrochemical testing. The electrochemical performance of this product NMC 111 was exceptional. Almost 100% of the transition metals were recovered by this

method.[20] The following year, Wang et al. conducted further investigation on the hydrometallurgical closed-loop recycling of the whole cell. This process adopts the similar leaching conditions to the 2013 study; however, the whole battery was processed rather than just the cathode material alone. Batteries were fully discharged and then shredded and separated using magnetic separation, sieving and chemical treatment. Battery processing steps led to the formation of $Ni_{0.33}Mn_{0.33}Co_{0.33}(OH)_2$ ($NMC(OH)_2$) which was a precursor to NMC 111. Recovered $NMC(OH)_2$ was also proposed as a precursor to lead to other NMC cathode materials depending on the required transition metal ratio. When exposed to the leaching stage, certain metal hydroxide impurities were yielded, namely iron/ aluminium/ copper hydroxides, as these metals are all found in LiBs in the current collectors, LFP batteries and steel casing. It was found that the impurities recovered alongside the desired $NMC(OH)_2$ material were fairly low, at around 50 ppm, which is desirable to ensure effective cathode performance, eluding to the success of this closed-loop processing.[43] In 2015 it was outlined that the processing of the aforementioned $NMC(OH)_2$ product in order to manufacture NMC 111 cathode material was viable, and it was demonstrated that there was practicality and feasibility for scaling up and commercialisation of this closed-loop process. Alongside this, recycled cathode material exhibited favourable electrochemical behaviour and can also be synthesised with different transition metal ratios.[44] In 2019, M. Chen et al. demonstrated that this hydrometallurgical closed-loop recycling method using NMC-LMO and NMC-LMO-NCA (NCA = nickel cobalt aluminium oxide) is commercially viable. They disclosed that compared to reference commercial cathode material, the closed-loop hydrometallurgical recycling product exhibited almost equivalent performance electrochemically, and rate enhancement.

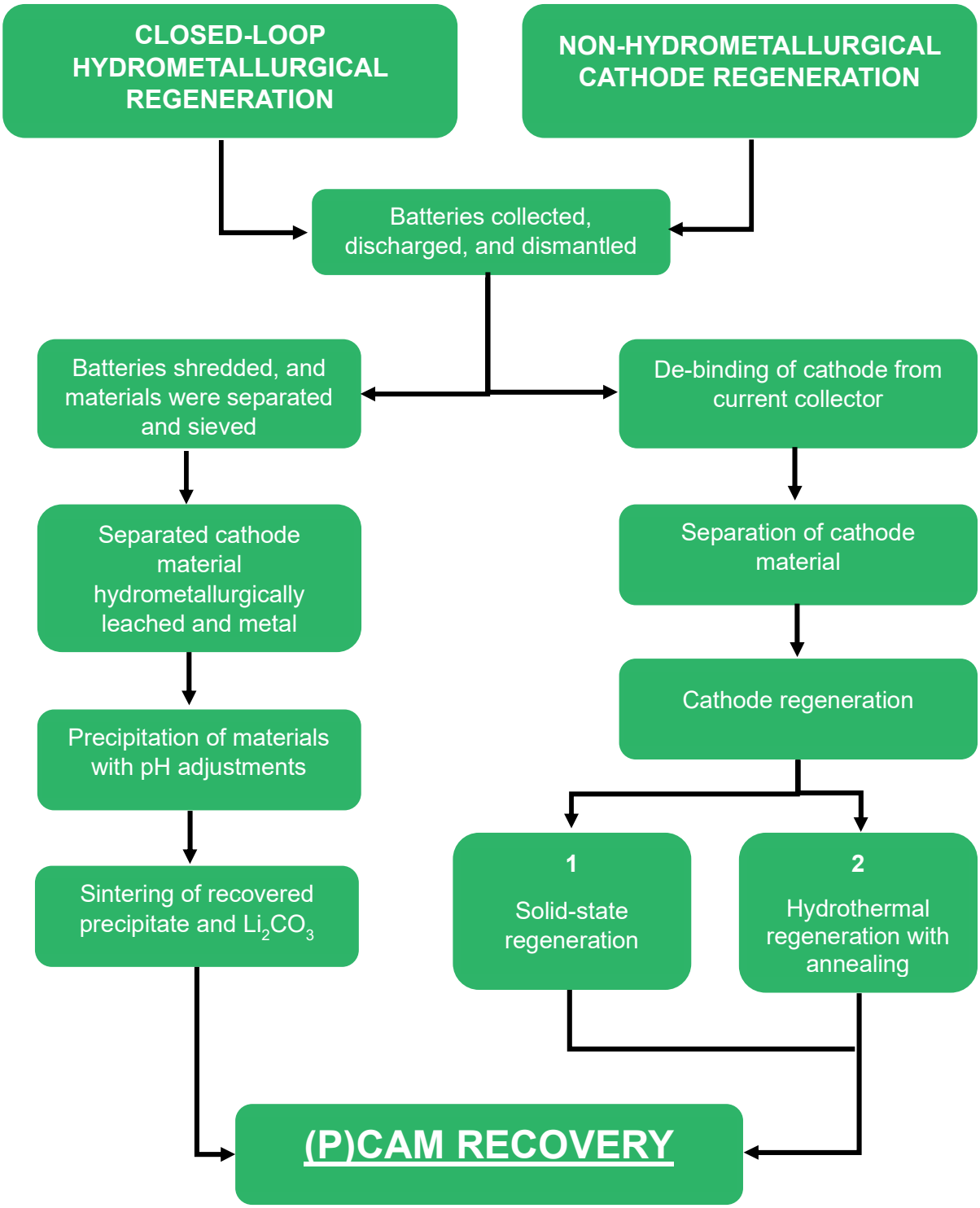


*Figure 1.7. General process flow of closed-loop recycling – with hydrometallurgical/non-hydrometallurgical routes outlined. Both can be used to generate precursor cathode active material (pCAM) or CAM. pCAM can be fed into CAM synthesis and CAM into electrode manufacturing.*

Experimentation on 1 kg of EOL batteries, in which reaction times were approximately 30 hrs, were successfully scaled up to 30 kg with a reaction time of just under 170 hrs. On the lab-scale, at 25 hrs, it was established that the precipitant particle size remained constant indicating co-precipitation had occurred. The final cathode material was synthesised by sintering the co-precipitant with $Li_2CO_3$, and it was realised that the particle morphology has a huge impact on the quality of the electrode material produced. Spherical particles with great uniformity were realised to enhance electrode capacity and energy density significantly.[45]

### *Other closed-loop recycling methods to regenerate precursor material*

The less commonly used method for closed-loop recycling involves recovery and regeneration, whereby cathode strips are extracted from EOL batteries and stripped from current collectors using sonication and solvents such as dimethyl carbonate and N-Methyl-2-pyrrolidone (NMP). Spent cathode material is then separated for subsequent regeneration. The closed-loop methods are indicated in the right-hand side of the flow chart in Fig. 1.7. Regeneration has been explored in several ways, including using high temperature solid-state method or through hydrothermal treatment followed by annealing. In 2018, Y. Shi et al. compared these two regeneration methods, and it was observed that solid-state regeneration provided the inferior cathode product, with little rate capability for application. They deemed the hydrothermal treatment to be superior for the following reasons:

- Regenerated active material provided a higher capacity and enhanced rate capability.
- Time and energy consuming heat treatment was not required as the dosage of lithium during hydrothermal treatment ensured stoichiometry is achieved.
- Its compatibility with batteries with an array of faded capacities.[46]

The chemistry of these hydrothermal regeneration with annealing has been streamlined in recent years. In 2021, P. Xu et al. optimised their hydrothermal step by striking a fine balance between reaction temperature, time and cost of reaction without compromising on the product of their recovered material, while reducing their annealing temperature too.[47] The following year, X. Yu et al. released a paper outlining their low-temperature hydrothermal method to reform different Ni-content NMC materials with a Li hydroxide Li source. They halved the relithiation temperature used in P. Xu et al.'s experiments with the use of environmentally sound additives within their reaction vessel.[48] Direct recycling research is reliant on improvement and modification of these low temperature methods in upcoming years.

## *Issues, future, and commercialised closed-loop lithium-ion battery recycling procedures*

Most previous research accounts for a single stream of EOL batteries for experiments involving their recycling and is still in the process of being scaled up. Unfortunately, the non-destructive closed-loop hydrometallurgical process requires numerous intricate steps to ensure effective metal recovery, making its scale-up viability challenging.[45] In some hydrometallurgical studies, it is of interest to battery recyclers to deduce whether

Ni/ Mn/ Co hydroxides can be precipitated out before Al and Fe impurities are, to ensure that the recycling process holds its efficiency.[43] As the chemistry of cathode materials change it is important to remember that the recycling stream is going to be several years old when it comes to future processing. LCO used to be the predominant cathode material, but now there are an array of chemistries including NMC, NCA, LMO, LNO, and LFP in the waste stream. In 2023, F. Maisel et al. put forward their estimate for the future raw metal demand scenarios for lithium, cobalt and nickel in electric vehicles based on 2 different cases: one being that Ni-rich chemistries will continue to be the most sought-after cathode in upcoming years, and the other that assumes that the market share of iron and manganese-based chemistries will expand more out to 2040. Alongside this, they also included three global socioeconomic outcomes that would enable forecasting of materials available worldwide to be done – shown in Figs. 1.8 and 1.9 in the low, medium, and high case. The low case corresponds to very little change into global movement towards sustainability, medium to a respectable effort in ensuring recycling and sustainable practices are adopted, and high in that governmental efforts worldwide are maximised to ensure there is a global commitment to tackling climate change through the EV industry.[49] It is clear from the diagram of the scale of material demand required will be immense with respect to Ni recovery if Ni-rich chemistries are required. In all cases the demand scenarios are in the case of kilotons of material, highlighting the sheer scale of this recovery operation.

To reduce battery cost, development into decreased Ni and Co content in cathode materials is growing, meaning infrastructure and processes which can handle such diverse battery waste need developing.[43] This being said, in the above-mentioned

hydrometallurgical closed-loop recycling investigation by M. Chen et al. in 2019, numerous advantages from their investigation were stated, including:

- The ability to apply their processing method to a range of LiB chemistries in the recycling waste stream, demonstrated by their use of EV batteries from multiple car manufacturers.
- The electrochemical performance of the recycled material had an equivalent or, in some cases, a superior performance when compared to commercial cathodes.

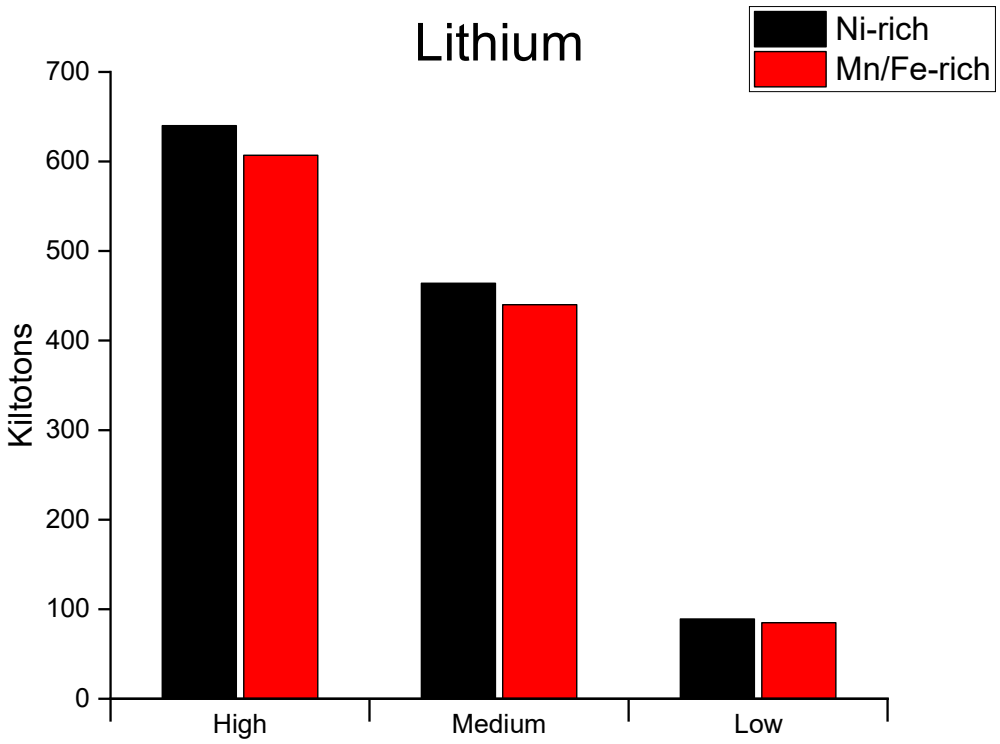


*Figure 1.8. Future Li demand for EV LIB cathodes in 2040. Numbers and definitions for 'high' 'medium' and 'low' case are taken from Maisel et al.*[49]

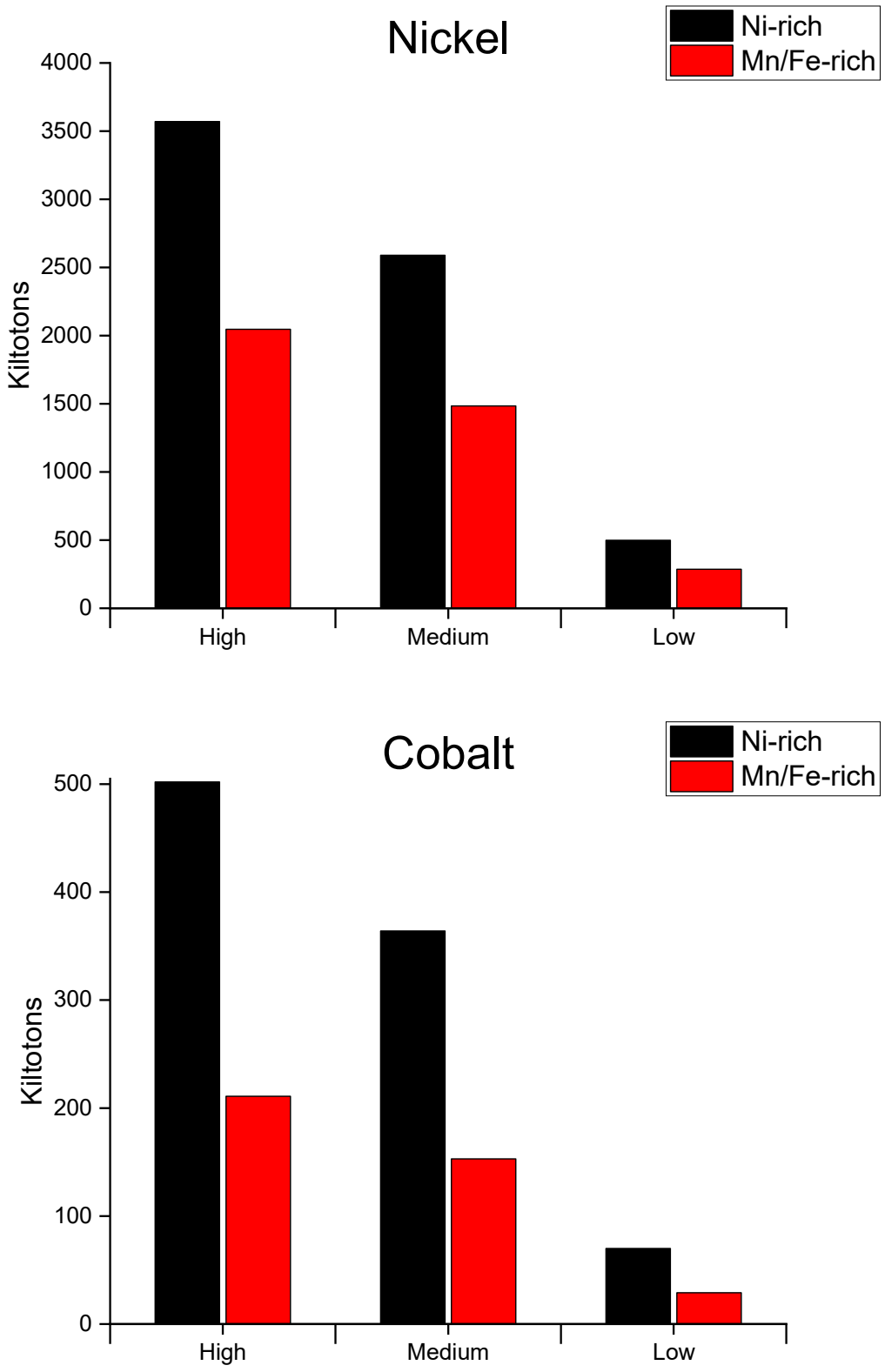


*Figure 1.9. Future Ni and Co demand for EV LIB cathodes in 2040 Numbers and definitions for 'high' 'medium' and 'low' case are taken from Maisel et al.*[49]

- Investigation has been done for scaling up their experiment from 30 kg of battery material to approximately 500 kg.[45]

These promising results, alongside the previously mentioned benefits of closed-loop recycling, provided an optimistic depiction for its future. Though there are numerous challenges to overcome, specifically related to recycling infrastructure, it is vital that there is ongoing study into scale-up operations and improvement of recycling efficiency, as closed-loop recycling has the potential to reap great reward if it is found to be feasible.

With respect to current companies using commercial closed-loop, or “direct”, recycling methods, there are a very few that have showcased this recycling route. One pioneering American company that has disclosed their closed loop recycling method is Princeton NuEnergy – they utilise a lower temperature closed-loop method which involves the use of plasma to aid material recovery. They claim that their process not only recovers and purifies end of life cathode and anode material, but also that they have the capability to improve the electrochemical performance. The process involves shredding and separation of the cells with anode, copper and aluminium foil recovery followed by plasma assisted purification steps in order to regenerate battery quality cathode materials that are ready for use in subsequent cathode applications.[50]

### 1.4.8 Current upcycling methods for spent cathode material

Regarding direct cathode recycling, one method which requires more extensive research is upcycling. Upcycling facilitates the reuse of discarded cathode material to

enhance its value/quality and environmental value in a closed-loop fashion. Currently in the literature, there are a limited number of battery recycling methods which focus particularly on upcycling, and there is a broad scope for its investigation. Regarding upcycling battery materials for use in a new application, V.P. Parikh et al. outlined their method for extraction of LCO from spent batteries for used as an additive in a graphene-based solid lubricant. LCO was particularly appealing for such an application due to its low price and nontoxicity, and therefore proved to be of great value when upcycled for this application.[51] Though this upcycling case is interesting, to keep the battery materials within the LiB supply chain, it is more useful for electrodes to be regenerated into new relevant electrode materials that can be used in LiB applications. One example of such an upcycling study comes from T. Wang et al., who used a 'reciprocal ternary molten salt system' to upcycle NMC 111, that had been chemically delithiated, into Ni-rich NMC material which resembled NMC 622. This upcycled material had extremely similar thermal stability and chemical composition to a pristine NMC 622 sample, and exhibited superior electrochemical performance to the low-nickel material, rendering the upcycling process highly promising.[52] Another example of a successful battery upcycling experiment comes from G. Qian et al., who outlined an experiment whereby degraded NMC 532 cathodes were upcycled into a high-performance single crystal NMC material with higher Ni content, using a molten salts method. The upcycled cathodes had over 94% capacity retention in full cells (and a graphite anode) after 500 cycles. This impressive capacity retention, and their extensive analysis of techno-economic viability of the upcycling process, renders the option of upcycling a very appealing one.[53]

### 1.4.9 Required upcycling methods – LMO cathode material

Within the EV industry, a sector that is rapidly expanding and will need plenty of materials available for future manufacture, there is a current focus on Ni-rich and LFP compositions. In previous batteries this was not the case: the first generation 24kWh Nissan Leaf, for example, was composed of an NCA/LMO composite cathode. Nowadays, the LMO portion of this cathode material has been phased out of subsequent Nissan Leaf models in favour of having a greater proportion of materials within these cells with higher energy density.[54] As first-generation electric vehicles reach end of life, the extraction of the constituent electrode materials for recycling and upcycling must be optimised, for effective repurposing into new valuable Mn-based materials for future Li-ion batteries, and LMO upcycling is not something that must be overlooked.

## 1.5 Alternative anode materials for Li-ion batteries

### 1.5.1 Current anodes - graphite

Graphite is a carbonaceous material that has been used commercially as an anode in lithium-ion batteries since Sony first commercialised the LiB in the 1990s. It is composed of layers of $sp^2$-bonded carbon atoms in a hexagonal array and can stack either in a hexagonal or a rhombohedral fashion, as shown in Fig. 1.10. A separation of ~ 3.36 Å is found between hexagonal layers, and the C─C distance within each graphene layer is approximately 1.42 Å. Graphite can be described as a carbonaceous material with no (or very minimal) turbostratic disorder.[55] The electrode

reaction which arises at the graphite anode are as follows in equation 1 (forward reaction corresponding to cell discharge):

$$Li_xC_6 \leftrightarrow Li_{x-y}C_6 + yLi^+ + ye^- \quad [1]$$

Graphite is desirable due to its a low electrochemical potential vs. Li, respectable cyclability and theoretical capacity (372 $mAhg^{-1}$) and abundance, which currently renders it as inexpensive.[56] Graphite can generally be classified as natural or synthetic graphite. Natural graphite is a naturally occurring form of graphite which was included in the 2022 US Geological Survey list of critical minerals as its current ubiquitous use in commercial lithium-ion batteries across the transport, portables, and ESS markets is not forecast to decline any time soon. In the US Geological Survey, from January 2023, it was estimated that current recoverable graphite resources surpass 800 million tonnes globally.[57] Though naturally occurring graphite is vital for the sector electrification, its uneven global distribution mean that this supply alone is not sufficient to meet demand, which is where synthetic graphite comes into action. Synthetic graphite is derived from carbonaceous material such as petroleum coke and coal tar – these materials require numerous treatment steps including carbonisation and graphitisation, amongst other stages, to generate the graphitic battery grade material required. Carbonisation involves converting the precursor materials into pure carbon, and graphitisation involves high temperature thermal treatment (to 2000 – 3000 °C).[58] In order to ensure optimum Li transport into the anode, graphite is often sphericalised to ensure lithium transport remains effective into the graphite structure during cell cycling. By sphericalising the graphite particles, the basal plane surface (parallel to the (001) crystal plane of the hexagonal

lattice) is exposed to the electrolyte so that Li transport into these graphene layers is optimised, and first cycle irreversibly capacity loss is reduced. [59]

### 1.5.2 Shortcomings of graphite circularity

Currently, graphite dominates the lithium-ion battery anode market, however a high number of recyclers do not focus on graphite recovery – examples of current reasons graphite loss occurs within industry include: [60]

- Usage as a reducing agent during battery pyrolysis.
- Sold as scrap material – often lost within the slag.
- Burnt off as $CO_2$ when recycled using high temperature techniques (such as pyrometallurgy or, recently in India, carbothermal treatment).

Even for those recyclers who focus on methods that would facilitate recovery of graphite from battery scrap; this material would be impure with undesirable morphology from its first life, and graphite must be phase pure and spherical for optimal anode performance, meaning regenerative steps would be essential to recover this material as battery grade graphite.[61] Due to its current low cost and abundance, incentivisation for companies to focus on labour intensive graphite recovery and regeneration are not currently in place. If the EV and EES markets expand as rapidly as predicted with no alternate commercial anode materials, reliance will be placed on countries with high graphite mining activity – such as China – which will cause supply bottlenecks and inflated stock prices.[62]

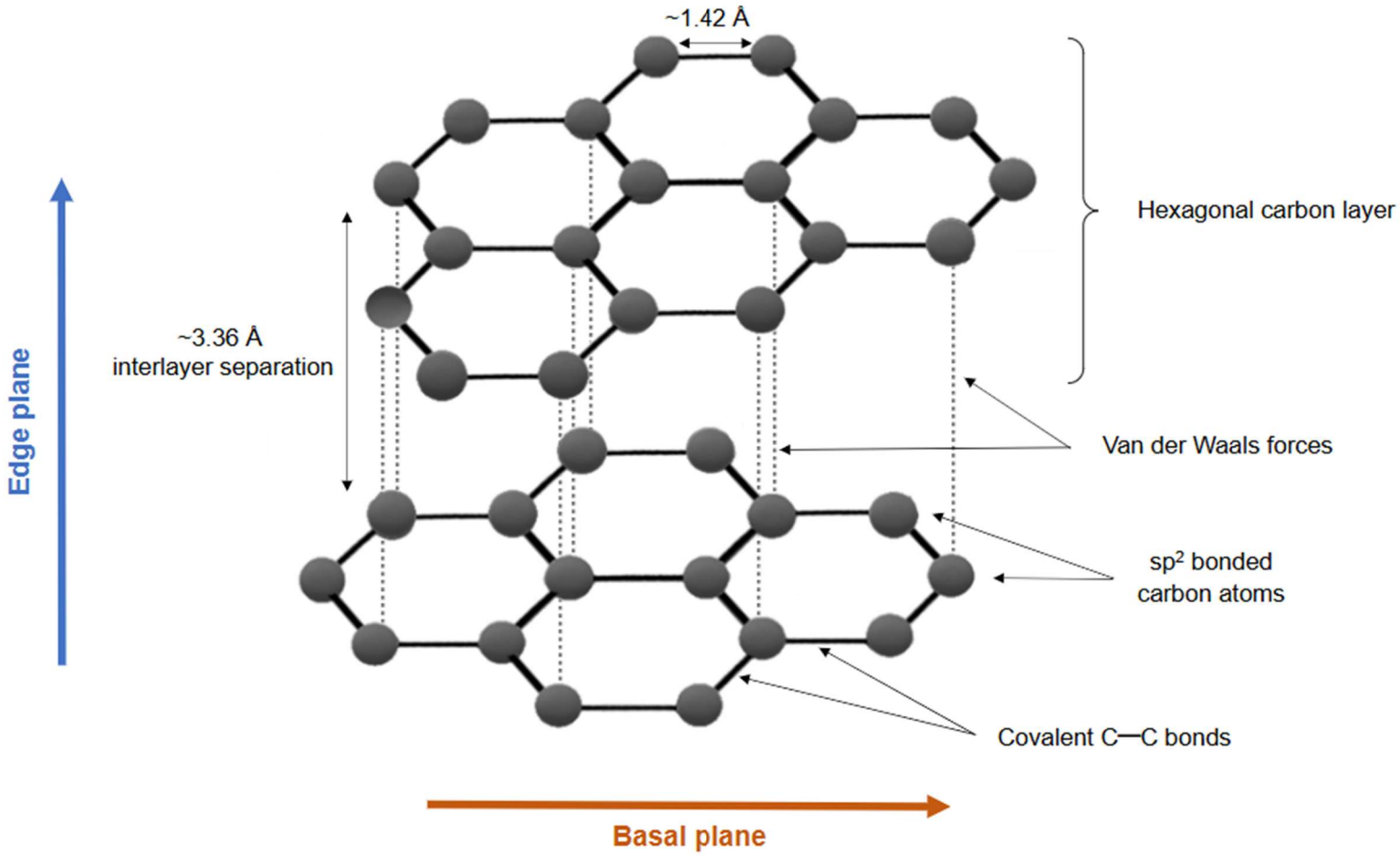


*Figure 1.10. Structure of graphite shown with inter and intra-layer bonding, directional planes and C-C bond distances labelled.*

Though graphite has an array of attributes, including its inexpensive primary extraction, well-understood performance and a considerable cycle life, this material is not routinely recycled industrially. As stated previously, the two most established recycling methodologies are pyro- and hydrometallurgy. Pyrometallurgical treatment involves high temperature incineration of spent battery material to produce an alloy of the precious cathode metals, a Li-rich slag, and a fly ash phase. During this heat treatment, graphite is lost as $CO_2$, therefore pyrometallurgy is not a viable option for graphite recovery. In the case of hydrometallurgy, graphite recovery is possible, however as an array of metal impurities contaminate the material during cell cycling, and as the structure degrades, repair of this material is necessary in order to bring the material to a similar quality to primary graphite.[61] The requirement for graphite repair increases the energy required in its due to these processing steps, reducing economic viability of recycling.[63,64] Due to these issues, it is vital that alternative anode materials are explored to reduce this high reliance on graphite.

### 1.5.3 Mn-based conversion anodes for Li-ion batteries

The low economics for recycling of graphite mean that alternate electrode material options are appealing, and conversion anodes have an array of attributes. Conversion electrodes store mobile ions through a conversion reaction, exhibited in equation 2:

$$M_aX_b + (b \cdot n)Li^+ + (b \cdot n)e^- \leftrightarrow aM + b\ Li_nX \qquad [2]$$

In this equation, M is a transition metal (such as Mn), X is an anionic species (such as O), a and b refer to the stoichiometry of the oxide, and n to that of the Li product.[65]

As observed in this equation, the host crystal structure of a conversion electrode reacts and forms a new phase. When compared with intercalation electrodes, in which only one alkali-ion is usually transferred per formula unit, conversion electrodes exhibit extremely superior ionic transfer and uptake.[66] Despite the noteworthy capacity that these materials can reach, their long-term cyclability has been compromised in the past due to large volume changes during the conversion reaction. These structural changes lead to loss of contact between grains and the current collector, isolating areas of the electrode and reducing the capacity drastically. Measures can be made to reduce the strain on the active material during the conversion reaction, which is where nanosizing and carbon composites have been investigated. Nanosizing has been found to reduce conversion-induced strain, and carbon composites increase the electrical conductivity of the conversion electrode materials while acting as a buffer for the drastic volume changes. Nanosized carbon composites therefore are commonly utilised when synthesising conversion anodes.[67,68] Additionally in conversion anode materials, first cycle irreversible capacity losses are commonly observed. This is partially due to the formation of solid electrolyte interphase (SEI) layer with the material. On one hand the SEI layer is vital for ideal cell cycling, as mentioned in section 1.3, as it is electronically insulating and ionically conductive to Li-ions. Once formed, it prevents further electrolyte consumption by creating a physical barrier between the electrode-electrolyte interface. On the other hand, SEI layer formation limits the optimal capacity of the cell, as there is a permanent loss of Li and electrolyte which occurs from this irreversible reaction.[69] Mn-based conversion anode materials are desirable alternatives to graphite, due to the abundance and non-toxicity of manganese and

the ability to accommodate a significant amount of lithium when compared to these Li-intercalation electrodes. Much research has been done into these manganese-based anodes' notable electrochemical performance and cyclability in Li-ion cells, and many methods have been outlined to enhance their cycling behaviour and reduce intrinsic conversion anode issues, such as voltage hysteresis and large first cycle irreversible capacity losses. Such experiments include through nano structuring, carbon anchoring and encapsulating of Mn-based nanoparticles in a carbon framework.[67,70–72] If these materials can first be recovered from leached electrode material with similar crystallographic properties and low proportions of impurities to the phase pure case, then there is an exciting opportunity to enhance the value of the LMO coming from battery scrap, through interconversion of these materials and effective upcycling.

### 1.5.4 MnO conversion anodes

MnO conversion anodes are promising due to their high theoretical capacity of 755 $mAhg^{-1}$ compared with 372 $mAhg^{-1}$ for graphite. Furthermore, MnO conversion anodes are known for their reasonable discharge potentials and their low overpotentials, as well as the non-toxicity of manganese itself.[73] The general reaction equation for de/lithiation of MnO is shown in equation 3:[74]

$$2Li + MnO \leftrightarrow Li_2O + Mn \quad [3]$$

As stated in the previous section, long-term cyclability of conversion anodes is often compromised due to volume changes that arise from de- and reconstruction of new phases during cell runtime, meaning that long-term cyclability is hindered due to

inevitable contact losses that arise between the active material coating and the current collector, causing isolation of areas of the electrode and reducing the capacity. This therefore means that when considering MnO conversion anodes, it is observed that nanosized MnO carbon composite ($_{nano}$MnO–C) materials already have the desired characteristics to reduce conversion anode shortcomings that are usually sought after by experimentalists. Furthermore, any issues relating to electrical conductivity of transition metal oxides are alleviated by integration of the Mn with a carbon matrix at the nanoscale. Not only does this material have desirable characteristics to reduce long-term cycling issues observed for conversion anodes but based on a study composed by X. Hua et al., it has been hypothesised that the magnitude of inevitable first cycle irreversible capacity losses can also be reduced when compared to other Mn oxide counterparts, such as $Mn_2O_3$ or $Mn_3O_4$. X. Hua et al. have thoroughly investigated the reaction pathway that $Mn_xO_y$ conversion anodes take during take during their first charge-discharge cycle using techniques including Metropolis non-negative matrix factorisation (NMF), a technique used to distinguish individual phases within a sample that are not known prior to measurement and operando PDF analysis amongst many others, outlined by X. Hua et al. Their investigation into the experimental intermediates showed that for MnO and $Mn_3O_4$ the reaction pathways for the first discharge-charge cycle (and subsequent cycles) can be hypothesised, shown in Fig. 1.11.[75,76] Shown in reaction scheme a, the first discharge of MnO pulverizes it into a nanosized MnO phase, and with further Li addition, the nanosized MnO converts to Mn metal and lithium oxide. For the $Mn_3O_4$ phase shown in reaction b, there is an initial conversion of $Mn_3O_4$ to $LiMn_3O_4$, which then breaks down into MnO and $Li_2O$. This

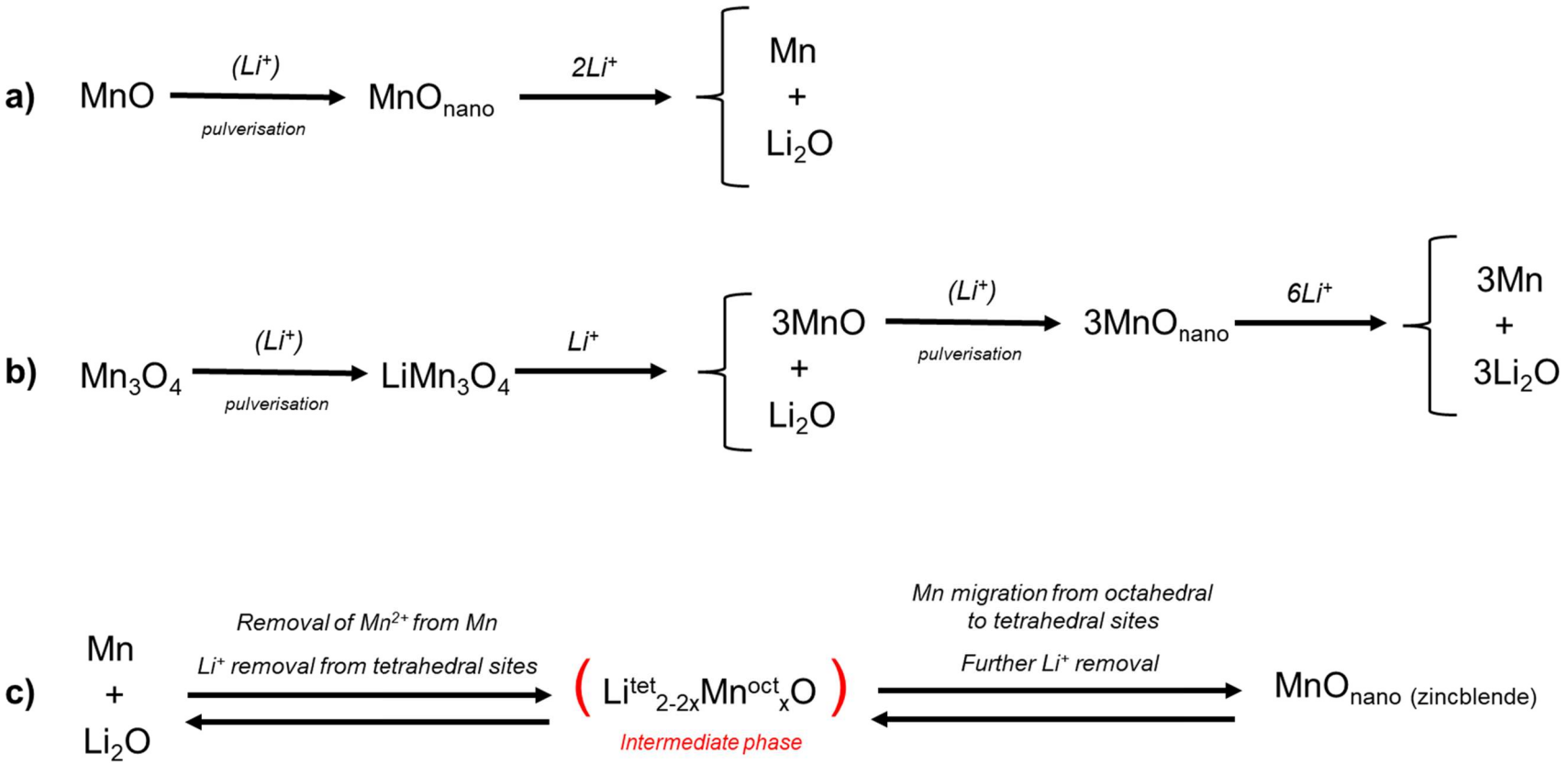


*Figure 1.11. Conversion reaction schemes for a) MnO in its first discharge b) $Mn_3O_4$ in its first discharge c) First charge in for both Mn oxides & subsequent charge-discharge cycles that will occur via this intermediate*

MnO phase then follows the same conversion mechanism as for MnO. In the first charge, shown in the forward reaction scheme c, the Mn metal and $Li_2O$ converts via an intermediate Li–Mn–O phase to form a nanosized zincblende-structured MnO. Subsequent cycles are then thought to convert between this zincblende MnO and Mn metal with $Li_2O$, meaning the original Mn oxides aren't reformed. This is likely to be one of a multitude of reasons behind the high first cycle irreversible capacity loss often seen for these Mn oxides, which means that X. Hua et al.'s conversion reaction pathways can be used to determine the best Mn oxide precursor to minimise this – which, in this case, would be to begin cycling with nanosized MnO. Not only do is the initial conversion step eliminated to reduce conversion anode losses, but beginning with a smaller particle size means that less pulverization would be needed.

### 1.5.5 $_{nano}$MnO–C composite electrochemical behaviour

It has been indicated in an investigation by J. Liu et al. that in the first discharge of MnO the initial MnO particles convert to form metallic manganese nanoparticles and lithium oxide in a disordered matrix all coated in an SEI layer. In their study on MnO/C nanocomposites for high capacity Li-ion battery applications, J. Liu at al. then stated that during charge this metallic manganese reconverts back into nanosized MnO with partial SEI decomposition.[77] Considering the electrochemical behaviour of these materials highlights the promise of this material as a conversion anode. In D. Zhan et al.'s study on biomass-derived MnO–C nanocomposites reliable cycling performance was observed after several hundred cycles which was ascribed to the carbon-rich framework from the biomass buffered the volume changes for the MnO

conversion reaction. The capacity of one of their MnO nanocomposites sat at 1326 $mAhg^{-1}$ with an initial coulombic efficiency of ~69 % in the first cycle.[78] For electrochemical investigations conducted by T. Wang et al., the initial discharge capacity observed for this nanocomposite was 1542 $mAhg^{-1}$ and the initial Coulombic efficiency was 64 %.[79] Morphological comparisons between electrochemical performances of MnO—C nanosheets formed from terephthalic acid and MnO—C microspheres have been done by J. Zhu et al, and it appeared that the nanosheets exhibited superior electrochemical performance to the microspheres. Their understanding of this superiority was due to the smaller sized MnO nanoparticles within the nanosheets that enabled more effective lithium diffusion than for the large MnO microspheres. Furthermore, in these investigations, first discharge of these samples aligns with those seen for the nanocomposites in this thesis with a significant voltage drop, to 0.25 V in this case, followed by a voltage plateau which is indicative of the reduction of $Mn^{2+}$ to Mn during the conversion reaction (as well as SEI formation). There is no plateau in the charge but rather an incline between 1 and 1.5 V which has been assigned to the oxidation of the manganese back to its divalent state.[80] For G. Nagajaru et al.'s MOF-derived nanocomposite electrodes, a great first cycle irreversible capacity loss was observed which was suspected to be due to the formation of the solid electrolyte interface layer in the initial discharge. After the first discharge there was no obvious plateau seen in the charge or discharge voltage curve for the nanocomposite. It was also observed that the discharge capacity of the MnO—C composite electrode increased after more cycles – which was thought to be due to electrode activation and stabilisation during cycling. At 100 cycles, the capacity was around 99.5% that of the original capacity, showing an impressive

retention rate. At 800 cycles, the capacity retention was around 89% - which still indicated an impressive retention for these materials, indicating the potential for $_{nano}$MnO─C composites to compete as an effective lithium-ion battery anode material.[81] As highlighted in these investigations, one significant feature to note when electrochemically testing MnO conversion anodes is that the capacity of the material far exceeds that of the expected theoretical value in the first cycle. This has been ascribed to the pulverisation of the crystalline material during this first cycle along with the reaction of the electrolyte at the surface of the anode to form the solid electrolyte interface (SEI), all contributing to this significant first cycle irreversible capacity loss for these materials.[79,82] Another phenomenon observed for MnO conversion anodes involves the increased capacity recorded during cycling, which investigators have ascribed to the oxidation of manganese to higher oxidation states during cell runtime.[77,82,83] To probe this further, an investigation by H. Liu et al. on MnO material involved assessment of the influence of Mn oxidation state on capacity behaviour by introducing transition metal composites, including as Co, Ni, and Cu, alongside the MnO structure to determine their impact on inhibition of manganese oxidation during cycling. Their results provided evidence for this phenomenon as the introduction of the transition metal interrupted the oxidation of the $Mn^{2+}$ during cycling which meant that the capacity behaviour could be adjusted.[83] Additional to this, theories for increased capacity include “activation and stabilization” within the anode during cycling, which can be ascribed to the continuous growth of a surface polymeric gel film during cycling, and/ or to capacitive lithium storage on the surface of the electrode and in these systems.[79,81,83]

### 1.5.6 $_{nano}$MnO─C composite synthesis

Within the literature, many experimentalists have explored synthetic routes to manufacture MnO─C nanocomposites for applications including lithium-ion battery anodes, supercapacitors, sensors, and water remediation materials.[78–82,84–87] One method for nanocomposite synthesis involve the use a carbon-rich precursors that are derived from biomass. For example, in 2 experiments conducted by D. Zhan et al. and Y. Lin et al. rice husks and camellia petals were used, respectively. After pretreatment of these biomass precursors (to remove unwanted organics, impurities etc.), they were each immersed in Mn acetate solutions to ensure the carbonaceous material was populated with manganese. In the calcination step of these experiments, the Mn-rich carbon materials heated in an inert atmosphere, leaving behind the desired $_{nano}$MnO─C composites.[78,85] In another investigation by T. Wang et al., MnO films were produced by synthesising a Mn oleate precursor in solution, which was then cast onto a substrate before heating in an inert atmosphere to produce the MnO-C nanocomposite. The oleate groups from the precursor were thermally decomposed into $CO_2$ which left behind the $_{nano}$MnO in the carbon framework.[79] Another well-documented method for $_{nano}$MnO─C composite synthesis involves the decomposition of a metal organic framework (MOF) precursor. In an investigation by P. Pachfule et al., a MOF precursor was a partially fluorinated Mn-metal organic framework (labelled Mn-HFMOF-D) whereas in a study by R. Wang et al., a Mn-MIL-100 MOF precursor was used. Both MOF precursors in their experiments were synthesised using solvent-based routes.[86,88,89] In both syntheses the respective Mn-MOFs were decomposed to form the $_{nano}$MnO─C composites, via a 900 °C heat treatment of the MOF in nitrogen/ air and a 700 °C calcination under

nitrogen with a 2-hour hold by P. Pachfule et al. and R. Wang et al., respectively.[86,90] In further MOF-derived $_{nano}$MnO─C composite experiments, J. Zhu et al. and G.Nagaraju et al. generated these materials for investigation as conversion anodes. As was the case for P. Pachfule et al. and R. Wang et al., the MOF precursors in these experiments were synthesised using solvent-based methods. In J.Zhu et al.'s experiments, the Mn-based MOF was synthesised using a trimesic and terephthalic acid precursors, as this afforded metal organic frameworks with differing morphological compositions, the former being a micro spherical Mn-based MOF and the latter being a nanosheet Mn-based MOF. To decompose the MOF structures to form the MnO-C material the precursors were heated to 700 °C for 3 hours under argon.[80] Terephthalic acid was also used for $_{nano}$MnO-C composite synthesis in this thesis, however a mechanochemical method was used to generate a MOF-like precursor rather than the solvent-based method used in J. Zhu et al.'s experiments – the decomposition conditions outlined in the aforementioned investigations were used to guide the experimental conditions explored within Chapter 5.

### 1.5.7 Mn oxalate conversion anodes

In the literature, there have been many investigations into Mn oxalate synthesis for an array of applications, including as precursor materials for oxide synthesis or as energy storage materials. When cycled electrochemically, Mn oxalate can be used a conversion anode which reversibly converts into a new product during cycling. In the literature, this reversible reaction has been described in equation 4.[72,91–94]

$$MnC_2O_4 + 2Li \leftrightarrow Li_2C_2O_4 + Mn \quad [4]$$

In previous studies of Mn oxalate anodes the oxalate source used for synthesis has been oxalic acid, as used in this chapter, however the Mn source and synthetic route vary greatly due to focus being placed on manipulation of Mn oxalate particle morphology in literature studies. Not only are the capacities reached for Mn oxalate far higher than the theoretical capacity calculated based on the Faradaic reaction (375 $mAhg^{-1}$), but these anodes have been known to increase in capacity while cycling. The origin of both these phenomena are yet to be fully understood, however it has been hypothesised that side reactions with the electrolyte, electrochemical activity of the conversion product ($Li_2C_2O_4$) and formation of a polymeric gel-like layer are all possible reasons for this increased capacity/ capacitive increase. [72,91–95] In studies between 2019 and 2023 by Y. Yang et al. Y. Duan at al., Y. Jia et al., and Y. Zhang et al., synthetic, and electrochemical performance investigations were made on Mn oxalate and transition metal-doped structures. In all cases, Mn oxalates (or TM─doped oxalates) were synthesised using a hydrothermal method that required Mn acetate Mn source and an oxalic acid oxalate source. In Y. Duan et al.'s study the oxalate source used was an oxalic acid dimethyl ester. In these studies, galvanostatic cycling voltage limits conditions discharged 0.001 or 0.01 V, but in all cases the cells were cycled to a 3 V maximum voltage.[72,93,95,96] As outlined in Yang et al.'s study in the first discharge there was a small plateau at 0.8 V, corresponding to solid electrolyte interphase formation, followed by a plateau in voltage at approximately 0.4 V, which corresponds to the reversible conversion of Mn oxalate, shown in equation 4. The slope down to the end of discharge from this plateau was assigned to a non-Faradaic Li storage mechanism which gave rise to pseudo capacitance. It was hypothesised that a surface gel-like film was formed on the electrode which caused

this. In all these studies, for the first cycle for each of these Mn oxalate half-cells, there was a huge first cycle irreversible capacity loss with first cycle coulombic efficiency as low as 29.4% in Y. Duan et al.'s study. This was hypothesised to be due a multitude of electrochemical characteristics, including the formation of $Li_2CO_4$ during discharge, radical volume changes from the active material pulverisation discharge during cycling, and due to side reactions in this first cycle – namely the reaction of the electrolyte on the anode surface to form solid electrolyte interphase (SEI). For the undoped Mn oxalates their capacities exceeded 1000 $mAhg^{-1}$ in the first discharge in all cases. In Y. Yang et al.'s study, Mn oxalate microtubes had an initial discharge capacity of 1287 $mAhg^{-1}$, and a first cycle coulombic efficiency of 48%. In Y. Zhang et al.'s investigations the first discharge capacities of these Mn oxalate samples of varying structures spanned capacities between 1061 and 1356 $mAhg^{-1}$. In Y. Jia et al.'s study the initial discharge capacity of the undoped material was as high as 1829 $mAhg^{-1}$, however the first cycle coulombic efficiency of this material was the poorest at 29.4%. [72,93,96] In all these studies, the cause of the capacity increase during cycling was the same – due to the reversible formation of a polymeric gel film that became activated during galvanostatic cycling of the Mn oxalate half-cells. The initial decrease in capacity during cycling was hypothesised to be due to impedance of Li diffusion through the polymeric gel film that had formed at the surface, but after several cycles this film was activated during electrochemical cycling. The growth of this film has been reported as a reversible phenomenon and this gives rise to (pseudo)capacitive Li storage – increasing the discharge capacity during cycling. Furthermore, it is determined by Y. Jia et al. that there is interaction between the organic oxalic framework and the Mn nanoparticles nano-particles

interact between themselves and the oxalate matrix, causing a catalytic effect for polymeric gel film formation. [72,93,95–97]

### 1.5.8 Oxalate contributions to capacity – combined cationic-polyanionic redox

In other oxalate-based electrochemical studies, there have been theories surrounding the involvement of the oxalate organic group in the high capacities achieved by the conversion anode. In a study by W. Song et al. a copper oxalate system was studied in a proton battery using an array of structural / imaging techniques, including Raman, X-ray photoelectron spectroscopy and XRD, amongst many others. It was found that during discharge both groups acting as synchronous redox centres in the system – not only was copper (II) reduced to Cu(0), as expected, but the C═O oxalate group also partially converted to C─O during discharge. This electrochemical activity provided this material with a maximum capacity of 350 $mAhg^{-1}$ which exceeded the capacity expected based on charge balancing with protons because of the involvement of the oxalate group in the increased capacity of this system. Though this study was for a proton battery and did not use a Mn transition metal source it is key to note the role of the oxalate as an oxidation centre in the setup.[98] In a study by W. Yao et al., an iron-based polyanionic system, $Li_2Fe(C_2O_4)_2$, was investigated and also found the involvement of oxalate in the redox activity of this material using techniques such as X-ray absorption and Raman spectroscopy. Again, the C═O oxalate group contributes to capacity by providing anionic redox alongside the cationic redox, which occurs without oxygen evolution due to the strong

covalency in the bonding of the polyanionic groups of the oxalate.[99] Though these oxalate systems are not precisely the same structure as the Mn oxalate outlined in Chapter 6, they provide evidence for the contribution of the oxalate group to half-cell capacity for these materials. This phenomenon, alongside the growth of an activated polymeric gel, could further explain the vast deviation from the theoretical capacity measured for the Mn oxalate half-cells.

### 1.5.9 Sustainable methods for Mn oxalate synthesis

To synthesise Mn oxalate all that is required is addition of a manganese-rich precursor and an oxalate anion source which, in the experiments outlined in this thesis, was $LiMn_2O_4$ and a 1.25 M solution of oxalic acid, respectively. Mn oxalate materials have traditionally been used as precursors for Mn oxides, as demonstrated in Chapter 4, and have frequently been overlooked as anode materials themselves, despite Mn oxalate having a similar theoretical capacity to graphite.[92] With effective extraction of Mn oxalate (or any appropriate Mn based precursor) from used LMO battery waste, upcycling Mn based material into a Mn oxalate conversion anodes has exciting potential, particularly if the oxalate source comes from a sustainable source. Worldwide there has been great global interest for carbon capture and utilisation technology as this can be used in an array of applications – one of which is the manufacture of oxalic acid. In 2008 a spin-out company from the University of Princeton, named Liquid Light, begun in-depth investigation of electrochemical conversion of $CO_2$ into major carbon-based chemicals. In 2017, this company was acquired by a chemical technology company, named Avantium, in order to harness

the experience in electrochemical conversion that Liquid Light had, and to utilise it to enhance Avantium's research and development into renewable production of major chemicals, including oxalic acid. [100,101] In recent years, Avantium have been working with the OCEAN project, a European Horizon project (funded by the European Research Institute of Catalysis) focussing on the electrochemical reduction of $CO_2$, for which they have developed demonstration plants for this carbon utilisation activity for oxalic acid production at scale.[102] As there is such a requirement for uptake of $CO_2$ in the current climate, and as deriving value from redundant Li-ion battery material is essential (and will continue to be the case as the LiB scrap pool grows), converting LMO battery waste into Mn oxalate provides a strong upcycling opportunity for LMO material, particularly if the oxalic acid source utilised carbon capture, and the energy required to do this came from a renewable resource.

## 1.6 Conclusions

With the global transition away from fossil fuels and the electrification of the transport, ESS and portables sectors, lithium-ion battery demand is surging and will continue to do so in upcoming years. With such a high number of lithium-ion batteries being manufactured and used within these sectors, there is going to be a significant amount of valuable process and end-of-life material set to enter the scrap pool in upcoming years. This means that the requirement for closed-loop recycling practice will increase in future, as legislative measures are put in place and component materials are depleted due to the mounting increase in LiB demand.[103] Though pyrometallurgy and hydrometallurgy are commercialised recycling technologies within the industry, there

are still shortcomings that need to be addressed, and direct recycling has not been implemented extensively on a commercial scale. One lesser researched Li-ion battery scrap treatment method is upcycling, which enables the reuse of discarded battery material to enhance its value, quality, and circularity. There is adequate upcycling research for NMC chemistries, but very little has been explored for LMO. As LMO is a common 1$^{st}$ generation LiB chemistry – it will be prevalent in the earlier EOL battery waste stream, therefore research into its recovery is essential for its imminence. Alongside this, there are a lack of alternative chemistries to graphite for anode usage. This material has a great capacity of 372 $mAhg^{-1}$; however, it has stringent morphological requirements which make recovery challenging. Furthermore, it is burnt off in pyrometallurgical processing which means adaptations/ alternatives must be used.[56] As recycling technology is currently targeted towards cathode material, it is remarkable that there is little focus on upcycling of lesser used cathode materials to manufacture new anode materials.

In this thesis, LMO is the material of choice for upcycling, as it is lesser used in current LiB applications and can be upcycled into exciting new materials with attractive electrochemical properties, which in this case are $_{nano}$MnO-C composite and Mn oxalate conversion anodes. Furthermore, finding an alternative anode material to graphite is of great concern – its near monopoly in the market will cause supply bottlenecks in future, and utilising redundant cathode material and keeping it within the battery supply chain provides great circularity in this process.

Much research has been done investigating the electrochemical behaviour of $_{nano}$-MnO–C composites and Mn oxalate conversion anodes, however the use of leached cathode material as a precursor to their synthesis has not been explored in either

case, due to the nascency of the lithium-ion battery recycling industry. Understanding how electrochemical performance of these leached materials compare to those from pristine sources will emphasise the value of upcycling.

With respect to $_{nano}$MnO-C composite anodes, syntheses have involved treatment of carbon-rich precursors derived from biomass, solvothermal methods, and inert atmosphere MOF degradation, to name a few. These synthetic routes are often moderately involved, therefore investigation of methods to streamline this synthesis further enhances the upcycling opportunity for redundant LMO cathode material.

Additionally, with respect to the Mn oxalate conversion anodes, manipulation of the electrochemical conditions required to stimulate the observed capacity increase have not been explored, nor have the electrochemical products formed in-situ, providing an enthralling avenue of research for these materials.

## 1.7 References


1 J.-M. Tarascon and M. Armand, *Nature*, 2001, **414**, 359–367.

2 H. Kawamura, M. LaFleur, K. Iversen and H. W. J. Cheng, *Lithium-Ion Batteries : a pillar for a fossil fuel free economy?*, 2021.

3 Transport and environment statistics 2022, https://www.gov.uk/government/statistics/transport-and-environment-statistics-2022/transport-and-environment-statistics-2022, (accessed 20 April 2023).

4 D. for B. E. and I. Strategy, 8th National Communication, https://unfccc.int/sites/default/files/resource/UKs 8th National Communication and 5th BR.pdf, (accessed 20 April 2023).

5 K. Ozawa, *Solid State Ionics*, 1994, **69**, 212–221.

6 L. Canals Casals, E. Martinez-Laserna, B. Amante García and N. Nieto, *J. Clean. Prod.*, 2016, **127**, 425–437.

7 A. Yoshino, in *Lithium-Ion Batteries: Advances and Applications*, Elsevier, 2014, pp. 1–20.

8 P. A. Nelson, K. G. Bloom and D. W. I Dees, *Modeling the performance and cost of lithium-ion batteries for electric-drive vehicles*, Chemical Sciences and Engineering Division Report, ANL-11/32, United States, 2011.

9 Jolanta Swiatowska and P. Barboux, in *Lithium Process Chemistry*, eds. A. Chagnes and J. Światowska, Elsevier Inc., 2015, pp. 125–166.

10 M. Contestabile, S. Panero and B. Scrosati, *J. Power Sources*, 2001, **92**, 65–

69.

11 S. Mandai, J. Manuel Amarilla, J. Ibanez and J. M. Rojo, *J. Electrochem. Soc.*, 2001, **148**, 24–29.

12 C. M. Costa, Y.-H. Lee, J.-H. Kim, S.-Y. Lee and S. Lanceros-Méndez, *Energy Storage Mater.*, 2019, **22**, 346–375.

13 A. N. Dey, *Thin Solid Films*, 1977, **43**, 131–171.

14 J. Popovic, in *Frontiers of Nanoscience*, Elsevier Ltd., 1st edn., 2021, vol. 19, p. 331.

15 A. Perner and J. Vetter, in *Advances in Battery Technologies for Electric Vehicles*, Elsevier Ltd., 2015, pp. 173–190.

16 Tesla, Q1 2022 Update, https://ir.tesla.com/press-release/tesla-releases-first-quarter-2022-financial-results, (accessed 20 February 2021).

17 S. Mao, Y. Zhang, G. Bieker and F. Rodriguez, Zero-emission bus and truck market in China : A 2021 update, https://theicct.org/publication/china-hvs-ze-bus-truck-market-2021-jan23/, (accessed 5 May 2022).

18 Y. Tao, Z. Wang, B. Wu, Y. Tang and S. Evans, *J. Clean. Prod.*, 2023, **389**, 136008.

19 U.S. Geological Survey, *Mineral Commodity Summaries 2022*, 2022.

20 H. Zou, E. Gratz, D. Apelian and Y. Wang, *Green Chem.*, 2013, **15**, 1183–1191.

21 S. F. Lux, J. Chevalier, I. T. Lucas and R. Kostecki, *ECS Electrochem. Lett.*,

2013, **2**, 2013–2016.

22 US Pat., US7820317B2, 2010.

23 H. Heimes, A. Kampker, C. Lienemann, M. Locke, C. Offermanns, S. Michaelis and E. Rahimzei, Lithium-ion battery cell production process, https://www.pem.rwth-aachen.de/global/show_document.asp?id=aaaaaaaaabdqbtk#:~:text=The production of the lithium,cell assembly and cell finishing., (accessed 5 May 2022).

24 Battery production scrap to be main source of recyclable material this decade, https://source.benchmarkminerals.com/article/battery-production-scrap-to-be-main-source-of-recyclable-material-this-decade, (accessed 26 February 2023).

25 International Energy Agency (IEA), Global EV Outlook 2022 - Securing supplies for an electric future, https://www.iea.org/reports/global-ev-outlook-2022, (accessed 8 July 2022).

26 D. for B. & Trade, UK Battery Strategy, https://www.gov.uk/government/publications/uk-battery-strategy, (accessed 4 January 2024).

27 K. Richa, C. W. Babbitt, G. Gaustad and X. Wang, *Resour. Conserv. Recycl.*, 2014, **83**, 63–76.

28 A. Mondal, Y. Fu, W. Gao and C. C. Mi, *Batteries*, 2024, **10**, 1–13.

29 MEPs want to strengthen new EU rules for design, production and disposal of batteries, https://www.europarl.europa.eu/news/en/press-

room/20220202IPR22435/meps-want-to-strengthen-new-eu-rules-for-batteries, (accessed 3 May 2023).

30 R. Sommerville, P. Zhu, M. A. Rajaeifar, O. Heidrich, V. Goodship and E. Kendrick, *Resour. Conserv. Recycl.*, 2021, **165**, 105219.

31 BASF to build commercial scale battery recycling black mass plant in Schwarzheide, Germany, https://www.basf.com/global/en/media/news-releases/2022/06/p-22-249.html, (accessed 3 May 2023).

32 Lithium Services, https://ecobat.com/our-business/ecobat-solutions/lithium-services/, (accessed 3 May 2023).

33 Delivering value through recovered materials and process innovation., https://li-cycle.com/products/#:~:text=mixed copper%2Faluminum.-,Battery Materials (Black Mass),as graphite%2C copper and aluminum., (accessed 3 May 2023).

34 POSCO builds EV battery recycling plant in Poland, https://newsroom.posco.com/en/posco-builds-ev-battery-recycling-plant-in-poland/, (accessed 3 May 2023).

35 The construction of Korean joint venture of Huayou Cobalt -- POSCO HY Clean Metal, was started!, https://en.huayou.com/news/600.html, (accessed 3 May 2023).

36 L. Gaines, *Sustain. Mater. Technol.*, 2018, **17**, e00068.

37 M. Roshanfar, R. Golmohammadzadeh and F. Rashchi, *J. Environ. Chem. Eng.*, 2019, **7**, 102794.

38 C. H. Jo and S. T. Myung, *J. Power Sources*, 2019, **426**, 259–265.

39 A. Vezzini, *Manufacturers, Materials and Recycling Technologies*, Elsevier, 2014.

40 D. P. Mantuano, G. Dorella, R. C. A. Elias and M. B. Mansur, *J. Power Sources*, 2006, **159**, 1510–1518.

41 L. Yang, G. Xi and Y. Xi, *Ceram. Int.*, 2015, **41**, 11498–11503.

42 R. C. Wang, Y. C. Lin and S. H. Wu, *Hydrometallurgy*, 2009, **99**, 194–201.

43 E. Gratz, Q. Sa, D. Apelian and Y. Wang, *J. Power Sources*, 2014, **262**, 255–262.

44 Q. Sa, E. Gratz, M. He, W. Lu, D. Apelian and Y. Wang, *J. Power Sources*, 2015, **282**, 140–145.

45 M. Chen, Z. Zheng, Q. Wang, Y. Zhang, X. Ma, C. Shen, D. Xu, J. Liu, Y. Liu, P. Gionet, I. O'Connor, L. Pinnell, J. Wang, E. Gratz, R. Arsenault and Y. Wang, *Sci. Rep.*, 2019, **9**, 1–9.

46 Y. Shi, G. Chen and Z. Chen, *Green Chem.*, 2018, **20**, 851–862.

47 P. Xu, Z. Yang, X. Yu, J. Holoubek, H. Gao, M. Li, G. Cai, I. Bloom, H. Liu, Y. Chen, K. An, K. Z. Pupek, P. Liu and Z. Chen, *ACS Sustain. Chem. Eng.*, 2021, **9**, 4543–4553.

48 X. Yu, S. Yu, Z. Yang, H. Gao, P. Xu, G. Cai, S. Rose, C. Brooks, P. Liu and Z. Chen, *Energy Storage Mater.*, 2022, **51**, 54–62.

49 F. Maisel, C. Neef, F. Marscheider-weidemann and N. F. Nissen, *Resour. Conserv. Recycl.*, 2023, **192**, 106920.

50 PNE Novel Plasma-Based Recycling Technology, https://pnecycle.com/pne-novel-plasma-based-recycling-technology/, (accessed 2 May 2023).

51 V. P. Parikh, A. Ahmadi, M. H. Parekh, F. Sadeghi and V. G. Pol, *Environ. Sci. Technol.*, 2019, **53**, 3757–3763.

52 T. Wang, H. Luo, J. Fan, B. P. Thapaliya, Y. Bai, I. Belharouak and S. Dai, *iScience*, 2022, **25**, 103801.

53 G. Qian, Z. Li, Y. Wang, X. Xie, Y. He, J. Li, Y. Zhu, S. Xie, Z. Cheng, H. Che, Y. Shen, L. Chen, X. Huang, P. Pianetta, Z. F. Ma, Y. Liu and L. Li, *Cell Reports Phys. Sci.*, 2022, **3**, 100741.

54 L. L. Driscoll, A. Jarvis, R. Madge, J. Price, R. Sommerville, F. S. Totini, M. Bahri, B. L. Mehdi, E. Kendrick, N. D. Browning, P. K. Allan, P. A. Anderson and P. R. Slater, *ChemRxiv*.

55 H. Shi, J. Barker, M. Y. Saïdi, R. Koksbang and L. Morris, *J. Power Sources*, 1997, **68**, 291–295.

56 T. Zheng and J. R. Dahn, *Applications of Carbon in Lithium-Ion Batteries*, Elsevier Science Ltd, 1999.

57 U.S. Geological Survey, GRAPHITE ( NATURAL ), https://pubs.usgs.gov/periodicals/mcs2023/mcs2023-graphite.pdf, (accessed 20 April 2023).

58 H. O. Pierson, in *Handbook of Carbon, Graphite, Diamonds and Fullerenes*, ed. H. O. Pierson, William Andrew Publishing, 1993, pp. 87–121.

59 M. Mundszinger, S. Farsi, M. Rapp, U. Golla-Schindler, U. Kaiser and M.

Wachtler, *Carbon N. Y.*, 2017, **111**, 764–773.

60 Metastable Materials commissions chemical-free recycling unit for dead lithium batteries, https://www.pv-magazine-india.com/2022/10/07/metastable-materials-commissions-chemical-free-recycling-unit-for-dead-lithium-batteries/, (accessed 8 November 2022).

61 A. T. Sargent, Z. Henderson, A. S. Walton, B. F. Spencer, L. Sweeney, W. R. Flavell, P. A. Anderson, E. Kendrick, P. R. Slater and P. K. Allan, *J. Mater. Chem. A*, 2023, **11**, 9579–9596.

62 X. Rui, Y. Geng, X. Sun, H. Hao and S. Xiao, *Resour. Conserv. Recycl.*, 2021, **173**, 105732.

63 I. Rey, C. Vallejo, G. Santiago, M. Iturrondobeitia and E. Lizundia, *ACS Sustain. Chem. Eng.*, 2021, **9**, 14488–14501.

64 D. Yang, Y. Yang, H. Du, Y. Ji, M. Ma, Y. X. Q. Pan, Q. Sun, K. Shi and L. Qie, *Green Energy Environ.*, , DOI:10.1016/j.gee.2022.11.003.

65 Y. T. Lee, C. T. Kuo and T. R. Yew, *ACS Appl. Mater. Interfaces*, 2021, **13**, 570–579.

66 L. Wang, L. Li, H. Wang, J. Yang, F. Wu and R. Chen, *ACS Appl. Energy Mater.*, 2019, **2**, 5206–5213.

67 K. Cao, Y. Jia, S. Wang, K. J. Huang and H. Liu, *J. Alloys Compd.*, 2021, **854**, 157179.

68 F. Ma, A. Yuan and J. Xu, *ACS Appl. Mater. Interfaces*, 2014, **6**, 18129–18138.

69 J. Libich, J. Máca, J. Vondrák, O. Čech and M. Sedlaříková, *J. Energy Storage*, 2017, **14**, 383–390.

70 B. Wang, F. Li, X. Wang, G. Wang, H. Wang and J. Bai, *Chem. Eng. J.*, 2019, **364**, 57–69.

71 J. Yoon, W. Choi, H. Kim, Y. S. Choi, J. M. Kim and W. S. Yoon, *J. Power Sources*, 2021, **493**, 229682.

72 Y. Yang, L. He, J. Lu, Z. Liu, N. Wang, J. Su, Y. Long, X. Lv and Y. Wen, *Electrochim. Acta*, 2019, **321**, 134673.

73 Y. Liu, X. Zhao, F. Li and D. Xia, *Electrochim. Acta*, 2011, **56**, 6448–6452.

74 K. Zhong, X. Xia, B. Zhang, H. Li, Z. Wang and L. Chen, *J. Power Sources*, 2010, **195**, 3300–3308.

75 X. Hua, P. K. Allan, H. S. Geddes, E. Castillo-Martínez, P. A. Chater, T. S. Dean, A. Minelli, P. G. Bruce and A. L. Goodwin, *Cell Reports Phys. Sci.*, 2021, **2**, 100543.

76 X. Hua, P. K. Allan, C. Gong, P. A. Chater, A. W. Robertson, P. G. Bruce, A. L. Goodwin, E. M. Schmidt and H. S. Geddes, *Nat. Commun.*, 2021, **12**, 1–11.

77 J. Liu and Q. Pan, *Electrochem. Solid-State Lett.*, 2010, **13**, A139.

78 D. Zhan, W. Luo, H. B. Kraatz, M. Fehse, Y. Li, Z. Xiao, D. F. Brougham, A. J. Simpson and B. Wu, *ACS Omega*, , DOI:10.1021/acsomega.9b03026.

79 T. Wang, Z. Peng, Y. Wang, J. Tang and G. Zheng, *Sci. Rep.*, 2013, **3**, 1–9.

80 J. Zhu, X. Zuo, X. Chen and Y. Ding, *Synth. Met.*, 2021, **280**, 116872.

81 G. Nagaraju, P. Santhoshkumar, S. C. Sekhar, B. Ramulu, M. Nanthagopal, P. S. S. Babu, C. W. Lee and J. S. Yu, *J. Power Sources*, 2022, **549**, 232113.

82 R. Jiao, L. Zhao, S. Zhou, Y. Zhai, D. Wei, S. Zeng and X. Zhang, *Nanomaterials*, 2020, **10**, 1–16.

83 H. Liu, W. Zhang, Z. Guan, N. Li, J. Wang, S. Zhang, Y. Du, J. Wang and F. Dan, *ACS Appl. Energy Mater.*, 2021, **4**, 12662–12670.

84 M. I. Said, *Solid State Sci.*, 2020, **108**, 106383.

85 Y. Lin, S. Zhao, J. Qian, N. Xu, X. Q. Liu, L. B. Sun, W. Li, Z. Chen and Z. Wu, *J. Mater. Sci.*, 2020, **55**, 2139–2154.

86 B. R. Wang, Y. Hu, Z. Pan and J. Wang, *RSC Adv.*, 2020, **10**, 34403–34412.

87 R. Su, Z. Wang, M. Zhao, F. Xiao, L. Zhang, L. Yang, Z. Wu, J. Bai and P. He, *J. Alloys Compd.*, 2023, **968**, 171896.

88 P. Pachfule, R. Das, P. Poddar and R. Banerjee, *Inorg. Chem.*, 2011, **50**, 3855–3865.

89 H. Reinsch and N. Stock, *CrystEngComm*, 2013, **15**, 544–550.

90 C. Nanoscale, R. Das, P. Pachfule, R. Banerjee and P. Poddar, 2012, 591–599.

91 A. N. Puzan, V. N. Baumer, D. V. Lisovytskiy and P. V. Mateychenko, *J. Solid State Chem.*, 2018, **260**, 87–94.

92 Y. N. Zhang, S. S. Li, H. X. Kuai, Y. F. Long, X. Y. Lv, J. Su and Y. X. Wen, *RSC Adv.*, 2021, **11**, 23259–23269.

93 Y. Jia, A. Cheng, W. Ke, J. Liu, S. Wang, Y. Zhao, Q. Yang and J. Zhang, *Electrochim. Acta*, 2021, **380**, 138217.

94 Y. Zhang, L. jin Wei, Z. Z. Liu, J. Su, Y. F. Long, X. Y. Lv and Y. X. Wen, *Ionics (Kiel).*, 2022, **28**, 3603–3614.

95 Y. Duan, Z. Huang, X. Dong, J. Ren, L. Lin, S. Wu, R. Jia and X. Xu, *J. Solid State Chem.*, 2022, **306**, 122728.

96 Y. Zhang, L. jin Wei, Z. Z. Liu, J. Su, Y. F. Long, X. Y. Lv and Y. X. Wen, *Ionics (Kiel).*, 2022, **28**, 3603–3614.

97 Y. He, D. Zeng, X. Huang, X. Chen, L. Lu and L. Xue, *J. Mater. Sci. Mater. Electron.*, 2023, **34**, 1–12.

98 W. Song, J. Zhang, C. Wen, H. Lu, C. Han, L. Xu and L. Mai, *J. Am. Chem. Soc.*, 2024, **146**, 4762–4770.

99 W. Yao, A. R. Armstrong, X. Zhou, M. T. Sougrati, P. Kidkhunthod, S. Tunmee, C. Sun, S. Sattayaporn, P. Lightfoot, B. Ji, C. Jiang, N. Wu, Y. Tang and H. M. Cheng, *Nat. Commun.*, 2019, **10**, 1–9.

100 Avantium Acquires Liquid Light, https://www.avantium.com/press-releases/avantium-acquires-liquid-light/, (accessed 3 July 2023).

101 Method and system for production of oxalic acid and oxalic acid reduction products, https://patents.google.com/patent/US9267212B2/en, (accessed 3 July 2023).

102 Oxalic acid from CO2 using Eletrochemistry At demonstration scale, https://cordis.europa.eu/project/id/767798, (accessed 3 July 2023).

103 C. Xu, Q. Dai, L. Gaines, M. Hu, A. Tukker and B. Steubing, *Commun. Mater.*, 2020, **1**, 1–10.

# 2 Aims

Though there has been extensive research into recycling of spent battery materials in the literature, very little research has been done on upcycling electrodes and, notably, on upcycling of spent LMO cathode material. Exploring routes to extract this dated cathode material and exploring methodologies to showcase the potential of the derived Mn-based materials from outmoded LMO cathodes will be studied extensively in this thesis.

Experiments outlined in Chapter 4 aim to investigate selective extraction of LMO from spent cathode material and the effectiveness of interconversion of this material into Mn oxalate, $Mn_2O_3$ and $Mn_3O_4$. To contextualise this, leached materials will be compared to their pristine counterparts to determine whether this interconversion route is effective in upcycling LMO into the desired Mn-based materials.

In Chapter 5, synthesis and electrochemical studies of $_{nano}$MnO-C composites will be explored. As outlined in section 1.5.6, synthesis of $_{nano}$MnO-C composites from MOF precursors involves complex solvothermal routes and little investigation has been done into mechanochemical synthesis of these materials. The first aim of this Chapter is therefore to determine a synthetic route that will streamline this manufacturing process significantly, emphasising the upcycling opportunity for this material. Secondly, the leached Mn oxalate materials derived in Chapter 4 will be used to manufacture these nanocomposites, and the electrochemical performance of these materials will be compared with that of the pristine equivalent, with the aim of demonstrating the effectiveness of these nanocomposites as conversion anode materials.

Finally, experiments outlined in Chapter 6 aim to develop understanding into the in-situ mechanism of Mn oxalate conversion, using in-situ pair distribution function (PDF) and galvanostatic cycling experiments. Furthermore, comparison of the electrochemical behaviour of Mn oxalate conversion anodes from pristine versus leached material sources will be investigated, in the aim of further indicating the success of upcycling LMO into this conversion anode material.

# 3 Experimental

## 3.1 Table of Figures

## 3.2 Crystallography and x-ray diffraction

'Crystallography' refers to the study of crystal structures and their properties. Crystallography was discovered in the early 1900s by Knipping and Friedrich using basic x-ray experiments, in which they also verified the nature of x-rays and x-ray diffraction (outlined further in section 3.2.2).[104] There are multiple sophisticated crystallographic techniques which use diffraction of radiation to characterise crystal structures. The most used radiation source, outlined in this chapter, is x-ray radiation however neutron and electron beams may also be used.

### 3.2.1 Crystal structures

Solids are crystalline materials when they are composed of a regular repeating arrangement of atoms or molecules with long-range order. The crystal structure of a material refers to the regular arrangement of atoms in a crystal lattice. The smallest repeating unit of the crystal structure is known as the unit cell, for which lattice points are repeated in three dimensions to form a full lattice. The origin of the unit cell is arbitrary. As depicted in Figure 3.1 for a cubic unit cell, the edges of the unit cell are defined by a, b and c, and the angles between edges by α, β and γ.[104,105] There are only 7 permitted unit cell shapes, or crystal systems, whose parameters are listed in Table 3.1.[106] In conjunction with the cell centring (for which the most common are body-centred cubic, hexagonal close packed and cubic close packed) there are 14 different Bravais lattices that exist in three-dimensional space. A 'Bravais lattice' refers to the number of lattices that can fill three dimensions using repeating unit cell units without overlap.[105]

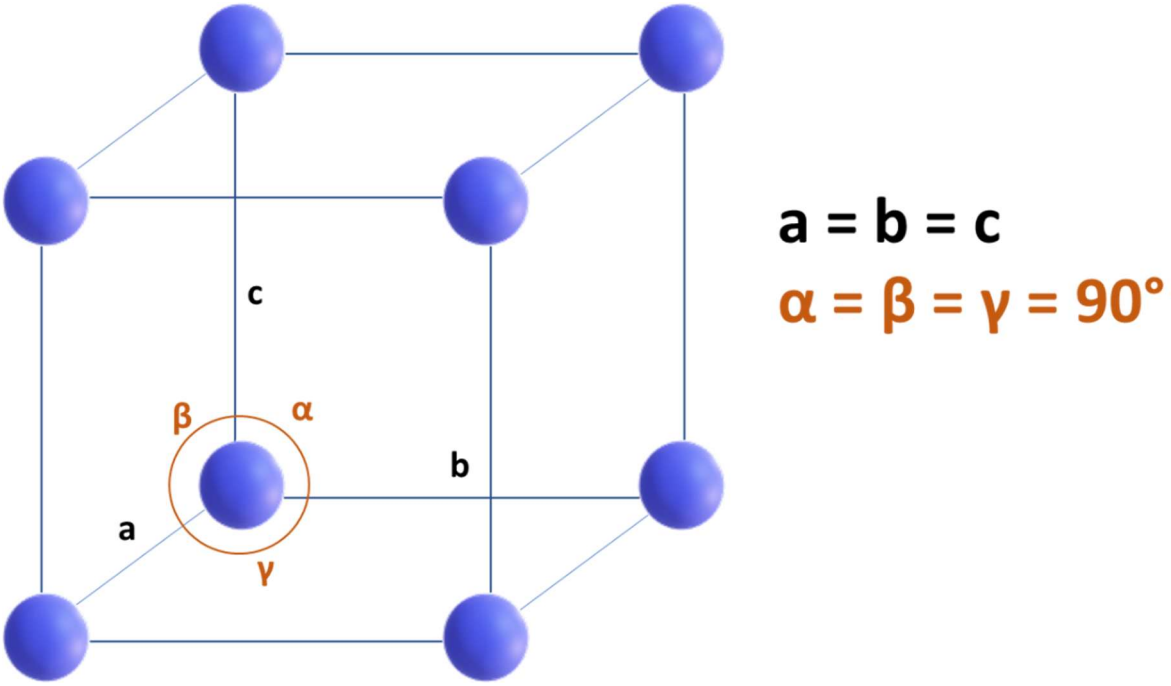


*Figure 3.1. Unit cell and parameters for the cubic crystal system*

*Table 3.1. The 7 crystal systems and their unit cell parameters* [106]

| Crystal system | Unit cell parameters | |
|---|---|---|
| | **α, β and γ** | **a, b and c** |
| **Triclinic** | No restrictions | No restrictions |
| **Monoclinic** | α = γ = 90° | No restrictions |
| **Orthorhombic** | α = β = γ = 90° | No restrictions |
| **Tetragonal** | α = β and γ = 90° | a = b |
| **Trigonal** | No restrictions | a = b = c |
| **Hexagonal** | α = β = 90° | a = b |
| **Cubic** | α = β = γ = 90° | a = b = c |

### 3.2.2 Laboratory x-ray diffraction (XRD)

XRD of a powder enables phase identification, purity, and unit cell parameters of crystalline materials to be determined by use of monochromatic x-rays. These x-rays are generated by firing electrons at a target metal anode. The anode is metal as it must be conductive to electrons; the most used metal target is copper, as it gives a sufficiently short wavelength (λ = 1.54056 Å). Copper, however, is not always an appropriate anode material, as for compounds containing iron, cobalt and manganese, significant background is observed in the XRD patterns because of fluorescence. To overcome this issue, a cobalt or iron anode is often used (λ = 1.78897 Å).[107] When these generated x-rays are targeted at a crystalline sample, the atoms within the sample (ordered in a regular arrangement), act as a diffraction grating for the x-ray beam – on reaching the sample, the x-rays diffract. In this process, constructive interference between diffracted x-rays arises when they are 'in-phase' with one another. To be considered 'in-phase', the beams must have a path length difference that is equivalent to a whole number of wavelengths. The XRD pattern comprises a series of peaks (or reflections) that arise when the diffracted x-rays reach the detector at an angle which satisfies Bragg's law, depicted in Figure 3.2 and equation 5. In the equation: n is an integer value, λ is the X-ray wavelength, d is the distance between lattice planes, (or path difference) and θ is the angle between the incident ray and the plane of scattering.

$$n\lambda = 2dsin\theta \qquad [5]$$

Due to the vast number of planes within a crystalline lattice, there are several diffraction peaks observed in an XRD pattern, as there are several occasions where

Bragg's Law is satisfied for a set of planes. When the x-ray beam is diffracted by a crystal, the detector records a series of 'spots' from the diffracted beams to generate a diffraction pattern, and all the information about the atomic positions of the atoms within a given lattice are resolvable from this pattern.[108] In the standard room temperature laboratory XRD experiments outlined in the thesis, the diffractometer used was a Bruker D2 Phaser diffractometer, which has a Co x-ray source and a β filter. A The use of a Co x-ray source was appropriate as all the compounds under analysis were rich in manganese. The use of a filter was necessary to ensure that only the wanted high intensity Kα radiation was utilized for the XRD analysis.[109] For peak indexing to take place, patterns were collected between 2θ values across the range of 10 – 100 °.  The XRD was performed in reflection mode, and samples were spun at 15 rpm. The scan duration varied between the timescale of 30 minutes (for simple pattern matching purposes) and 12 hours (for use in Rietveld refinements, outlined in section 3.2.3).

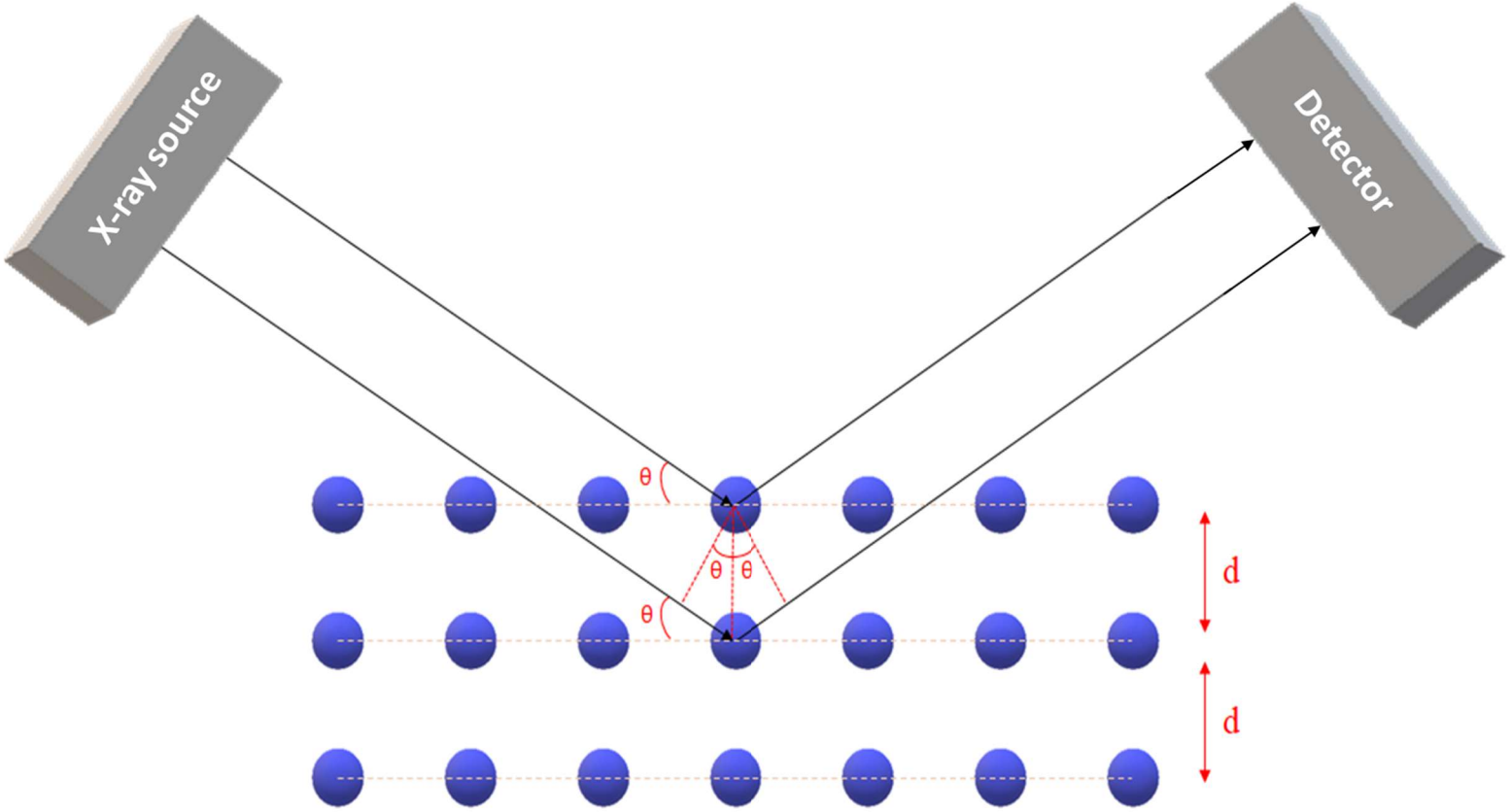


*Figure 3.2. d-spacing between lattice planes is used for crystal identification, by use of incident x-rays which are fired at the sample. The incident angle is measured and detected, and Bragg's law is used to determine the d-spacing between the planes*

### 3.2.3 Rietveld refinement

In order to determine lattice parameter data from the XRD patterns, Rietveld refinement was used, via the programme GSAS.[110] This refinement technique is ideal for crystalline powders as it distinguishes between overlapping Bragg peaks in an XRD pattern using the least squares method. During each refinement, differences between the measured experimental data (from a 12-hour XRD scan in each case) and a reference model pattern, taken from a scientific database, are minimised. In each case, factors such as pattern peak shape, sample displacement, sample micro strain, alongside numerous other features of the material under analysis, are used to fit the experimental data to the model and extract the lattice parameters. The sample position is an example of one property of the sample that is refined during the calculation. During the Rietveld refinement, intensities and peak profiles of the peaks are reproduced, which can be defined by the structure of the material and through the instrument used. To reduce the number of variables to be refined during the Rietveld refinement, an instrument parameter is used, which is measured prior to the refinement and gives rise to the instrumental configuration. This means that during the refinement of the sample of interest, instrumental parameters are set and sample-specific calculations (such as micro strain and crystallite size of the sample under analysis) can be modelled in situ to determine the lattice parameter data. Once fitted, there are an array of validation indicators that can be utilised to help determine the success/progression of the fitting, including $R_{wp}$, $R_{exp,}$ and $\chi^2$. $R_{wp}$ refers to the weighted profile factor, $R_{exp}$ refers to the expected R factor, and $\chi^2$ to the goodness of fit, where $\chi$ is equal to the weighted profile factor divided by the expected factor. The calculated R factors are to be as low as possible and $\chi^2$ should fall as closely to one as possible

to indicate a decent fit. In these experiments, the weighted R factor is shown in the experimental tables as this is considered to be the most important reliability factor of these parameters, with a lower value indicating a better fit in conjunction with the other validation indicators.[111]

## 3.3 Synchrotron light sources

### 3.3.1 What is a synchrotron?

A synchrotron is a particle accelerator that accelerates electrons through arrangements of magnets around a ring until they reach velocities close to the speed of light.[112] A general diagram of a synchrotron x-ray source is shown in Figure 3.3. To generate synchrotron radiation, an electron gun is used to fire electrons under vacuum through a linear accelerator which leads into a booster ring, where electrons are accelerated to near the speed of light, before being injected into a storage ring which is joined up using a series of bending magnets. The electrons are injected into the storage ring at 10-minute intervals to minimise the effect of energetic losses. As these high velocity electrons move around the ring they emit high energy light (known as synchrotron light) as they are bent by the magnetic field within this ring.[113] At regular intervals around the spherical particle accelerator is a beamline, which utilises the tuneable synchrotron light for tailored experiments. In this project Diamond Light Source (UK), used a synchrotron light source to generate tuneable beams of light with high-energy/ brilliance for experimentation. Modern third generation synchrotrons utilise insertion devices, mainly undulators (although sometimes they may use wigglers), to cause oscillation of electrons within a

generated magnetic field at straight portions of the ring. If the amplitude of the oscillation is small enough, then they can generate an in-phase series of wavelengths and a tuneable x-ray beam that can be utilised by experimentalists for an array of experiments, including diffraction and pair distribution function analysis. The tuneability of this beam and its high brilliance means that determination of the local order of samples is facilitated with synchrotron radiation.[114] The experiments conducted at Diamond were done on a dedicated beamline – the I15-1 x-ray Pair Distribution Function (XPDF) beamline.[12] The theory of pair distribution function is outlined in section 3.4.

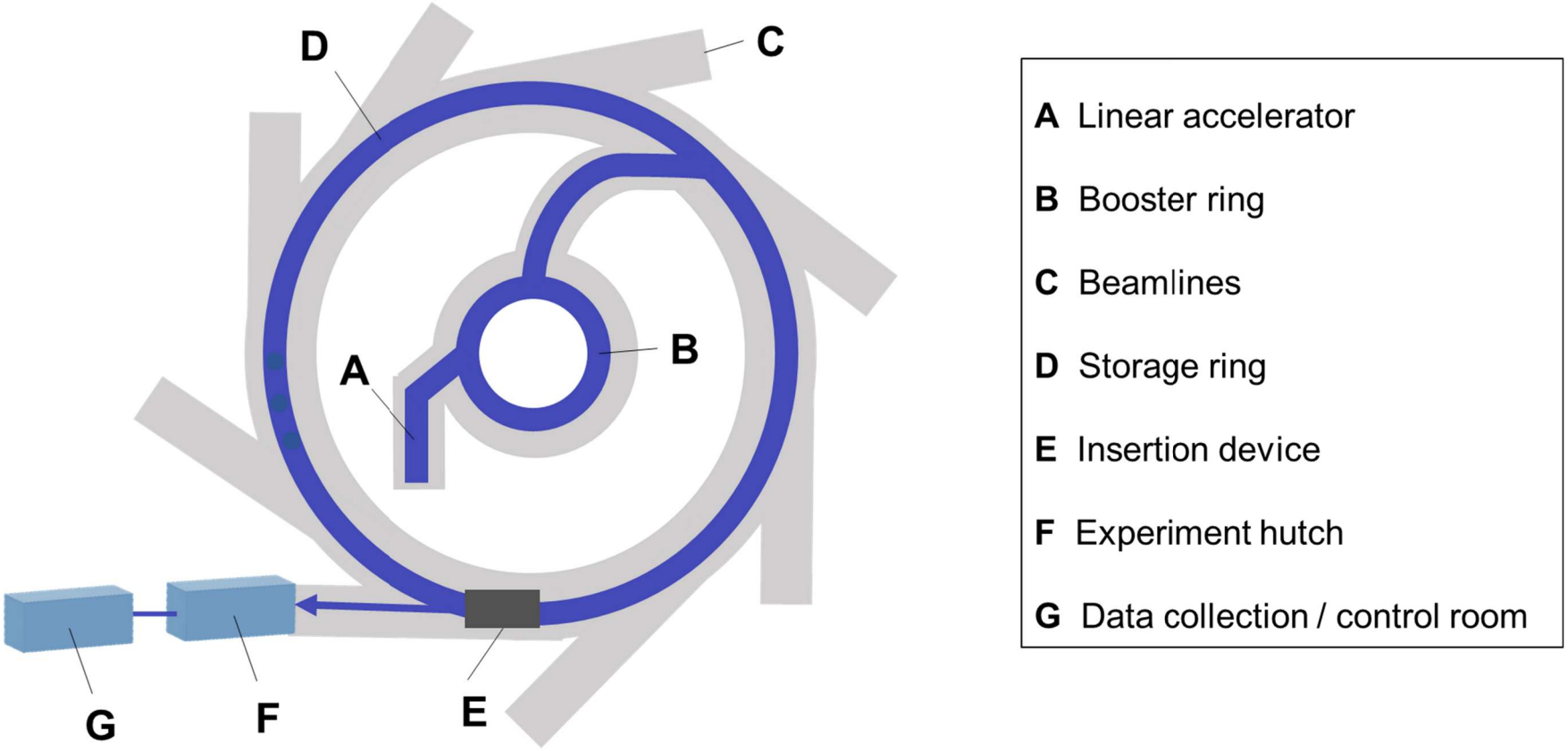


*Figure 3.3. Labelled diagram showing the main features and layout of a synchrotron x-ray source*

### 3.3.2 Synchrotron radiation for in-situ experiments

To develop chemical understanding of the reactions occurring in lithium-ion batteries, synchrotron x-ray analysis has proven to be extremely valuable. Information regarding degradation mechanisms, electrochemical products and charge storage mechanisms can be uncovered in operando/ in-situ synchrotron experiments using high energy radiation generated at these facilities. Instantly probing the reaction taking place during battery runtime provides a more reliable idea of the chemical reactions occurring due to electrochemistry alone.[117] The frequent measurements taken in operando/in-situ experiments provide equally spaced data points that enable precise and accurate data analysis, which in turn gives a reliable idea of how the electrochemical conversion reaction is happening at a given time/ point within the experimental voltage window. Additionally, any short-lived phases are immeasurable ex-situ (due to the requirement for cell disassembly) can be identified through this technique. The results from this are valuable in predicting and elucidating common electrode material conversion reactions and products during cell cycling which is vital for the experiments outlined in this thesis.

### 3.3.3 In-situ data collection at Diamond – the DRIX cell

At Diamond Light Source, a Diamond radial in-situ x-ray (DRIX) cell was used to analyse the electrochemical behaviour of selected materials during cycling. The DRIX cell is illustrated in Fig. 3.4 and has a radial geometry cell which facilitates the focus of the x-ray beam on the sample within a quartz capillary that has been stacked and compressed between two current collector rods which, in these experiments, were

composed of stainless steel. The cell facilitates the observation of the active material layer during battery runtime and reduces the interference of other components within the battery with the in-situ scan, due to the DRIX cell being placed parallel to the x-ray beam which enables isolation of each Li / separator/ active material layer within the measurement. Due to the requirement for isolation of the active material layer, the active material required a thickness of at least 100 microns, as depicted in Fig. 3.4. Stainless steel was the only available current collector that was suitable for use in these experiments due to its electrochemical inertness in the voltage ranges being studied, however, this metal is known to be highly scattering which causes sloping in the background of the resultant x-ray diffraction data. Though this cannot be eliminated in this setup, the DRIX cell has been designed to minimise the effects of current collector interference, which facilitates more straightforward correction of the collected data and better accuracy in the data produced. The quartz capillary body in the DRIX cell is kept airtight setup by use of two Swagelok unions to keep the system sealed. The design of this cell setup reduces the likelihood of parasitic scattering by keeping the number of optical elements before the target sample as minimal as possible. Furthermore, this setup also minimises absorption from the cell, while enabling collection of high-quality total scattering and PDF data, which is essential to ensure that short-range order features, such as amorphous phases that are vital to observe in the experiments outlined in this thesis, are collectable in a matter of minutes.[117]

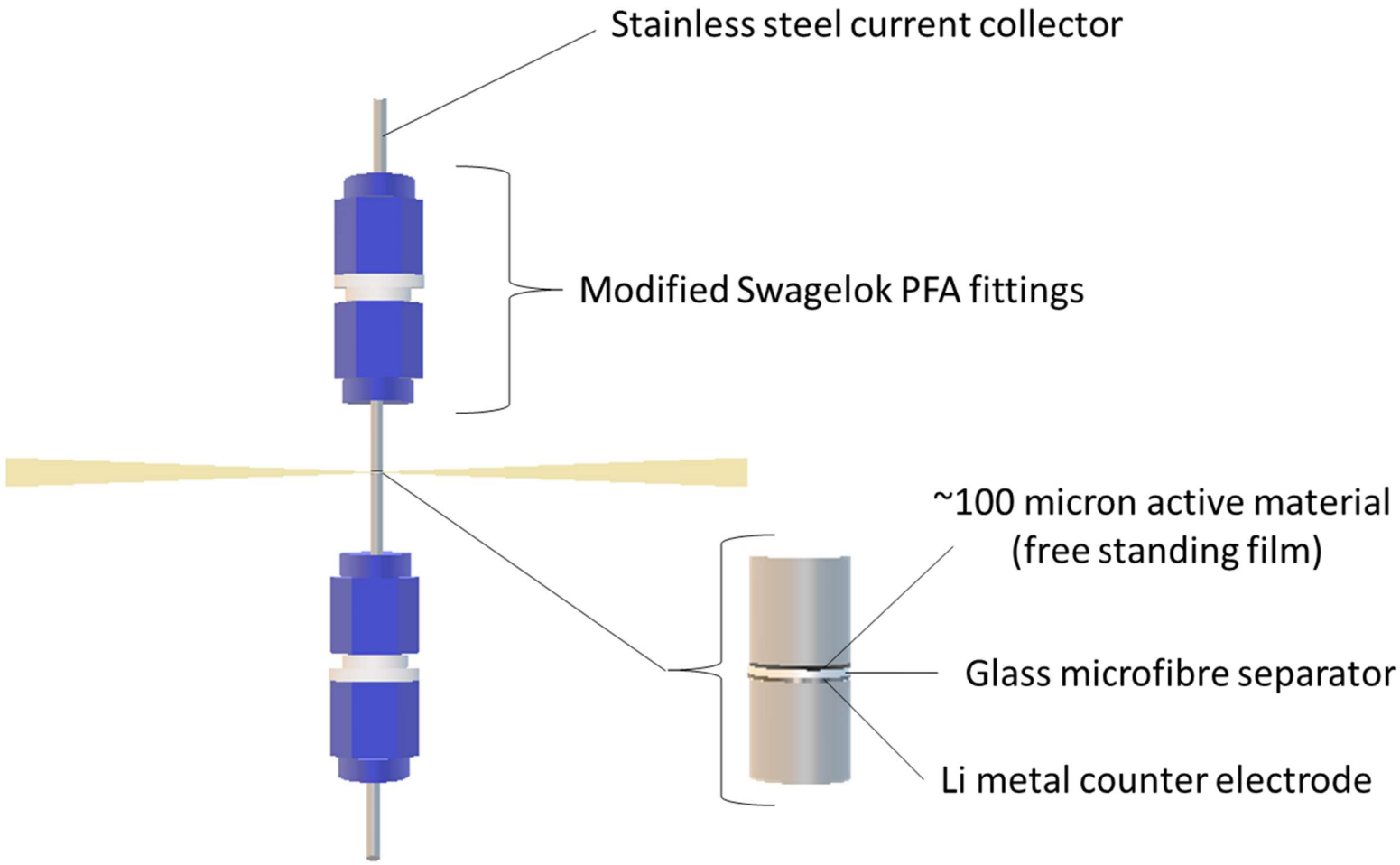


Figure 3.4. Diamond Light Source's DRIX cell setup. Diagram based off one from "Fast operando X-ray pair distribution function using the DRIX electrochemical cell" from M. Diaz-Lopez et. al.[117]

## 3.4 Pair distribution function (PDF)

Pair distribution function (PDF) analysis is a technique used to probe the structure of a material on the atomic scale. As stated in the section 3.2.2 – when x-rays are targeted at a crystalline solid the interatomic distance between atoms in each plane act as a grating for x-rays to diffract. As a result of this, the generated diffraction pattern is a Fourier transformation of the interatomic distances within this 'grating'. PDF is based on the collection of an XRD pattern which is then Fourier transformed to provide information on the spacing between atoms within the sample – the distribution shown in a PDF pattern shows the radial distance r (in Angstroms, Å) of atom pairs with respect to an average atom located at the origin. To obtain this information, high energy x-rays are required, which is why PDF data is predominantly collected at synchrotron x-ray sources. PDF analysis not only takes into account the Bragg peaks and the diffuse scattering within the diffraction pattern – the analysis of the diffuse scattering enables experimentalists to analyse irregular interatomic distances that are not collected using Bragg peaks within XRD analysis.[118] In crystallographic PDF analysis, the ability to use the diffuse scattering to determine interatomic distances at short-range order means this technique can be used to gain insight into the structure of nanosized samples, or those with localised defects/ vacancies, as these features do not give rise to sharp diffraction peaks due to their lack of long-range order. In a PDF distribution, the y axis shows G*(r)* which represents the number of atoms in a spherical shell of unit thickness at a distance r from the reference atom (at the origin). Equation 6 exhibits G*(r)*, where ρ(r) and $\rho_o$ correspond to the local and average atomic number densities, respectively.[119]

$$G(r) = 4\pi r[\rho(r) - \rho_o] \quad [6]$$

## 3.5 Electrochemical testing

### 3.5.1 CR2032 half-cell synthesis

In these experiments, the manganese-based materials were employed as working electrodes for non-aqueous half-cell testing to analyse their electrochemical behaviour vs Li/ $Li^+$. To synthesise electrode slurries, sodium carboxymethyl cellulose binder (CMC) was first dissolved into deionised water using a THINKY centrifugal mixer at a speed of 1300 rpm for 10 minutes. After this, carbon black (CB) was added to the slurry along with more deionised water and centrifuged for a further 10 minutes at 1300 rpm. Once these had mixed effectively, the Mn-based active material was added with the appropriate amount of water and centrifuged for a further 10 minutes at 1300 rpm, before one final degassing step at 1800 rpm for 3 minutes. The slurry was then coated onto a sheet of copper foil with a thickness of 15 microns. Unless stated otherwise, all films used in these experiments used an 80:10:10 ratio of active material: CB: CMC. this coating was dried for 2 hours in a fume hood at 80 °C, before being transferred to a vacuum oven for 24 hours 110 °C to completely dry the film under vacuum. Once dried, 14 mm diameter discs of the given anode material were cut, and these electrode discs were then transferred into an inert atmosphere glovebox for subsequent coin cell assembly. The CR2032-type coin cells were assembled as per the schematic outlined in Fig. 3.5, with a Li metal counter electrode. The composition/ concentration of the electrolyte used was (1.0 M $LiPF_6$ EC:DEC = 50:50). Once assembled and crimped in the glovebox, the coin cells were

rested for 16 hours, to ensure electrolyte wetting had occurred sufficiently. The cells were then galvanostatically cycled using a Biologic VPM3 potentiostat.

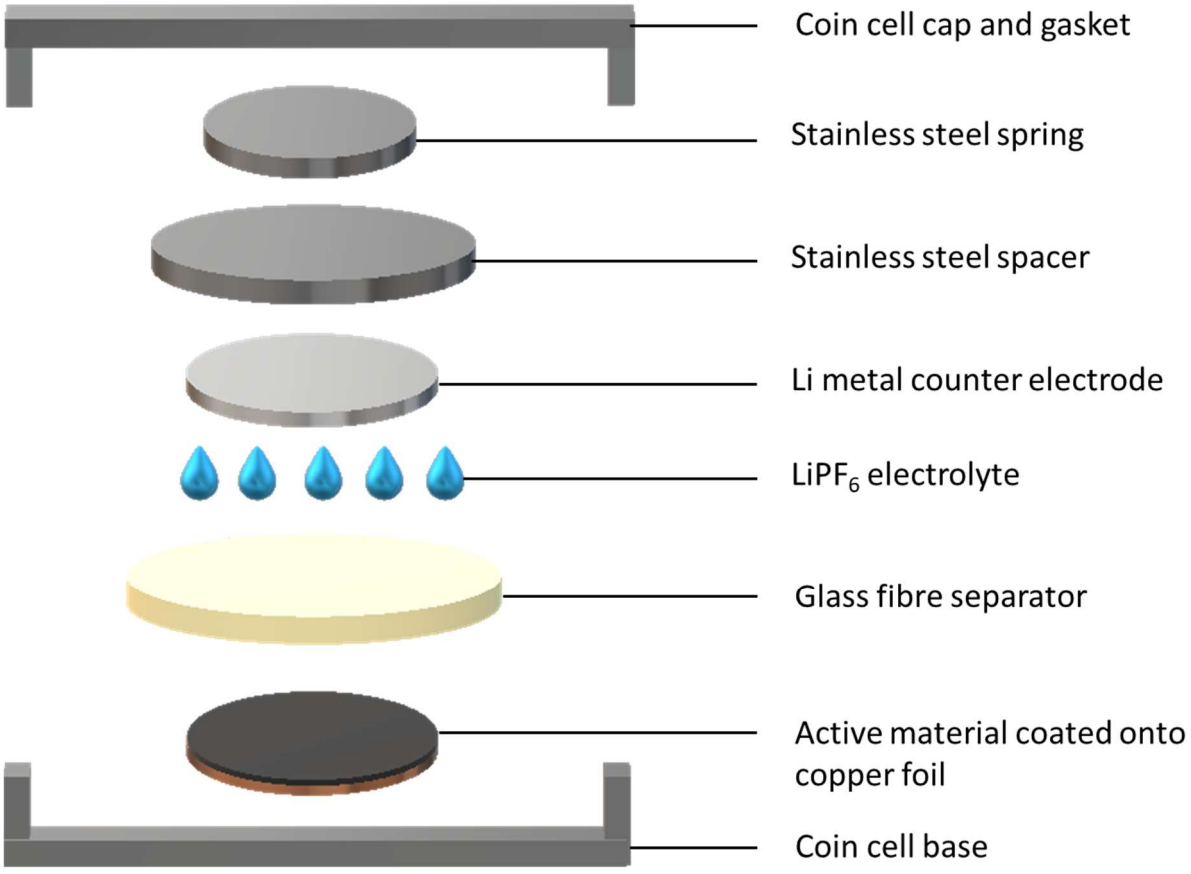


*Figure 3.5. Order of assembly for each CR2032 coin cell for galvanostatic cycling experiments.*

## 3.6 Galvanostatic cycling and differential capacity analysis

For all electrode materials outlined in this thesis, the general electrochemical procedure used was known as ‘Galvanostatic Cycling with Potential Limitation’. In these experiments, this technique involved testing the performance of half cells during charge and discharge between assigned voltage limits at predetermined current rates (determined by applying a given current per active material mass). Based on the performance of the half-cell, the specific gravimetric capacity can be calculated. This technique therefore not only enables the investigator to assess how the cell capacity changes over time but also enables understanding of the cell’s coulombic efficiency.[120] The voltage profiles produced also enable the investigator to analyse whether polarisation of cells occurs during cycling, and the differential capacity curve (known as dQ/dE vs E curve) enables resolution of phase transition behaviour that is less obvious in the plateaus in the complementary E vs capacity curve. Plotting differential capacity versus voltage curves means that these plateaus are observed as peaks, and determination of changes in peaks between cycles is much easier. These peaks can correspond to key phase transitions in the electrode materials and can highlight the reversibility of the process.[121]

## 3.7 Raman spectroscopy

When a sample is exposed to monochromatic laser light (known as incident light), most of the radiation is transmitted to the sample, however, some is scattered in all directions by the sample. Of this scattered radiation, around 99 % is equal in energy to the incident light, known as Rayleigh scattering, and the remaining 1 % scatters

and exhibits the ‘Raman effect’. The Raman effect refers to the difference in frequency of the incident ($v_i$) and scattered ($v_s$) radiation and is exhibited in Fig. 3.6. The difference in $v_i$ and $v_s$ arises because of the interaction of this radiation with vibrating molecules within the sample. Raman is known as a two-photon process, as the irradiated molecule absorbs a photon during excitation to a state known as the virtual energy state (which arises due to the excitation wavelength of the light source) and emits one upon relaxation. The scattered inelastic light gives the structural information of the sample, depending on the polarizability of the molecules within it, as this is what affects the energy of the scattered radiation.[122–124] In these experiments, a Renishaw inVia confocal microscope was used. For these measurements, a 633 nm laser source with a 633 filter was used. The Raman shifts obtained ranged between 200 – 1800 $cm^{-1}$ and all measurements were accumulated 20 times 25 mW laser power irradiating the sample.[125]

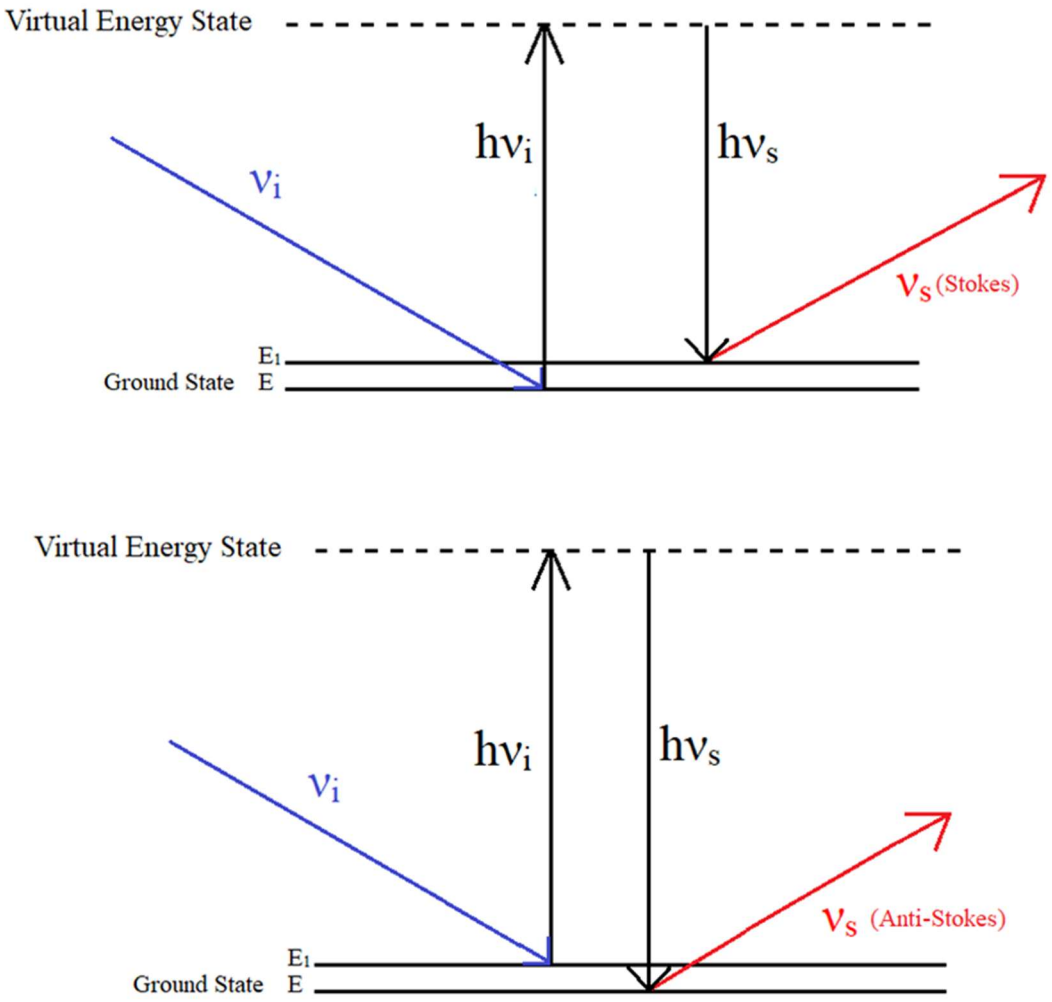


*Figure 3.6. Initial ($v_i$) and scattered ($v_s$) radiation leads to Stokes and Anti-Stokes inelastic scattering (Stokes: $v_i < v_s$, Anti-Stokes: $v_i > v_s$). Raman scattering arises due to the difference in incident and scattered radiation frequencies.*

## 3.8 Scanning electron microscopy (SEM) and energy dispersive x-ray (EDX) analysis

To obtain high resolution images of the surface of a sample, SEM utilises a focussed electron beam under vacuum, which rasters across the surface of a sample. A vacuum is essential to ensure the electrons can travel the required distance that they would not be able to in air. The electron source is an electron gun which produces electrons using a high temperature filament. The filament used in these experiments was made of tungsten and has acceleration voltages between 5 and 20 kV.[126,127] The detection of backscattered and secondary electrons that are ejected as a result of this electron beam, shown in Figure 3.7, provide an image of the sample surface. Backscattered electrons are used to produce images which show atomic number variations, whereas secondary electrons give insight into the topography of the sample. When SEM is combined with an EDX analyser, x-rays from the sample can also be used to obtain chemical information. EDX analysers are used to identify elemental composition at the surface of a sample as well as quantitative compositional information. Each atom in a sample possesses a distinct number of electrons in shells with distinct energies. When the electron beam strikes the inner shell of an atom, the inner electron is ejected which leaves a positive electron vacancy. This positive vacancy attracts another electron from an outer shell to fill the ‘electron hole’. This replacement electron releases energy in the form of an x-ray as it moves into a lower energy inner shell. The x-ray emitted possesses an energy which is exclusive to the element and electronic transition.[126] This two-step process is exhibited simplistically in Figure 3.8. In these experiments, a HITACHI TM4000 plus

table-top microscope was used for SEM measurements, and a micsF+ x-stream-2 EDX analysis machine for the EDX analysis.

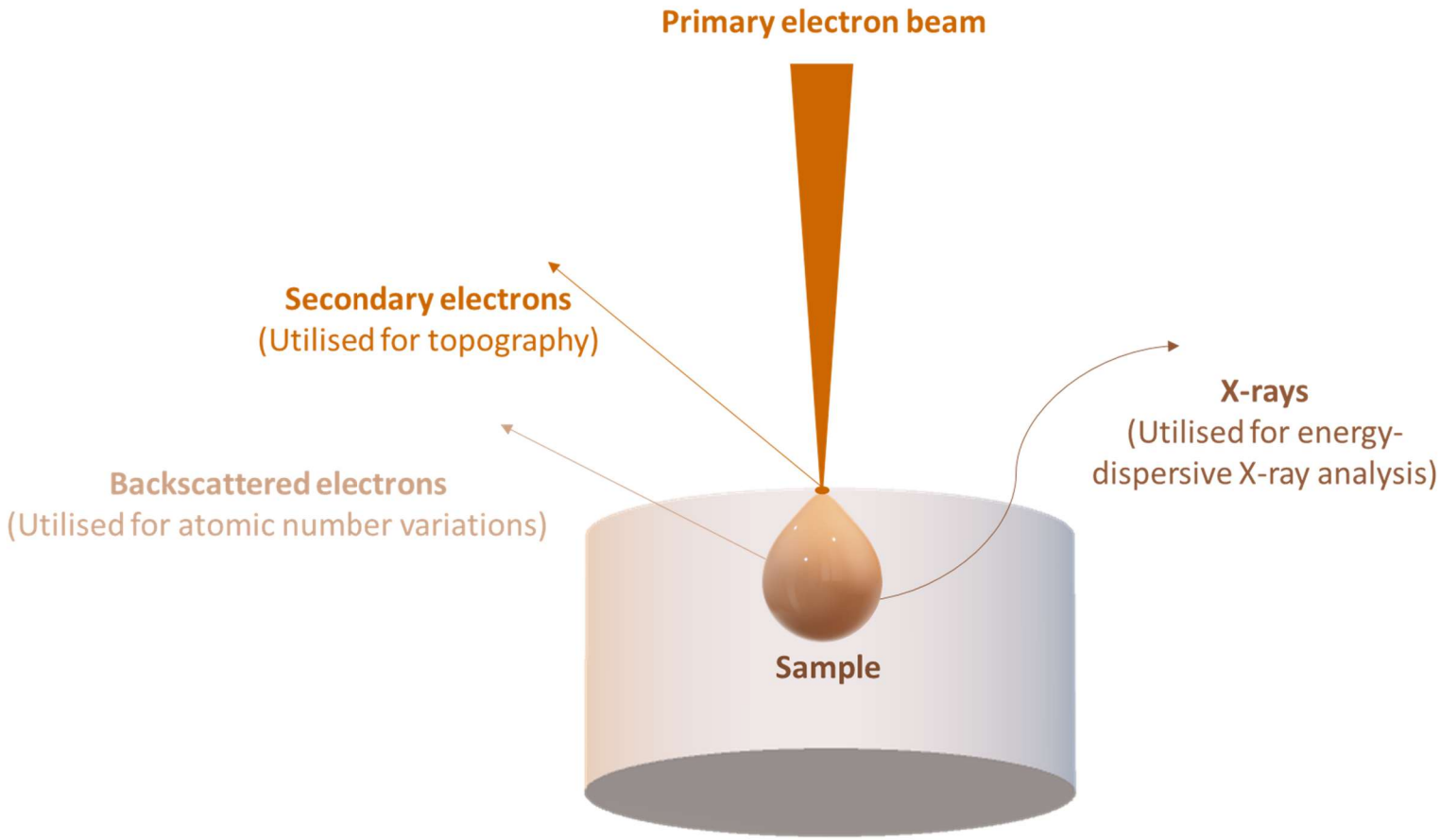


*Figure 3.7. Schematic illustrating the electrons and x-rays that are practical for SEM and EDX analysis*

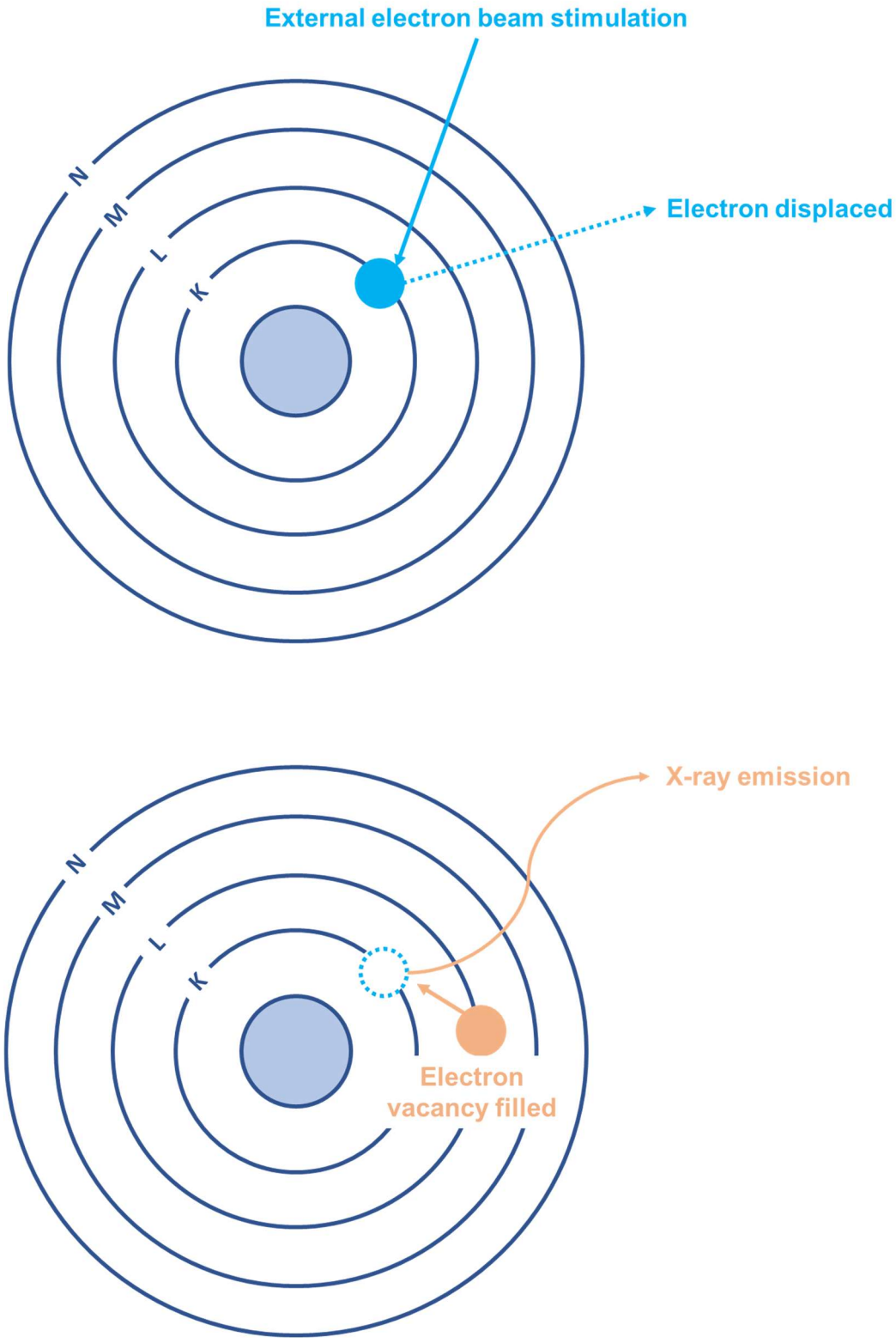


*Figure 3.8. Schematic showing how x-rays are generated for EDX analysis through electron displacement, electron vacancy filling, and subsequent x-ray emission in a two-step process.*

## 3.9 Transmission electron microscopy (TEM)

Like SEM, TEM utilises a focussed electron beam to gather information on samples, however, the image is created by transmitted electrons that pass through the selected sample as opposed to scattered electrons. Transmission electron microscopy is therefore better suited for evaluating nanosized materials, which is why it was selected for analysis of Mn oxides suspended in a carbon framework in these experiments. Key differences between SEM and TEM include higher energy electrons in TEM to ensure they pass through the sample, and a greater number of electromagnetic lenses when compared to a scanning electron microscope to enhance the resolution. Furthermore, samples must be extremely thin in order to ensure transmitted electrons are generated which is not necessary for analysis in SEM, making sample preparation in TEM far more labour intensive.[128] TEM analysis was preferable in some of these experiments due to the requirement of materials on the nanoscale, for which the resolution of the available benchtop SEM was not high enough. The microscope used in these experiments was a JEM-1400Plus transmission electron microscope to produce images with high precision and resolution.

## 3.10 Inductively coupled plasma – optical emission spectroscopy (ICP-OES)

To gravimetrically determine the contaminants contained within the synthesised materials in these experiments, the Agilent 5110 Synchronous Vertical Dual View

ICP-OES was selected. This is a superior quantitative technique to X-ray Fluorescence Spectrometry (XRF), as the detection limits for the desired elements in these upcycling experiments are inferior for XRF compared to ICP-OES (there are over 70 elements that are detectable using ICP-OES with high sensitivity and low interference). The main reason for qualitative elemental analysis in these experiments is to determine the presence of minor contaminant ions from the upcycling experiments, which is facilitated by ICP-OES due to its coordinated multiple elemental analysis capabilities at high speeds.[129] In order to analyse the samples by ICP-OES, they must be introduced into the high temperature plasma in a form that means that the sample can be vaporised and atomised. As a result of this, in these experiments, all powder samples were microwave digested using a Milestone ETHOS UP microwave digester. Each solid sample was added to a Teflon liner along with 10 ml of aqua regia solution and digested for an hour. The dissolved materials were then filtered and diluted using ultrapure dilute nitric acid, ready for sample introduction to the plasma torch under Argon. A nitric acid matrix was ideal for these experiments as all the desired elements (such as Ni/ Co/ Mn/ Li, etc.) in the experiments were stable and soluble under this matrix.[130] The sample of choice is introduced to the high temperature plasma as a liquid aerosol, at temperatures ranging between 5000 and 9000 K, breaking the chemical bonds between the materials and leaving behind individual atoms for detection. Each atom in these samples emits light which has an intensity that is attributed to the given element within the sample. Calibration standard solutions are used to ensure the elemental concentration of these elements is determined using calibration curves and the associated emission intensities – in these experiments, a standard containing all the

expected contaminant elements was used. Regarding sample detection: there are a series of optics that direct the light emitted from the elements in a sample into the spectrometer. The intense light is measured through separation of the light into specific wavelengths, and these wavelengths are detected between 167 and 785 nm in unison. Each element is identifiable through the specific emission lines specific to them for which there can be numerous) and the highest intensity emission line is generally used for analysis. The Agilent ICP-OES setup is shown in Figure 3.9.

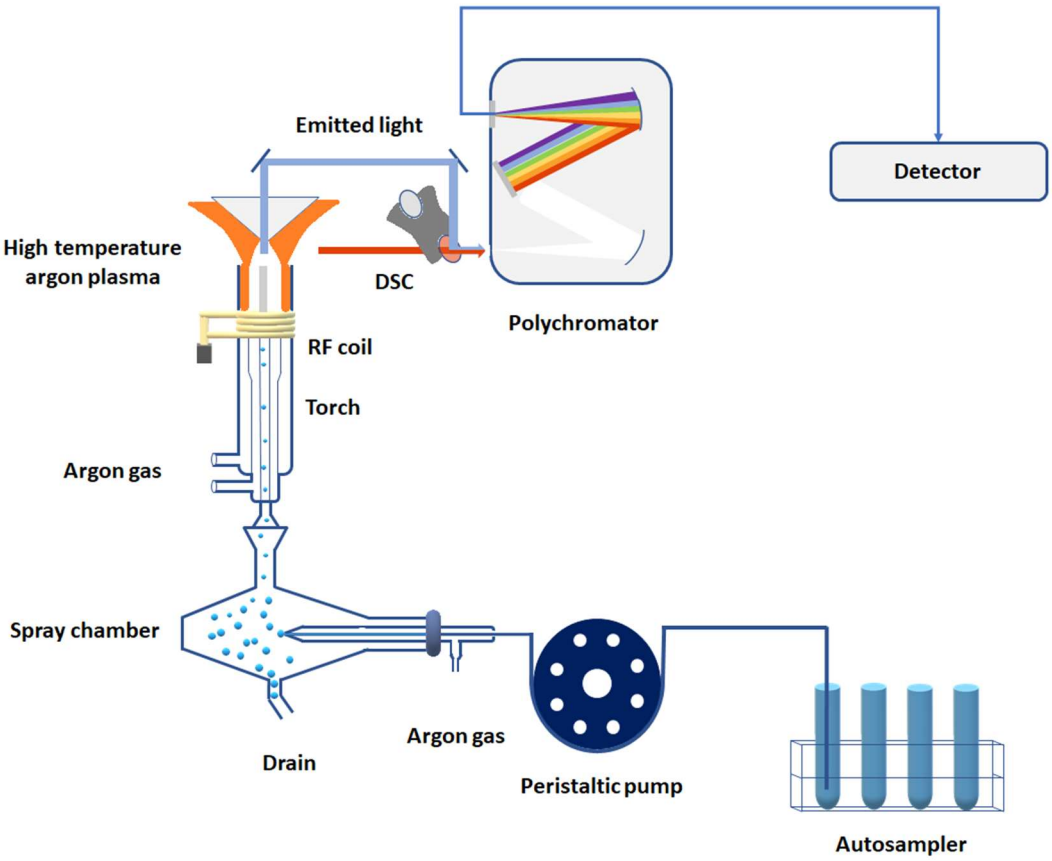


*Figure 3.9. Schematic showing the key components of an ICP-OES setup.*

## 3.11 Thermogravimetric analysis – mass spectrometry (TGA-MS)

Thermogravimetric analysis-mass spectrometry (TGA-MS) is a technique used to determine the thermal behaviour of a solid by use of mass variation. After a calibration measurement, a small amount of solid (microgram scale) is loaded into the instrument, and is heated and weighed simultaneously, using a balance with high precision. This means that the change in mass of the solid is recorded over time and can be observed by a characteristic descending curve. The resultant plot of temperature vs weight % can then be used to determine the decomposition processes, and the degradation products can be calculated from the total mass lost during the thermal decomposition steps. Gas, water and solvent evolution can also be monitored during heating.[131] In these experiments, a Netzsch STA 449 F1 Jupiter Thermal Analyser and an QMS 403C Aëolos Quadro Mass Spectrometer were used.

## 3.12 References (continued)


104 M. Dowsett, R. Wiesinger and M. Adriaens, in *Spectroscopy, Diffraction and Tomography in Art and Heritage Science*, eds. M. Adriaens and Mark Dowsett, Elsevier Inc., 2021, pp. 161–207.

105 T.-T. Fang, *Chapter 3 - The Structures of Crystalline Crystals*, Elsevier, 2018.

106 G. Burns and A. M. Glazer, in *Space Groups for Solid State Scientists*, eds. G. Burns and A. M. Glazer, Academic Press, 2013, pp. 25–44.

107 General Electric Company, X-ray Diffraction Tubes (Seifert Analytical X-ray), http://www.ge-mcs.com/download/it-common/GEIT-30212EN_xraytubes-print.pdf, (accessed 18 August 2023).

108 A. K. Chatterjee, in *Handbook of Analytical Techniques in Concrete Science and Technology*, eds. J. J. Beaudoin. and V. Ramachandran, William Andrew Publishing/Noyes, Ottawa, 2001, pp. 275–332.

109 J. Epp, in *Materials Characterization Using Nondestructive Evaluation (NDE) Methods*, eds. G. Hübschen, I. Altpeter, R. Tschuncky and H.-G. Herrmann, Woodhead Publishing, 2016, pp. 81–84.

110 A. C. Larson and R. B. Von Dreele, *General Structure Analysis System*, Los Alamos, 1989, vol. 53.

111 E. Takeshi and S. J. L. Billinge, in *Underneath the Bragg Peaks*, eds. T. Egami and S. J. L. Billinge, Pergamon, London, 2003, vol. 16, pp. 27–54.

112 About Synchrotrons - Diamond Light Source,

https://www.diamond.ac.uk/Home/About/FAQs/About-Synchrotrons.html#:~:text=A synchrotron is a type,bright light%2C called synchrotron light., (accessed 15 August 2023).

113 Inside the Machine - Diamond Light Source, https://www.diamond.ac.uk/Home/About/FAQs/Inside-the-Machine.html, (accessed 15 August 2023).

114 F. D'Acapito, *Appl. Surf. Sci.*, 2004, **226**, 313–320.

115 Beamlines Information - Advanced Photon Source, https://www.aps.anl.gov/Beamlines/Directory/Details?beamline_id=16, (accessed 15 August 2023).

116 XPDF (I15-1) - Diamond Light Source, https://www.diamond.ac.uk/Instruments/Crystallography/I15-1.html;jsessionid=DD9A035428ED9934878E12AF0BD7A532, (accessed 15 August 2023).

117 M. Diaz-Lopez, G. L. Cutts, P. K. Allan, D. S. Keeble, A. Ross, V. Pralong, G. Spiekermann and P. A. Chatera, *J. Synchrotron Radiat.*, 2020, **27**, 1190–1199.

118 X. Wang, S. Tan, X. Q. Yang and E. Hu, *Chinese Phys. B*, 2020, **29**, 1–12.

119 V. Petkov, in *Characterization of Materials*, John Wiley & Sons, Inc., 2012, pp. 1361–1372.

120 G. I. T. Techni-, P. Intermittent, T. Techniques and S. P. E. Spectro-, 2005, 31–34.

121 How to read battery cycling curves - BioLogic Learning Center,

https://www.biologic.net/topics/how-to-read-cycling-curves/, (accessed 21 August 2023).

122 Bhim Prasad Kafle, in *Chemical Analysis and Material Characterization by Spectrophotometry*, ed. B. P. Kafle, Elsevier, 2019, pp. 245–268.

123 G. S. Bumbrah and R. M. Sharma, *Egypt. J. Forensic Sci.*, 2016, **6**, 209–215.

124 N. John and S. George, in *Spectroscopic Methods for Nanomaterials Characterization*, ed. R. K. M. Sabu Thomas, Raju Thomas, Ajesh K. Zachariah, Elsevier, 2017, pp. 95–127.

125 Y. F. Han, F. Chen, Z. Zhong, K. Ramesh, L. Chen and E. Widjaja, *J. Phys. Chem. B*, 2006, **110**, 24450–24456.

126 M. de Assumpcão Pereira-da-Silva and F. A. Ferri, in *Nanocharacterization Techniques*, ed. O. N. O. Alessandra L. Da Róz, Marystela Ferreira, Fabio de Lima Leite, William Andrew Publishing, 2017, pp. 1–35.

127 M. Abd Mutalib, M. A. Rahman, M. H. D. Othman, A. F. Ismail and J. Jaafar, in *Membrane Characterization*, ed. D. O.-R. Nidal Hilal, Ahmad Fauzi Ismail, Takeshi Matsuura, Elsevier B.V., 2017, pp. 161–179.

128 B. J. Inkson, in *Materials Characterization Using Nondestructive Evaluation (NDE) Methods*, ed. H.-G. H. Gerhard Hübschen, Iris Altpeter, Ralf Tschuncky, Woodhead Publishing, 2016, pp. 17–43.

129 J. W. Olesik, in *Mass and Optical Spectroscopies*, 1974, pp. 633–644.

130 P. R. Gaines, ICP Operations Guide A Guide for using ICP-OES and ICP-MS, https://www.inorganicventures.com/pub/media/IV_ICP_OperationsGuide_6x9.p

df.

131 Thermal Analysis – Mass Spectrometer Capillary Coupling Thermal Analysis and Evolved Gas Analysis - NETZSCH, https://analyzing-testing.netzsch.com/_Resources/Persistent/4/a/b/1/4ab1e1d673ffbc43a69e825134f5966755b6e25e/TA-QMS_Aeolos_Quadro_Coupling_en_web.pdf.

# 4 Upcycling LMO through selective leaching and interconversion

## 4.1 Table of Figures

## 4.2 Chapter introduction

In this chapter, experiments will focus on the synthesis of Mn oxalate, $Mn_2O_3$ and $Mn_3O_4$ through selective extraction of $LiMn_2O_4$ (LMO) from redundant battery material followed by interconversion. When extracting lesser used and redundant cathode chemistries from preliminary cells, it is imperative that the value of this product is exploited once this material has been selectively removed. The process of extraction and repurposing recycled material to increase its value is known as upcycling and, as outlined in section 1.4.8, LMO is a prime example of a lesser used material which can be upcycled to form a variety of Mn-rich materials with interesting properties. For these leached materials, what is unknown is how extraction of spent electrode material and upcycling will impact the product formed, due to the potential presence of contaminants from the extraction process that may interrupt the interconversion process. The aim of this chapter is therefore to explore selective extraction of LMO from spent cathode material and the effectiveness of interconversion of this material into Mn oxalate, $Mn_2O_3$ and $Mn_3O_4$. The leached materials will be compared to their pristine counterparts to contextualise these findings and verify whether this interconversion route is effective in upcycling LMO into the desired Mn-based materials.

## 4.3 Methods

In this chapter, comparison will be made between samples which have been synthesised from three different LMO precursors. Each LMO precursor was used to synthesise Mn oxalate, which was then used to synthesise $Mn_2O_3$ and $Mn_3O_4$.

### 4.3.1 Sample origins

Depending on the LMO precursor, samples are defined as follows:

- Pristine material – This is used to define any samples which were formed from commercially-purchased (Alfa Aeser, 99.5 %) LMO powder. These samples were used as a reference for the expected interconversion behaviour of the leached LMO material.
- Nissan Leaf quality-control-rejected (QCR) material – Any ‘QCR’ samples have been synthesised from LMO which had been leached from the cathode of a first-generation Nissan Leaf pouch cell cathode from the Nissan’s production line, which appear to have undergone some formation cycles prior to being discarded. This cell was discharged below 0% state-of-charge to give an open circuit voltage of 0 V by Nissan, which then rose after resting.
- EOL (EOL) Nissan Leaf material – Any ‘EOL’ samples are those formed from LMO that has been leached from a first-generation Nissan Leaf pouch cell cathode, however, prior to disassembly the cell had been cycled in a vehicle which had covered 40,000 miles prior to a mild overcharging regime, as outlined by P.S. Attidekou et al. The regime involved cycling the pouch cell for 500 cycles, by the end of which only 13% of the original capacity was lost.[132]

After this cycling, the cell was discharged to 0% state of charge prior to disassembly.

To obtain the individual QCR and EOL sheets for chemical testing, R. Sommerville and A. Zurin dismantled the pouch cells in the school of metallurgy and materials at the University of Birmingham. The open circuit voltage (OCV) of the EOL and QCR cells prior to disassembly were 3.22 V and < 1.0 V, respectively, the latter OCV being due to over-discharging of the QCR cell, which has been reported to cause copper dissolution.[61,133] The pouch cells were opened using a nonmetal scalpel in an inert Argon glovebox, whereby the $H_2O$ and $O_2$ concentration was < 0.1 ppm, to remove the cell casing to enable easy extraction of the stacked electrodes and separators. Once removed these layers were separated and dried.[134]

### 4.3.2 Leaching process

In these first-generation cells there is a mixed Ni-rich layered phase mixed with a LMO spinel phase. Selective extraction of LMO is vital to leave behind a Ni-rich phase that can be relithiated and used in second-generation cells, but the LMO must be repurposed within the cells as it is not sought after for second-generation Nissan Leaf pouch cells. In this Chapter, repurposing of this outmoded material is demonstrated through interconversion into Mn oxalate and oxides. Based on a method developed by L.L. Driscoll et. al, reductive acidic leaching was used to reduce lithium manganese oxide from the Nissan Leaf composite cathode into solution.[54] Reductive leaching refers to the process whereby high valence metal ions in a solid material are reduced into an aqueous state with lower valence. By leaching

out manganese into solution and adding oxalic acid, Mn oxalate is formed by precipitation. The acid employed for reductive leaching of lithium manganese oxide from the electrode strip was ascorbic acid. This inorganic acid works by reducing all the insoluble $Mn^{3+}$ found in the strip to soluble $Mn^{2+}$ which can then be extracted from the solution. The cathode strip left behind contained only a nickel-rich phase, which could be reformed into a new Ni-rich cathode sheet through re-lithiation and reintroduction of transition metals to ensure the correct stoichiometry was achieved. A detailed explanation of this experiment is outlined below:

The composition of the cathodes extracted from Nissan Leaf material was a 75:25 LMO:NCA composite cast onto an Al current collector. To remove the aluminium current collector, the cathode sheet was cut, weighed, shredded, and added to 10% (by weight) sodium hydroxide (NaOH) solution to cause the Al to react (shown in equation 7):

$$2NaOH_{(aq)} + 2Al_{(s)} + 2H_2O_{(l)} \rightarrow 2NaAlO_{2(aq)} + 3H_{2(g)} \quad [7]$$

Once all the Al had reacted (once there was no more effervescence of $H_2$) the remaining strip was filtered using a Büchner funnel and washed several times with deionised water. After drying the strip at 60 °C in air for 60 minutes, the strip was weighed and then stirred into a 1.25 M solution of ascorbic acid which had been heated to 70 °C on a hotplate. Using ascorbic acid, LMO was selectively leached from the composite electrode and reduced all insoluble manganese in the spinel to $Mn^{2+}$. After 10 minutes, the remaining strip and brown leachate were removed from the hotplate and a Büchner funnel was used to filter the strip from the solution. The strip was dried, re-weighed, and characterised using XRD to ensure all LMO had

been leached out of the strip. The brown leachate was then saved for subsequent treatment. To obtain LMO powder, the leachate was dried at 150 °C for 12 hours to evaporate off the ascorbic acid and form a 'honeycomb' dried product. The honeycomb mixture of was then ground and annealed in air at 700 °C for 12 hours to form LMO (either categorised as QCR or EOL LMO depending on the condition of the precursor cathode). The formation of a honeycomb-like structure from an acidic transition metal solution has been outlined by Y. Han et al. in another $LiMn_2O_4$ synthetic procedure, whereby a modified Pechini synthesis was used to generate a 'puffed char' containing Li and Mn for subsequent calcination to $LiMn_2O_4$.[135]

### 4.3.3 Interconversion process

The pristine, QCR and EOL LMO powders were used as precursor material for the interconversion reactions. To synthesise Mn oxalate dihydrate, LMO powder was added to a 1.25 M solution of oxalic acid at 70 °C and was stirred until a pale pink precipitate had evolved. This pale pink precipitate was Mn oxalate dihydrate, which was dried overnight in air at 70 °C. The remaining filtrate from the oxalate precipitation was rich in Li and could be used to precipitate out the valuable Li which could then be used in the re-lithiation of the Ni-rich cathode strip. This would ensure closed-loop recycling of the Ni-rich portion of the strip and upcycling of the redundant LMO material. To interconvert $Mn_2O_3$, the Mn oxalate dihydrate powder was transferred to an alumina crucible and heated up to 700 °C in air at a ramp rate of 5 °C/ min for 12 hours. To interconvert into $Mn_3O_4$, this $Mn_2O_3$ material was heated in

air to 1000 °C at a ramp rate of 5 °C/ min for 12 hours. A flow chart to illustrate the interconversion process is outlined in Fig. 4.1.

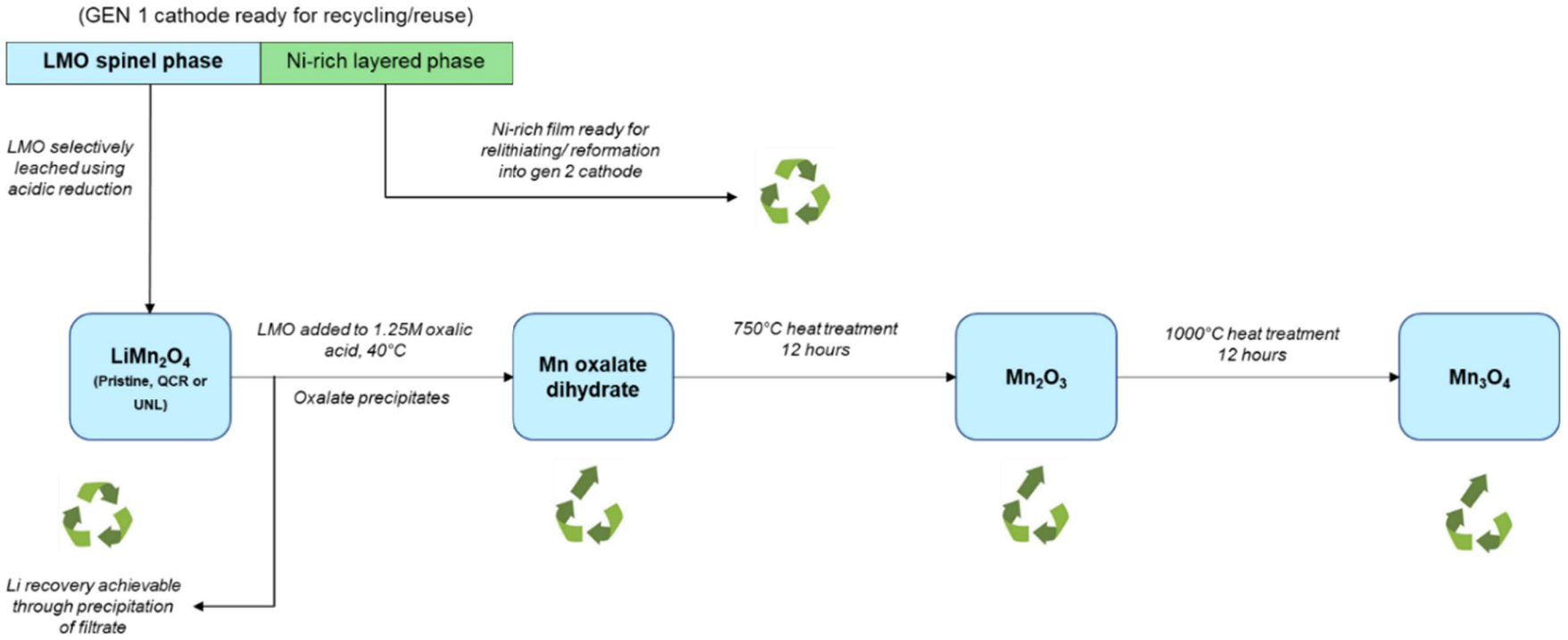


*Figure 4.1 Schematic illustrating how $LiMn_2O_4$ is extracted from first generation Nissan Leaf cathode material and interconverted into an array of Mn-based products.*

## 4.4 Results

Pristine, QCR and EOL products from the LMO interconversion experiments were compared to determine compositional and structural differences between the materials obtained. Samples were analysed using x-ray diffraction (XRD) and Rietveld refinement, Raman spectroscopy, thermogravimetric analysis with mass spectrometry (TGA-MS), scanning electron microscopy (SEM), energy dispersive x-ray analysis (EDX) and inductively coupled plasma optical emission spectroscopy (ICP-OES).

### 4.4.1 Structural identification and contaminant detection of leached materials using XRD, ICP-OES, and TGA-MS

**LiMn2O4**

Initially, XRD patterns of each of the LMO materials were measured, shown in Fig. 4.2. In all cases XRD patterns were pattern matched to classify the structure as a cubic close-packed spinel with space group $Fd\bar{3}m$. In the $Fd\bar{3}m$ spinel structure, oxygen anions occupy the 32e site, lithium ions occupy the tetrahedral 8a site and the tri- and tetravalent manganese ions occupy the octahedral 16d site.[136–139] As numerous transition metal contaminant ions have been identified through ICP elemental analysis for QCR and EOL LMO, the XRD patterns can provide evidence for their presence within the $Fd\bar{3}m$ cubic spinel structure. In doping studies in the literature, all three ions have been found to occupy the 16d octahedral sites within the structure, therefore it is expected that this will occur in these samples.[136,138] One feature of the pattern which can be used to identify cationic occupancies in the

literature is the peak intensity ratio between the (311) and (400) peaks ($I_{311}/I_{400}$).[136,140–142] This ratio provides evidence for the different occupancies of cations between the 8a tetrahedral and 16d octahedral sites in $LiMn_2O_4$. As stated in the literature findings, the more dopant ions incorporated into the $Fd\bar{3}m$ structure increases the value of $I_{311}/I_{400}$. When comparing QCR and EOL LMO, $I_{311}/I_{400}$ values were 1.08 and 1.14, respectively. A higher intensity ratio for the EOL material could be suggestive of a greater occupancy of contaminant cations in the 16d sites, however as the expected transition metal contaminant ions (Ni and Co) scatter almost identically to Mn, it could be due to a change the Li positions and therefore observed scattering. To determine whether this observation was consistent with contaminant ions detected, elemental analysis was done using ICP-OES. Using this technique, contaminant metal ratios in $LiMn_2O_4$ (LMO) were detectable from pristine, QCR and EOL LMO. The percentage masses of the samples have been calculated and depicted in table 4.1. The columns where there is no value shown corresponds to negligible amounts of elements present in the sample (≤ 0.01% mass).

The $I_{311}/ I_{400}$ intensity ratio observation is consistent with elemental analysis using ICP: 1.68% of the QCR and 2.54% of the EOL material, respectively, was composed of Ni/ Co/ Al contaminant ions, expected to come from the Ni-rich phase. The presence of copper in the QCR leached sample is because of over-discharging of the cell prior to disassembly, as stated previously. The decreased % Mn content for the leached $LiMn_2O_4$ is indicative of manganese loss from the cathode, which is expected, and has been commonly reported to occur during aging from studies of Li-ion battery cycling in the literature.[143–145] Furthermore, in study by A. Sargent et al. on the reclamation of graphite from the Nissan Leaf pouch cells (with the QCR and EOL

cells described in this thesis corresponding to the QCR and EOL II cells in their study), Mn deposition has been observed on the anode for these aged pouch cells from expected disproportionation of trivalent manganese on the surface of the cathode which led to Mn dissolution into the electrolyte. In their experiments, XPS and Raman analysis was used to show the presence of Mn species on the surface of spent graphite material from this aging mechanism during cell runtime.[61]

*Table 4.1. ICP data showing % mass of Li, Mn, Ni, Co, Al, and Cu within the pristine, QCR and EOL leached $LiMn_2O_4$*

| **LMO sample** | **% mass (% standard deviation)** | | | | | | | |
|---|---|---|---|---|---|---|---|---|
| | **Li** | **Mn** | **Ni** | **Co** | **Al** | **Cu** | **Total** | **Un-measured** |
| Pristine | 3.65 (0.03) | 70.44 (0.24) | - | - | - | - | 74.09 | 25.91 |
| QCR | 3.80 (0.04) | 62.13 (0.26) | 0.39 (0.001) | 0.05 (0.002) | 1.18 (0.01) | 0.06 (0.0004) | 67.61 | 32.39 |
| EOL | 4.17 (0.02) | 67.55 (0.12) | 0.64 (0.003) | 1.31 (0.002) | 0.59 (0.001) | - | 74.26 | 25.73 |

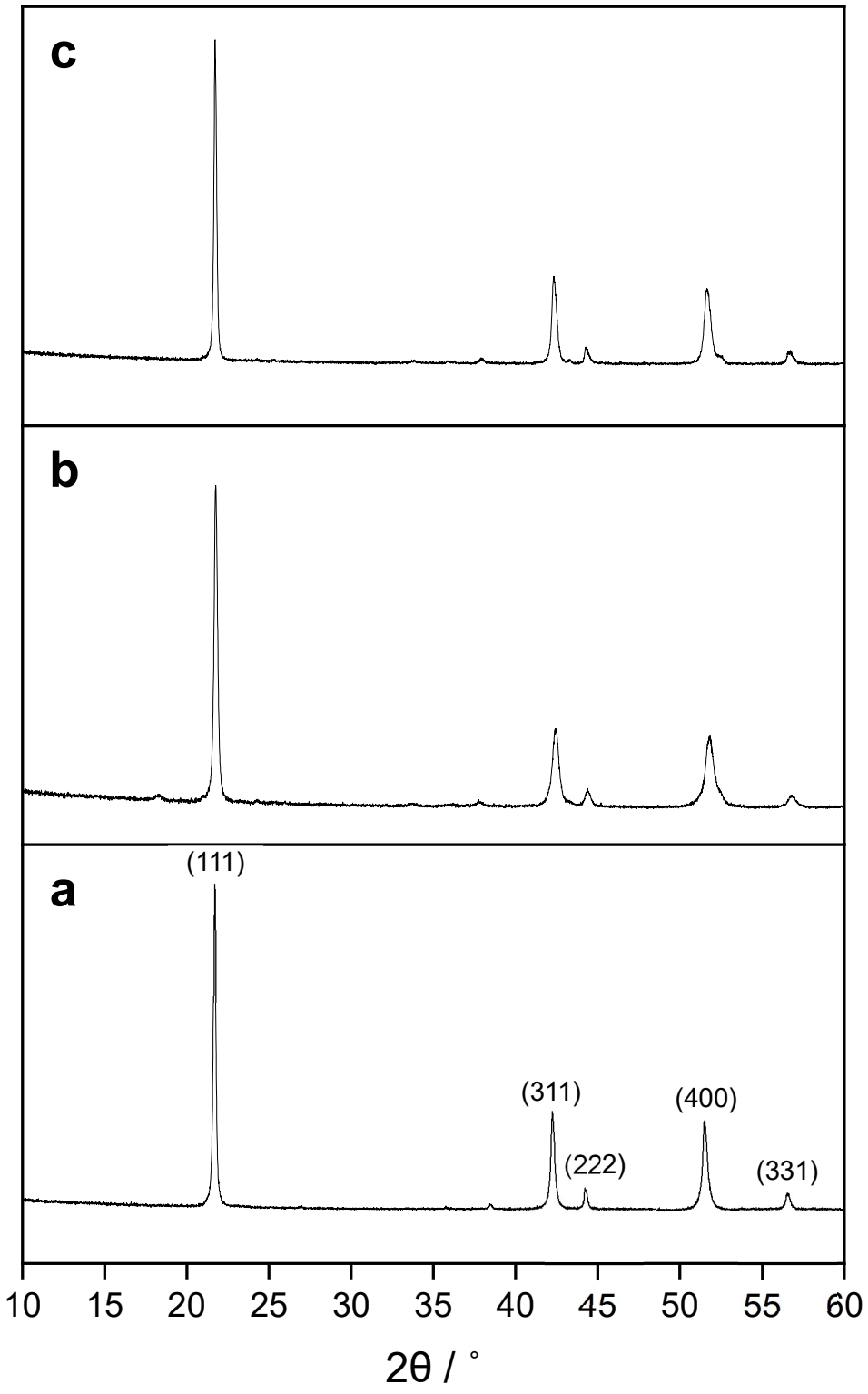


*Figure 4.2 XRD patterns (with indexing) of $LiMn_2O_4$ with space group $Fd\bar{3}m$ – pristine (a), QCR (b) and EOL (c).*

Rietveld refinement was used to determine the lattice parameters and cell volumes of each LMO spinel sample. The *a*-parameters and cell volumes for each LMO sample are shown in table 4.2, the refinements are shown in Fig. 4.3 a, b, and c, and the lattice parameter and cell volume plots are shown in Fig. 4.4.

*Table 4.2. Calculated* a*-parameters and cell volumes for pristine, QCR and EOL* $LiMn_2O_4$.

| Sample | a parameter (Å) | Cell volume (Å) | $Rw_p$ (%) |
|---|---|---|---|
| **Pristine** | 8.2351(1) | 558.470(3) | 6.74 |
| **QCR** | 8.1879(2) | 548.856(5) | 7.68 |
| **EOL** | 8.2086(2) | 553.015(4) | 8.62 |

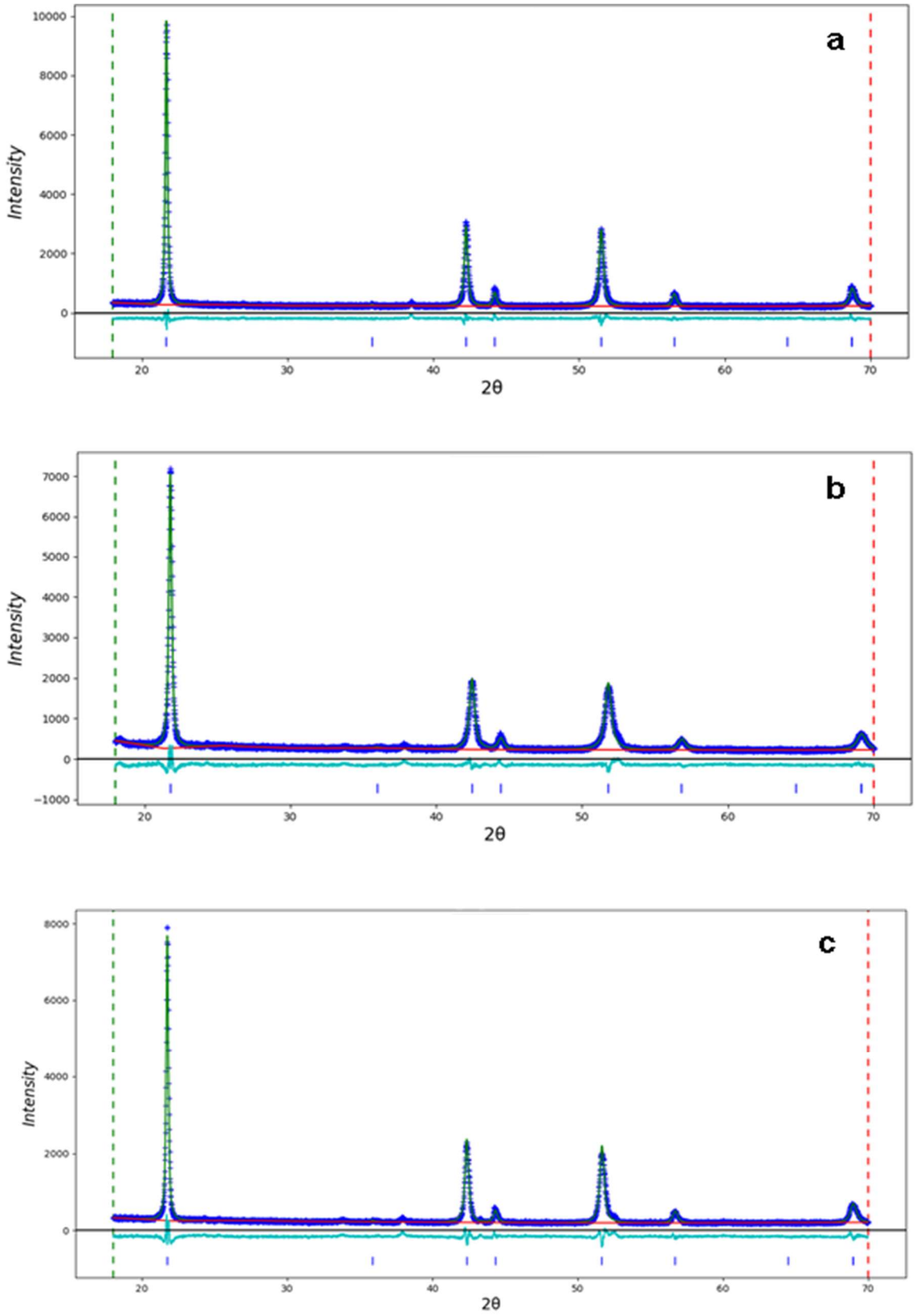


*Figure 4.3. Refined XRD patterns (with indexing) of $LiMn_2O_4$ with reflections for space group $Fd\bar{3}m$ marked in blue – pristine (a), QCR (b) and EOL (c).*

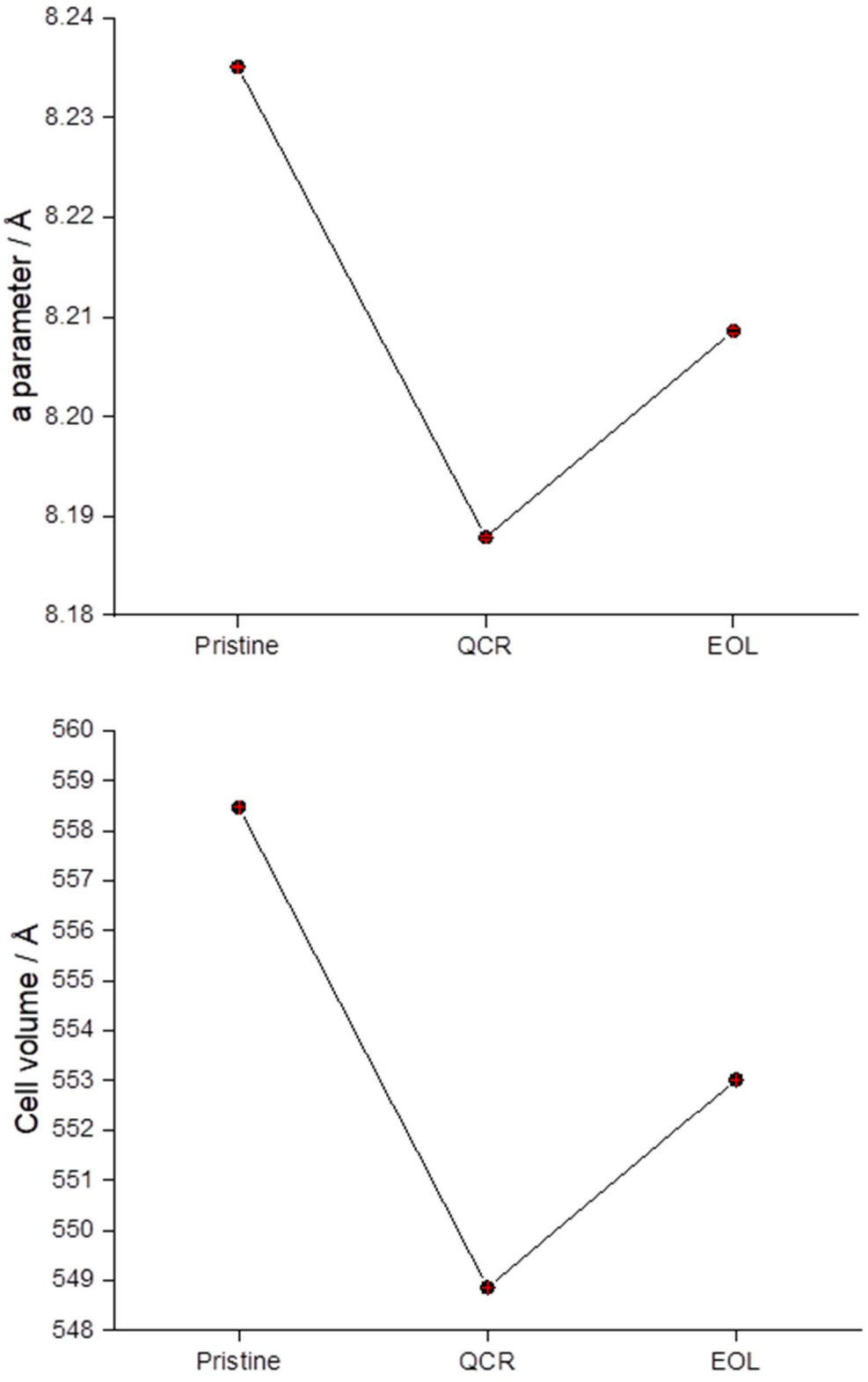


*Figure 4.4. Calculated a parameters and cell volumes for pristine, QCR, and EOL $LiMn_2O_4$.*

When comparing the QCR and EOL sample lattice parameters to those observed for the pristine material, there was an *a*-parameter contraction by 0.57 % and 0.32 % and a cell volume contraction of 1.72 % and 0.98 % for the QCR and EOL samples, respectively. There was shrinkage in the lattice parameters and cell volumes of the leached LMO structures when compared with the pristine sample (with the most drastic shifting seen in the QCR sample). The presence of contaminant ions in the 16d sites rationalises these observed values. In the QCR material, most of the contamination in the material is from aluminium. Nickel can be seen in much lower quantities, followed by cobalt and copper are in even lower measures. In EOL material, the aluminium and the cobalt are the highest contaminants with a lower quantity of nickel.

In the literature, these M ions (with valences $Al^{3+}$, $Ni^{2+}$, $Co^{3+}$, $Cu^{2+}$) have been doped into the LMO structure on the 16d octahedral $Mn^{3+}$ site, and in all cases have been found to cause a lattice parameter shrinkage due to ionic radii changes and/or increased M─O bond strengths when compared to Mn─O.

In the case of Co, in a study by R. S. Liu et al., the substitution of Mn for Co causes a lattice parameter shrinkage of between 0.12 – 0.97 % in $Li(Mn_{2-x}Co_x)O_4$, between x values of 0.1 – 0.5. This was deduced to be due to the low spin state of the $Co^{3+}$ ion having an ionic radius in an octahedral environment which is lower than that of the $Mn^{3+}$ ions it will be replacing, at 0.545 Å and 0.645 Å, respectively. Though there is tetravalent Mn in $LiMn_2O_4$ which would lead to an increase in lattice parameter with Co substitution, only shrinkage was observed with Co doping in their study, indicating the 0.53 Å $Mn^{4+}$ ion was not substituted.[146] With respect to $Ni^{2+}$, based on a Ni-doping study by H. Bai et al., this ion is expected to substitute for the high spin state $Mn^{3+}$ ions

as they have similar ionic radii (0.690 Å for the bivalent Ni). The low spin state $Mn^{3+}$ ions were deduced to charge balance this replacement by changing to $Mn^{4+}$, which have an ionic radius of 0.53 Å. Furthermore, the Ni—O bond is (1.915 Å) shorter than the Mn—O bond (1.937 Å) which further justifies the reason for the observed lattice contraction. The lattice parameter contraction observed for $LiMn_2O_4$ to $LiNi_{0.1}Mn_{1.9}O_4$ is down to 0.5 % less than its original value.[147] A similar case to Ni can be put forward for $Cu^{2+}$ substitution in the 16d octahedral sites in a study by S. Wang et al., with a smaller lattice contraction of 0.05% for $LiCu_{0.05}Mn_{1.95}O_4$.[148] For $Al^{3+}$, in a study on Al doping by W. Xu et al., it has been hypothesised that $Al^{3+}$ substitutes for the $Mn^{3+}$ ion in the 16d site, which causes a lattice shrinkage due to its smaller ionic radius (0.535 Å for $Al^{3+}$ vs 0.58 Å for the low spin state of $Mn^{3+}$ in an octahedral environment).[149] Based on both the shortened bond lengths and decreased ionic radii introduced with all the dopant ions, it is unsurprising that this lattice contraction is seen in the case of the QCR and EOL samples, due to a compounded effect of all these contaminants being introduced into the structure. The larger lattice shrinkage in QCR material may also be due to the higher proportion of Al ions within the structure, which have the smallest ionic radii of the contaminant ions detected.

**Mn oxalate dihydrate**

Regarding the hydrated Mn oxalates, it is notoriously challenging to refine their structure using Rietveld refinement due to the high degree of structural disorder within the crystalline phase, as discussed in a study by A.N. Puzan et al. on structural disorder and decomposition of Mn oxalate dihydrate.[91] From initial observations, the XRD patterns appear to correlate to the structure as centred type α'-Mn oxalate dihydrate with space group C12/c1, meaning that any contaminant ions seen in the leached samples did not change the lattice structure of the material.

TGA-MS was used to approximate the stoichiometry of the water associated with each hydrated Mn oxalate. Each Mn oxalate (pristine, QCR and EOL) was heated to 300 °C at a rate of 5 K/min to remove the water from the structure and determine the stoichiometry of the hydrated material through the resultant mass of the compound after heating. Water loss was confirmed to be responsible for the % mass loss, as there was a peak corresponding to a high ionic current of ions detected with mass 18 (highlighted in blue) during the mass loss, shown in Figs. 4.5 – 4.7.

Based on the percentage mass lost, the amount of water associated with each Mn oxalate was determined below:

- Pristine: $MnC_2O_4 \cdot 1.91H_2O$
- QCR: $MnC_2O_4 \cdot 2.02H_2O$
- EOL: $MnC_2O_4 \cdot 2.05H_2O$.

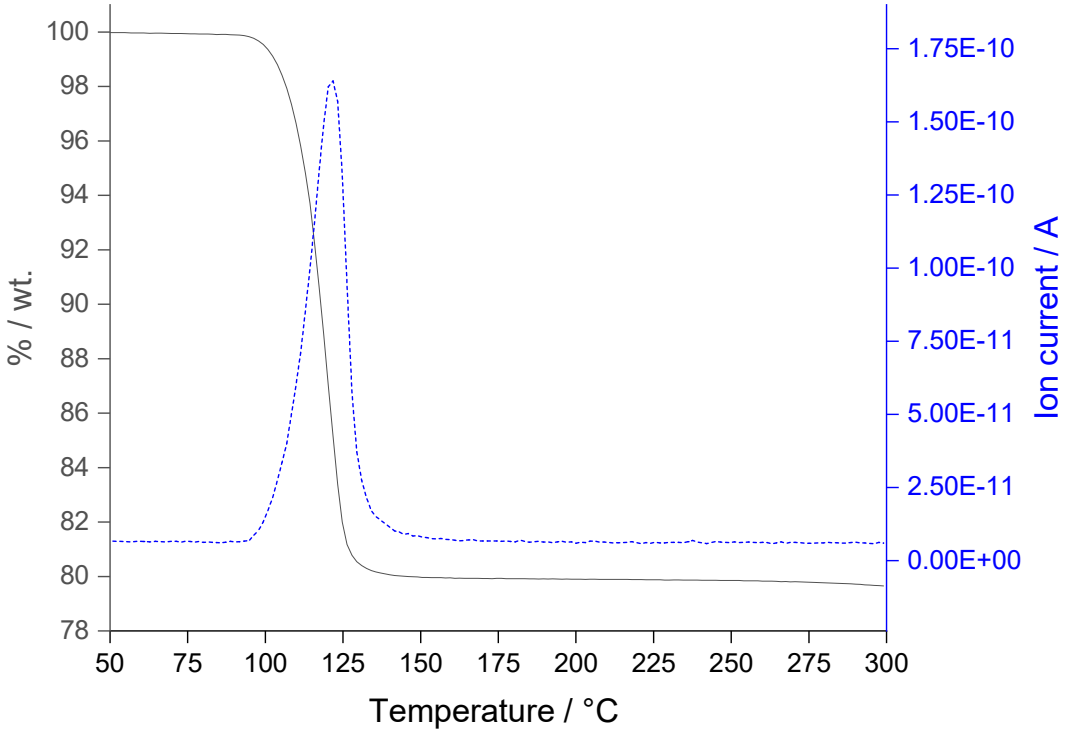


*Figure 4.5. TGA-MS data showing water losses associated with pristine Mn oxalate.*

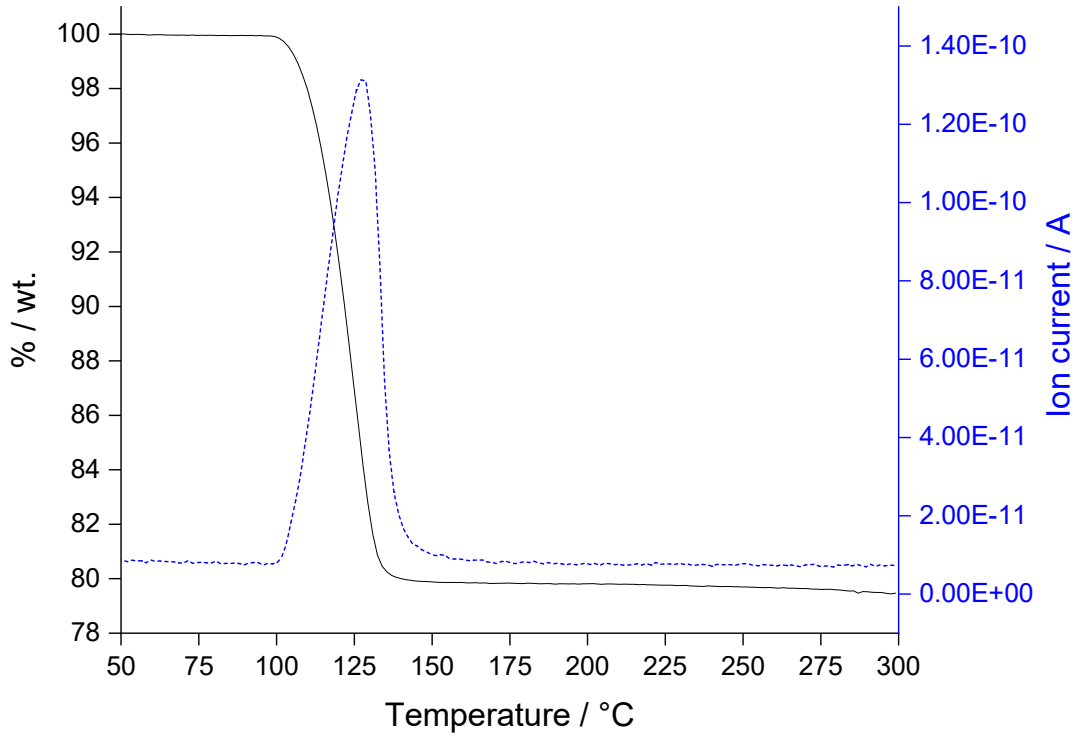


*Figure 4.6. TGA-MS data showing water losses associated with QCR Mn oxalate.*

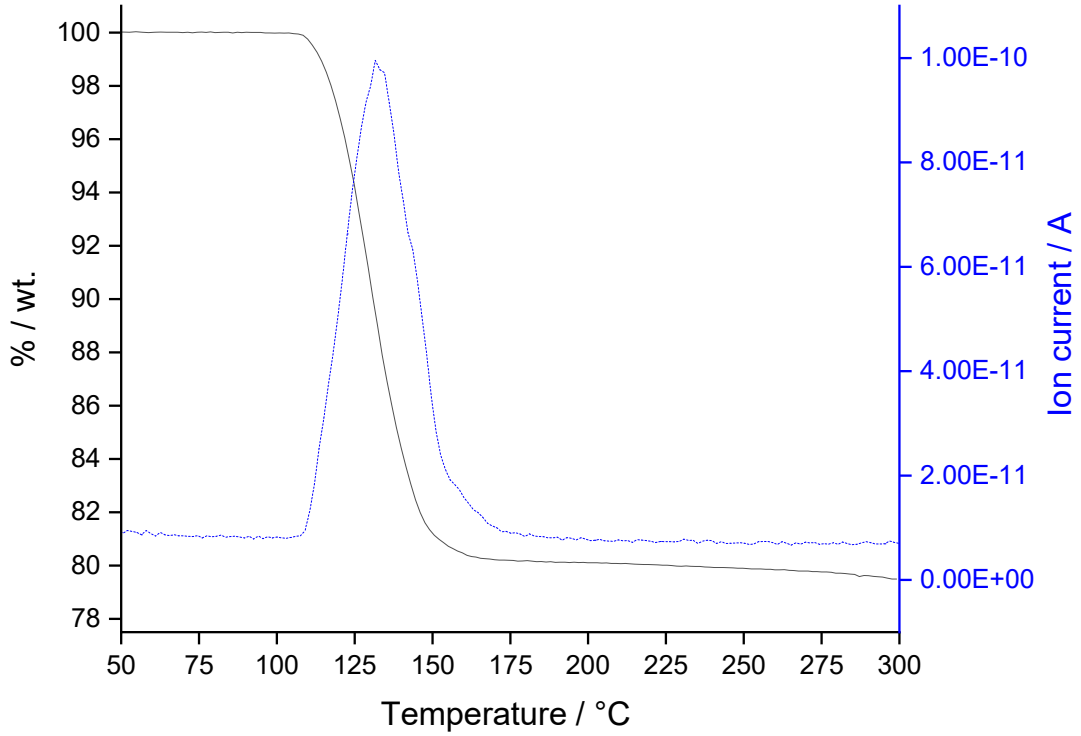


*Figure 4.7. TGA-MS data showing water losses associated with EOL Mn oxalate.*

ICP-OES analysis was used to determine the contamination in interconverted Mn oxalate from pristine, QCR and EOL LMO precursor materials. The percentage masses of the samples have been calculated and depicted in table 4.3.

*Table 4.3. ICP data showing % mass of Li, Mn, Ni, Co, Al, and Cu within the pristine, QCR and EOL leached $LiMn_2O_4$*

| **LMO sample** | **% mass (% standard deviation)** | | | | | | | |
|---|---|---|---|---|---|---|---|---|
| | **Li** | **Mn** | **Ni** | **Co** | **Al** | **Cu** | **Total** | **Un-measured** |
| Pristine | - | 37.57 | - | - | - | - | 37.57 | 62.43 |

| | | | | | | | | |
|---|---|---|---|---|---|---|---|---|
| | | (0.3) | | | | | | |
| QCR | 0.03 (0.0002) | 37.73 (0.1) | 0.41 (0.001) | 0.05 (0.0002) | - | 0.03 (0.0002) | 38.25 | 61.75 |
| EOL | - | 36.20 (0.11) | 1.33 (0.002) | 0.91 (0.01) | - | - | 38.44 | 61.56 |

In the QCR sample there is the Cu contamination observed because of the over discharging of the cell before disassembly. In both samples there is Ni and Co contamination from the layered phase, however there is minimal Al/ Li precipitation through from the LMO, despite there being > 3% Li in the starting spinel material along with notable Al contamination from the layered phase (1.18 and 0.59 % mass for QCR and EOL, respectively). This suggests that Li and Al do not precipitate out as metal oxalates as readily as the other ions when LMO is added to the oxalic acid solution.

These findings for Li are consistent with solubility values in the literature. For Li oxalate precipitation to occur in water at 20°C, > 6.6 g of Li oxalate must be present per 100g water, shown in Table 4.4. All the transition metal solubility values are documented in the literature, and are at least $10^2$ times less soluble than Li in water at 20 °C. This finding agrees with the observed elemental contamination in the samples.

*Table 4.4. Literature findings for solubility/gram per 100g water – used to aid discussion on elements seen in samples after interconversion.*

| Element | Solubility/gram per 100g water |
|---|---|
| **Li** | 6.6[150] |
| **Al** | - |
| **Mn** | 0.032[151] |
| **Co** | 0.0037[151] |
| **Cu** | 0.0026[151] |
| **Ni** | 0.0012[151] |

As Al oxalate solubility was not identified within the literature, a qualitative method was used to clarify that Al should not interconvert into the oxalate species when LMO was treated in the oxalic acid solution. A $LiMn_{1.95}Al_{0.05}O_4$ sample (denoted Al-LMO in table 4.5) was synthesised using a solid-state method – this material was used to determine whether Al would be expected in the interconverted Mn oxalate sample. The Al-doped sample was then added to the 1.25 M oxalic acid solution under the same conditions as those used for interconversion of LMO samples into Mn oxalate, to determine whether Al precipitated along with the Mn during this process. The precipitate (labelled Al-Mn ox) was then analysed using ICP to determine the elemental composition of the resulting Mn oxalate product, shown in table 4.5 and Fig. 4.8.

*Table 4.5. ICP data showing percentage composition by mass of Li, Mn, Ni, Co, Al and Cu within the Al-LMO and interconverted Mn oxalate samples*

| **Sample** | **% mass** | | | | | | | |
|---|---|---|---|---|---|---|---|---|
| | **Li** | **Mn** | **Ni** | **Co** | **Al** | **Cu** | **Total** | **Unmeasured** |
| **Al-LMO** | 3.83 (0) | 66.56 (0.22) | - | - | 0.77 (0) | - | 71.16 | 28.84 |
| **Al-Mn ox** | - | 31.90 (0.11) | - | - | - | - | 31.90 | 68.10 |

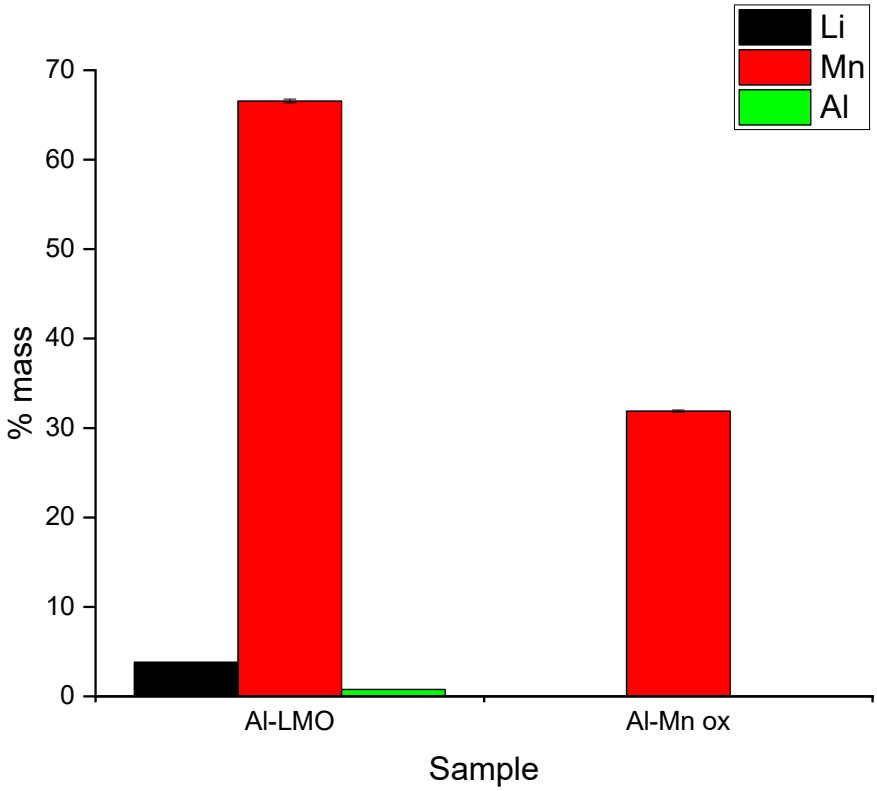


*Figure 4.8. Bar chart presenting ICP data: percentage composition by mass of Li, Mn and Al within the Al-LMO and interconverted Mn oxalate samples.*

As expected, the results show that negligible Li and Al contaminants were detected in the resultant Mn oxalate, clarifying the absence of these ions is due the fact that they do not precipitate as readily in these experimental conditions as the other contaminant elements seen in the precipitation process do. Regarding materials recovery and regeneration, the findings from this process show no Li precipitation when upon treatment of LMO with oxalic acid. This therefore means that Li present in the filtrate could be recovered to ensure this valuable Li is reused/ repurposed, ensuring all the LMO is upcycled into useful products. Due to the rapid expansion of the energy storage industry and the increasing popularity of Li-ion batteries, the

requirement for recovery of lithium is increasing exponentially. In the literature one recovery method that often arises is precipitation using $Na_2CO_3$. The precipitate product, lithium carbonate, is very valuable and may be used in electrode formation of new LiBs which would ensure the circularity of the lithium-ion battery recycling process. Outside of the battery industry, lithium carbonate may also be used in catalysis, ceramics and other significant industrial applications.[152–154,155]

Rietveld refinement was used to determine the lattice parameters and cell volumes of each Mn oxalate dihydrate sample. The *a*-parameters, *c*-parameters and cell volumes for each sample are shown in table 4.6 the refinements are shown in Fig. 4.9 a, b, and c, and the lattice parameter and cell volume plots are shown in Figs. 4.10 – 4.12.

Due to the degree of error observed in these measurements differences between lattice parameters indicated there was no significant lattice parameter contraction between Mn oxalate samples and further data collection is required. In Mn oxalate dihydrate, the $Mn^{2+}$ cation is coordinated to 2 water molecules and 2 bidentate oxalate ligands in an octahedral fashion. Due to the expected shorter bond length of Ni–O and Co–O or due to the replacement of Mn for these contaminant ions with decreased ionic radii, it was expected that the substitution of Mn ions for Ni/ Co ions would give rise to unit cell contraction.  Furthermore, the overlap of error in the cell volume data for the pristine and QCR samples give no evidence of any structural change. In the EOL material, however, the values suggest that there is lattice contraction. As both Co and Ni contamination were higher in the EOL sample (as recorded in the ICP-OES data), a greater cell volume contraction for EOL > QCR >

pristine sample is rationalised, however more measurements are still necessary to resolve the structural differences between these samples.

*Table 4.6. Calculated a-parameters, c-parameters, and cell volumes for pristine, QCR and EOL Mn oxalate dihydrate*

| Sample | ***a*-parameter (Å)** | ***c*-parameter (Å)** | **Cell volume (Å)** | **$Rw_p$ (%)** |
|---|---|---|---|---|
| **Pristine** | 12.01(1) | 9.979(8) | 529.7(1) | 10.96 |
| **QCR** | 12.01(1) | 9.973(11) | 529.6(2) | 7.64 |
| **EOL** | 12.00(1) | 9.968(8) | 528.4(1) | 6.85 |

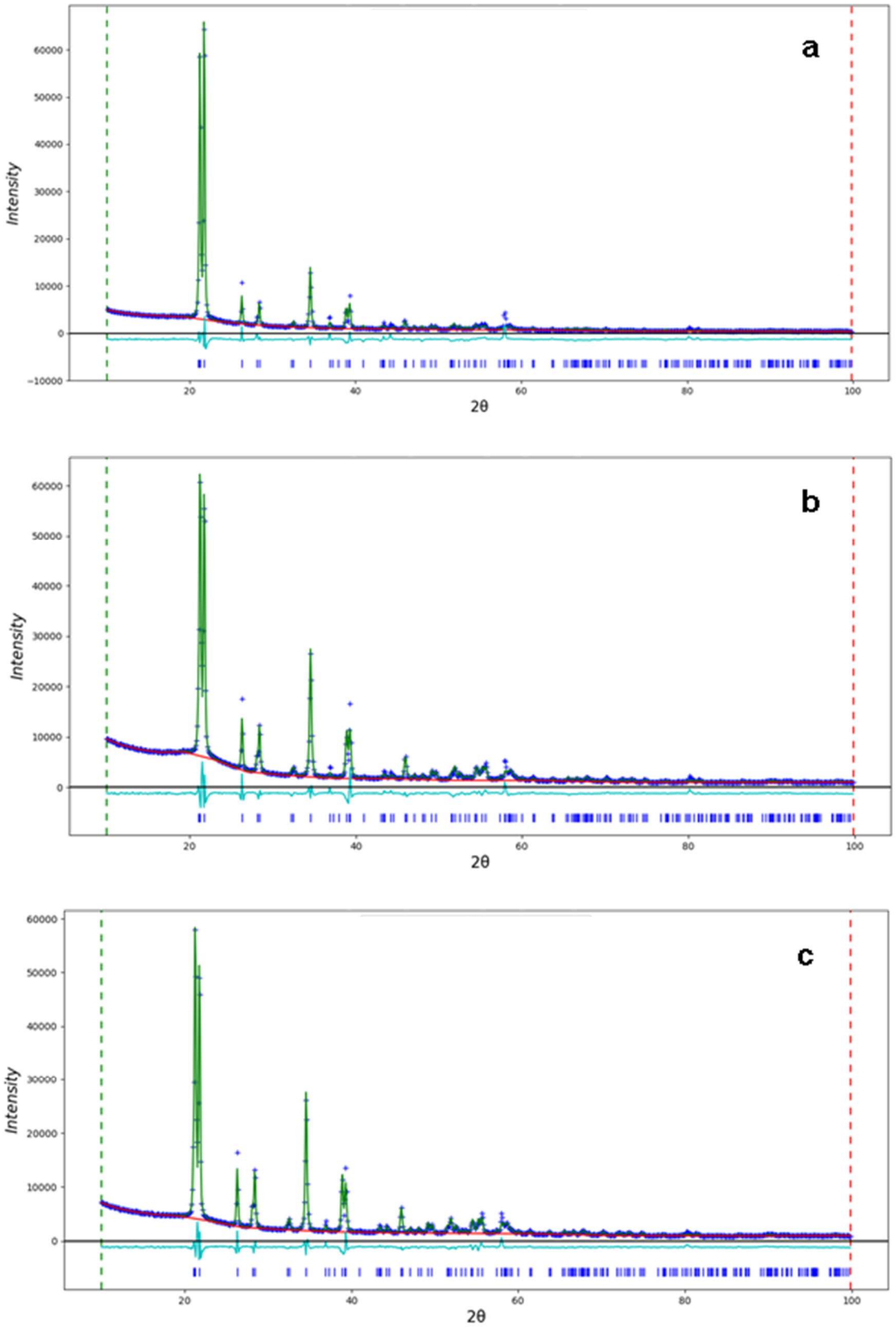


*Figure 4.9. Refined XRD patterns of α'-Mn oxalate dihydrate with reflections for space group C12/c1 marked in blue – pristine (a), QCR (b) and EOL (c).*

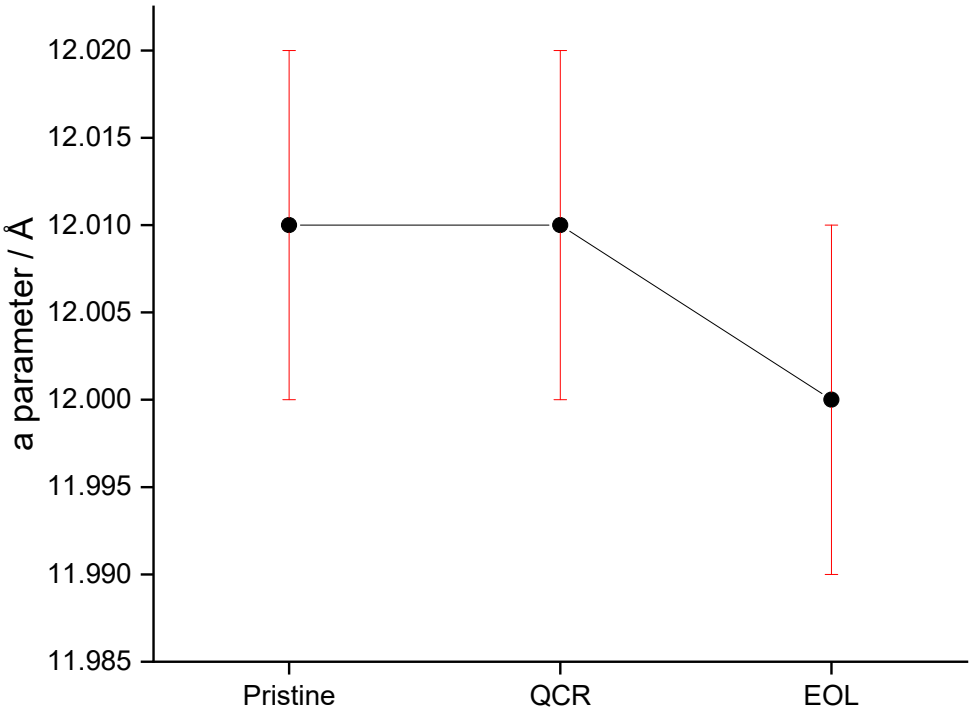


*Figure 4.10. Calculated a-parameters for pristine. QCR and EOL Mn oxalate dihydrate.*

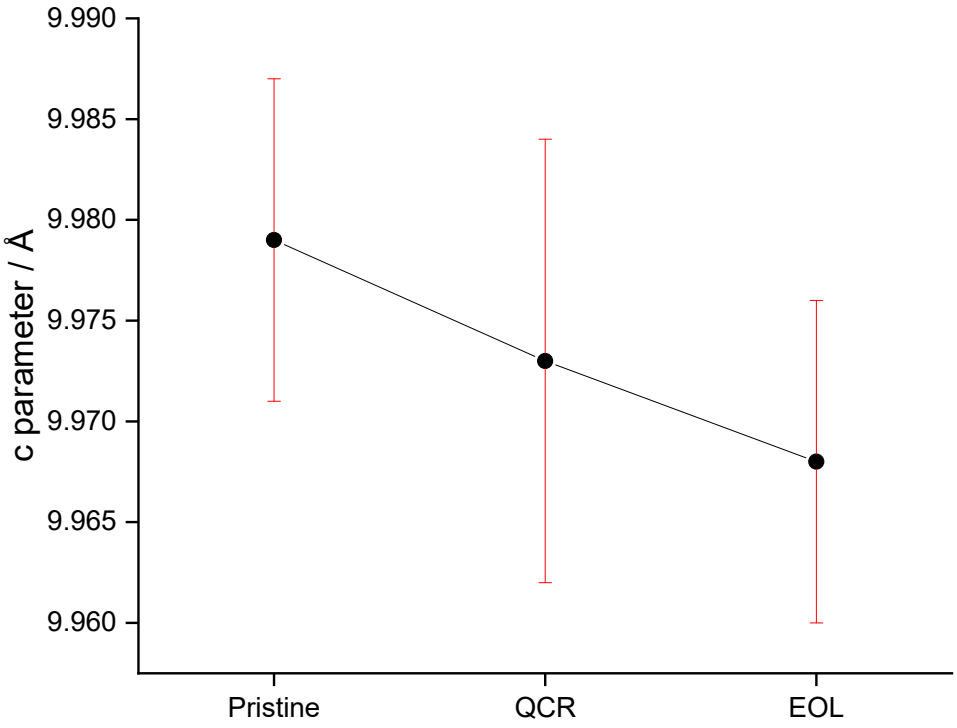


*Figure 4.11. Calculated c-parameters for pristine, QCR and EOL Mn oxalate dihydrate.*

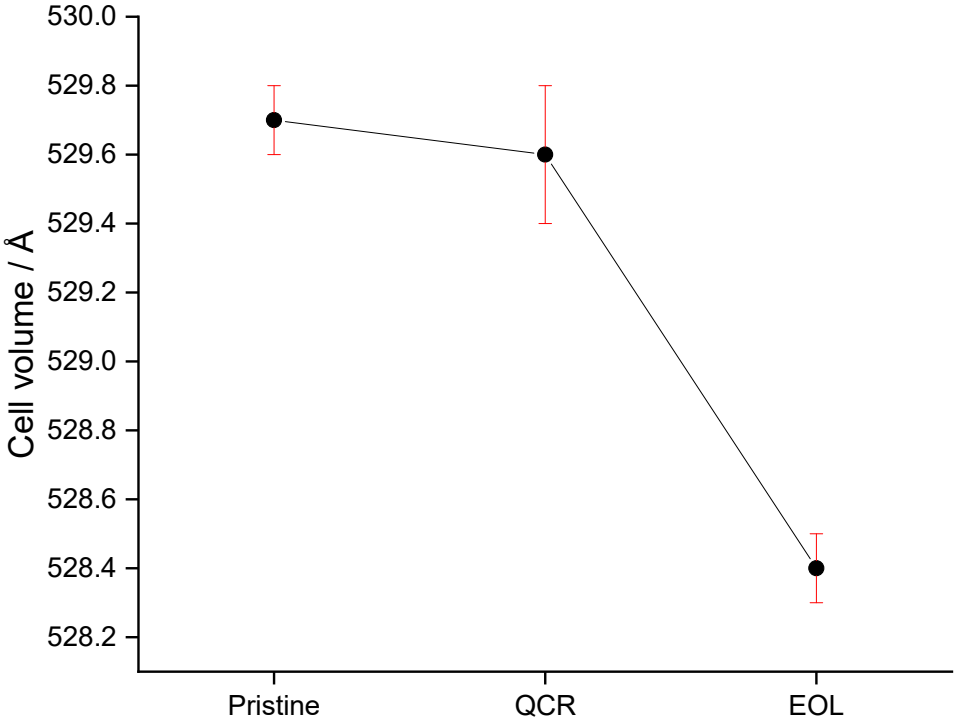


*Figure 4.12. Calculated cell volumes for pristine, QCR, and EOL Mn oxalate dihydrate.*

**$Mn_2O_3$**

XRD patterns of all the $Mn_2O_3$ samples materials are shown with indexing in Fig. 4.13. After assessment of the XRD patterns through pattern matching, it was identified that an orthorhombic $Mn_2O_3$ structure with space group Pcab had successfully been synthesised in all cases. Upon observation, there is very little difference between XRD patterns for the three materials, aside from an additional reflection beside the (123) reflection of the EOL sample (marked with a red * in Figure 4.13). Through pattern matching and refinement, shown in Fig. 4.14, this extra peak has been identified as an $Mn_3O_4$ phase with space group $I4_1/amd$. Rietveld refinement indicates that the weight fraction of $Mn_3O_4$ present in the EOL material is 0.04% (±0.01).

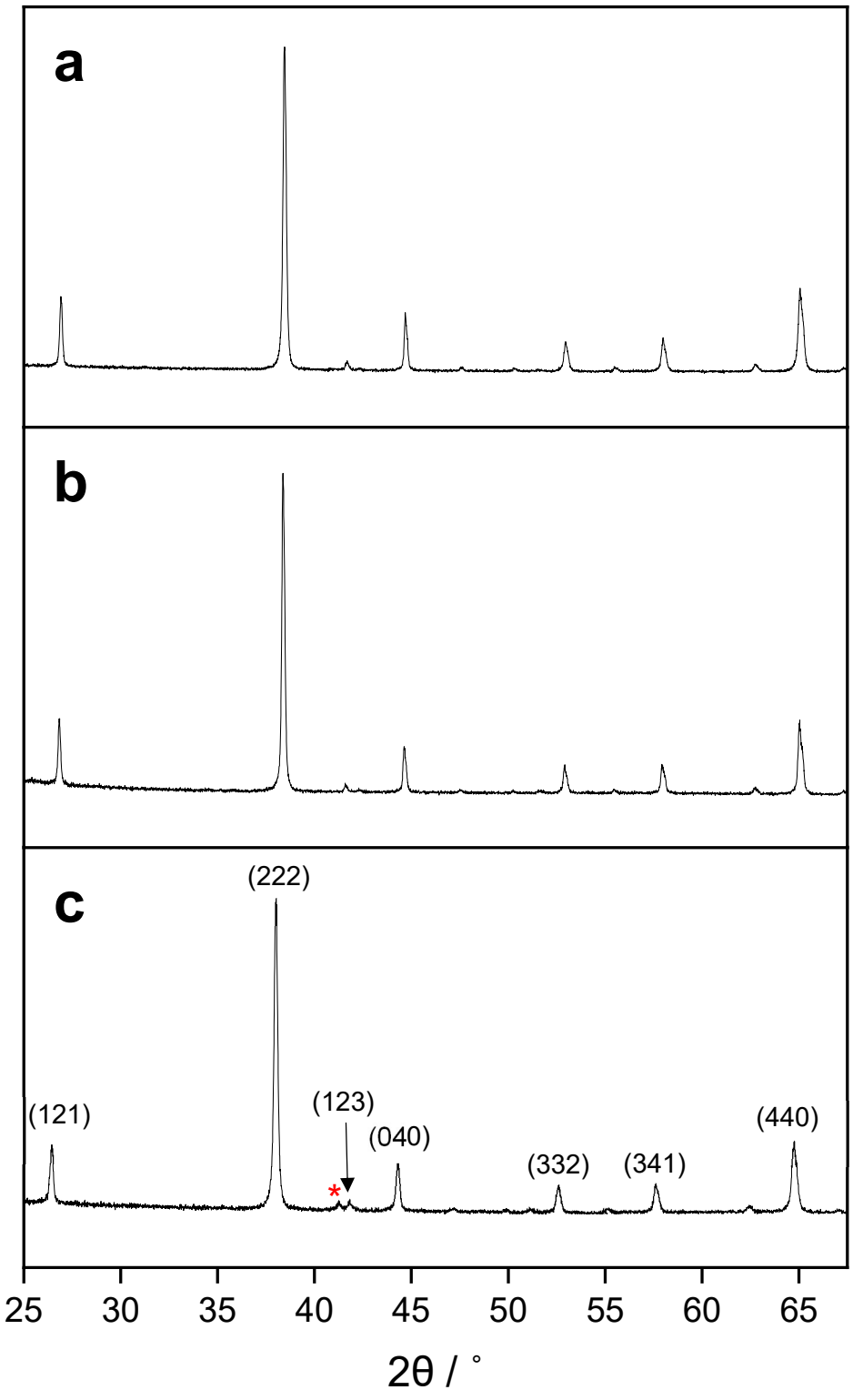


*Figure 4.13. XRD patterns (with indexing) of $Mn_2O_3$ with space group Pcab – pristine (a), QCR (b) and EOL (c) – with an impurity phase marked with a red *.*

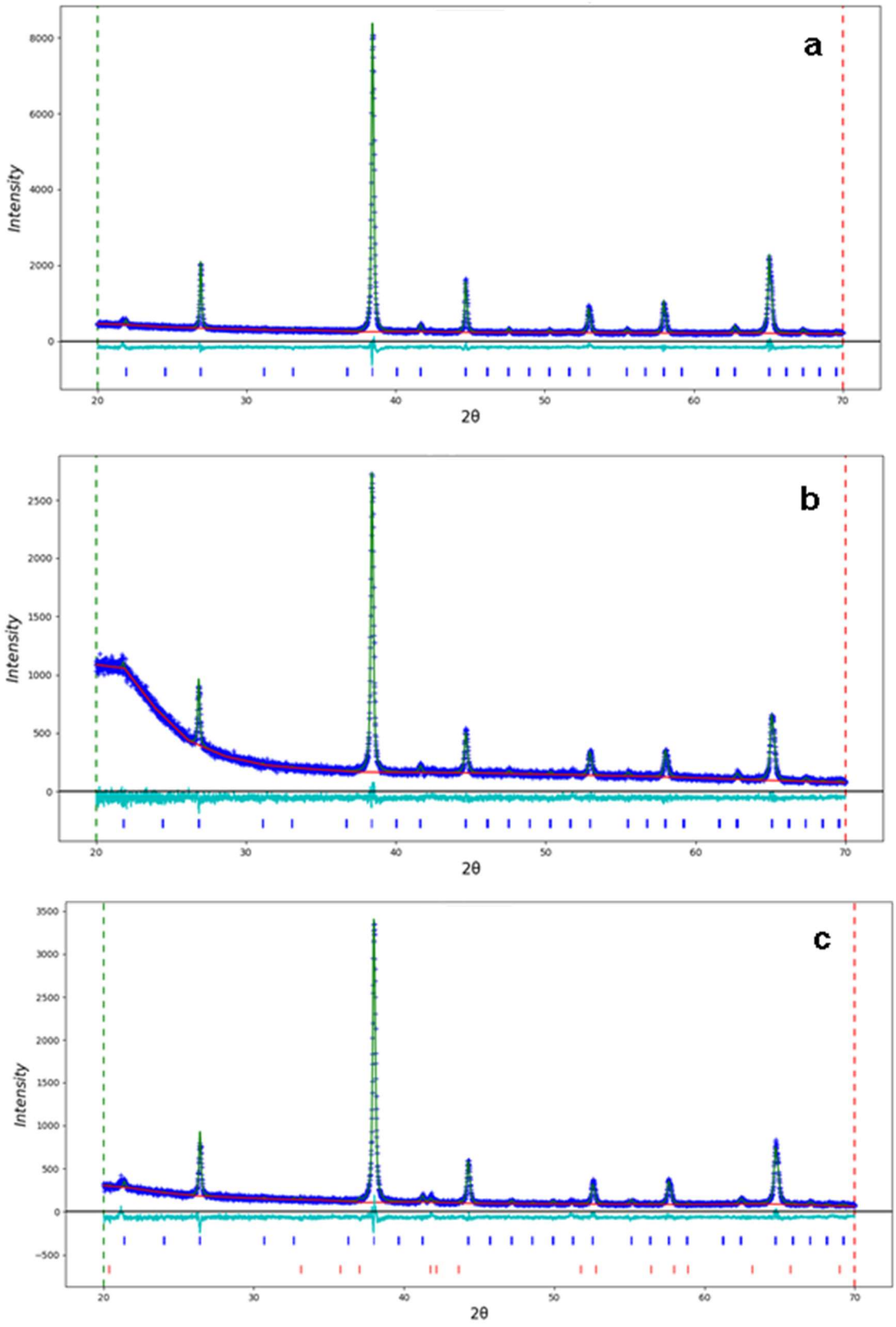


*Figure 4.14. Refined XRD patterns (with indexing) of $Mn_2O_3$ with* reflections for group *space group Pcab in blue and $Mn_3O_4$ in red – pristine (a), QCR (b) and EOL (c)*

ICP-OES analysis was used to determine the contamination in interconverted $Mn_2O_3$ from pristine, QCR and EOL LMO precursor materials. The percentage masses of the samples have been calculated and depicted in table 4.7. As observed for the Mn oxalate sample, Ni, Co, and Cu contamination is interconverted through for the QCR and EOL leached samples from the layered phase and the dissolution of the current collector during overcharge. The alumina crucible used to form the Mn oxides in are likely to be the cause of the minor Al contamination (~0.02%) in QCR $Mn_2O_3$.

The cell volumes and *a* and *c*-parameters for the $Mn_2O_3$ phase (in each sample) are shown in table 4.8 and Fig. 4.15. As was the case for LMO, lattice parameter and cell volume contraction occurred in all cases for the QCR and EOL $Mn_2O_3$ samples when compared to pristine material. This shrinkage was expected, as the occupancy of TM contaminants in Mn sites within the structure were thought to have similar effects to those outlined for LMO (stronger M—O bonding and decreased ionic radius effects). The degree of error overlap between lattice parameter values for the leached samples shows their parameter contraction was statistically significant when compared to the pristine sample, but not to one another. For the cell volume values, however, the higher degree of contamination in the EOL sample indicated the greatest cell volume shrinkage.

*Table 4.7. ICP data showing % mass of Li, Mn, Ni, Co, Al, and Cu within the pristine, QCR and EOL interconverted $Mn_2O_3$ samples*

| Sample | % mass | | | | | | | |
|---|---|---|---|---|---|---|---|---|
| | **Li** | **Mn** | **Ni** | **Co** | **Al** | **Cu** | **Total** | **Unmeasured** |
| **Pristine** | - | 80.72 (0.44) | 0.03 (0.01) | - | - | - | 80.75 | 19.25 |
| **QCR** | 0.05 (0) | 75.62 (0.2) | 1.56 (0.004) | 0.19 (0.0004) | 0.02 (0.0004) | 0.05 (0) | 77.49 | 22.51 |
| **EOL** | - | 76.61 (0.05) | 0.53 (0.0008) | 1.63 (0.004) | - | - | 78.77 | 21.23 |

*Table 4.8. Calculated a-parameters, c-parameters, and cell volumes for pristine, QCR and EOL $Mn_2O_3$*

| Sample | ***a*-parameter (Å)** | ***c*-parameter (Å)** | **Cell volume (Å)** | **$Rw_p$ (%)** |
|---|---|---|---|---|
| **Pristine** | 9.4122 (6) | 9.408 (6) | 832.75 (6) | 6.62 |
| **QCR** | 9.3870 (2) | 9.387 (2) | 828.30 (9) | 6.31 |
| **EOL** | 9.3900 (2) | 9.387 (3) | 827.52 (9) | 7.10 |

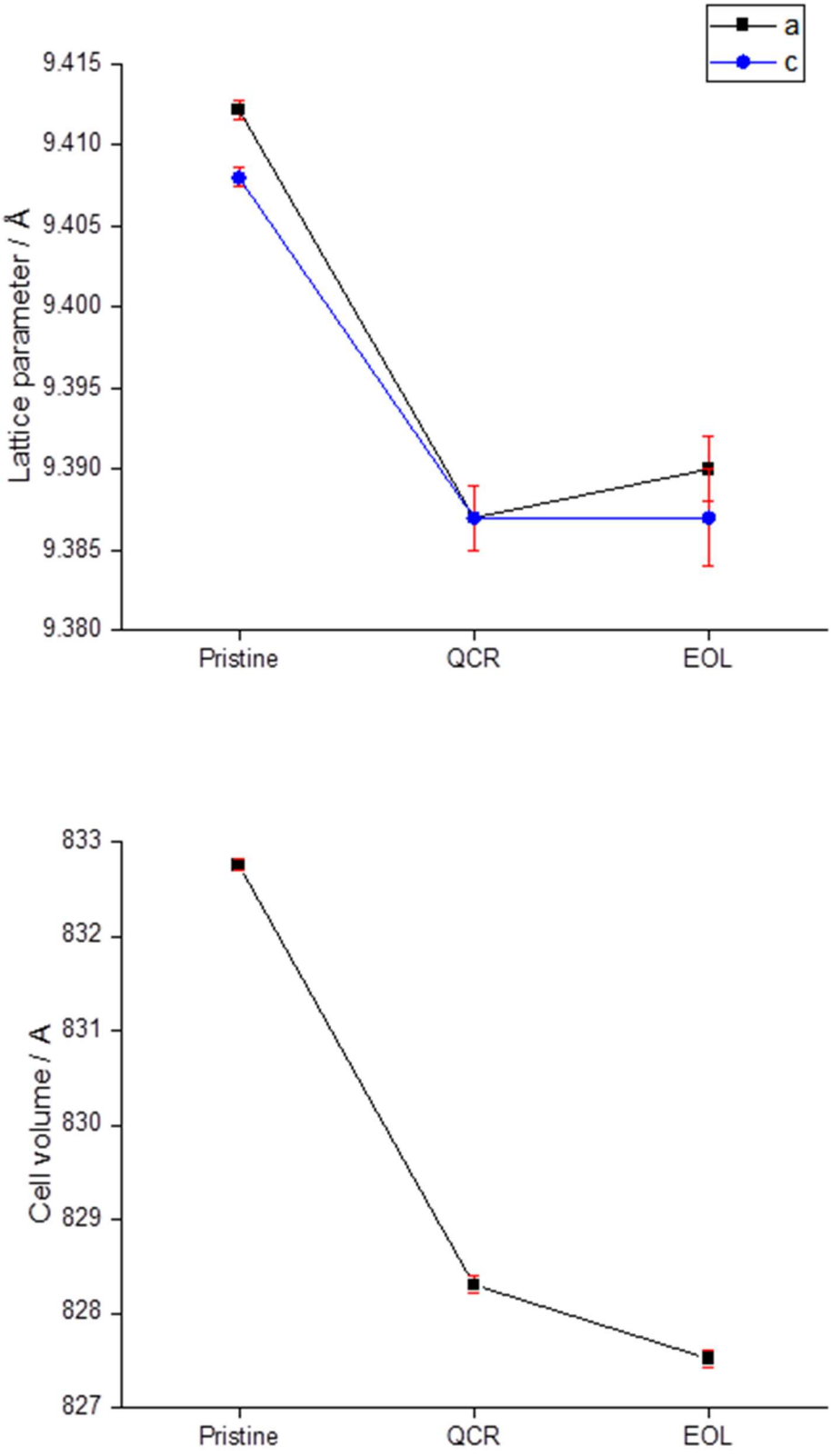


*Figure 4.15. Calculated a-parameter, c-parameters, and cell volumes for pristine, QCR, and EOL $Mn_2O_3$*

**$Mn_3O_4$**

XRD patterns were taken of all the $Mn_3O_4$ samples materials their composition was identified through pattern matching. It was observed that a tetragonal $Mn_3O_4$ structure of space group $I4_1/amd$ had successfully been synthesised in all cases, and the contaminant ions had incorporated into the structure without any phase change, as was observed in a $Mn_3O_4$ Cu-doping study by Chen et al.[156] Upon further comparison of the XRD patterns, there is peak broadening in the $Mn_3O_4$ material when leached, which is likely due to cationic contamination of the sample by the leached ions. The origin of this is likely due to the contaminant Ni and Co ions the structure, that lower the symmetry of this material. In an $Mn_3O_4$ doping study by Raja et al., it was noted that the most intense peak in the XRD pattern was widened by increasing the Ni content in their study, as is observed here for the $Mn_3O_4$ sample in the refinements shown in Fig.4.16 indicating the transition metal ions are substituting for Mn ions within the lattice.[157]

ICP-OES analysis was used to determine the contamination in interconverted $Mn_3O_4$ from pristine, QCR and EOL LMO precursor materials. The percentage masses of the samples have been calculated and depicted in table 4.9. As observed for all other interconverted samples, Ni, Co, and Cu contamination is interconverted through for the QCR and EOL leached samples from the layered phase and the dissolution of the current collector during overcharge. The alumina crucible used to form the Mn oxides in are likely to be the cause of the minor Al contamination (~0.02%) in QCR $Mn_3O_4$.

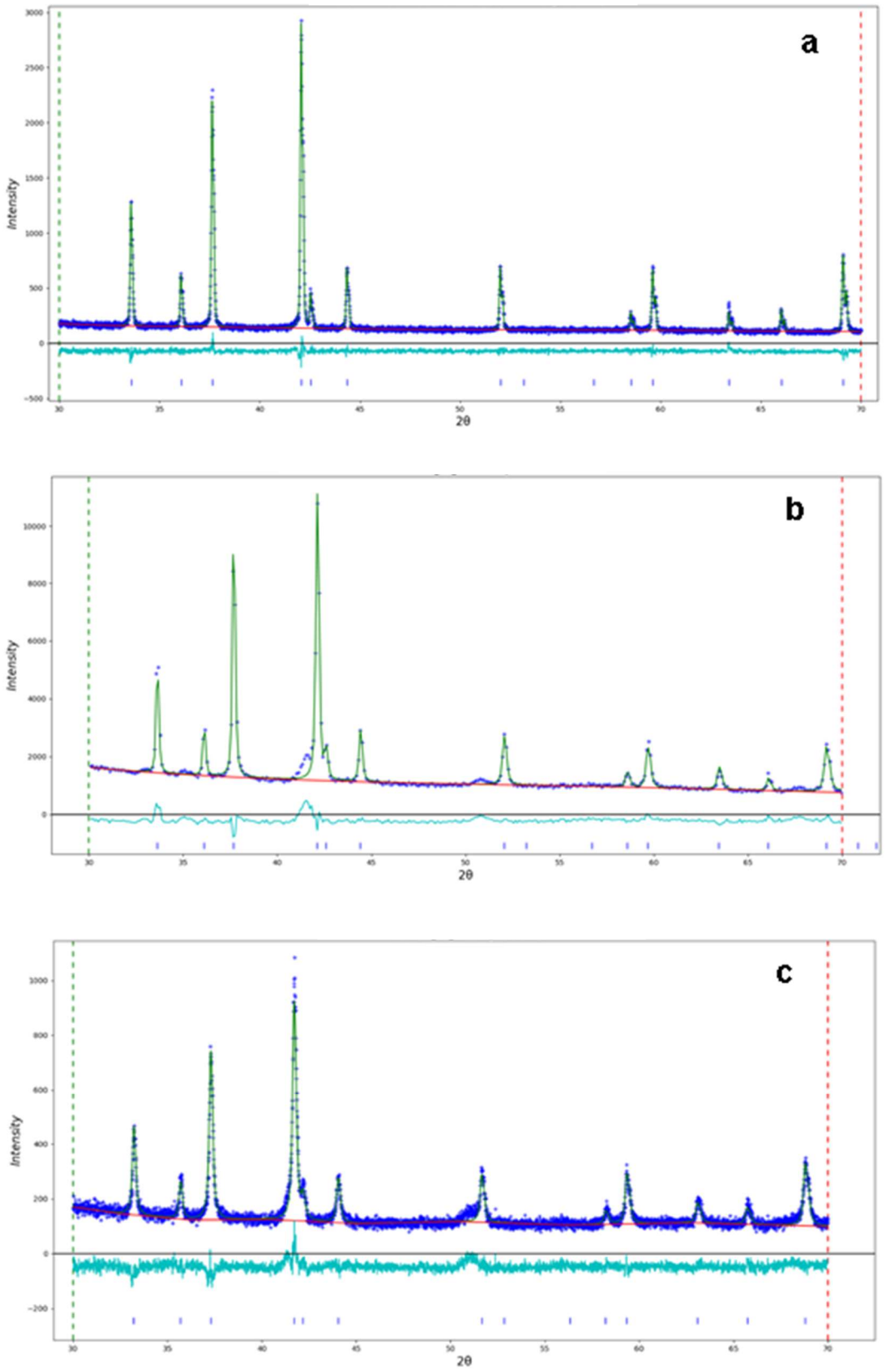


*Figure 4.16. Refined XRD patterns of $Mn_3O_4$ with reflections for space group $I4_1/amd$ marked in blue – pristine (a), QCR (b) and EOL (c).*

*Table 4.9. ICP data showing % mass of Li, Mn, Ni, Co, Al, and Cu within the pristine, QCR and EOL interconverted $Mn_3O_4$ samples*

| Sample | % mass | | | | | | | |
|---|---|---|---|---|---|---|---|---|
| | **Li** | **Mn** | **Ni** | **Co** | **Al** | **Cu** | **Total** | **Unmeasured** |
| **Pristine** | - | 82.74 (0.03) | 0.02 (0.0005) | - | - | - | 82.76 | 17.24 |
| **QCR** | 0.04 (0) | 81.57 (0.12) | 0.59 (0.0004) | 0.07 (0) | 0.02 (0.0004) | 0.04 (0) | 82.33 | 17.67 |
| **EOL** | - | 77.62 (0.2) | 0.53 (0.001) | 1.65 (0.006) | - | - | 79.8 | 20.2 |

The cell volumes and a and c parameters for the $Mn_3O_4$ phase (in each sample) are shown in table 4.10 and Figs. 4.17 and 4.18. Through refinement of the XRD patterns, displayed in Fig. 4.19, the unit cell parameters and cell volumes of the $Mn_3O_4$ products provide valuable information about the doping behaviour of the contaminant ions. Lattice parameter and cell volume contraction occurred in all cases for the QCR and EOL $Mn_3O_4$ samples. The occupancy of TM contaminants in Mn sites within the structure were thought to have similar effects to those outlined for LMO (stronger M─O bonding and decreased ionic radius effects), as seen in the $Mn_2O_3$ phase. Additionally, as outlined by S. Zhang et al. and S. Hirai et al., an increased concentration of dopant ions will affect the Jahn-teller distortion within the structure of $Mn_3O_4$, by reducing the number of Jahn-teller active $Mn^{3+}$ ions present within the structure. The degree of Jahn-teller distortion within Co-doped $Mn_3O_4$

samples in their studies has been quantified using the Jahn-teller distortion indicator, with equation $\frac{c}{\sqrt{2}a}$ .[158,159] The increased number of dopant ions within the structure has an inverse effect on the Jahn-teller distortion indicator. For pristine, QCR and EOL samples the Jahn-teller distortion indicators were 2.78607(1), 2.78426(2) and 2.78186(9), respectively, which was the expected trend due to the introduction of a greater proportion of contaminant ions in structure of the material (pristine < QCR < EOL, according to ICP). In $Mn_3O_4$, the $Mn^{3+}$—O octahedra are elongated along the [001] direction. The reduction in *c*-parameters and Jahn-Teller distortion values with introduction of a greater proportion of contaminant ions therefore provides further evidence of replacement of $Mn^{3+}$ ions within the structure for the dopant ions and/or smaller charge balancing $Mn^{4+}$ ions.

*Table 4.10. Calculated a-parameters, c-*parameters, *and cell volumes for pristine, QCR and EOL $Mn_3O_4$*

| **Sample** | ***a*-parameter (Å)** | ***c*-parameter (Å)** | **Cell volume (Å)** | **$Rw_p$ (%)** |
|---|---|---|---|---|
| **Pristine** | 5.7597(2) | 9.4560(2) | 313.69(3) | 7.58 |
| **QCR** | 5.7560(4) | 9.4468(4) | 312.99(4) | 10.72 |
| **EOL** | 5.7563(5) | 9.4389(7) | 312.76(6) | 18.52 |

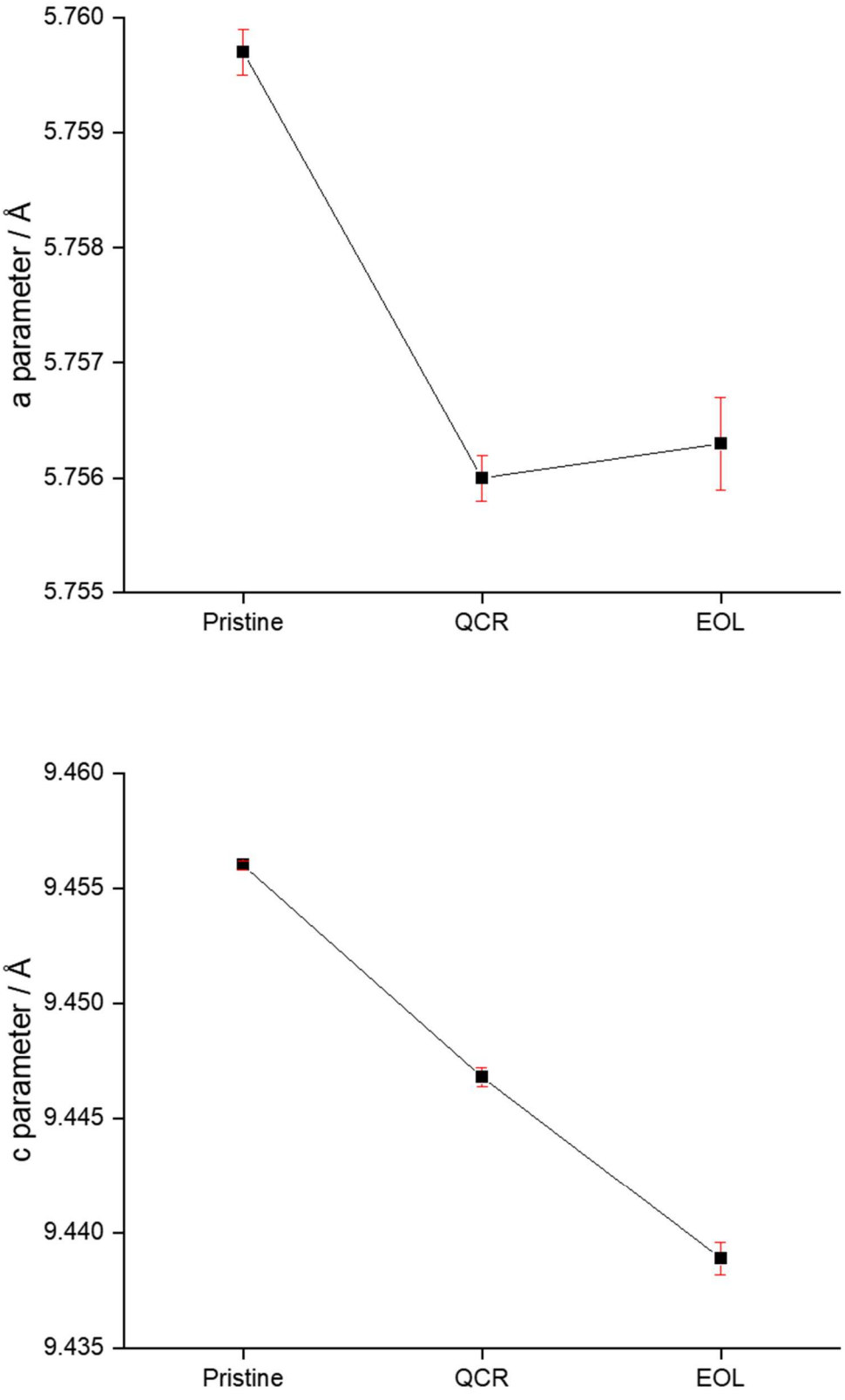


*Figure 4.17. Calculated a and c-parameters pristine, QCR, and EOL $Mn_3O_4$*

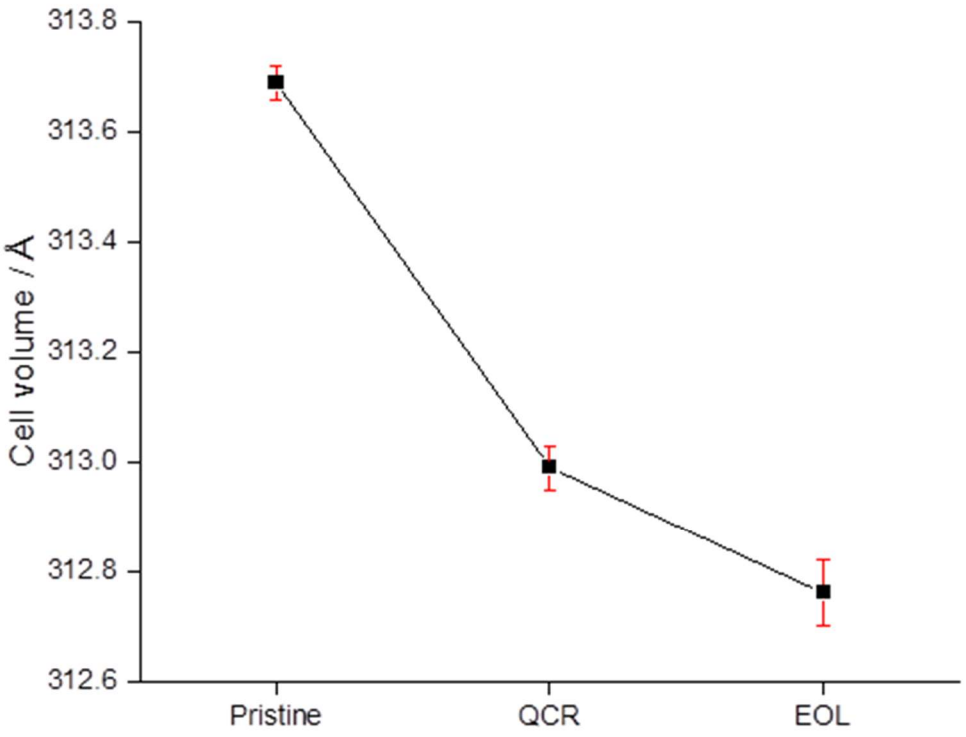


*Figure 4.18. Calculated cell volumes for pristine, QCR, and EOL $Mn_3O_4$*

## 4.4.2 Raman spectroscopy

To analyse the structural evolution of LMO, Mn oxalate, $Mn_2O_3$ and $Mn_3O_4$ samples, Raman spectroscopy was used, as this technique complements XRD in the analysis of cation-oxygen coordination on a local scale.[122] As previously determined – there are numerous contaminant ions present within the leached samples which, based on XRD analysis, appear to occupy manganese sites within the crystal lattice of these materials. As Raman spectroscopy is used to determine vibrational modes between atoms in the lattice structure, any contaminant ions present that are expected to disrupt the crystal symmetry/ replace Mn should impact the vibrational modes and

therefore Raman bands observed in this technique. In each comparison, the Raman spectra were normalised between 0 and 1 to enable clear understanding of the differences between samples through peak visualisation. The normalisation was performed by taking the maximum peak intensity as 100% in each Raman spectrum and dividing the remainder of the peaks by the maximum intensity to generate a normalised peak intensity relative to the maximum intensity. All the Raman scans outlined in this section were run for the same duration and wavelength.

Add The Raman spectra for pristine, QCR and EOL LMO are shown in Fig. 4.19. The Raman bands detected for this material further confirm that the $LiMn_2O_4$ phases formed with space group $Fd\bar{3}m$, as opposed to the ordered spinel structure (space group $P4_332$) which is fairly indistinguishable using x-ray diffraction, but very distinct using Raman spectroscopy.[160] Distinguishing between M─O Raman bands,(e.g $Mn^{4+}$─O, $Mn^{3+}$─O and $Ni^{2+}$─O) is not always straightforward due to the similarity between Raman scattering of particular M─O bonds, therefore information can be taken from the comparison of pristine LMO to the Raman scattering plots of the leached materials. According to the symmetry rules of normal $LiMn_2O_4$ spinel, there should be $A_{1g}$, $E_g$ and $3F_{2g}$ Raman active modes observed for the cubic space group $Fd\bar{3}m$. Despite these symmetry rules, only two distinguishable Raman bands are detected in the pristine $LiMn_2O_4$ sample. This can be rationalised by the high relative electrical conductivity of uncontaminated LMO spinel, whereby the equal occupancy of tri- and tetravalent Mn ions in the 16d octahedral sites causes a fast rate of electron hopping rate between ions. This electronic hopping results in reduced scattering intensity of the incident laser beam, causing fewer Raman active modes to be observed. The presence of contaminant ions in the LMO spinel disrupts the

structure of the materials, causing an unequal occupancy of $Mn^{3+}$ and $Mn^{4+}$ ions in the octahedral sites, reducing the relative electrical conductivity and the electron hopping rate. This phenomenon can be used to explain the presence of an increased number of Raman bands in the QCR and EOL materials.[161,162] The large peak observed at ~633-639 $cm^{-1}$ in all three LMOs is characteristic of symmetric Mn-O stretching in an octahedral environment, and it corresponds to $A_{1g}$ symmetry with $O^7_h$ spectroscopic symmetry. The peak at ~342 $cm^{-1}$ in the pristine LMO sample corresponds to the Li-O vibrational mode of the $LiO_4$ tetrahedra within the structure. Due to the presence of various extra vibrational modes in the contaminated leached samples, this Li sublattice vibration is less obvious. The significant difference between the pristine and leached samples is the broadening of the peak at ~633-639 $cm^{-1}$ with more metal contamination, alongside multiple shouldering peaks. It has been well-documented that if dopant ions are incorporated into LMO an $Fd\bar{3}m$ structure at the octahedral 16d sites, the dopant ions will randomly distribute themselves alongside charge balanced Mn ions, as has been supported by the XRD data. [163–166] The broadening seen with leaching can be attributed to the fact that Mn-O vibrational modes (and therefore the Raman bands produced) are highly sensitive to the valence of the manganese ions in the structure. As the contaminant ions sit in in these octahedral Mn sites, these directly affect the valence of Mn due to charge balancing effects. For example, the Raman active $F^12g$ vibrational modes observed (at ~578 and 573 $cm^{-1}$ for QCR and EOL, respectively) provide evidence for this, as an increased concentration of $Mn^{4+}$ within the structure means that the shoulder $Mn^{4+}$—O Raman band is clearly visible for the QCR and EOL samples. The prominence of this Raman band is greater in the EOL sample, which may be

rationalised due to the larger proportion of divalent contaminant ions which were incorporated into the EOL sample than the QCR material (determined using ICP). The greater number of lower valence ions introduced requires more charge balancing from $Mn^{4+}$, rationalising the prominence of this shoulder. The peak at 492 $cm^{-1}$ in the QCR and EOL samples can be attributed to $F^2_{2g}$ Mn—O stretching mode (or a $Ni^{2+}$—O stretch) and the bands located at ~380 $cm^{-1}$ to $F^3_{2g}$ symmetry.

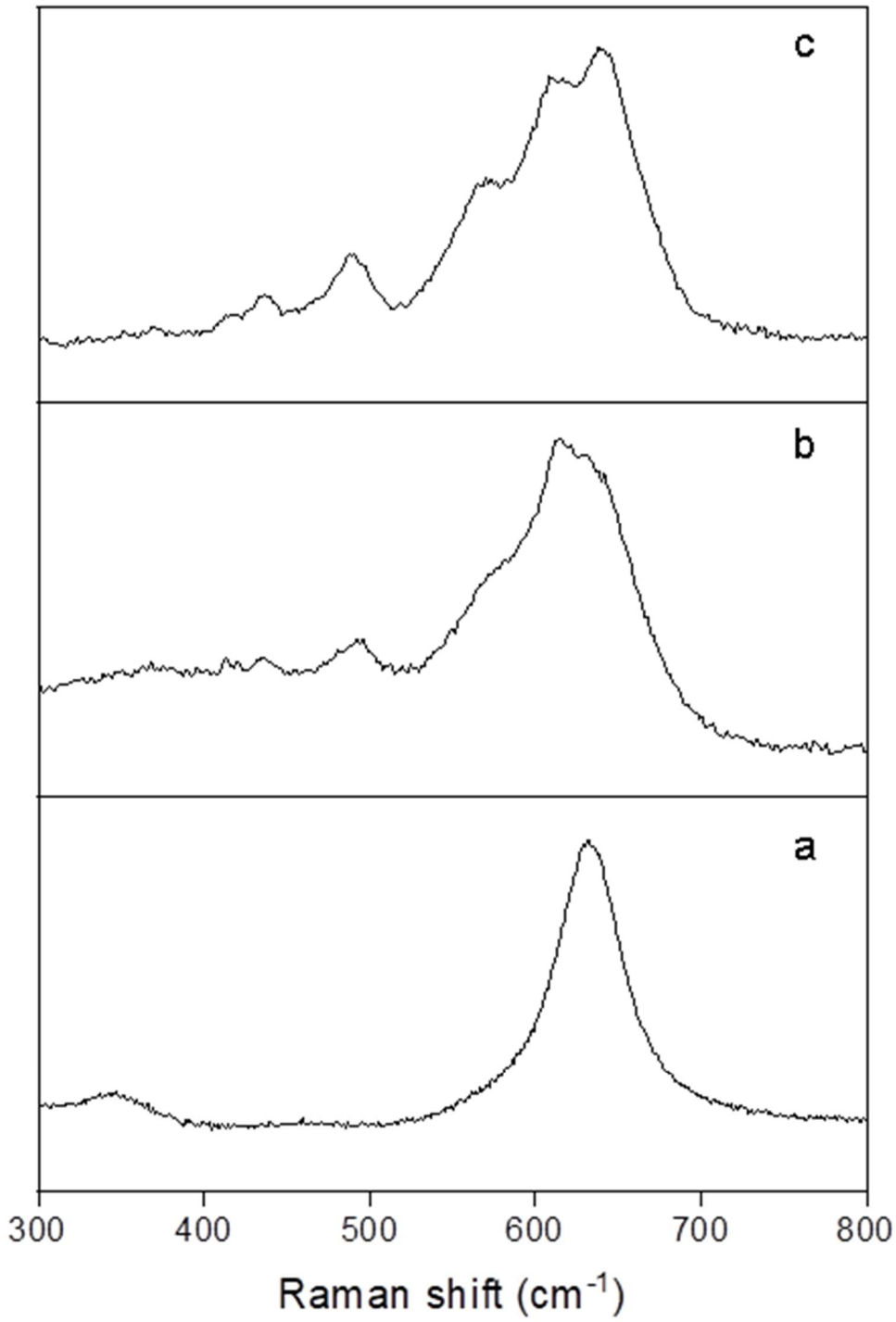


*Figure 4.19. Raman spectrum of $LiMn_2O_4$ with space group $Fd\bar{3}m$ – pristine (a), QCR (b) and EOL (c).*

The Raman spectra for the pristine, QCR and EOL monoclinic α'-Mn oxalate dihydrates are shown in Fig. 4.20 and 4.21. The commonalities in oxalate Raman modes can be described as follows:[167–169]

- 515 – 574 $cm^{-1}$: O─C─O bending
- 854 – 905 $cm^{-1}$: O─C─O stretching or C─C stretching
- 1418 – 1462 $cm^{-1}$: symmetric C─O stretching
- 1614 – 1707 $cm^{-1}$: asymmetric C─O stretching

In Mn oxalate dihydrate, the $Mn^{2+}$ cation is coordinated to 2 water molecules and 2 bidentate oxalate ligands in an octahedral fashion. With the presence of contaminant ions within the structure, this site occupation may be affected, and the Raman spectrum indicates this with the presence of additional peaks. To focus on differences between pristine, QCR and EOL samples, particular focus has been paid on the lower wavenumber region of the spectrum where there are different Raman bands observed between samples (between 400 and 1000 $cm^{1}$). In this region, distorted oxalate ion modes are anticipated, as well as M─O stretching vibrations within the octahedral metal centre.[170,171] There are peaks observed at 612 and 640 $cm^{-1}$ in the QCR and EOL samples, respectively, which are not present in the pristine Mn oxalate sample, indicating that introduced contaminant ions present within the structure are causing localised distortion and further indicating that the contaminant ions are being introduced in place of Mn within the structure.

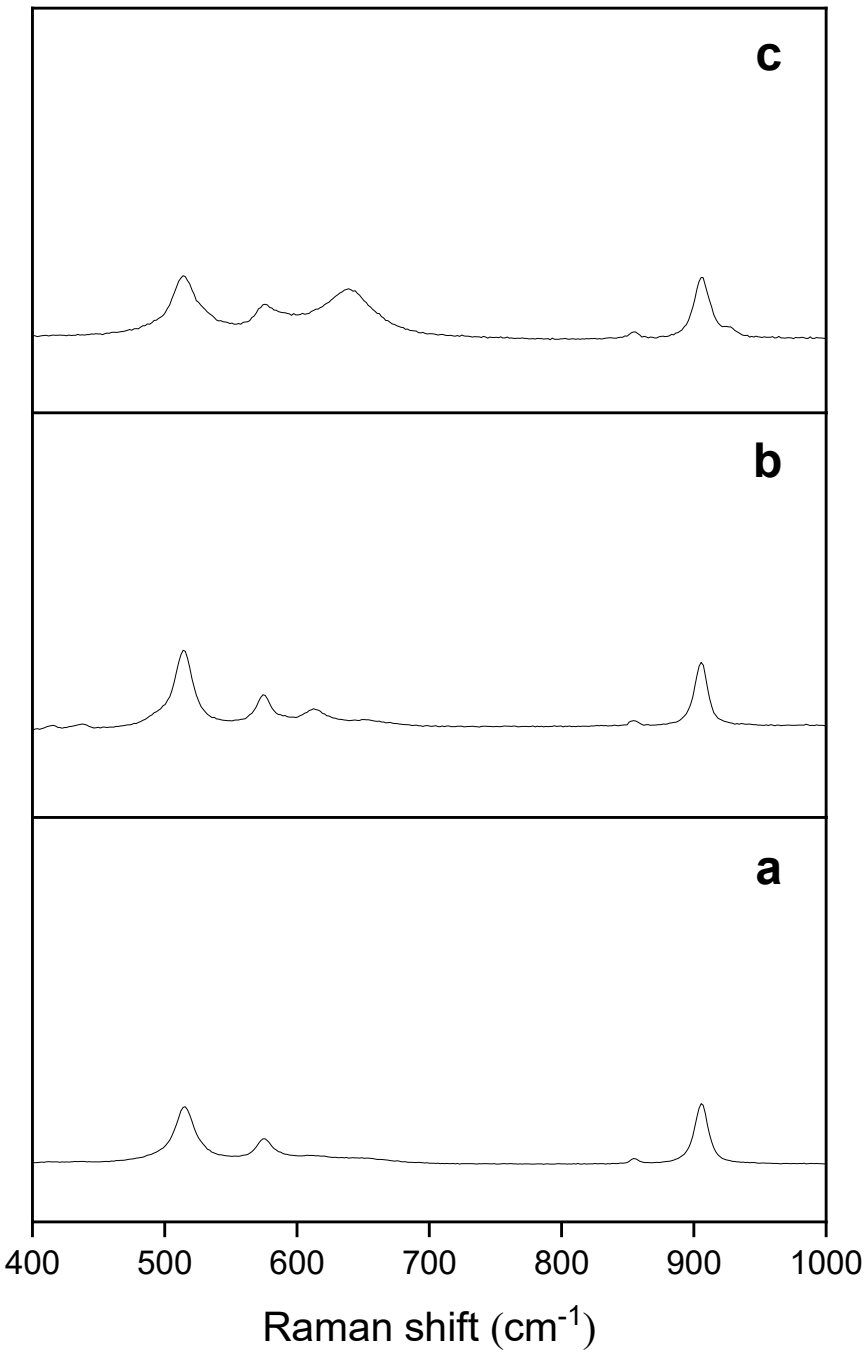


*Figure 4.20. Lower region Raman spectra of α'-Mn oxalate dihydrate with space group C12/c1 – pristine (a), QCR (b) and EOL (c).*

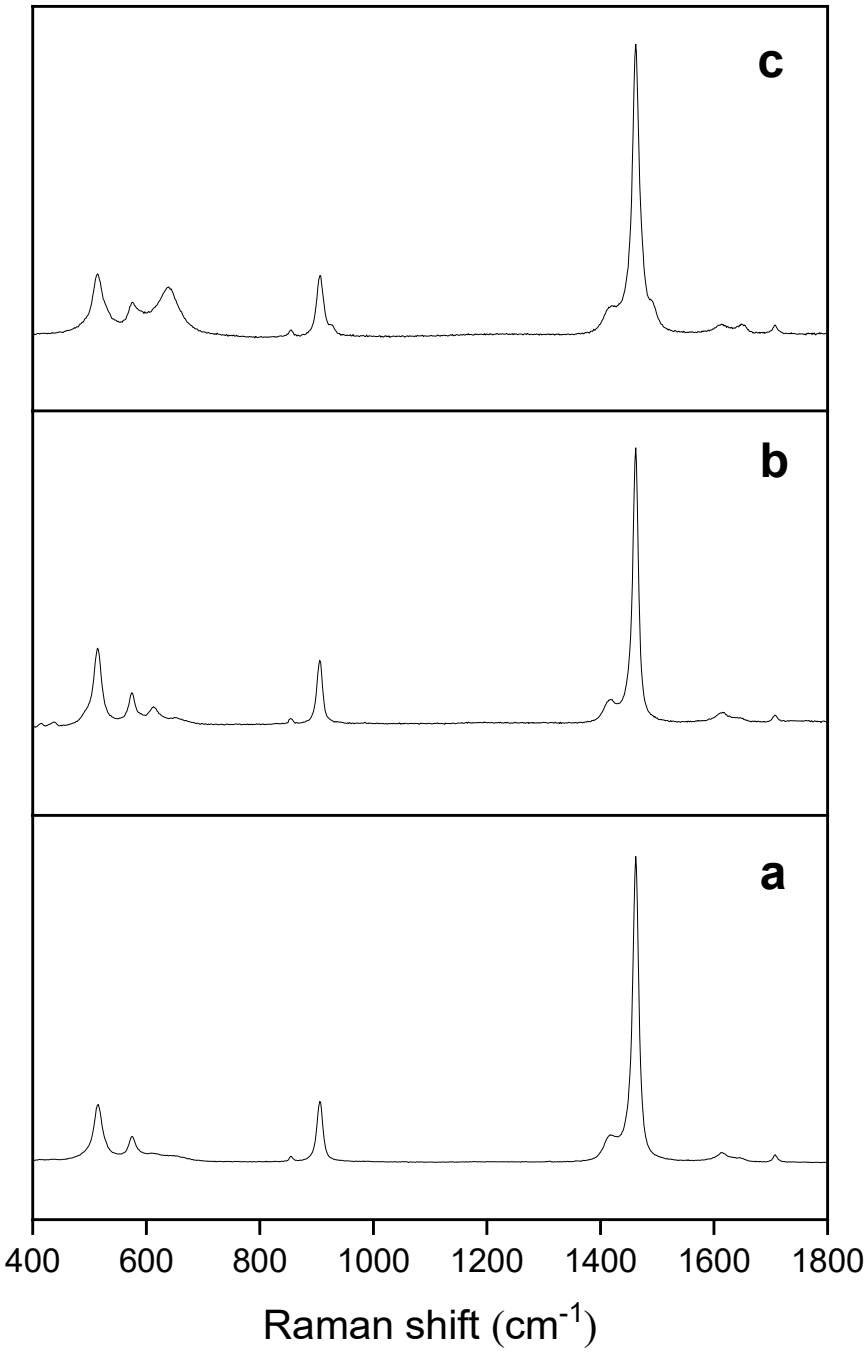


*Figure 4.21. Extended Raman spectra of α'-Mn oxalate dihydrate with space group C12/c1 – pristine (a), QCR (b) and EOL (c).*

The Raman spectrum for each $Mn_2O_3$ is shown in Fig. 4.22. The three Raman bands (observed in all 3 materials) arose at 624 $cm^{-1}$, 337 $cm^{-1}$ and 281 $cm^{-1}$ in the pristine sample. The most intense peak at 624 $cm^{-1}$ is assigned to the symmetric $Mn^{3+}$—O stretching modes in the filled octahedral sites (seen at 636 $cm^{-1}$ in QCR and 634 $cm^{-1}$ in EOL). The Raman bands at 337 $cm^{-1}$ and 281 $cm^{-1}$ are assigned to the Mn—O—Mn asymmetric stretching mode and the out-of-plane bending modes of $Mn_2O_3$, respectively. These bands are shifted to wavenumbers of at 348/342 $cm^{-1}$ and 293/290 $cm^{-1}$ for QCR/EOL materials, respectively.[172–174] The higher shift of these Raman bands further clarifies the existence of contaminant ions within the local structure of these manganese oxides, with the highest shift seen for the QCR material with the highest proportion of contaminant ions. It is also clear that the highest intensity of the Raman bands is seen for the pristine sample, which is drastically reduced in QCR and EOL material. This reduced intensity and broadening of the symmetric peak are defects which are introduced with contaminant ion addition. The addition of divalent cations in place of $Mn^{3+}$ ions results in the need for charge compensation within the structure of the $Mn_2O_3$, which is correlated with oxygen vacancy formation in Mn oxides.[173]

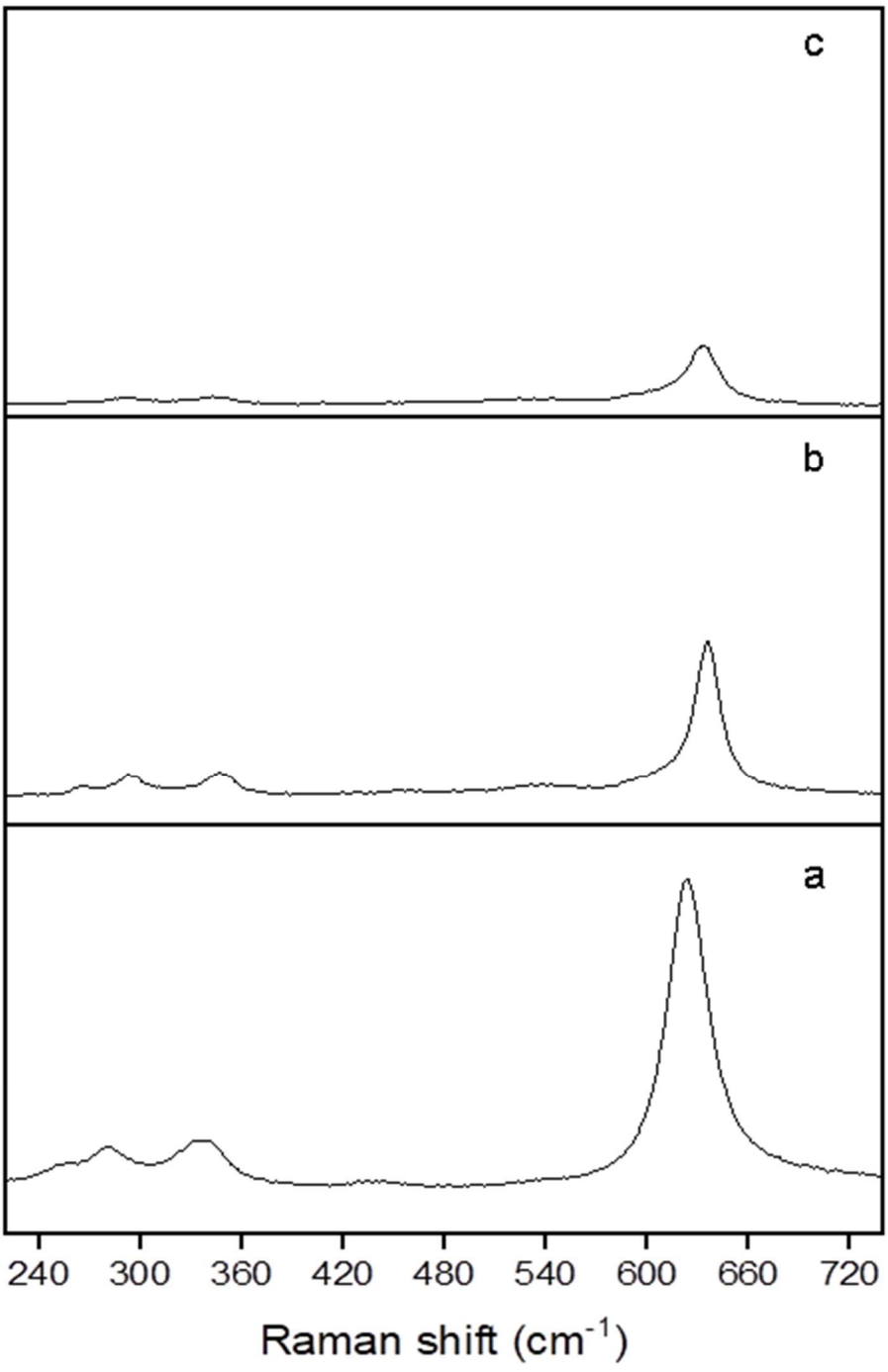


*Figure 4.22. Raman spectra of $Mn_2O_3$ with space group Pcab – pristine (a), QCR (b) and EOL (c)*

The Raman spectrum for $Mn_3O_4$ is shown in Fig. 4.23. Crystalline $Mn_3O_4$ has an extremely distinctive Raman spectrum, with a dominant Raman band observed at 637 $cm^{-1}$ in the pristine sample which is characteristic of the spinel structure. This intense peak is assigned with $A_{1g}$ symmetry and is caused due to the Mn-O stretching vibration of the tetrahedrally coordinated $Mn^{2+}$ ions found in the structure. In the pristine sample, the broad, low intensity peak at 455 $cm^{-1}$ is attributed to a $T_{2g}$ symmetry mode, caused by tetrahedral $Mn^{2+}$ motion within the structure (as observed in experiments conducted by L. Malavasi et al.).[175] The vibrations at 350 $cm^{-1}$ and 267 $cm^{-1}$ can also be attributed to the $T_{2g}$ symmetry mode, and the peak at 297 $cm^{-1}$ can be assigned the $E_g$ symmetry mode.[162,175–180] As seen for the $Mn_2O_3$ samples, there is peak shifting and intensity reduction of the most intense Raman band when compared with the pristine sample. The higher shift of these Raman bands further clarifies the existence of contaminant ions within the local structure of $Mn_3O_4$, and the reduced intensities of the Raman spectra for the leached materials correlate with oxygen vacancy formation in Mn the contaminated $Mn_3O_4$ samples.

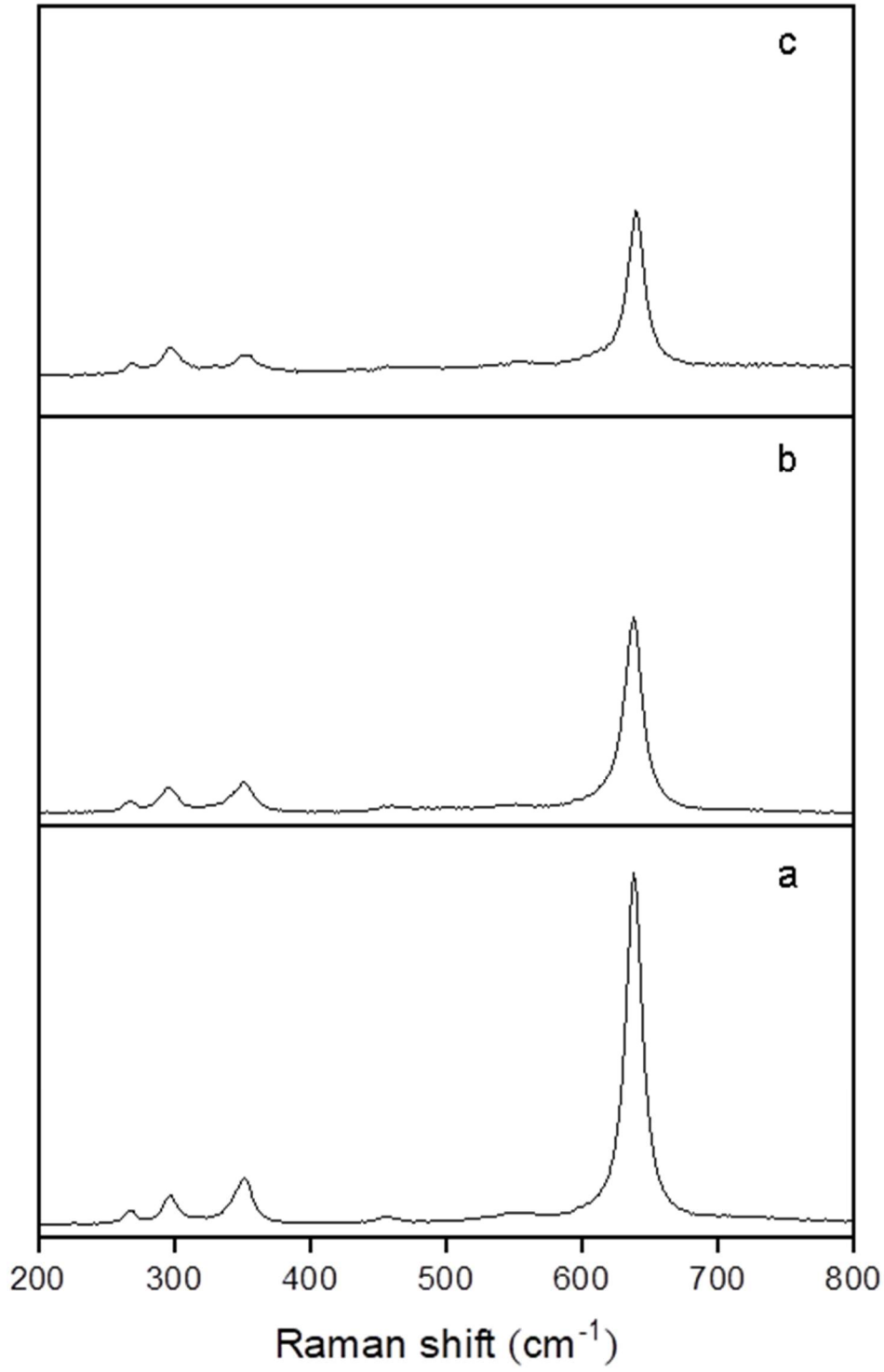


*Figure 4.23. Raman spectra of $Mn_3O_4$ with space group I41/amd – pristine (a), QCR (b) and EOL (c).*

### 4.4.3 SEM / EDX analysis

Scanning electron microscopy (SEM) was used to identify whether interconversion had occurred through morphological comparison between samples. EDX analysis was used to identify where contaminant ions were situated, to further determine whether previous hypotheses about their location within the structures were correct. SEM comparisons are shown in Figs. 4.24 – 4.29. Looking first at LMO, average particle size is much lower in the pristine sample than in the QCR and EOL samples, with most agglomeration arising in the EOL material. From this, it can be assumed that an alternative lower temperature method was used to synthesise the pristine LMO with finer particles, such as a sol-gel or precipitation method. Comparison of the Mn oxalates also shows interesting morphological differences between the pristine, QCR and EOL samples. The polyhedral-like structure of the Mn oxalate becomes less apparent in the QCR and EOL samples, with the QCR sample exhibiting a smaller particle size distribution, and the EOL sample exhibiting the smallest particle size distribution of all the samples. Based on a Mn oxalate transition metal (TM) doping study performed by Y. Duan et. al, it can be hypothesised that the TM contaminant ions present in the leached Mn oxalate structures have a considerable effect on the oxalate morphology. In the study, it was found that Ni-doping causes aggregation of rod-like particles, Co doping causes fusiform morphology with larger particle sizes, and Cu doping causes large particles with collaroid morphology.[95] As Ni, Co, and Cu contamination is seen amongst the QCR and EOL samples, these contrasting morphologies are expected with increased contamination. For the $Mn_2O_3$ samples, the 750 °C heat treatment of the Mn oxalate precursors has resulted in $Mn_2O_3$ products with similar morphological differences to the oxalates. The QCR

sample has the smallest particle size distribution, and both pristine and EOL samples have a similar degree of particle agglomeration. The pristine particles of $Mn_2O_3$ appear to be larger, with microcracks on the surface of the particles seen in all three cases. For the $Mn_3O_4$ samples, the 1000 °C heat treatment of the Mn oxalate has resulted in $Mn_3O_4$ particles with a smooth surface, and the agglomerated particles appear more spherical in structure when compared to LMO, Mn oxalate and $Mn_2O_3$. The greatest degree of particle agglomeration and average particle size appears to arise in the pristine $Mn_3O_4$; however, it can be seen in all cases.

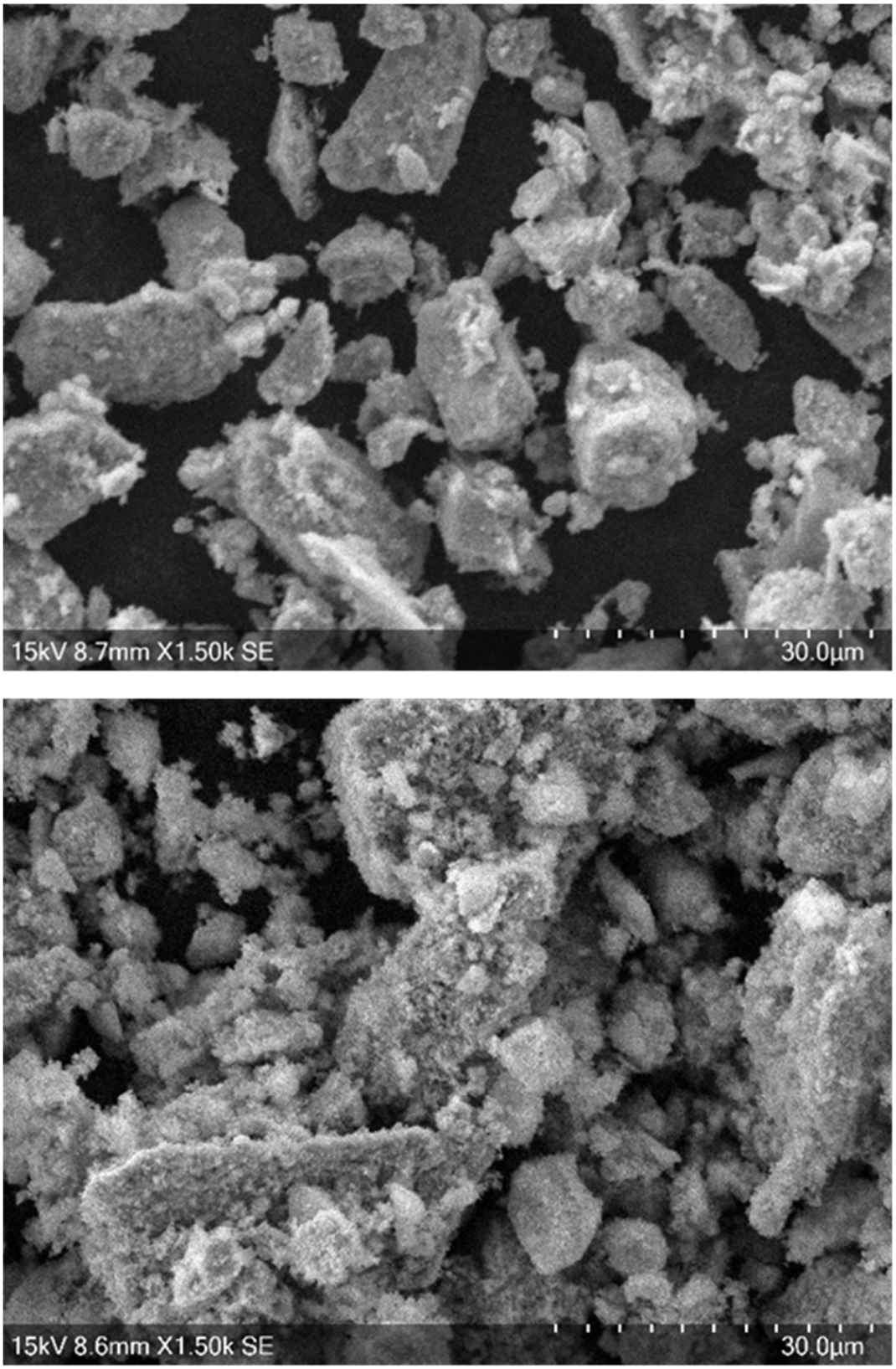


*Figure 4.24. SEM image showing pristine (top) and QCR $LiMn_2O_4$ (bottom).*

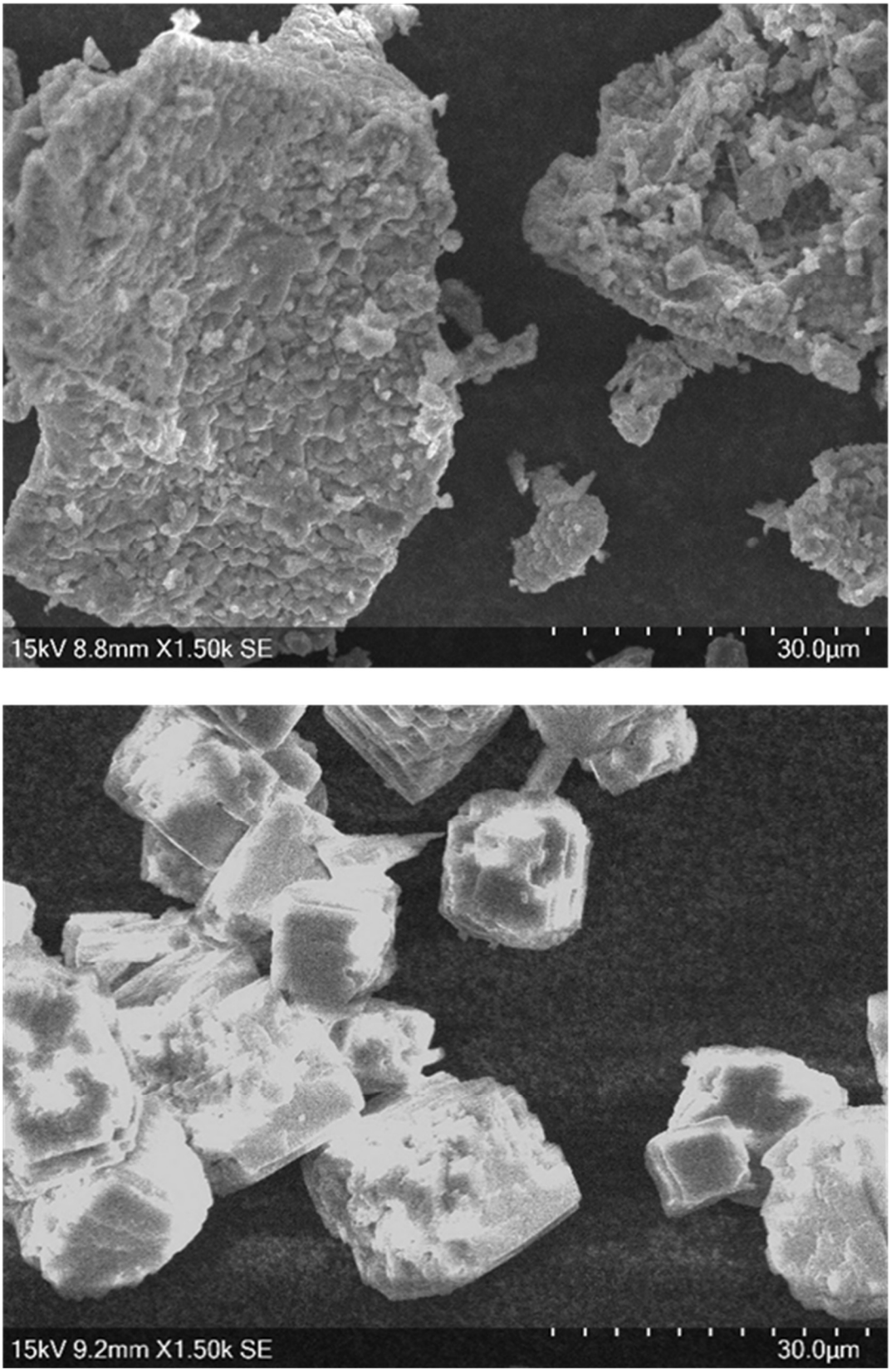


*Figure 4.25. SEM image showing EOL $LiMn_2O_4$ (top) and pristine Mn oxalate dihydrate (bottom).*

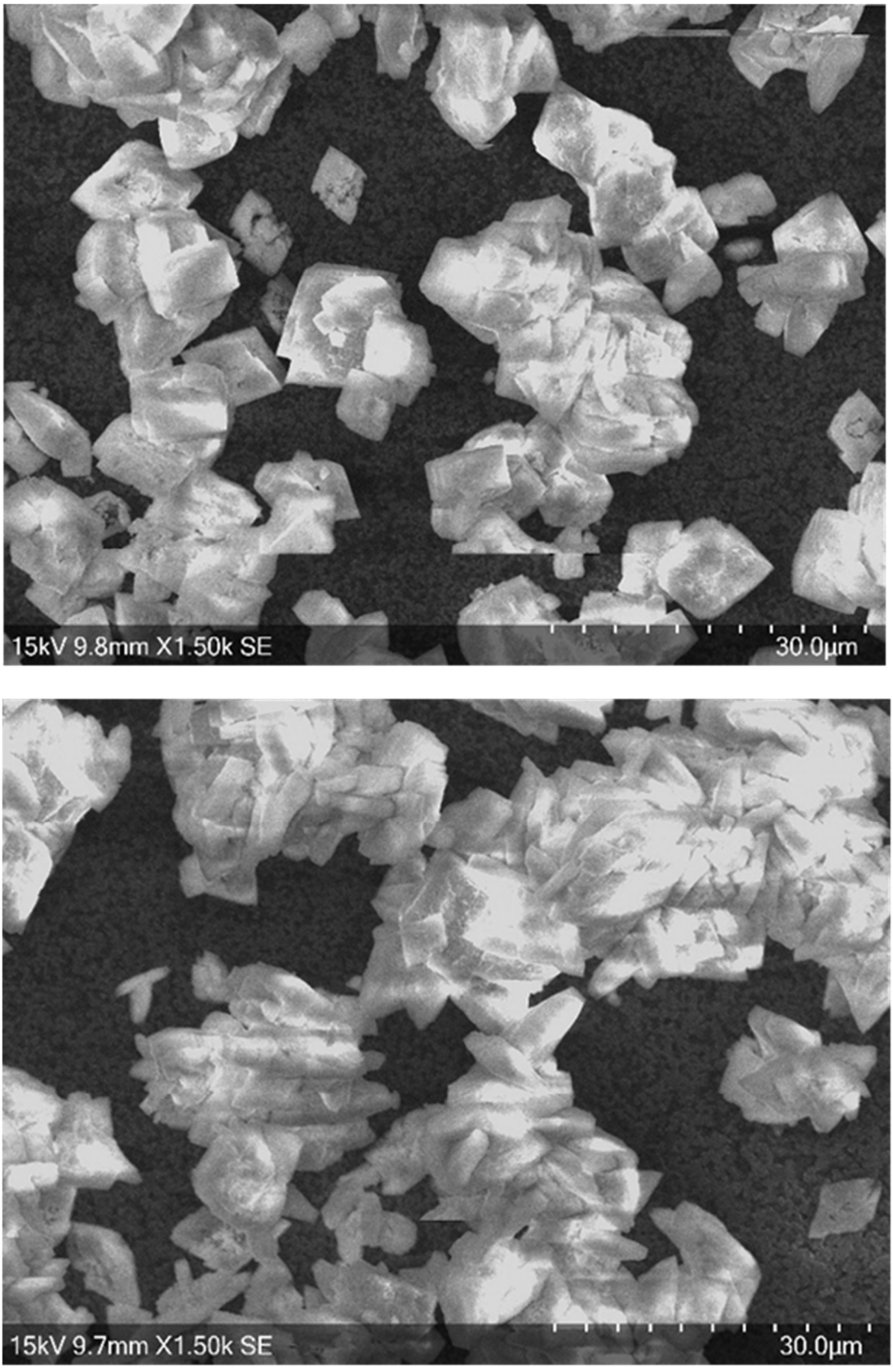


*Figure 4.26. SEM image showing QCR (top) and EOL Mn oxalate dihydrate (bottom).*

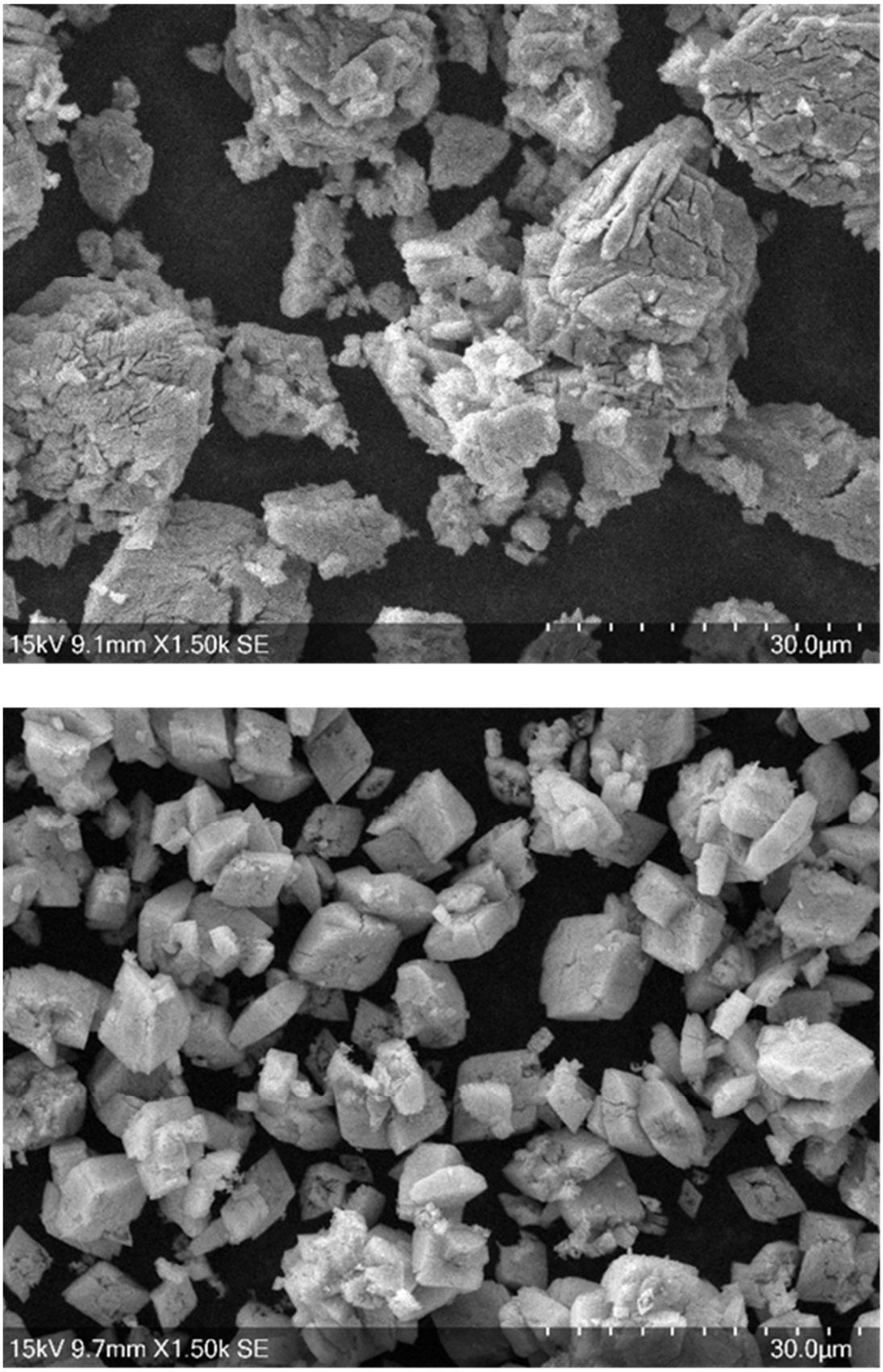


*Figure 4.27. SEM image showing pristine (top) and QCR $Mn_2O_3$ (bottom).*

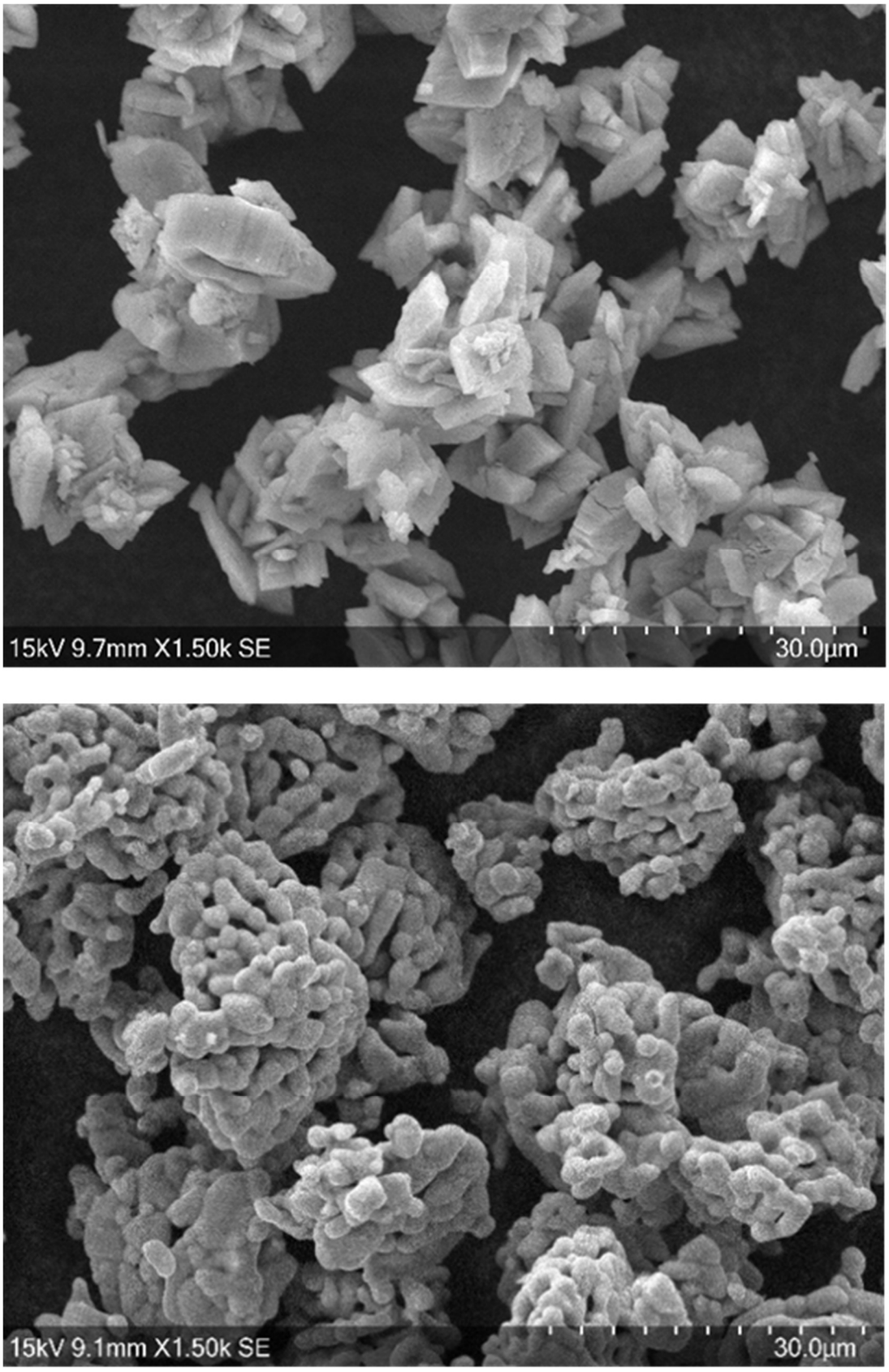


*Figure 4.28.SEM image showing EOL $Mn_2O_3$ (top) and pristine $Mn_3O_4$ (bottom).*

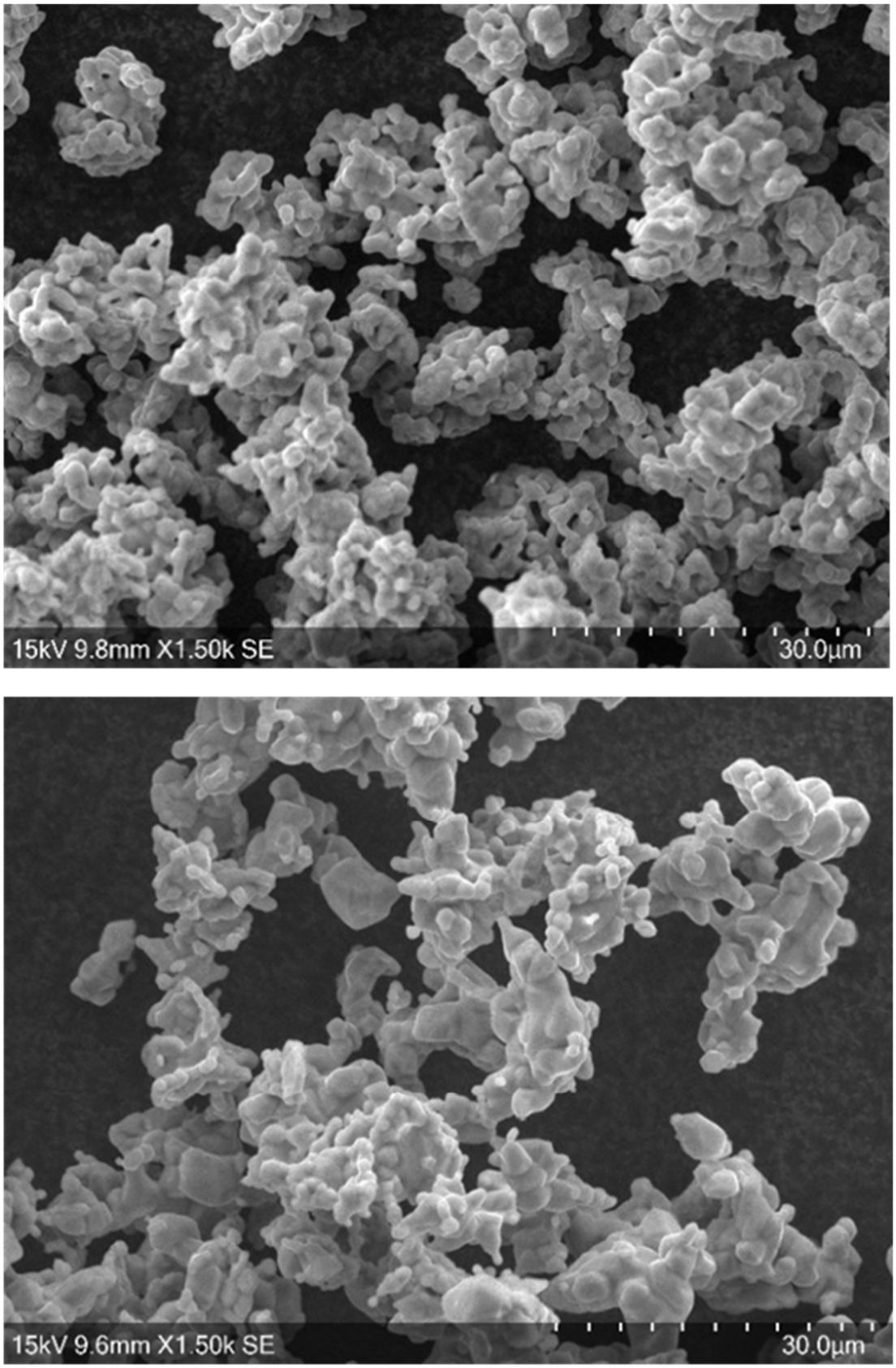


*Figure 4.29. SEM image showing QCR (top) and EOL $Mn_3O_4$ (bottom).*

EDX analysis was used to aid explanation of where the contaminant ions were located within the interconverted oxide structures. The EDX images are all shown in Appendices 10.1 – 10.3. As Li emits radiation, which is too low in energy to be detected, only Mn, O and contaminant ions were observed in the LMO samples. In the pristine materials, there are no contaminant ions detected (as established in the ICP-OES data). The manganese and oxygen (and carbon in the case of Mn oxalate) was distributed across all the samples in a uniform fashion in the pristine material. In the EDX images of QCR LMO, there were Ni and Al contaminant ions detected; however Co and Cu were not observed (even though they were seen in the ICP data). The amount of Co and Cu observed was much lower in the LMO sample than for Al and Ni (0.05% and 0.06% vs 1.18% and 0.39%, respectively), therefore it is reasonable that they were not detected. Once interconverted into the Mn oxalate sample, the Al was no longer observed in the QCR sample, just Ni (again, no Co or Cu due to their low quantities). The interconverted $Mn_2O_3$ and $Mn_3O_4$ QCR samples also showed Ni contamination. In all the QCR samples, the Ni was distributed with the Mn and O across the surface in a uniform fashion. This data does not disprove the hypothesis that the contaminant ions replace Mn at octahedral sites within the structure, hypothesised using ICP-OES, XRD and Raman analysis. In the EOL LMO samples, contamination from Ni, Co and Al was expected based on the ICP percentage mass data (0.64%, 1.31% and 0.59%, respectively). The EDX data for LMO clarified these contaminant ions were present, and upon formation of EOL Mn oxalate from this sample, Al was no longer detected, just Ni and Co, as seen in the ICP-OES data. The subsequent Mn oxides had Ni and Co distributed uniformly

across their surface again aligning with the hypothesis that these contaminants were incorporated into the sample structure at Mn sites.

## 4.5 Conclusions

Through selective extraction of $LiMn_2O_4$ from quality control-rejected and end-of-life battery Nissan Leaf cathodes, it has been demonstrated that this material can not only be extracted but it can also be interconverted into an array of new Mn-based products with the same crystal structure as their pristine counterpart.

The leached $LiMn_2O_4$ forms a cubic close-packed spinel structure with space group $Fd\bar{3}m$. For the interconverted materials, α'-Mn oxalate dihydrate formed with space group C12/c1, $Mn_2O_3$ with space group Pcab, and $Mn_3O_4$ with space group I41/amd. Through interconversion, most of the contaminant ions are incorporated into the subsequent Mn-based structures, aside from Al were observed in the subsequent materials, but did not cause any structural deviation from the pristine material.

In summary, these results have highlighted that LMO can be leached and interconverted into an array of Mn-based products with minimal contamination. Additionally, these experiments have highlighted that this minor contamination does not impact the formation of the crystalline material with the desired space group based on their comparison to the pristine case. These experiments lay emphasis on the value that can be extracted from redundant LMO material from quality-control rejected and end-of-life cathode material.

## 4.6 Future work

To gain further understanding into the site at which the contaminant ions dope into the interconverted materials is one avenue of research that would be interesting. This investigation can be done through quantification of the average oxidation state of the manganese ions within the pristine /QCR / EOL materials using X-ray absorption spectroscopy (XAS). XAS is a technique which utilises the occupation of the d-orbitals within the Mn atoms to determine the oxidation state that has been used within studies of Mn oxide oxidation state in the past, and therefore would be a valuable way to investigate this further.[71]

To ensure all constituent materials are utilised in this upcycling process, future work could involve the extraction of the Li from the filtrate, to close the loop within this process. The extraction of Li carbonate is vital, as this product can be utilised as a precursor material for new electrode manufacture when extracted as a battery grade material.[181] Furthermore, this would highlight its commercial viability of this process – by ensuring that not only the NCA phase left in-tact from the selective leaching of the LMO, then that the Mn-based material is upcycled, but also that the Li material is extracted too. Additionally, to ensure the circularity of this upcycling process by keeping the materials within battery-based applications, investigation into the electrochemical behaviour of Mn oxalate and Mn oxide samples will be of great interest as ensuring materials remain within the battery supply chain is something that could be of great value. Experiments investigating electrochemical behaviour of these materials are outlined in Chapters 5 and 6 – the electrochemical behaviour of Mn oxalate and MnO-C nanocomposites generated from pristine and leached material will be investigated as conversion anode materials.

## 4.7 References (continued)


132 P. S. Attidekou, Z. Milojevic, M. Muhammad, M. Ahmeid, S. Lambert and P. K. Das, *J. Electrochem. Soc.*, 2020, **167**, 160534.

133 D. Juarez-Robles, *J. Electrochem. Soc.*, 2021, **168**, 050535.

134 J. Marshall, D. Gastol, R. Sommerville, B. Middleton, V. Goodship and E. Kendrick, *Metals (Basel).*, 2020, **10**, 1–22.

135 Y. Han and H. Kim, *J. powe*, 2000, **88**, 161–168.

136 R. Gonçalves, P. Sharma, P. Ram, S. Ferdov, M. M. Silva, C. M. Costa, R. Singhal, R. K. Sharma and S. Lanceros-Méndez, *J. Alloys Compd.*, 2021, **853**, 1–8.

137 S. H. Oh, K. Y. Chung, S. H. Jeon, C. S. Kim, W. Il Cho and B. W. Cho, *J. Alloys Compd.*, 2009, **469**, 244–250.

138 D. Song, H. Ikuta, T. Uchida and M. Wakihara, *Solid State Ionics*, 1999, **117**, 151–156.

139 A. M. Hashem, A. E. Abdel-Ghany, H. M. Abuzeid, R. S. El-Tawil, S. Indris, H. Ehrenberg, A. Mauger and C. M. Julien, *J. Alloys Compd.*, 2018, **737**, 758–766.

140 L. Chladil, D. Kunický, T. Kazda, P. Vanýsek, O. Čech and P. Bača, *J. Energy Storage*, 2021, **41**, 102907.

141 J. Liu, G. Li, Y. Yu, H. Bai, M. Shao, J. Guo, C. Su, X. Liu and W. Bai, *J. Alloys Compd.*, 2017, **728**, 1315–1328.

142 H. Zhao, D. Li, Y. Wang, F. Li, G. Wang, T. Wu, Z. Wang, Y. Li and J. Su, *Materials (Basel).*, 2018, **11**, 9–14.

143 T. Liu, A. Dai, J. Lu, Y. Yuan, Y. Xiao, L. Yu, M. Li, J. Gim, L. Ma, J. Liu, C. Zhan, L. Li, J. Zheng, Y. Ren, T. Wu, R. Shahbazian-Yassar, J. Wen, F. Pan and K. Amine, *Nat. Commun.*, 2019, **10**, 1–11.

144 J. Wandt, A. Freiberg, R. Thomas, Y. Gorlin, A. Siebel, R. Jung, H. A. Gasteiger and M. Tromp, *J. Mater. Chem. A*, 2016, **4**, 18300–18305.

145 C. Zhan, J. Lu, A. J. Kropf, T. Wu, A. N. Jansen, Y. Sun, X. Qiu and K. Amine, 2013, 1–8.

146 R. S. Liu and C. H. Shen, *Solid State Ionics*, 2003, **157**, 95–100.

147 H. Bai, W. Xu, J. Guo, C. wei Su, M. Xiang, X. Liu and R. Wang, *J. Mater. Sci. Mater. Electron.*, 2018, **29**, 14668–14678.

148 S. Wang, H. Liu, M. Xiang, J. Guo, W. Bai, H. Bai, X. Liu and C. Su, *New J. Chem.*, 2020, **44**, 10569–10577.

149 W. Xu, Y. Zheng, Y. Cheng, R. Qi, H. Peng, H. Lin and R. Huang, *ACS Appl. Mater. Interfaces*, 2021, **13**, 45446–45454.

150 di-Lithium oxalate, https://www.sigmaaldrich.com/GB/en/product/mm/822085, (accessed 21 January 2022).

151 J. R. Rumble, Ed., *CRC Handbook of Chemistry and Physics*, CRC Press/ Taylor & Francis, Boca Raton, 102nd edn., 2021.

152 S. G. Zhu, W. Z. He, G. M. Li, X. Zhou, X. J. Zhang and J. W. Huang, *Trans.*

*Nonferrous Met. Soc. China (English Ed.*, 2012, **22**, 2274–2281.

153 R. Zheng, L. Zhao, W. Wang, Y. Liu, Q. Ma, D. Mu, R. Li and C. Dai, *RSC Adv.*, 2016, **6**, 43613–43625.

154 J. Chen, H. Zhang, Z. Zeng, Y. Gao, C. Liu and X. Sun, *Hydrometallurgy*, 2021, **206**, 105768.

155 B. Han, A. Porvali, M. Lundström and M. Louhi-Kultanen, *Chem. Eng. Technol.*, 2018, **41**, 1205–1210.

156 X. Chen, C. Chen, T. Xu, Y. Xu, W. Liu, W. Yang and P. Yang, *RSC Adv.*, 2018, **8**, 35878–35887.

157 G. Raja, A. Nallathambi, A. Prakasam, S. Gopinath, C. Ragupathi, S. Narayanan, P. Tamizhdurai, R. Kumaran, N. S. Alsaiari, K. M. Abualnaja and M. Ouladsmane, *J. Saudi Chem. Soc.*, 2022, **26**, 101440.

158 S. Zhang, H. Li, Z. Wu, J. E. Post, B. Lanson, E. J. Elzinga, Y. Liu, H. Li, M. Hong, F. Liu and H. Yin, *Chem. Geol.*, 2021, **582**, 120448.

159 S. Hirai, S. Yagi, A. Seno, M. Fujioka, T. Ohno and T. Matsuda, *RSC Adv.*, 2016, **6**, 2019–2023.

160 R. Heintz, D. Ph and T. F. Scientific, Raman Analysis of Lithium-Ion Battery Components – Part I : Cathodes, https://assets.thermofisher.com/TFS-Assets/MSD/Application-Notes/AN52443-raman-analysis-lithium-ion-battery-components-cathodes.pdf, (accessed 15 August 2023).

161 Y. Wei, K. B. Kim and G. Chen, *Electrochim. Acta*, 2006, **51**, 3365–3373.

162 C. M. Julien and M. Massot, *J. Phys. Condens. Matter*, 2003, **15**, 3151–3162.

163 G. B. Zhong, Y. Y. Wang, Y. Q. Yu and C. H. Chen, *J. Power Sources*, 2012, **205**, 385–393.

164 S. W. Oh, S. T. Myung, H. B. Kang and Y. K. Sun, *J. Power Sources*, 2009, **189**, 752–756.

165 R. Alcántara, M. Jaraba, P. Lavela and J. L. Tirado, *J. Electrochem. Soc.*, 2004, **151**, A53.

166 Z. Cai, Y. Ma, X. Huang, X. Yan, Z. Yu, S. Zhang, G. Song, Y. Xu, C. Wen and W. Yang, *J. Energy Storage*, 2020, **27**, 101036.

167 S. Hug, B. Grohe, J. Jalkanen, B. Chan, B. Galarreta, K. Vincent, F. Lagugné-Labarthet, G. Lajoie, H. A. Goldberg, M. Karttunen and G. K. Hunter, *Soft Matter*, 2012, **8**, 1226–1233.

168 C. Frausto-Reyes, S. Loza-Cornejo, T. Terrazas, M. De La Luz Miranda-Beltrán, X. Aparicio-Fernández, B. M. López-Mací, S. E. Morales-Martínez and M. Ortiz-Morales, *Appl. Spectrosc.*, 2014, **68**, 1260–1265.

169 H. L. Barazorda-Ccahuana, M. Nedyalkova, I. Kichev, S. Madurga, B. Donkova and V. Simeonov, *ACS Omega*, 2020, **5**, 9071–9077.

170 R. I. Bickley, H. G. M. Edwards and S. J. Rose, *J. Mol. Struct.*, 1991, **243**, 341–350.

171 H. G. M. Edwards and P. H. Hardman, *J. Mol. Struct.*, 1992, **273**, 73–84.

172 H. Rahaman, R. M. Laha, D. K. Maiti and S. K. Ghosh, *RSC Adv.*, 2015, **5**,

33923–33929.

173 X. Niu, H. Wei, K. Tang, W. Liu, G. Zhao and Y. Yang, *RSC Adv.*, 2015, **5**, 66271–66277.

174 A. Ginsburg, D. A. Keller, H. N. Barad, K. Rietwyk, Y. Bouhadana, A. Anderson and A. Zaban, *Thin Solid Films*, 2016, **615**, 261–264.

175 L. Malavasi, P. Galinetto, M. C. Mozzati, C. B. Azzoni and G. Flor, *Phys. Chem. Chem. Phys.*, 2002, **4**, 3876–3880.

176 Z. Y. Tian, P. Mountapmbeme Kouotou, N. Bahlawane and P. H. Tchoua Ngamou, *J. Phys. Chem. C*, 2013, **117**, 6218–6224.

177 M.-C. Bernard, *J. Electrochem. Soc.*, 1993, **140**, 3065.

178 Y. Liu, Z. Liu and G. Wang, *Appl. Phys. A Mater. Sci. Process.*, 2003, **76**, 1117–1120.

179 M. Kim, X. M. Chen, Y. I. Joe, E. Fradkin, P. Abbamonte and S. L. Cooper, *Phys. Rev. Lett.*, 2010, **104**, 1–4.

180 F. Buciuman, F. Patcas, R. Craciun and D. R. T. Zahn, *Phys. Chem. Chem. Phys.*, 1999, **1**, 185–190.

181 W. Gao, X. Zhang, X. Zheng, X. Lin, H. Cao, Y. Zhang and Z. Sun, *Environ. Sci. Technol.*, 2017, **51**, 1662–1669.

# 5 Extracting value from upcycled Mn-based material: synthesis and electrochemistry of nanosized MnO—C composites

## 5.1 Table of Figures

## 5.2 Chapter introduction

As stated in the introduction, manganese (II) oxide, or MnO, is a material which can be used as a high-capacity conversion anode for Li-ion batteries, and the focus in this chapter is the synthesis of a nanosized MnO—C composite ($_{nano}$MnO—C) by reacting interconverted Mn oxalate (produced from both pristine LMO and from LMO leached from quality-control rejected and end of life cathode sheets, as demonstrated in Chapter 4) with a carbon-rich linker. As highlighted in section 1.5.6, synthesis of nanoMnO—C composites from MOF precursors involves complex solvothermal routes and little investigation has been done into mechanochemical synthesis of these material. The first aim of this Chapter is therefore to determine a synthetic route that will streamline this manufacturing process, further enhancing the upcycling opportunity for the leached material. The second aim of this chapter is to signify the effectiveness of manufacturing these nanocomposites from leached cathode material by comparing the electrochemical performance of these materials to that of the pristine nanocomposite equivalent.

## 5.3 Methods

In these experiments, several $_{nano}$MnO-C composites have been synthesised and compared. There are comparisons between particle sizes of pristine $_{nano}$MnO-C composites (with precursors derived from Alfa Aeser $LiMn_2O_4$, as defined in Chapter 3) through different heating temperatures, followed by comparisons between $_{nano}$MnO-C composite materials derived from pristine, quality control-rejected (QCR) and end-of-life (EOL) lithium manganese oxide spinel ($LiMn_2O_4$, LMO). As stated in

previously, L. L.Driscoll et al.'s reductive acidic leaching method has been used to extract $LiMn_2O_4$ from QCR and EOL Nissan Leaf composite electrodes (detailed description of this process is outlined in section 4.3.2 – 4.3.3), which has been added to oxalic acid to form Mn oxalate dihydrate. After a series of optimisation steps the $_{nano}$MnO-C composite was successfully synthesised by grinding Mn oxalate dihydrate powder with terephthalic acid in a 1:1 molar ratio for 12 hours at 800 rpm, with 5-minute rest periods programmed every 10 minutes. Once ball milled, this material was transferred to an alumina crucible and heated to a given temperature under nitrogen at a ramp rate of 5 °C/ min and held at this temperature for 4 hours. For the particle size analysis, the pristine Mn oxalate/ terephthalic acid mixture is heated to 400 °C, 600 °C, 800 °C and 1000 °C with a 4 hr hold time (all ramp rates used are 5 °C/ min). The pristine, QCR and EOL samples are compared based on the 600 °C heat treatment with a 4 hour hold time. A flow chart to illustrate the interconversion process is outlined in Fig. 5.1.

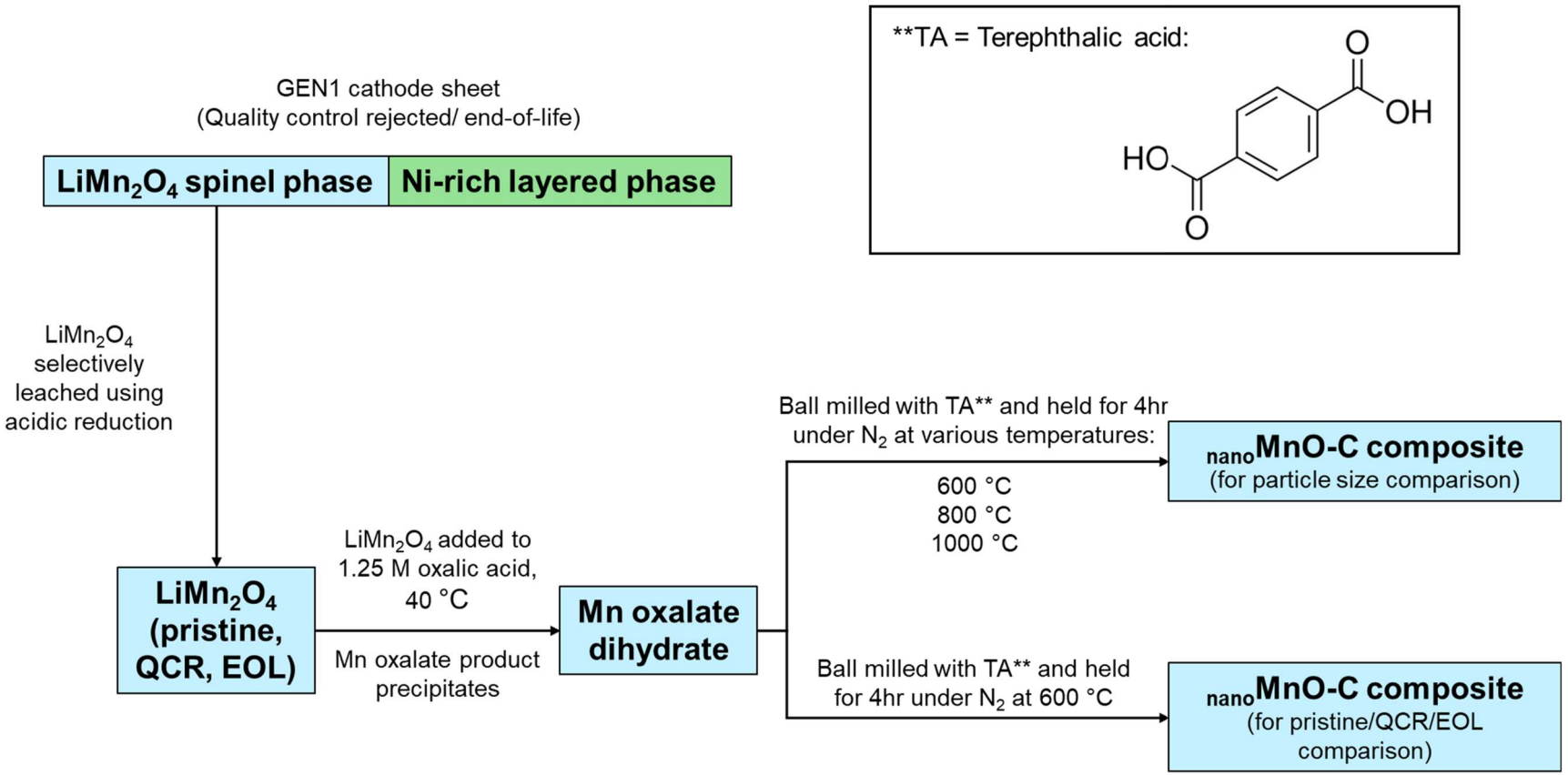


*Figure 5.1. Summary for $_{nano}$MnO–C composite syntheses outlined in this Chapter with the terephthalic acid linker shown*

## 5.4 Results – $_{nano}$MnO–C synthesis

In this section synthetic conditions of the $_{nano}$MnO–C composites are optimised, and structural differences compared using Mn oxalate dihydrate from pristine, QCR and EOL $LiMn_2O_4$ sources (synthesised using the method outlined in Fig. 5.1). As tackling waste from QCR and EOL batteries is an issue that has only become apparent in recent years, Mn oxalate synthesised from leaching of $LiMn_2O_4$ from battery waste has not yet been explored as a precursor for the synthesis of $_{nano}$MnO–C composites. This novel synthetic route therefore requires investigation using pristine material to verify its success, outlined in sections 5.4.1 – 5.4.2. Synthesis of these nanocomposites has been done with the aim of upcycling redundant battery material into $_{nano}$MnO-C composites that can be used as conversion anodes in battery applications. As hypothesised in section 1.5.4, beginning with a smaller particle size means that less pulverization of the nanocomposite in an electrochemical environment is expected. This therefore means that, in section 5.4.3, particle size optimisation experiments were outlined to ensure resultant nanocomposites were fit for anode utilisation. Following on from these optimisation experiments, these $_{nano}$MnO-C composites are then synthesised from Mn oxalates from leached battery material and compared, outlined in section 5.4.4, ready for electrochemical testing in section 5.5

### 5.4.1 Determining reaction conditions to synthesise the $_{nano}$MnO–C composite

To obtain to a $_{nano}$MnO─C composite using this novel synthetic route, multiple reaction conditions have been explored using commercial Mn oxalate dihydrate powder (Mn oxalate derived from Alfa Aeser $LiMn_2O_4$), termed “pristine” in the following sections. Synthetic investigations outlined in in sections 4.2.2 guided for the conditions explored in this section.

Firstly, to determine whether any additional precursors materials were required to form a MnO product, the Mn oxalate dihydrate was heated in an inert nitrogen atmosphere up to 600 °C at a rate of 5 °C/ min and held at this temperature for 4 hours. The selected annealing conditions are based on an array of heating conditions and temperature hold times that have been explored for $_{nano}$MnO─C composite synthesis in the literature, which span times between 600 – 800 °C and 2 – 4 hours.[86,87,182] The resulting powder was analysed using x-ray diffraction, and it was observed that the despite performing the reaction under nitrogen, the Mn oxalate decomposed, and the Mn predominantly oxidised to form the $Mn_3O_4$ phase, with a minor phase of MnO. The predominant $Mn_3O_4$ phase formed with space group $I4_1/amd$ and MnO with space group $Fm\bar{3}m$, marked in the refined phase in Fig. 5.2. The percentage composition of each of the phases, calculated using Rietveld refinement, were calculated at 97.9% $Mn_3O_4$ and 2.1% MnO.

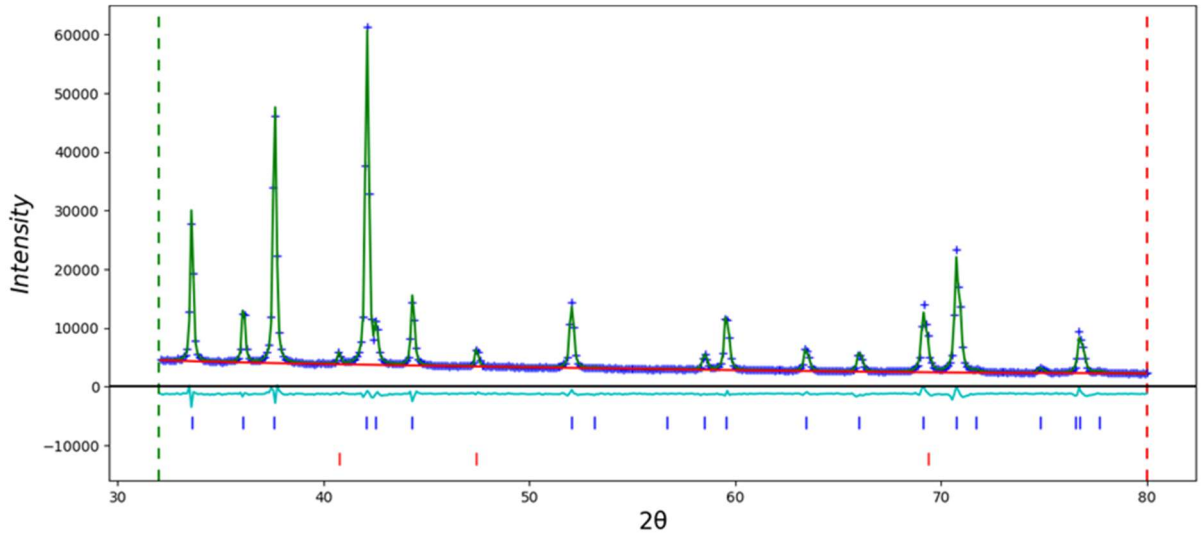


*Figure 5.2. Rietveld refinement showing composition of product obtained from heating of Mn oxalate dihydrate under $N_2$ to 600 °C at a rate of 5 °C/ min and held at this temperature for 4 hours. Peak matching shows a mixture of $Mn_3O_4$ with reflections for space group I41/amd marked in blue and MnO with space group $Fm\bar{3}m$ marked in red.*

The next avenue of research for the synthesis of this nanoMnO–C composite was to form and decompose a Mn-based metal organic framework (MOF), something that has been explored extensively in the literature, due to their simple synthesis with great homogeneity in the resultant carbon framework.[79–81] In a study conducted by R. Das et al., it was demonstrated that transition metal oxide (TMO) nanoparticles are synthesisable by heat treatment of transition method MOFs, with effective TMO dispersion within the carbon matrix – this is a desirable characteristic for an electrode as it ensures homogeneity across the electrode which ensures electrode stability during cycling.[183] As outlined in section 1.5.6, MOFs can synthesised using complex solvothermal methods, however, for this investigation, a mechanochemical method was used. This was due to the fact that these methods are considered to be

environmentally friendly, effective and scalable, which is desirable in the context of these upcycling experiments.[184] Additionally, the resultant MOF was to be used as a sacrificial precursor material for decomposition into a $_{nano}$MnO–C composite, therefore a straightforward the synthetic route was chosen to streamline the synthesis. To generate a Mn-MOF that could be decomposed into the desired -$_{nano}$MnO–C composite two precursors were nominated: Mn oxalate, as the transition metal source, and a terephthalic acid organic linker (the structure of this is shown in Fig. 5.1). Methods akin to this to produce MOFs have been explored in the literature, using terephthalic acid and transition metals precursors to generate the relevant transition metal organic frameworks though mechanochemistry, as explored by B. Karadeniz et al. in a mechanochemical Zr-MOF study: they used a Zr-acetate precursor synthesised using Zr propoxide and acetic acid, not too dissimilar from the synthesis of the Mn oxalate precursor utilised in this Chapter, combined with a series of terephthalic acid / other acid based linkers and water to generate the desired Zr-MOF.[185] Another example of such synthesis involves a solvent-free mechanochemical study by W.L.Teo et al., whereby chromium nitrate nonahydrate and terephthalic acid were mixed together through ball milling. After mixing they were heat treated in an autoclave in order to synthesise the desired Cr-MOF product.[186] The use of a substantial organic linker ensured there will be enough carbon present so that after oxidation there would still be enough carbon to form the carbon composite product. Multiple simple mechanical routes were explored to generate the MOF-like precursor prior to decomposition. In all cases, the Mn oxalate dihydrate precursor was ground with terephthalic acid in a 1:1 molar ratio. The XRD patterns comparing the products of these mechanochemical conditions are shown in Fig 5.3.

Figs. 5.3.a and b show the individual XRD patterns for the two precursor materials to act as a comparison to the ground/ ball milled products. The least ‘aggressive’ technique was to grind by hand for 20 minutes using a pestle and mortar, shown in Fig. 5.3.c. This method caused no mechanochemical reaction as exhibited by the XRD pattern whereby there is a mixture of the two precursor materials. To increase the prospect of reaction a planetary ball mill was used, and two different milling times were explored. The 1:1 oxalate: organic linker molar ratio was maintained, and one experiment involved milling at 800 rpm for 2 hours, and the other involved milling at 800 rpm for 12 hours. The 2-hour milling time was not sufficient to cause a mechanochemical reaction, as shown in Fig. 5.3.d, whereas the longer milling time, shown in Fig. 5.3.e, appeared to show some differences to the precursor Bragg peaks. In the Fig 5.3.e, the Mn oxalate phase is still present, but the peaks had broadened, and the diffraction peaks corresponding to the terephthalic acid linker had clearly decreased in intensity and broadened, indicating that the terephthalic acid had significantly begun to react in the mechanical process as the crystallite size decreased. Terephthalic has been reported to react effectively using mechanochemical methods, as outlined in the Cr-MOF study by W.L.Teo et al. What is key to note from their study is that the ball milling was the preliminary step in the reaction, and there was a 300 °C heat treatment step required to generate the desired MOF product.[186] Seeing as the experiments in this Chapter only focussed on generating a sacrificial MOF material that could then be heat treated to form the $_{nano}$MnO-C composite, a series of heat treatment analyses were undertaken on the material depicted in Fig. 5.3.e. This product was heated to temperatures exceeding 300 °C , to determine whether this initial ball milling reaction was sufficient to cause a

preliminary reaction between the precursors that could subsequently be heated to generate a $_{nano}$MnO-C composite product.

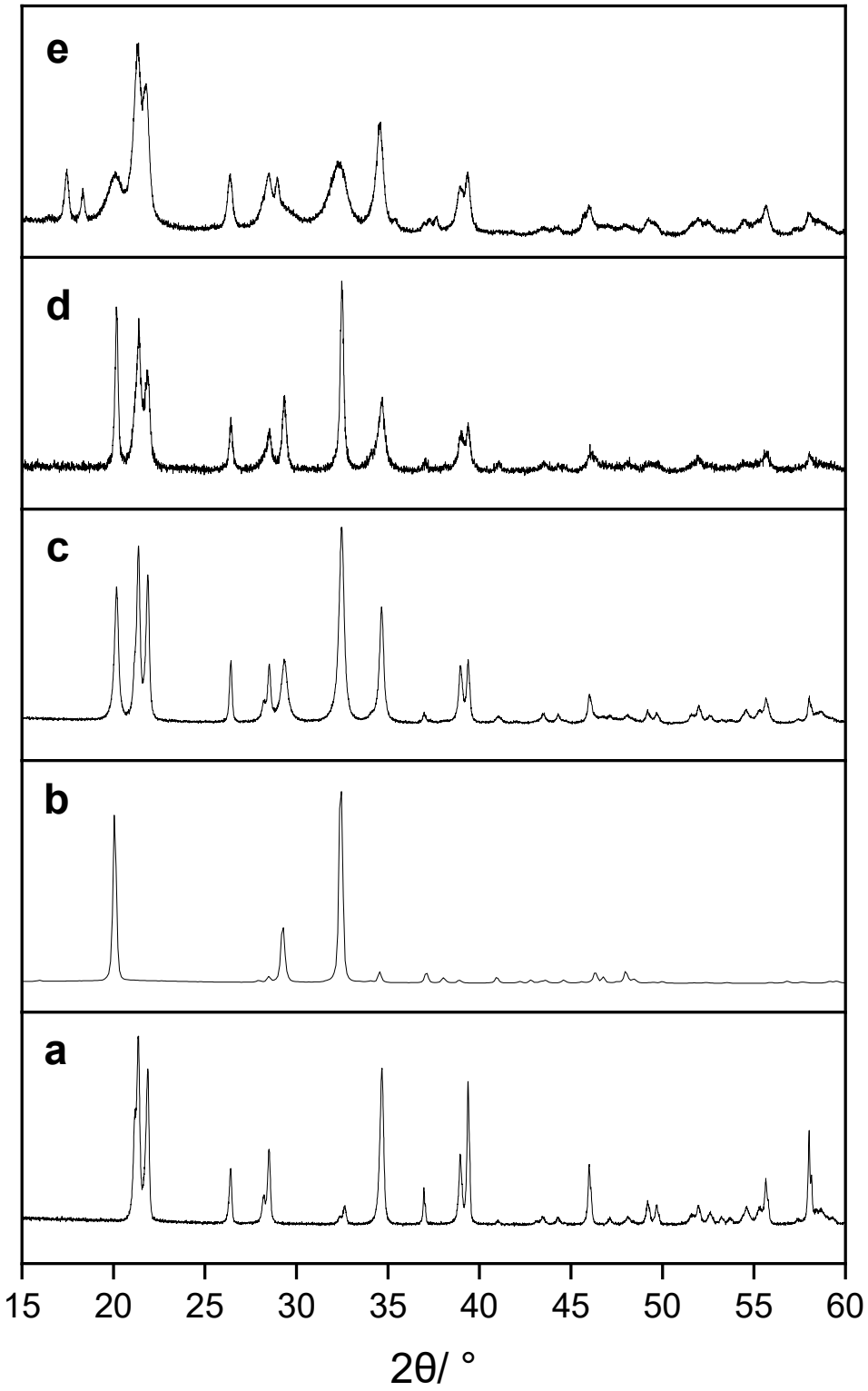


*Figure 5.3. XRD patterns of the precursors: Mn oxalate dihydrate (a) and terephthalic acid organic linker (b) and the products after mechanical treatment: hand ground product (c) and: 2-hr planetary ball milled product (d), 12-hour planetary ball milled product (e).*

To synthesise the $_{nano}$MnO—C composite, the 12-hour ball milled sample was heated to 600 °C in an inert $N_2$ atmosphere and held for 4 hours at this temperature, to act as a direct comparison to the heating of Mn oxalate alone (shown in Fig. 5.2). The XRD pattern for this attempted synthesis is shown in Fig. 5.4 with peak indexing. Using pattern matching, the XRD pattern correlates to a face centred cubic MnO structure with space group $Fm\bar{3}m$. Based on this and Rietveld refinement, shown in Fig. 5.5, it was clear that crystalline MnO had formed. The large broad peak at approximately 20 ° 2θ in Fig. 5.4 be assigned to that of amorphous carbon seen within the structure, as has been identified by J. Hou et al. in a previous MnO—C composite study.[182] This indicates that the $_{nano}$MnO—C composite had formed

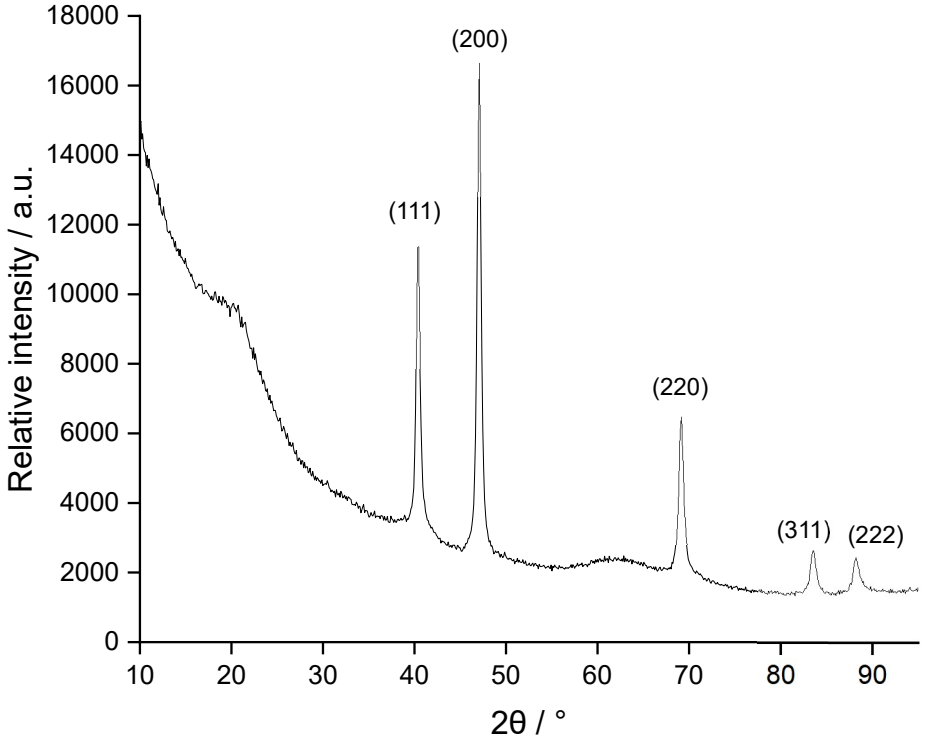


*Figure 5.4. XRD pattern showing the $_{nano}$MnO-C composite product from heating 12 hr ball milled Mnox : TA 1:1 mixture to 600 °C at a rate of 5 °C/ min with a 4-hour hold. The space group of the MnO phase is $Fm\bar{3}m$.*

successfully. Further experiments to verify these findings are outlined in section 5.4.2.

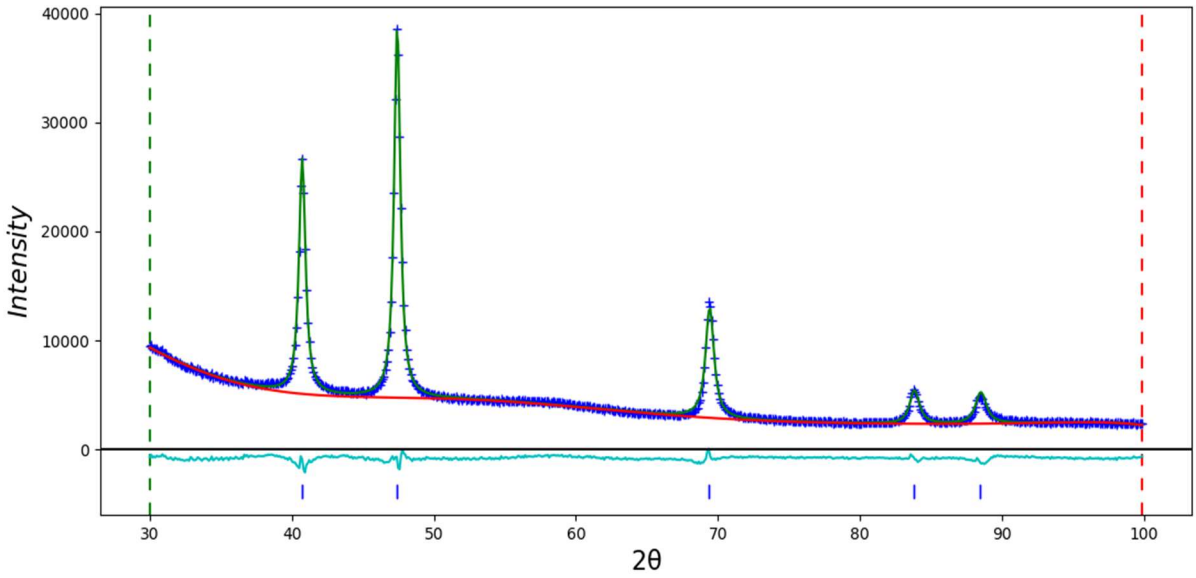


*Figure 5.5. Rietveld refinement showing composition of product obtained after Mn oxalate dihydrate/ terepthalic acid mechanochemical product was heated under $N_2$ to 600 °C at a rate of 5 °C/ min and held at this temperature for 4 hours. Peak matching shows MnO with with* reflections for *space group $Fm\bar{3}m$ marked in blue.*

## 5.4.2 Experimental confirmation for the synthesis of the $_{nano}$MnO–C composite

Though XRD analysis gave initial clarification that the $_{nano}$MnO–C composite had been synthesised, further characterisation techniques were used to verify that these had formed before tailoring the synthesis and applying it to the leached QCR and EOL Mn oxalate material. For further verification Raman, SEM-EDX, and TEM were used.

X-ray diffraction did not give clear diffraction peaks for the carbonaceous portion of this material, due to the lack in long range order, therefore Raman spectroscopy was used for further clarification. The Raman spectrum for this material is shown in Fig. 5.6. Focussing firstly between 300 and 700 $cm^{-1}$ there are 3 observable peaks that correspond to the Mn-oxide phase, at around 314, 364 and 653 $cm^{-1}$. These vibrational modes may correspond to a $Mn_3O_4$ impurity phase within the $_{nano}$MnO—C composite, as a previous study on nanosized manganese oxides by N. Mironova-Ulmane et al. reports similar vibrational results from synthesised MnO samples. What is certain is that the Mn-O vibrational mode is the reason for the sharp peak at 653 $cm^{-1}$.[187] This $Mn_3O_4$ impurity phase must be nanosized, as there is no evidence for it in the XRD pattern of this $_{nano}$MnO-C composite. Focussing on the carbonaceous

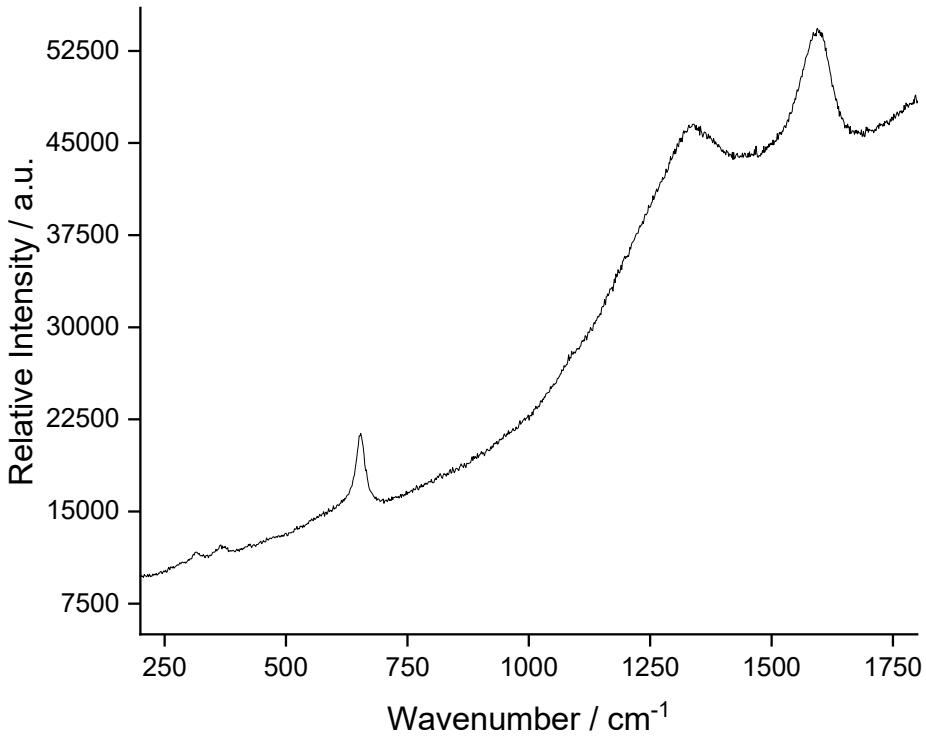


*Figure 5.6. Raman spectrum of the $_{nano}$MnO—C composite product from heating 12hr ball milled Mnox : TA 1:1 mixture to 600 °C at a rate of 5 °C/ min with a 4-hour hold.*

region of the spectrum there are two large peaks at 1337cm$^{-1}$ and 1594 cm$^{-1}$, that are associated with carbon in the structure. The peak at 1337 cm$^{-1}$ is assigned to the disordering of the carbon and the peak at 1594 cm$^{-1}$ corresponds to the ordered graphitic carbon. These peaks have also been identified in a MnO–C nanocomposite study by J. Zhu et al.[80] The D and G bands correspond to $sp^2$ and $sp^3$ hybridised carbon stretching modes, and the intensity ratio ($I_D/I_G$) has been used to evaluate the degree of disorder of the material by experimentalists in the past. The $I_D/I_G$ ratio is described further in section 5.5.[188] To determine the crystallite domain size of the MnO particles, the Scherrer equation was used, outlined in equation 8:

$$\tau = \frac{K\lambda}{\beta_\tau cos\theta} \qquad [8]$$

Where τ corresponds to the mean size of the crystalline material domains, K is the shape factor (which is usually set to 0.94), λ is the wavelength, $B_\tau$ is the full width at half maximum (FWHM), and θ corresponds to the Bragg angle.[189] In these calculations, the full width at half maximum can be defined as the width of the gaussian Bragg peak at half of the maximum peak height in the XRD pattern. The most intense peak at ~47.4 ° 2θ – the (200) peak – was selected for mean crystallite calculation, since it is the most defined peak meaning the FWHM error was expected to be minimised the most effectively. This calculation is shown in Table 5.1.

*Table 5.1. The mean crystallite size calculation for the $_{nano}$MnO—C composite heated to 600 °C at a rate of 5 °C/ min with a 4-hour hold*

| **Temperature held for 4 hours (°C),** | **Full width at half maximum (2θ)** | **(200) peak (°)** | **Mean crystallite domain size (nm)** |
|---|---|---|---|
| **600** | 0.56508 | 47.43 | 19.53 |

Based on this calculation, it can be clarified that nanosized MnO particles were synthesised using this method. To determine the elemental distribution of the $_{nano}$MnO-C composite and to see the morphology, SEM-EDX analysis was used. Fig. 5.7 and Appendix 10.4 show the SEM image and the EDX analysis of the material,

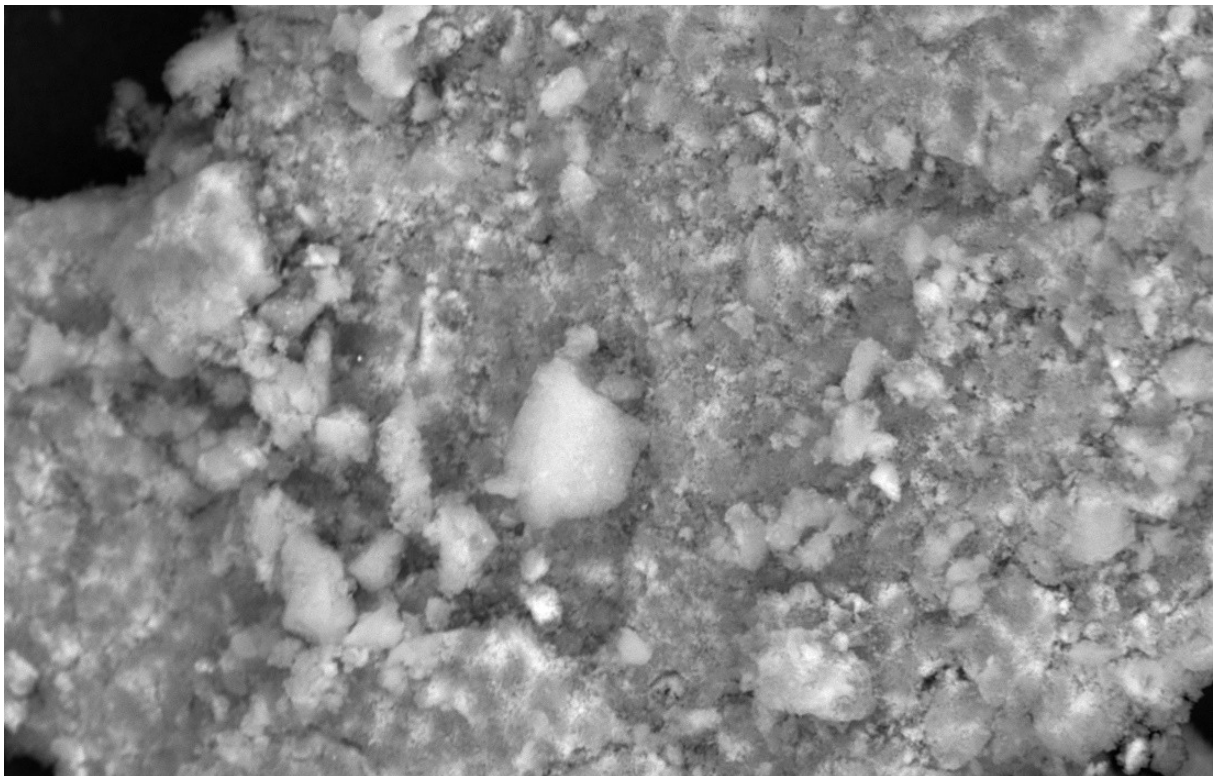

*Figure 5.7. SEM image of the $_{nano}$MnO-C composite product from heating 12hr ball milled Mnox : TA 1:1 mixture to 600 °C at a rate of 5 °C/ min with a 4-hour hold*

respectively. In the SEM image there appears to be partial particle aggregation with an array of discrete particle sizes observed. From the EDX analysis, there is a clear uniform distribution of manganese, oxygen, and carbon, as shown by the surface of the material showing their uniform dispersal across the image surface.

To obtain better resolution to distinguish the MnO phase within the carbon framework, transmission emission spectroscopy (TEM) was used, shown in Fig. 5.8. In a MOF-derived MnO–C nanocomposite study by G. Nagajaru et al. TEM imaging was used to highlight the presence of MnO in a carbonaceous framework and the images produced in this study were valuable for ensuring the nature of the carbon framework was of a similar nature. As observed by G. Nagajaru et al., the MnO nanoparticles appear to be immersed in the carbon framework. Additionally the transparency of the carbon framework highlights how thin in nature indicating that the

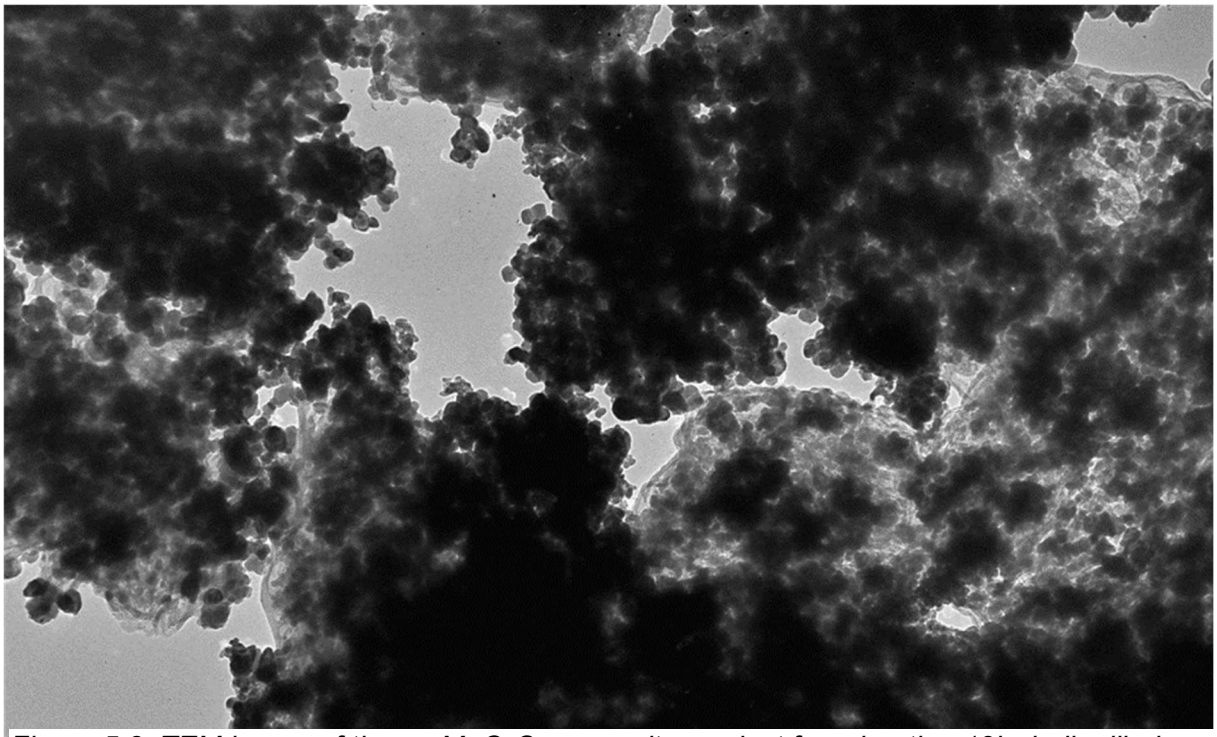

*Figure 5.8. TEM image of the $_{nano}$MnO-C composite product from heating 12hr ball milled Mnox : TA 1:1 mixture to 600 °C at a rate of 5 °C/ min with a 4-hour hold.*

high surface area of the carbonaceous material in this structure may enable charge storage during electrochemical cycling.[81] The TEM image in Fig. 5.8 clearly shows the suspension of nanoparticles of similar morphology and particle size present amongst a framework which, based on the EDX analysis in Appendix 10.4 and comparison with the literature, can be assigned as this carbon matrix. Based on these combined analysis techniques (XRD, Raman, SEM-EDX and TEM), it was verified that the $_{nano}$MnO–C composites have successfully been synthesised.

To quantify the approximate carbon content within the 600 °C / 4 hr $_{nano}$MnO-C composite, a leaching method was used, since it was recognised in the leaching experiments in Chapter 4 that the manganese and oxygen could be leached using ascorbic acid. The $_{nano}$MnO-C composite was weighed and then added to a 1.25 M solution of ascorbic acid that was heated to 60 °C, stirred for 60 minutes and then filtered afterwards. The remaining powder after leaching represented 29% by weight of the original material, which was suspected to correspond to the carbonaceous portion of this material, which means that 71% of the sample mass was composed of manganese oxide. This therefore means that an approximate 7:3 ratio of MnO:C in these samples can be rationalised. For clarification that the MnO had been removed XRD and SEM-EDX were used, shown in Fig. 5.9 and Appendix 10.5, respectively. Though there were a few impurity peaks seen in the XRD pattern of the leached material in Fig. 5.9.b, the peaks corresponding to the MnO phase were no longer present, indicating that the MnO been successfully leached from the original sample. Comparison between the original 600 °C / 4 hr $_{nano}$MnO–C composite sample in Fig. 5.9.a and the leached sample indicates this. To further clarify the leaching of the MnO from the nanocomposite, SEM-EDX analysis was used. Based on the analysis, only

0.3 % Mn by weight remained on the filter paper after leaching, indicating that the vast majority of the MnO material had been extracted from the carbonaceous framework.

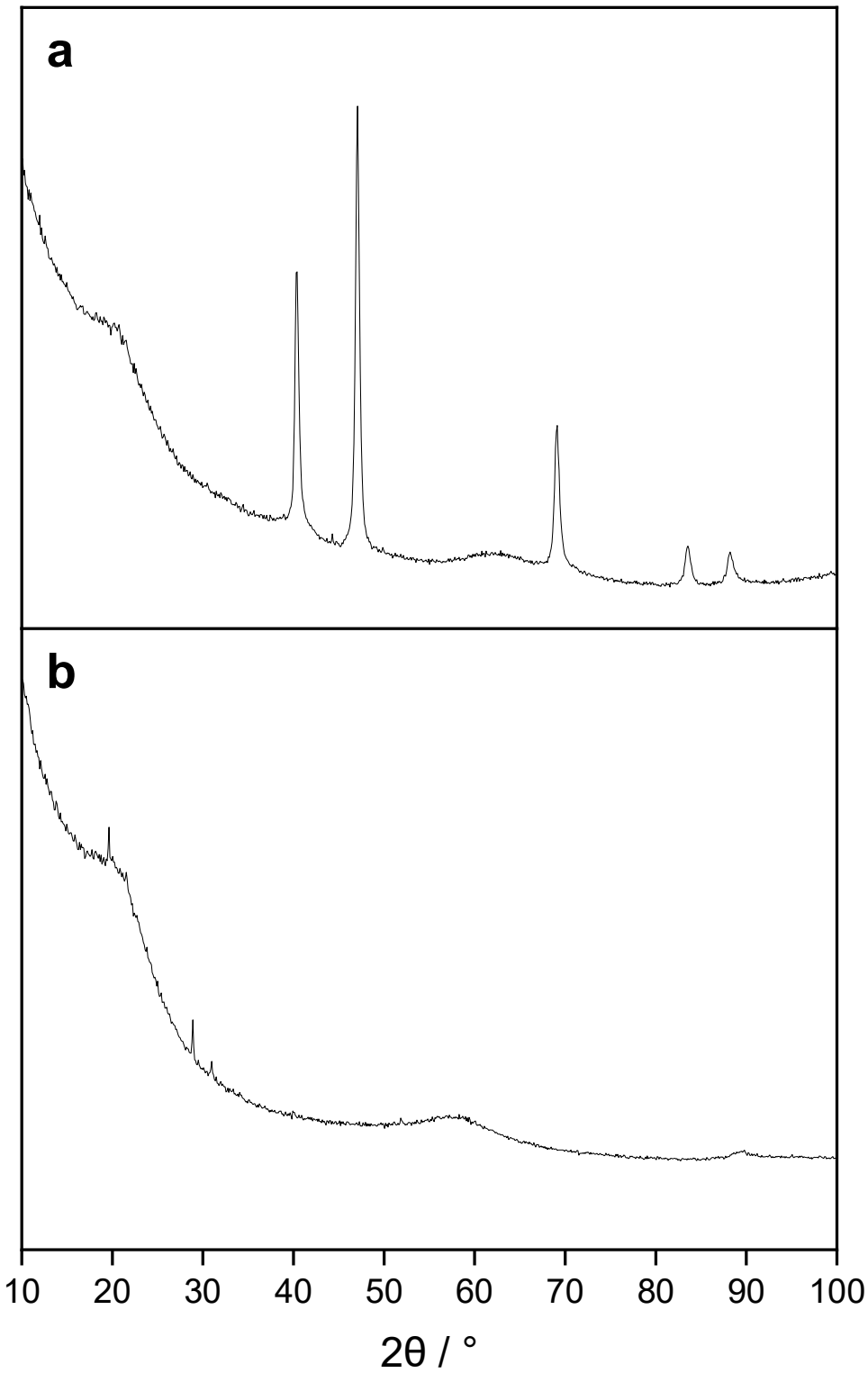


*Figure 5.9. XRD comparisons of remaining powder after leaching (a) and the original 600 °C / 4 hr $_{nano}$MnO—C composite (b) the remaining powder after leaching*

### 5.4.3 Tailoring reaction conditions for the $_{nano}$MnO–C composite

After having found a successful synthetic route for this $_{nano}$MnO–C composite using the aforementioned 12 hour ball-milling-MOF degradation method, now referred to as the 12BM-method, various annealing conditions were trialled in order to determine how particle size was affected, as it was hypothesised in section 1.5.4 that synthesis of nanosized MnO particles were crucial in order to minimise first cycle irreversible capacity losses in anode applications, as it was predicted that there would be less MnO pulverisation prior to the MnO conversion reaction in the first discharge, which would lead to less first cycle irreversible capacity loss. Based on the particle sizes of the materials synthesised in these experiments, numerous conditions would be selected to test this prediction using galvanostatic cycling. Particle size optimisation experiments were explored to synthesise the $_{nano}$MnO–C composite using the 12BM-method outlined in section 5.4.3; however, the holding temperatures were varied:

- 400 °C
- 600 °C (from original 12BM method)
- 800 °C
- 1000 °C

The different heat treatment results are shown in Fig. 5.10. The 400 °C heat treatment did not afford a crystalline $_{nano}$MnO-C composite product (shown in Fig.5.10.a), as this did not provide sufficient energy to reach the required activation energy for the reaction, whereas the 600 °C, 800 °C and 1000 °C heat treatment of these materials produced a crystalline phase which pattern matched to a face-centred cubic MnO structure with space group $Fm\bar{3}m$ (shown in Figs. 5.10.b– d). For

initial crystallite size comparison of these materials, the Scherrer equation was used (see equation 8).

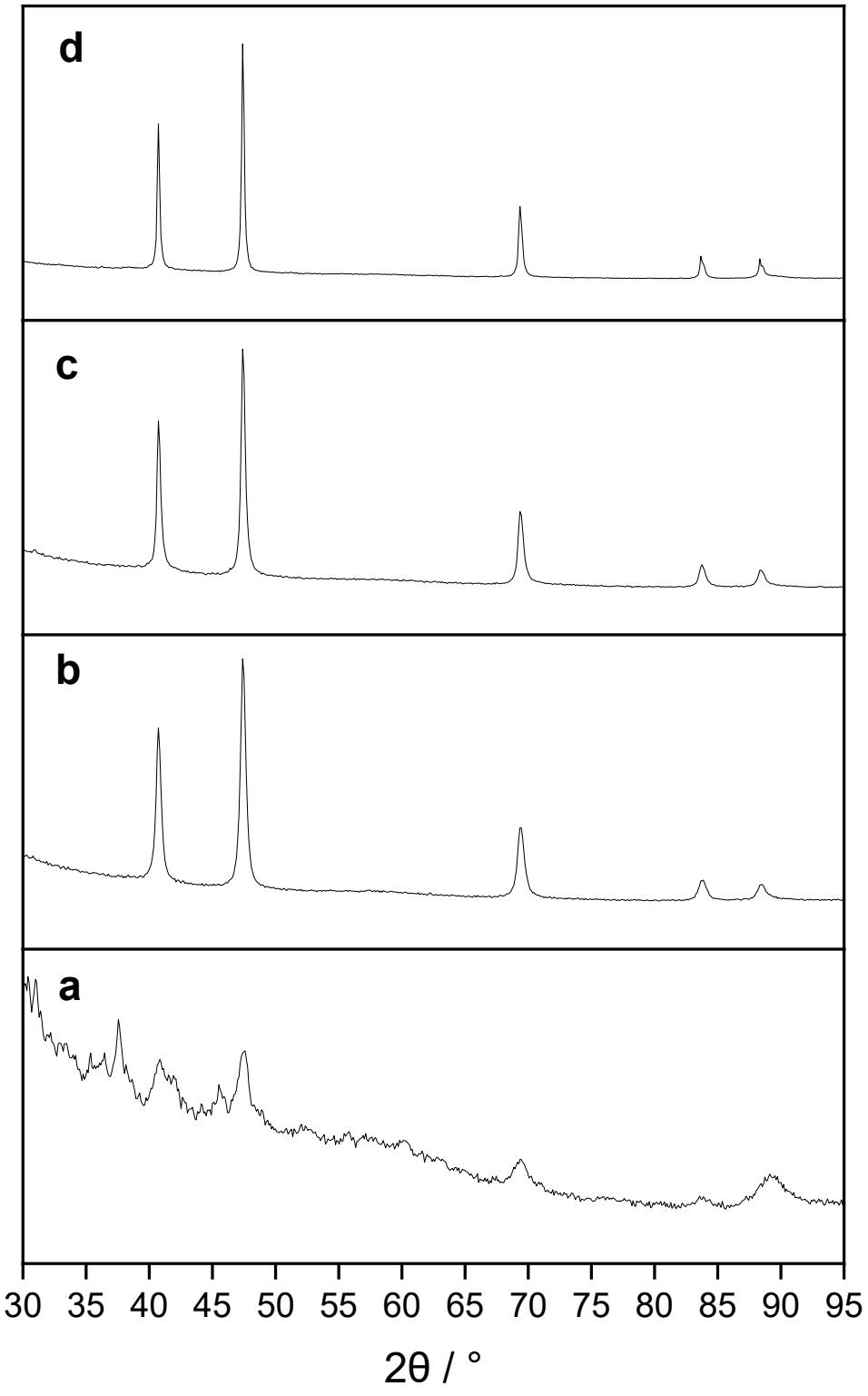


*Figure 5.10. XRD patterns of 12hr BM-MOF samples that had been heated at 5 °C/ hr under $N_2$ to temperatures of 400 °C (a), 600 °C (b), 800 °C (c), and 1000 °C (d) and held at these temperatures for 4 hours.*

For each heat treatment, calculated crystallite sizes were shown in Table 5.2. These calculations indicate that higher heating temperatures afforded the largest average crystallite size, therefore it was hypothesised that 600 °C heat treated material would produce $_{nano}$MnO–C composite materials that had the lowest degree of first cycle irreversible capacity loss as anode materials (as hypothesised in section 1.5.4). To act as further comparison, cubic MnO with space group $Fm\bar{3}m$ from Fisher scientific (Mn 76.0-78.0%, typically 99%) (labelled Fisher MnO in the discussion) was ground using the same ball milling conditions of the active material with carbon black prior to being formed into a slurry for anode manufacture. The FWHM and crystallite domain size calculations are shown in Table 5.2, and the refinement of this material is shown in Fig. 5.11. The calculated value for the crystallite domain size is generated based on the FWHM of the ~47.4 ° 2θ peak and the Scherrer equation and is calculated at 33.35 nm.  Thus, the primary difference between this pristine MnO was that it was lacking in the carbon composite network seen in the 600 °C and 1000 °C nanocomposites – which was a useful reference point to determine whether this carbon network had any influence on electrochemical behaviour/ capacity retention.

*Table 5.2. Comparing hold temperatures for 12hr BM-MOF samples that had been heated at 5 °C/ hr under $N_2$ and held at 4 hours at 600 °C, 800 °C, and 1000 °C.*

| Temperature held for 4 hours (°C) / sample name | Full width at half maximum (2θ) | (200) peak (°) | Mean crystallite domain size (nm) |
|---|---|---|---|
| **600** | 0.56508 | 47.43 | 19.53 |
| **800** | 0.45005 | 47.43 | 24.52 |
| **1000** | 0.28168 | 47.41 | 41.90 |
| **MnO (Fisher)** | 0.26713 | 47.50 | 33.35 |

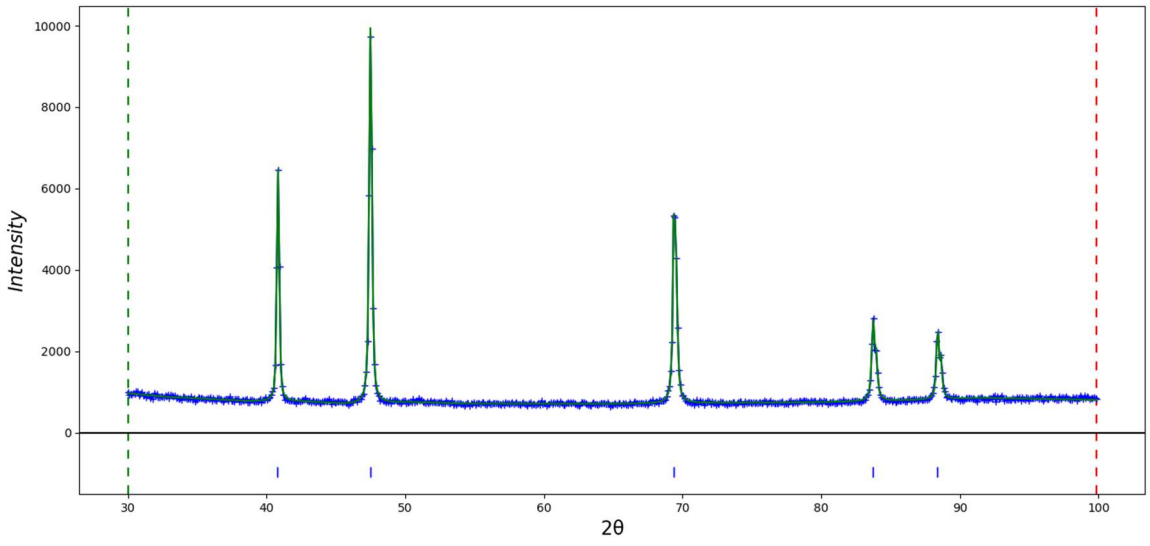


*Figure 5.11. Rietveld refinement showing Fisher MnO sample that had been ground at 350 rpm for 30 minutes. Peak matching shows MnO with reflections for space group $Fm\bar{3}m$ marked in blue.*

To further clarify differences in the materials, Rietveld refinement was used. The refined samples for Fisher MnO and the 600 °C, 800 °C, and 1000 °C heat treated nanocomposites are shown in Figs. 5.11, 5.5, 5.12 and 5.13, respectively. The calculated lattice parameters and cell volumes for all MnO samples are shown in Table 5.3 and Figs. 5.14 and 5.15. The cell volumes and lattice parameters show that there is significant lattice parameter and cell volume shrinkage for the 1000 °C sample compared with the 600 °C and 800 °C samples, the latter two having such a significant standard deviation error bar overlap that the difference in these samples is not statistically significant. One cause for this may be differing amounts of oxygen vacancies (V*ö*) between samples. V*ö* are common in manganese oxides which means they are commonly utilised in catalytic experiments owing to their versatile oxidation behaviour, as explored in a study of $MnO_2$ nanosheets by Wu et al.[190] Additionally, the cell volume/ lattice parameter values align with the significant difference of 1000 °C $_{nano}$MnO─C composite crystallite domain size compared to the 600 °C and 800 °C samples. This Fisher MnO material has the highest lattice parameter and cell volume dimensions of the MnO samples and is expected to have the poorest capacity retention due the absence of the carbon composite which would buffer any volume changes of the electrode due to the conversion reaction. As a result of these findings, the cells chosen for electrochemical analysis were therefore the 600 °C / 4 hr, the 1000 °C / 4 hr and the Fisher MnO (or 350 rpm / 30-min) samples. Due to the similarities in lattice parameters and cell volumes between the 600 °C / 4 hr and 800 °C / 4 hr nanocomposites, the former material was chosen due to the reduced energy required to generate the nanocomposite by using a lower hold-time temperature.

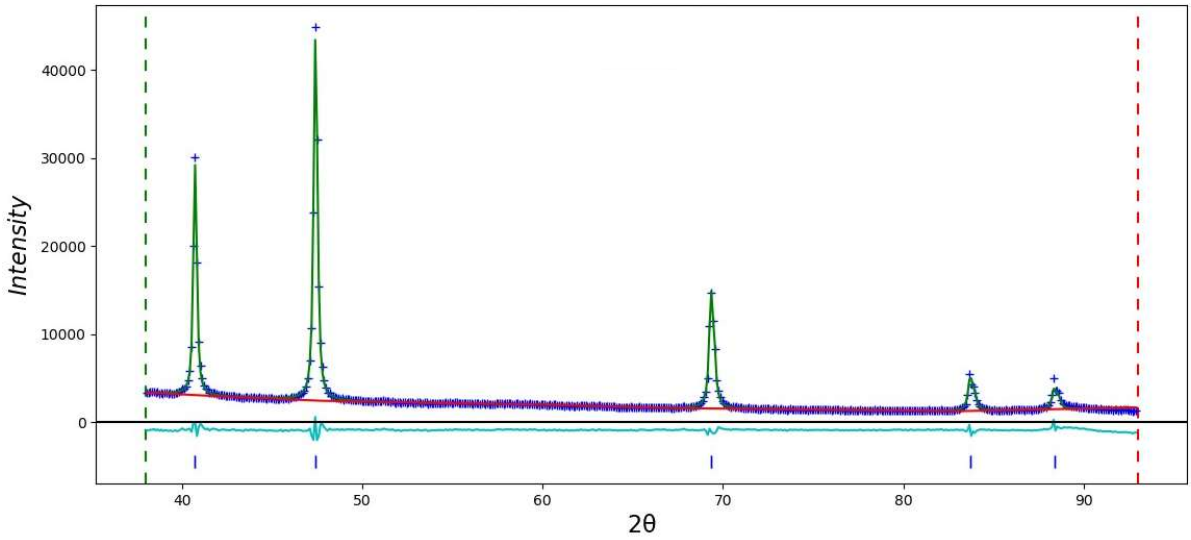


*Figure 5.13. Rietveld refinement showing composition of product obtained after Mn oxalate dihydrate/ TA mechanochemical product was heated under $N_2$ to 800 °C at a rate of 5 °C/ min and held at this temperature for 4 hours. Peak matching shows MnO with reflections for space group $Fm\bar{3}m$ marked in blue.*

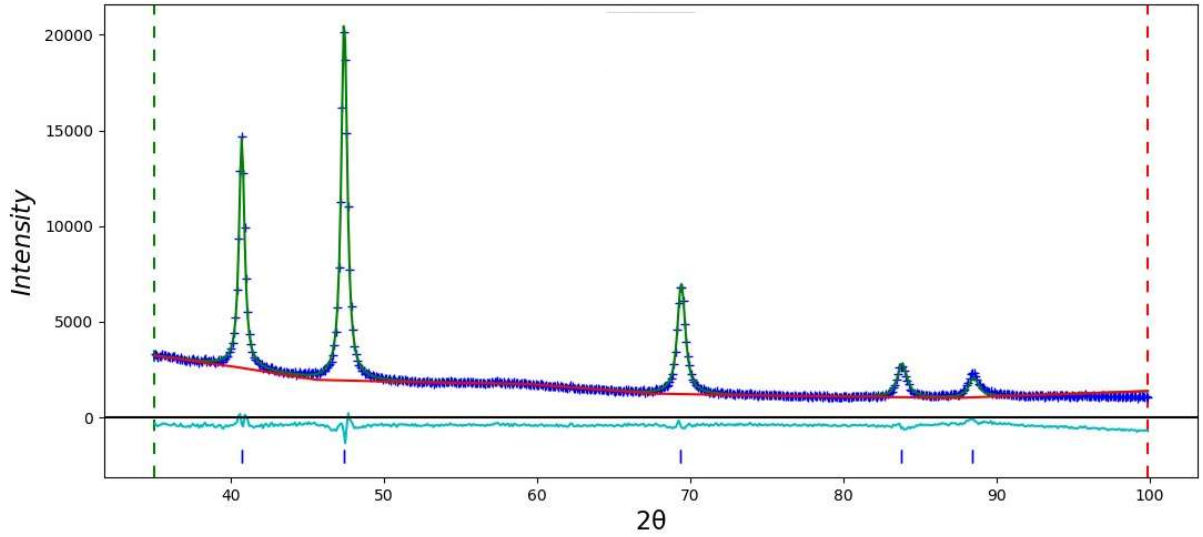


*Figure 5.12. Rietveld refinement showing composition of product obtained after Mn oxalate dihydrate/ TA mechanochemical product was heated under $N_2$ to 1000 °C at a rate of 5 °C/ min and held at this temperature for 4 hours. Peak matching shows MnO with reflections for space group $Fm\bar{3}m$ marked in blue.*

*Table 5.3. Calculated lattice parameters and cell volumes for 12hr BM-MOF samples that had been heated at 5 °C/ hr under $N_2$ to temperatures of 600 °C, 800 °C, and 1000 °C and held at these temperatures for 4 hours, and of the Fisher MnO sample that had been ground for 30 min at 350 rpm.*

| **Sample conditions / I.D.** | ***a*, *b* and *c* lattice parameter (Å)** | **Cell volume (Å)** | **$Rw_p$ (%)** |
|---|---|---|---|
| **600 °C / 4 hr** | 4.4384(3) | 87.430(2) | 3.25 |
| **800 °C / 4 hr** | 4.4385(5) | 87.440(3) | 5.52 |
| **1000 °C / 4 hr** | 4.4420(2) | 87.650(1) | 4.90 |
| **Fisher** | 4.4446(1) | 87.802(4) | 3.87 |

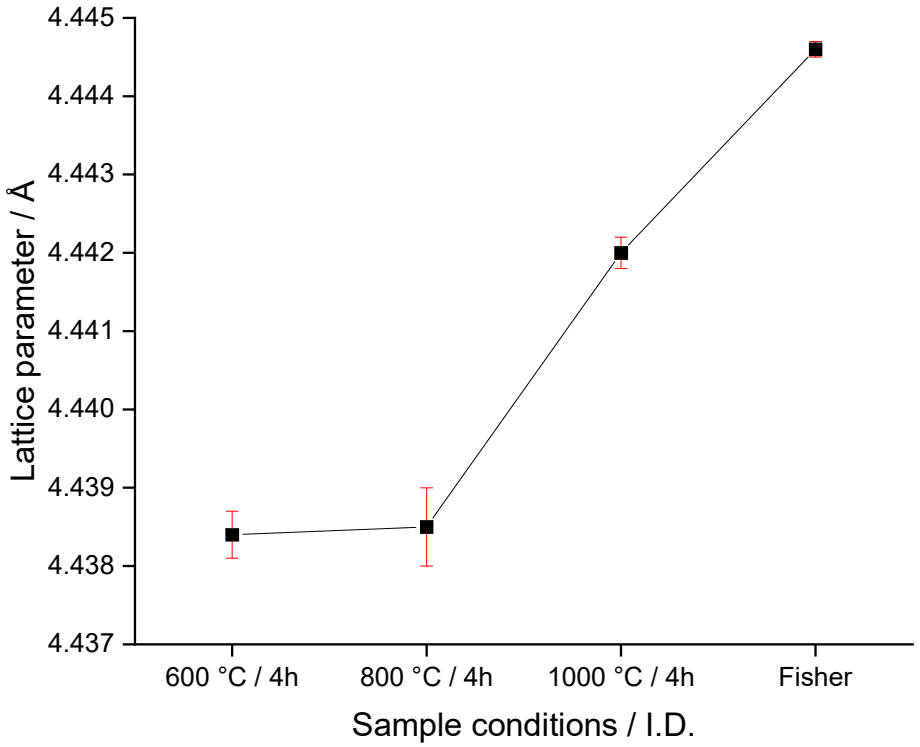


*Figure 5.14. Calculated lattice parameters for 12hr BM-MOF samples that had been heated at 5 °C / hr under $N_2$ to temperatures of 600 °C, 800 °C, and 1000 °C and held at these temperatures for 4 hours, and of the Fisher scientific MnO sample that had been ground for 30 min at 350 rpm.*

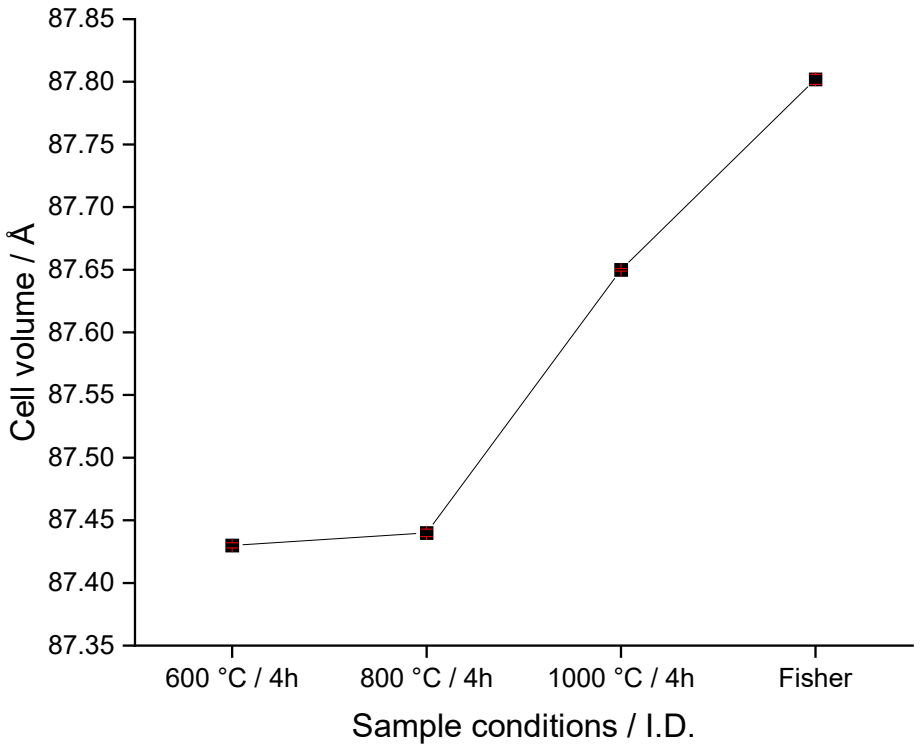


*Figure 5.15. Calculated lattice parameters for 12hr BM-MOF samples that had been heated at 5 °C / hr under $N_2$ to temperatures of 600 °C, 800 °C, and 1000 °C and held at these temperatures for 4 hours, and of the Fisher scientific MnO sample that had been ground for 30 min at 350 rpm.*

To clarify the presence of the carbon framework in the 1000 °C/ 4 hr sample heat treated sample, TEM imaging was used, shown in Fig. 5.16. In the TEM image the carbon framework encapsulates the MnO particles and is highly transparent in the image, highlighting its high surface area and elucidating the increased redox activity and resultant extra charge storage observed in these nanocomposite samples, as observed for the 600 °C/ 4 hr sample.

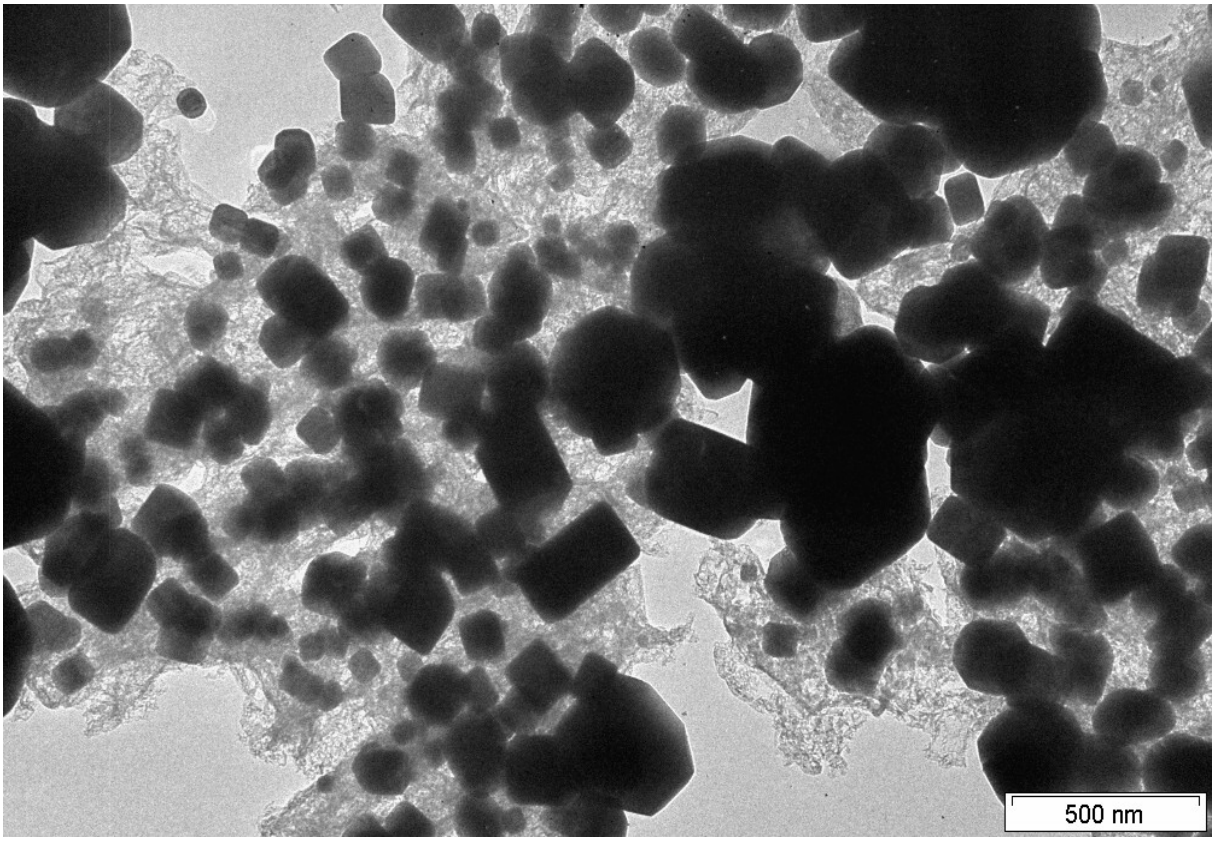


*Figure 5.16. TEM image of the $_{nano}$MnO–C composite product from heating 12hr ball milled Mnox : TA 1:1 mixture to 1000 °C at a rate of 5 °C/ min with a 4-hour hold.*

## 5.4.4 Synthesis of $_{nano}$MnO–C composites from pristine, QCR and EOL leached LMO cathode material

After having established that varying the hold-time in the 12BM synthetic method afforded materials of different particle sizes, and as it was hypothesised in section 1.5.4 that synthesis of nanosized MnO particles were crucial to minimise first cycle irreversible capacity losses, heating conditions of 600 °C/ 4h (the original 12BM conditions, outlined in section 5.4.3) were selected to synthesise $_{nano}$MnO–C composites from QCR and EOL Mn oxalate precursors. The synthetic route for this is outlined in section 5.3 – instead of a pristine Mn oxalate precursor, $LiMn_2O_4$ extracted

from QCR and EOL battery material was used to synthesise Mn oxalate (labelled QCR and EOL Mn oxalates). As stated at the beginning of section 5.4, $_{nano}$MnO–C composites synthesised from leached battery material have not been explored in the past, therefore determining a synthesis for the QCR and EOL nanocomposites as well as understanding structural differences prior to testing was imperative for these novel conversion anodes. $_{nano}$MnO–C composites were synthesised via the 12BM-method using pristine, QCR and EOL Mn oxalate precursors. XRD patterns comparing the pristine, QCR and EOL $_{nano}$MnO–C composites are compared in Fig. 5.17, where all the Mn oxalate precursors afforded a crystalline product which pattern matched to a face centred cubic MnO structure with space group $Fm\bar{3}m$. To quantify and compare crystallite sizes of these materials, the Scherrer equation was used. Based on the FWHM of the ~47.4 ° 2θ peak and the Scherrer equation, the crystallite domain sizes for these materials are shown in Table 5.4.

*Table 5.4. The effect of Mn oxalate source on crystallite domain size in $_{nano}$MnO–C composite*

| **Mn oxalate source (held for 4 hours at 600 °C)** | **Full width at half maximum (FWHM)** | **(200) peak (°)** | **Mean crystallite domain size (nm)** |
|---|---|---|---|
| **Pristine** | 0.56508 | 47.43 | 19.53 |
| **QCR** | 0.53425 | 47.44086 | 19.96 |
| **EOL** | 0.60765 | 47.51206 | 14.35 |

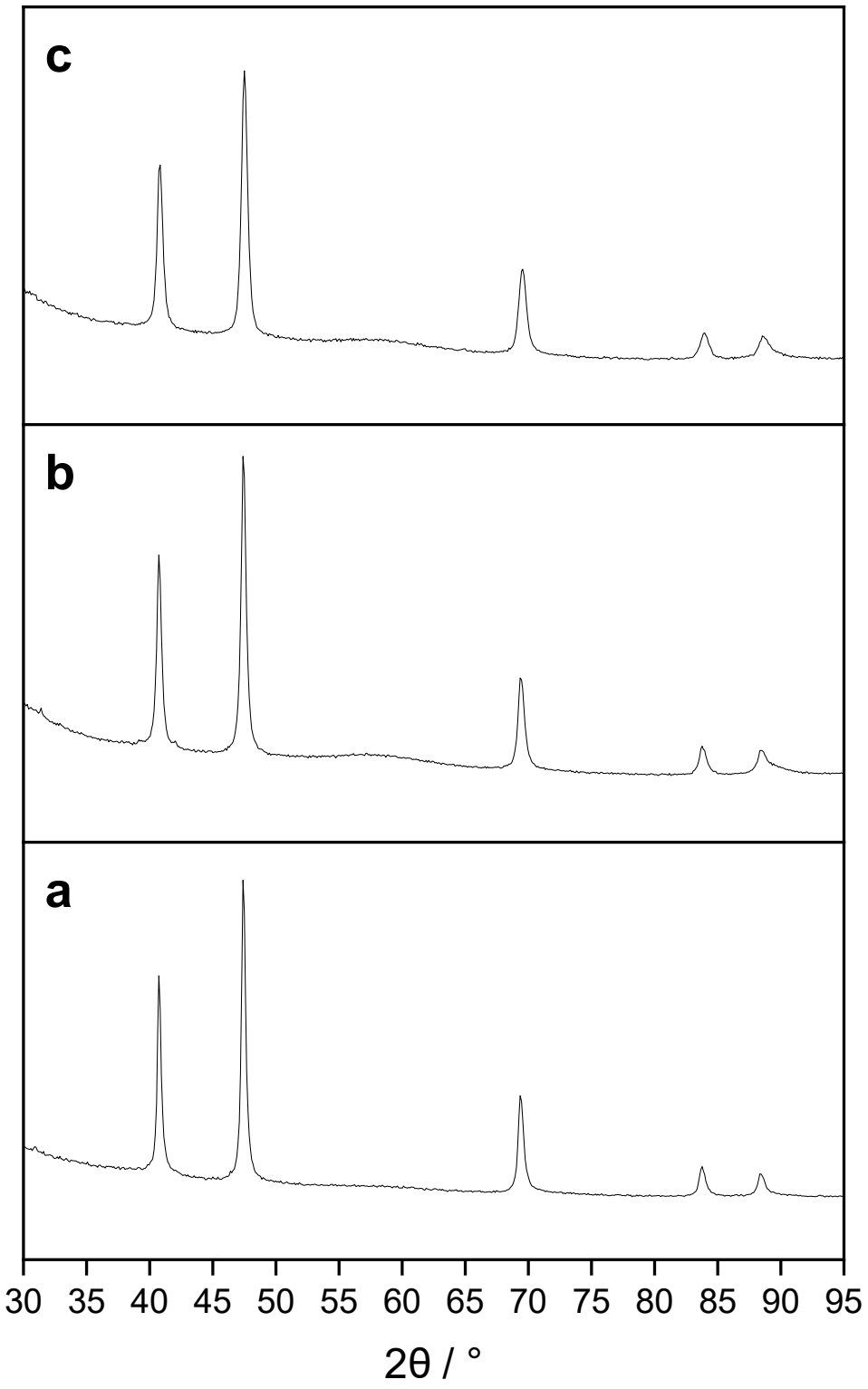


*Figure 5.17. XRD patterns of pristine (a), QCR (b) and EOL (c) $_{nano}$MnO—C composites formed from pristine, QCR and EOL Mn oxalate dihydrate, respectively, heated to 600 °C at a rate of 5 °C/ min with 4-hour hold.*

To quantify the lattice parameter/ cell volume variation in the materials, Rietveld refinement was used. The calculated lattice parameters and cell volumes are shown in Table 5.5 and Fig. 4.18, and the refinement of the pristine is shown in Fig. 5.5, and the QCR, and EOL $_{nano}$MnO─C composites are shown in Fig. 5.19. The cell volumes and lattice parameters show that there is significant lattice parameter and cell volume shrinkage for the EOL sample compared with the QCR and pristine samples, the latter two having such a significant standard deviation error bar overlap that the difference in these samples is not statistically significant. This aligns with the significant difference of EOL $_{nano}$MnO─C composite crystallite domain size compared to the pristine sample.

*Table 5.5. Calculated lattice parameters and cell volumes for pristine, QCR, and EOL $_{nano}$MnO─C composite 12hr BM-MOF samples that had been heated at 5 °C/ hr under $N_2$ to a temperature of 600 °C and held for 4 hours.*

| **Mn oxalate source (held for 4 hours at 600 °C)** | ***a, b* and *c* lattice parameter (Å)** | **Cell volume (Å)** | **$Rw_p$ (%)** |
|---|---|---|---|
| **Pristine** | 4.4384(3) | 87.430(2) | 3.25 |
| **QCR** | 4.4384(4) | 87.434(2) | 4.23 |
| **EOL** | 4.4339(6) | 87.170(4) | 4.04 |

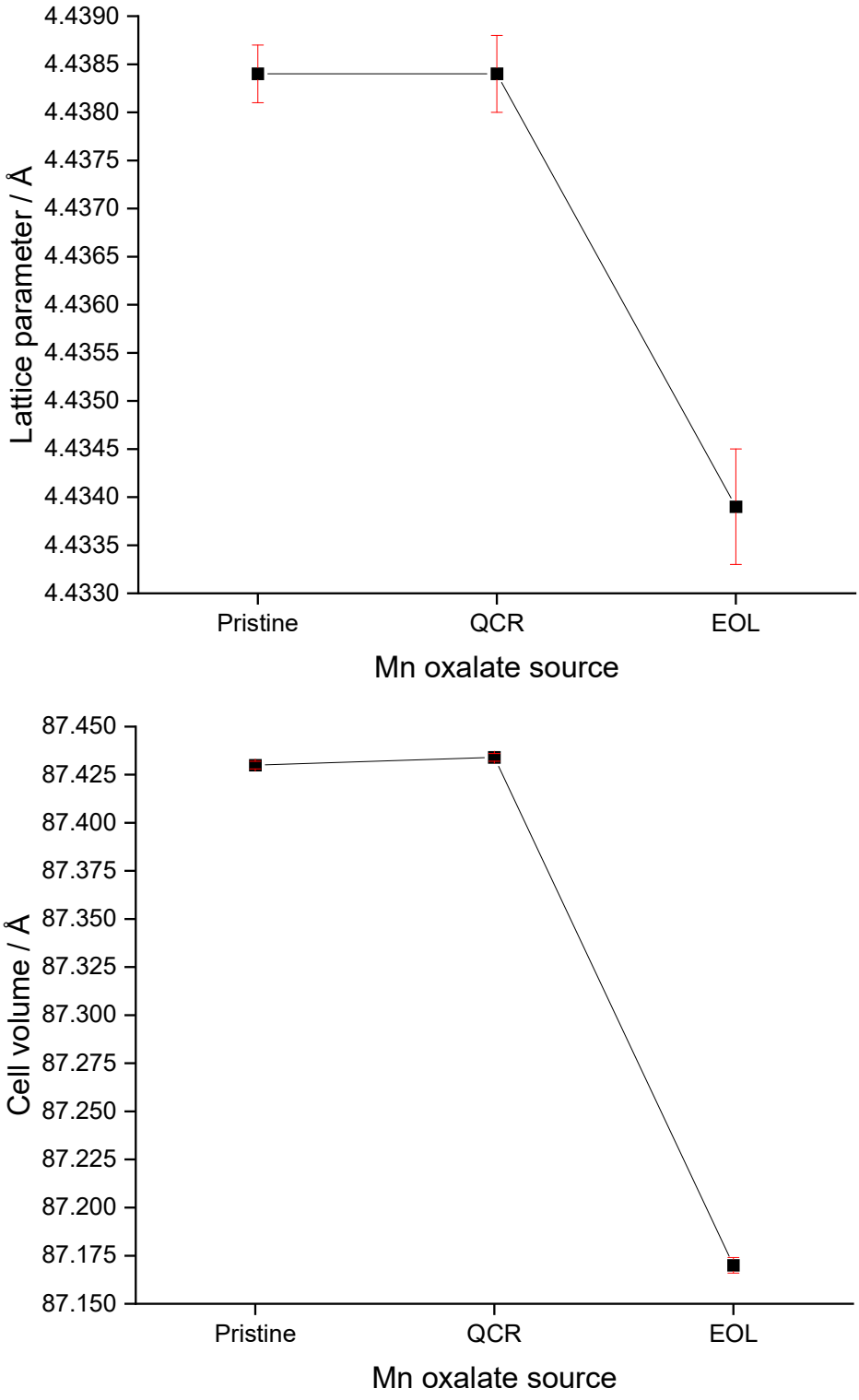


*Figure 5.18. Calculated lattice parameters (top) and cell volumes (bottom) for pristine, QCR, and EOL $_{nano}$MnO—C composites for 12hr BM-MOF samples that had been heated at 5 °C/ hr under $N_2$ to a temperature of 600 °C and held for 4 hours.*

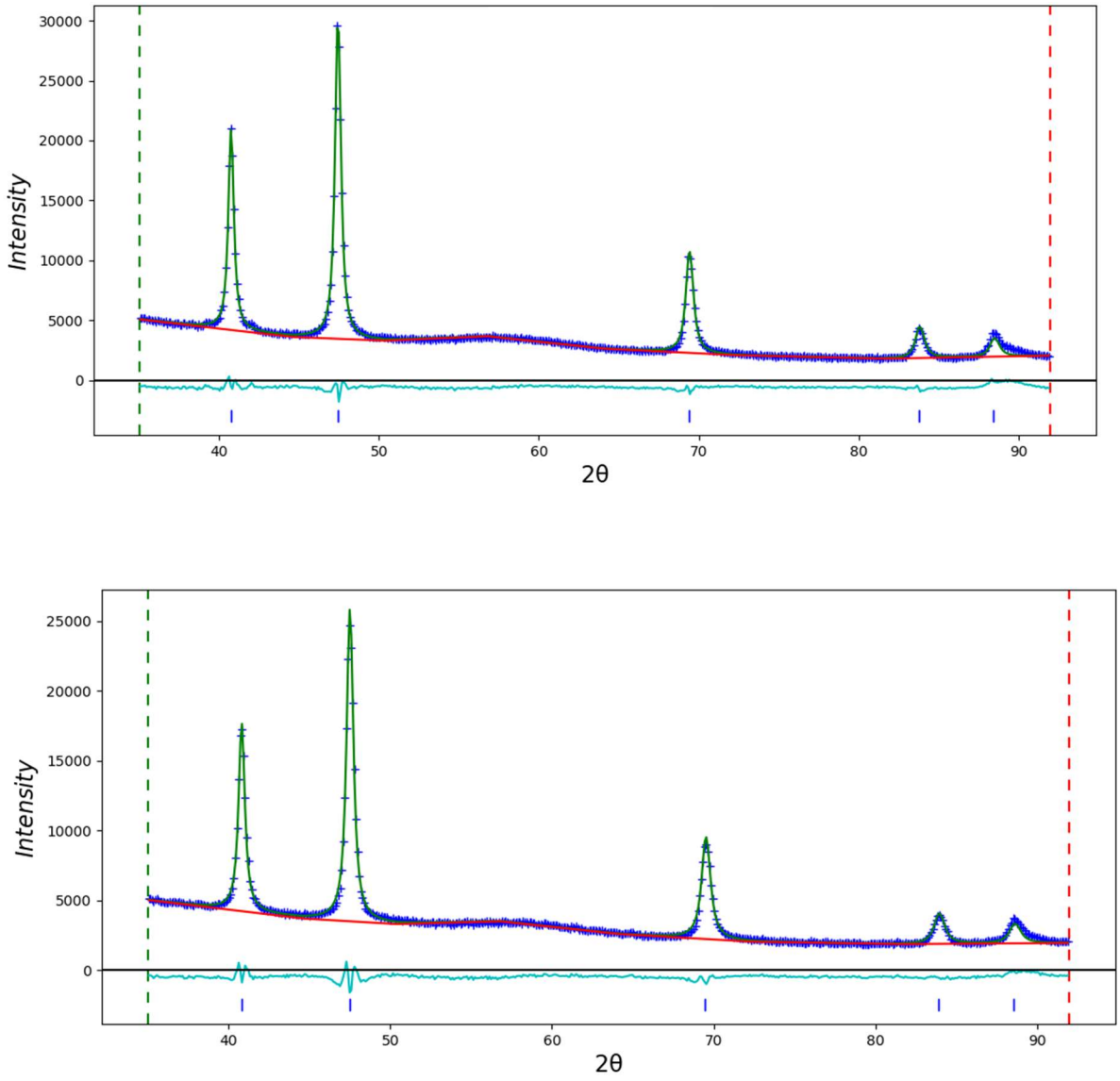


*Figure 5.19. Rietveld refinements showing composition of product obtained after QCR (top) and EOL (bottom) Mn oxalate dihydrate/ TA mechanochemical product was heated under $N_2$ to 600 °C at a rate of 5 °C/ min and held at this temperature for 4 hours. Peak matching shows MnO with space group $Fm\bar{3}m$*

As investigated in Chapter 3, transition metal element contamination is expected in the QCR and EOL samples, due to their presence in the interconverted Mn oxalate precursors, with the most significant contamination for the precursor expected to come from Ni and Co, due to the presence of the Ni-rich NCA phase and the longer leaching time required in the EOL sample. Though ICP-OES was used to analyse the pristine, QCR and EOL nanocomposites outlined in this section, sampling errors meant that confidence in accurate quantification of the impurities present in these samples using microwave digestion and ICP-OES was not assured. The aqua regia microwave digestion medium used to dissolve the nanocomposites prior to dilution did not dissolve the carbonaceous framework that surrounded the MnO nanoparticles which meant that filtration of the digested samples was necessary prior to ICP-OES analysis. Due to uncertainty that all the carbonaceous material had been accurately collected in the filtration process, the calculated weight of the dissolved sample was not assured. Though quantification of contamination was not assured, transition metal presence can be used to compare differences between the pristine and the leached (QCR/ EOL) nanocomposites. The presence of contamination in the samples have been depicted in Appendix 10.6. Based on the ICP-OES data, negligible contamination was observed for the pristine sample, as expected, whereas for the for the QCR and EOL samples, contamination from Al, Co, Li, and Ni was observed. Based on previous degrees of contamination for the QCR and EOL samples, outlined in Chapter 4, it is hypothesised that the degree of contamination for these materials is higher for the EOL material than for the QCR material. The electrochemical behaviour of this leached material, investigated in section 5.5.2, will provide more evidence as to whether this is the case.

## 5.5 Results and discussion – $_{nano}$MnO–C electrochemical comparisons

The nanocomposites synthesised in section 5.4.3 were first galvanostatically cycled to see how nanocomposites of different particle sizes impacted electrochemical behaviour followed by differential capacity analysis comparisons of these samples, outlined in section 5.5.1. Sections 5.5.1 consolidates selection of the preferred synthetic conditions to generate QCR and EOL $_{nano}$MnO–C composites. Following on from this, in section 5.5.2, the pristine, QCR, and EOL samples are compared using galvanostatic cycling and differential capacity calculations aid comparisons between these upcycled $_{nano}$MnO–C composites to support understanding of the differences in electrochemical behaviour.

### 5.5.1 Electrochemical comparisons of $_{nano}$MnO–C composites with differing crystallite domain sizes

The general half-cell manufacturing procedure is outlined in Experimental 3.5.1. To compare the influence of particle size on electrochemistry, each of the 600 °C and 1000 °C $_{nano}$MnO–C composites and the Fisher MnO were mixed with carbon black and sodium carboxymethylcellulose (CMC) in an 80:10:10 ratio, respectively, and coated onto a copper film before cutting out electrodes to test in a Li-ion battery half-cell vesus $Li/Li^+$. Before adding water to make the anode slurry, the active material and carbon black for each of the MnO samples were ground together using a planetary ball mill at 350 rpm for 30 minutes to ensure effective mixing had taken

place. Once Li-ion half cells of these materials had been synthesised, they were cycled using galvanostatic cycling with potential limitation, which is the standard technique used for electrochemical analysis of batteries. These conversion anodes were cycled between 0.05 and 3 V vs $Li^+/Li$ for 20 cycles. The Fisher MnO and 600 °C / 4 hr $_{nano}$MnO—C composite half-cells were cycled using constant current of 10 $mAg^{-1}$ for the first few formation cycles, followed by 50 $mAg^{-1}$ current applied for subsequent cycles. For the 1000 °C/ 4 hr $_{nano}$MnO—C composite half-cells, only 10 $mAg^{-1}$ current was applied as the cells failed when increased to 50 $mAhg^{-1}$.

Focussing on the first cycle in the voltage-capacity plot for these three cells, shown in Figs. 5.20 – 5.22, the voltage rapidly drops to 0.2, 0.3, and 0.35 V during discharge for the Fisher, 600 °C/ 4 hr and 1000 °C/ 4 hr samples, respectively. This rapid drop corresponds to the decomposition of the electrolyte and subsequent formation of the solid-electrolyte interphase.[78] After the voltage drop, there is a plateau in voltage, as expected, corresponding to the lithiation process, which is indicative that the $Mn^{2+}$ within the oxide is being reduced to Mn during discharge (shown in the forward reaction in equation 1 in section 1.5.1). The voltage drop from the plateau to 0.05 V at the end of discharge is has also been observed in experimentation into MnO—C nanocomposites by Y. Lin et al., where it was thought to be indicative of further Li insertion into the carbon framework.[85] In the first charge a slope between 1 and 1.75 V for Fisher samples, and between 1 and 2.15 V for both the 600 °C/ 4 hr and 1000 °C/ 4 hr samples, is indicative of the oxidation of metallic manganese to the divalent Mn which corresponds to the reverse reaction shown in equation 3.

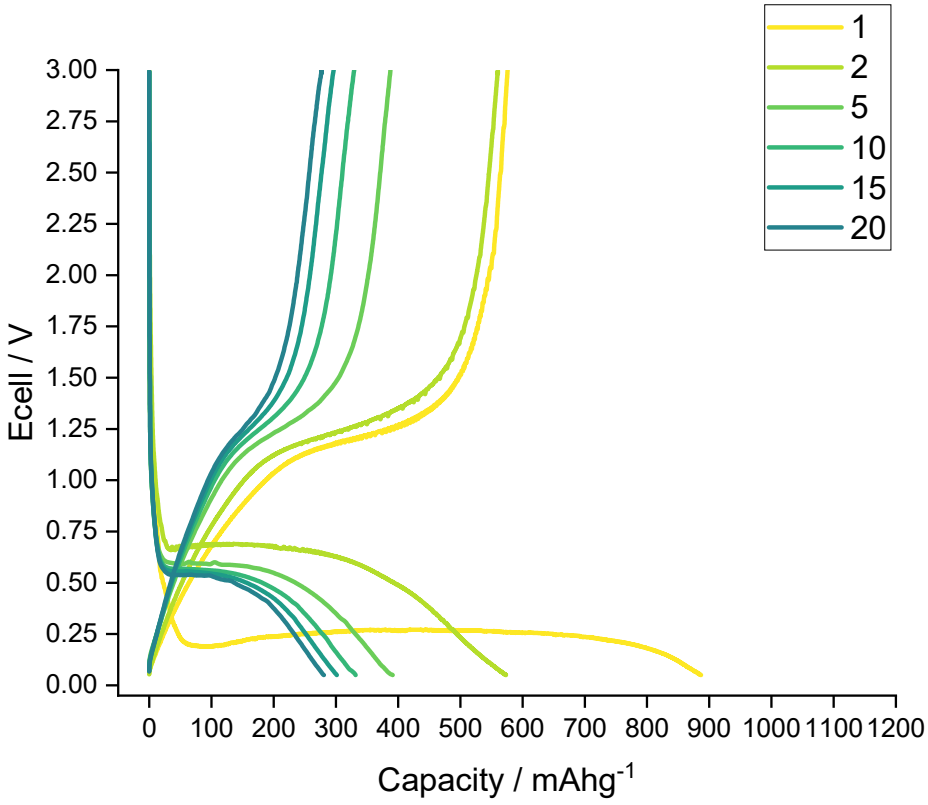


*Figure 5.20. Voltage-capacity curve of one of the MnO (Fisher) half-cells.*

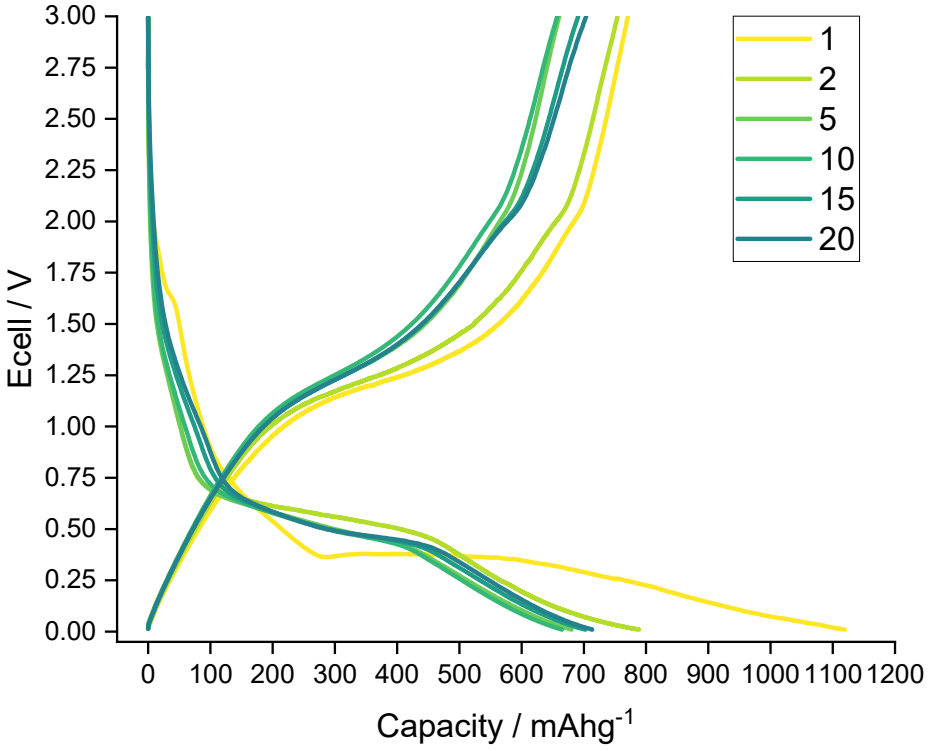


*Figure 5.21. Voltage-capacity curve of one of the 600 °C / 4 hr half-cells*

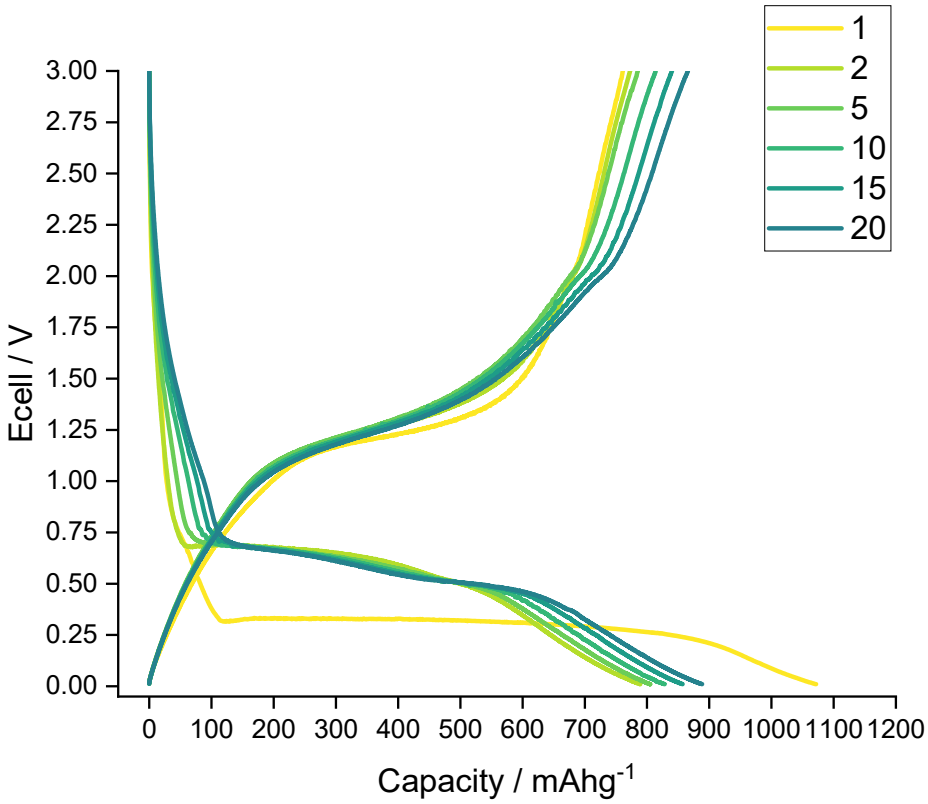


*Figure 5.22. Voltage-capacity curve of one of the 1000 °C/ 4 hr half-cells.*

The average first discharge/charge capacities and coulombic efficiencies of the half-cells are shown in table 5.6.

*Table 5.6. First discharge/charge capacities of each MnO sample with calculated coulombic efficiency*

| **MnO sample/ heating conditions** | **First discharge capacity ($mAhg^{-1}$)** | **First cycle irreversible capacity loss ($mAhg^{-1}$)** | **Coulombic efficiency (%)** |
|---|---|---|---|
| **Fisher 350 rpm / 30 min** | 901 (±24) | 312 (±8) | 65 (±0.004) |
| **600 °C/ 4 hr** | 1060 (±90) | 320 (±45) | 70 (±0.02) |
| **1000 °C/ 4 hr** | 1092 (±13) | 320 (±11) | 71 (±0.01) |

In the first cycle, the coulombic efficiency quantifies the extent of the first cycle irreversible capacity loss exhibited for each MnO studied. The greatest first cycle capacity loss arises in the Fisher sample. One reason for this may be that beginning cycling the material from a smaller particle size limits pulverisation of electrodes and minimises these first cycle losses, as hypothesised in the introduction of this Chapter. Additionally, in the Fisher sample, there is no carbon framework to buffer the volume changes that arise during material conversion, which could cause electrode cracking leading to a loss of electrical contact in the cell. The 600 °C/ 4h and 1000 °C/ 4h $_{nano}$MnO─C composites exhibit almost identical coulombic efficiencies despite the 1000 °C/ 4 hr sample being just over double the mean crystallite domain size than the 600 °C/ 4 hr material, shown in table 5.2, which is suggestive that the carbonaceous composite framework in these nanocomposites enhances the capacity retention in these – the difference would make sense seeing as different hold

temperatures were applied to these materials, which would impact the graphitisation of the carbon framework. One way to understand the differences in these carbon frameworks degree of graphitisation of the carbon for these two samples, the $I_D/I_G$ intensity ratio of the G and D peaks can be used to investigate the differences between the carbon composites.[14]. It is key to mention that precise quantitative information is not always possible using Raman spectra due to features such as a high background signal in the Raman spectrum. Unfortunately, the $I_D/I_G$ intensity ratio of the G and D peaks was not investigated in this study due to time constraints.

The next thing to consider for these MnO samples is the differences in capacity exhibited – the first discharge capacity is much greater for the carbon nanocomposites than for the Fisher sample, with both nanocomposites exhibiting capacities of > 970 $mAhg^{-1}$, whereas on average for the Fisher sample, the first discharge capacity never exceeds 940 $mAhg^{-1}$. MnO sample. The large nanoparticle surface area of the composite materials may have affected the capacity by increasing the number of side-reactions and degree of SEI formation in the Li-ion half cells (as exhibited in the first discharge capacities), leading to a loss of Li inventory, however the carbon composite network is expected to reduce the electrolyte decomposition and enhance Li uptake and by enriching conversion anode conductivity. The much greater theoretical capacities exhibited by the nanocomposites suggests that the carbon framework has influence on the capacity reached.[73] To see the effect on capacity of these materials in subsequent cycles, these MnO half-cells were galvanostatically cycled in triplicate, and their average capacities were calculated and displayed in Fig. 5.23. The first clear difference in capacity fading behaviour is from the poor capacity retention observed for the Fisher MnO sample: such significant

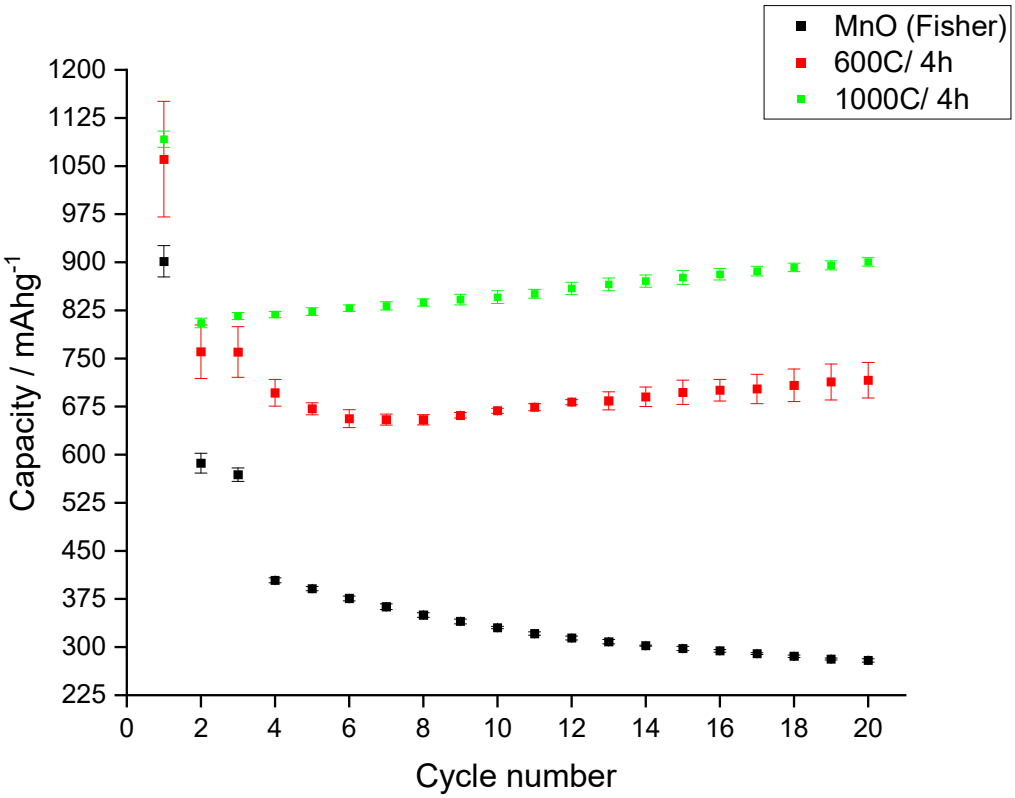


*Figure 5.23 Capacity versus cycle number plot comparing the capacity fade of Fisher MnO, 600 °C / 4 hr and 1000 °C / 4 hr $_{nano}$MnO—C composites.*

capacity decay exhibited in Fisher MnO sample highlights the effectiveness of the carbon composite network in buffering the conversion reaction. With the absence of this framework, the volume changes from the conversion reaction during galvanostatic cycling will have caused electrode active film cracking, leading to loss of contact between the active material and the current collector, resulting in the observed rapid capacity decay. To probe the degree of electrode cracking for the cycled pristine MnO electrode, one of these half-cells was disassembled in an argon atmosphere glovebox and washed using dimethyl carbonate prior to drying. This electrode was then studied using SEM, shown in Fig. 5.24. As expected, the electrode cracking is severe for the pristine sample, which aligns with the observed

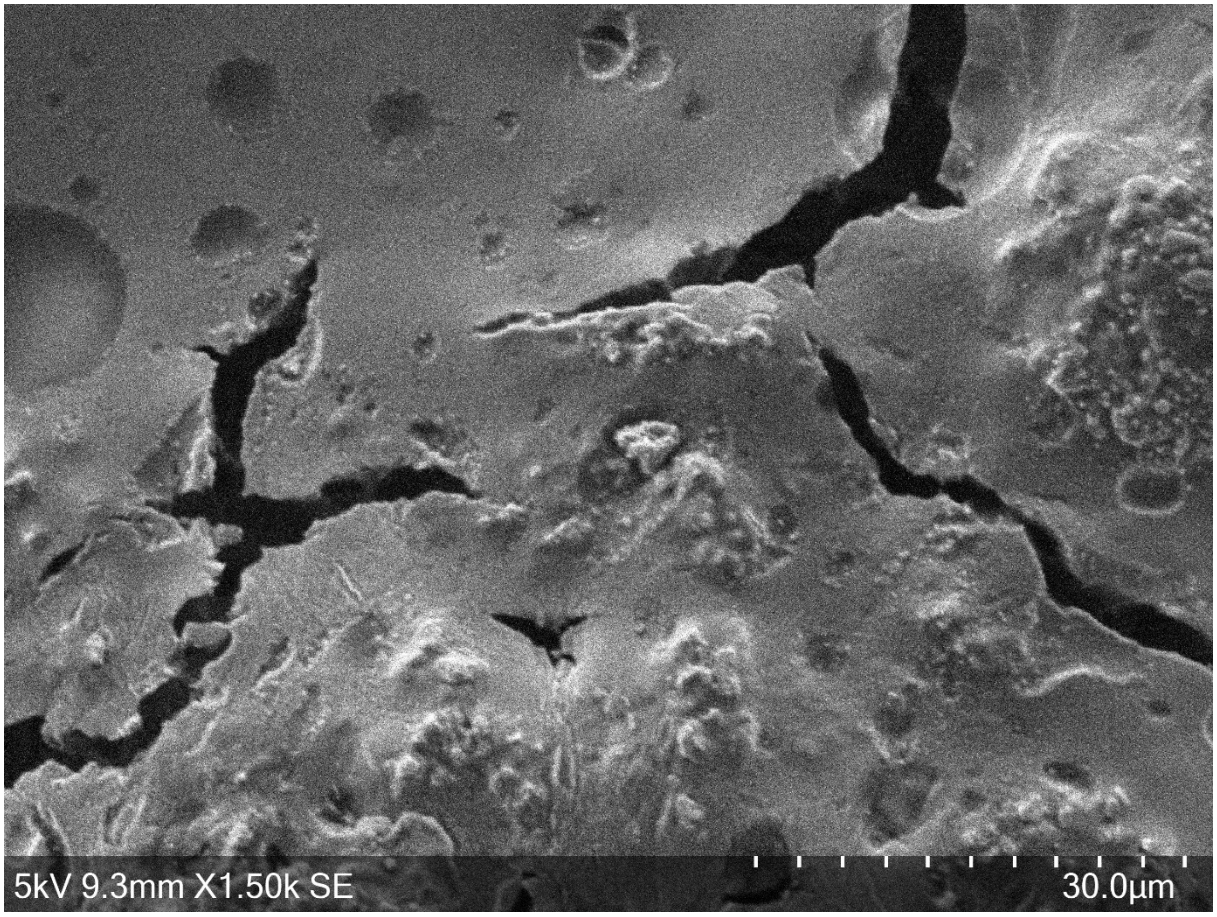

*Figure 5.24. SEM image showing Fisher MnO electrode surface post-cycling (20 cycles).*

electrochemical capacity retention for this anode material after 20 cycles – the electrode cracking will cause contact loss between the electrode and current collector during cell runtime, giving rise to the observed poor capacity retention in the half-cells.

To further understand the influence framework has influence on the capacity reached the voltage versus Li was calculated for each sample during cycling. Based on equation 3 it is expected that lithiation/ delithiation is expected via transfer of 2 $Li^+$ ions during discharge/ charge, corresponding to a theoretical capacity of 755 $mAhg^{-1}$, and based on the capacities observed in Fig. 5.23 it is clear in all cases that this value is exceeded in the first discharge. For the pristine, 600 °C / 4 hr and 1000 °C /

4 hr half-cells the average Li concentration in the first discharge was 2.4, 2.8, and 2.9 $Li^+$, respectively. In the pristine sample, the capacity gradually decreases during cycling, most likely due to the contact losses from the electrode cracking shown in Fig. 5.24, however for the nanocomposites, the capacity is recovered during cycling. It is also key to note that the $_{nano}$MnO–C composites gradually began to increase in capacity (after 2 cycles and 8 cycles for the 1000 and 600 °C/ 4 hr half-cells, respectively). For the 600 °C / 4 hr $_{nano}$MnO–C composite this value never exceeds the expected theoretical Li uptake capacity after 2 cycles, whereas for the 1000 °C / 4 hr $_{nano}$MnO–C composite, the theoretical capacity is always exceeded during cycling out to 20 cycles. This is indicative that the carbon framework enhances Li uptake more effectively in the 1000 °C / 4 hr $_{nano}$MnO–C composite. In a MOF-derived MnO-C composite investigation conducted by Zhu et al., capacity increase for these systems have been attributed to an array of electrochemically-activated processes, including increased electrolyte incorporation as cycling occurs, kinetically-enhanced lithium diffusion, activation of the nanocomposite during cycling, and even the access of higher oxidation states of manganese – which are all possibilities for these nanocomposites. [80]

To further understand the differences in capacity fade and electrochemical behaviour between the pristine MnO and the nanocomposites using redox behaviour, differential capacity analysis was used. Differential capacity versus voltage phase transition behaviour enables redox activity to be distinguished that is less obvious in the plateaus in the complementary voltage-capacity data.[191] As differential capacity plots give rise to peaks at particular voltages corresponding to redox active transitions it is easy to observe when a system is cycling through a Faradaic (redox active) or a non-

Faradaic (capacitive) process. One half-cell of each of the pristine MnO and the 600 °C/ 4 hr and 1000 °C/ 4 hr nanocomposites were compared and summarised in Table 5.7, and the differential capacity plots are shown in Figs. 5.25 – 5.27.

*Table 5.7. Differential capacity analysis comparisons for Pristine MnO, 600 °C/ 4 hr and 1000 °C/ 4 hr half-cells.*

| Cycle no. | Reaction | Pristine | 600 °C/ 4 hr | 1000 °C/ 4 hr |
|---|---|---|---|---|
| **C1** | **Discharge** | Peak at **0.25 V** shows conversion of MnO to metallic Mn. | Peak at **0.38 V** shows conversion of MnO to metallic Mn. | Peak at **0.3 V** shows conversion of MnO to metallic Mn. |
| | **Charge** | Oxidation peak at **1.2 V** | Oxidation peak at **1.2 V,** extra redox peak at **2.0 V** | Oxidation peak at **1.2 V,** extra redox peak at **2.0 V** |
| **C2** | **Discharge** | **0.7 V** conversion | **0.55 V** conversion | **0.6 V** peak, shoulder at **0.52 V** |
| | **Charge** | See C1 | See C1 | See C1 |
| **C5** | **Discharge** | **0.52 V** conversion | **0.45 V** conversion (potential | **0.6 V** peak, shoulder **at 0.52 V** |

| | | | | |
|---|---|---|---|---|
| | | | shoulder **at 0.6 V**) | |
| | **Charge** | See C1 | See C1 | See C1 |
| **C10** | **Discharge** | See C5 | **0.45 V** conversion with potential shoulder **at 0.6 V** | Two peaks: **0.6 V** (strongest) & **0.5 V** |
| | **Charge** | See C1 | See C1 | See C1 |
| **C15** | **Discharge** | See C5 | **0.45 V** conversion with potential shoulder **at 0.6 V** | Two peaks: **0.6 V** & **0.5 V** (strongest) |
| | **Charge** | See C1 | See C1 | See C1 |
| **C20** | Discharge | **0.5 V** conversion | **0.45 V** conversion | Two peaks: **0.6 V** & **0.5 V** (strongest) . |
| | Charge | See C1 | See C1 | See C1 |

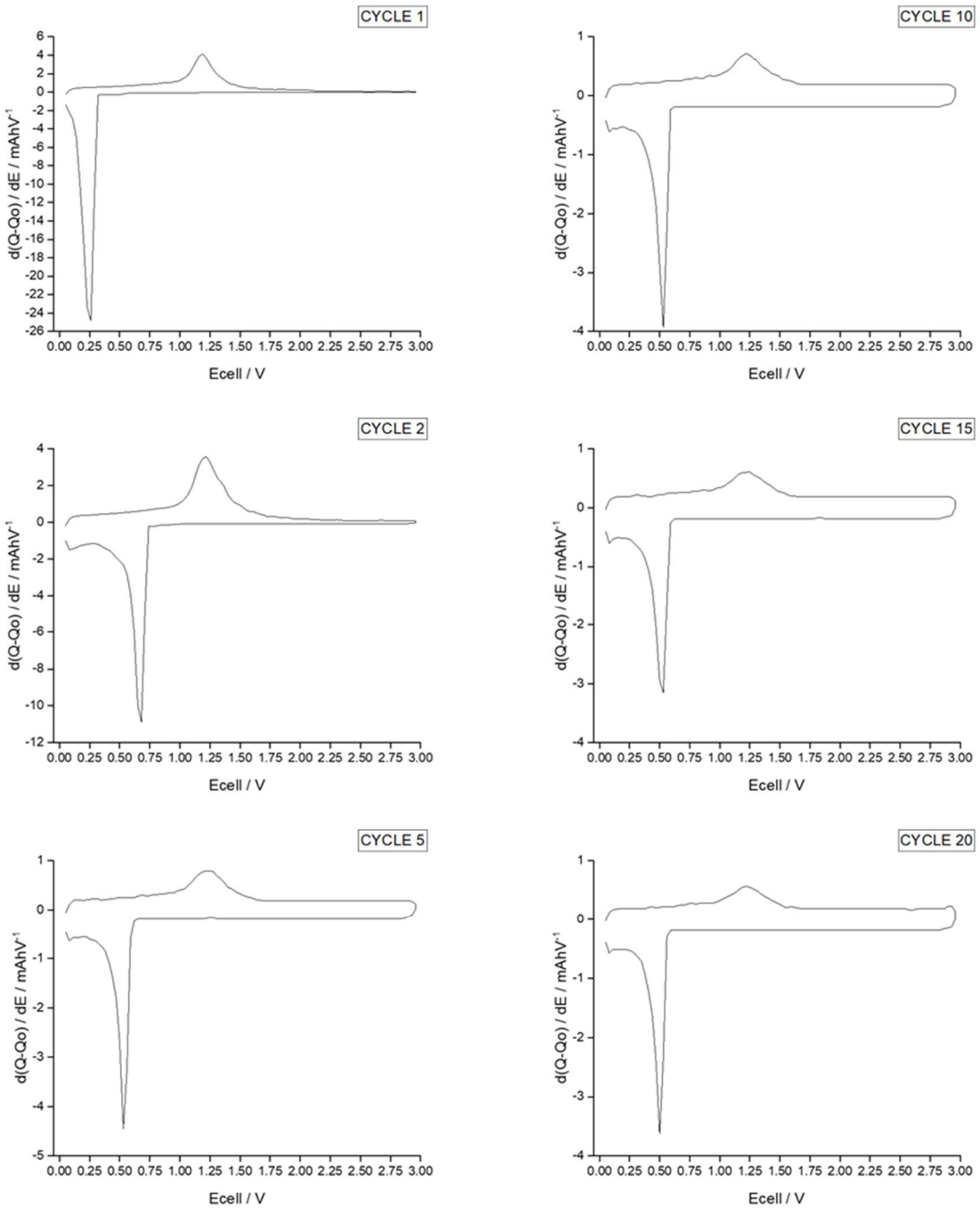


*Figure 5.25. Differential capacity plots for cycles 1 – 20 of the Fisher MnO sample.*

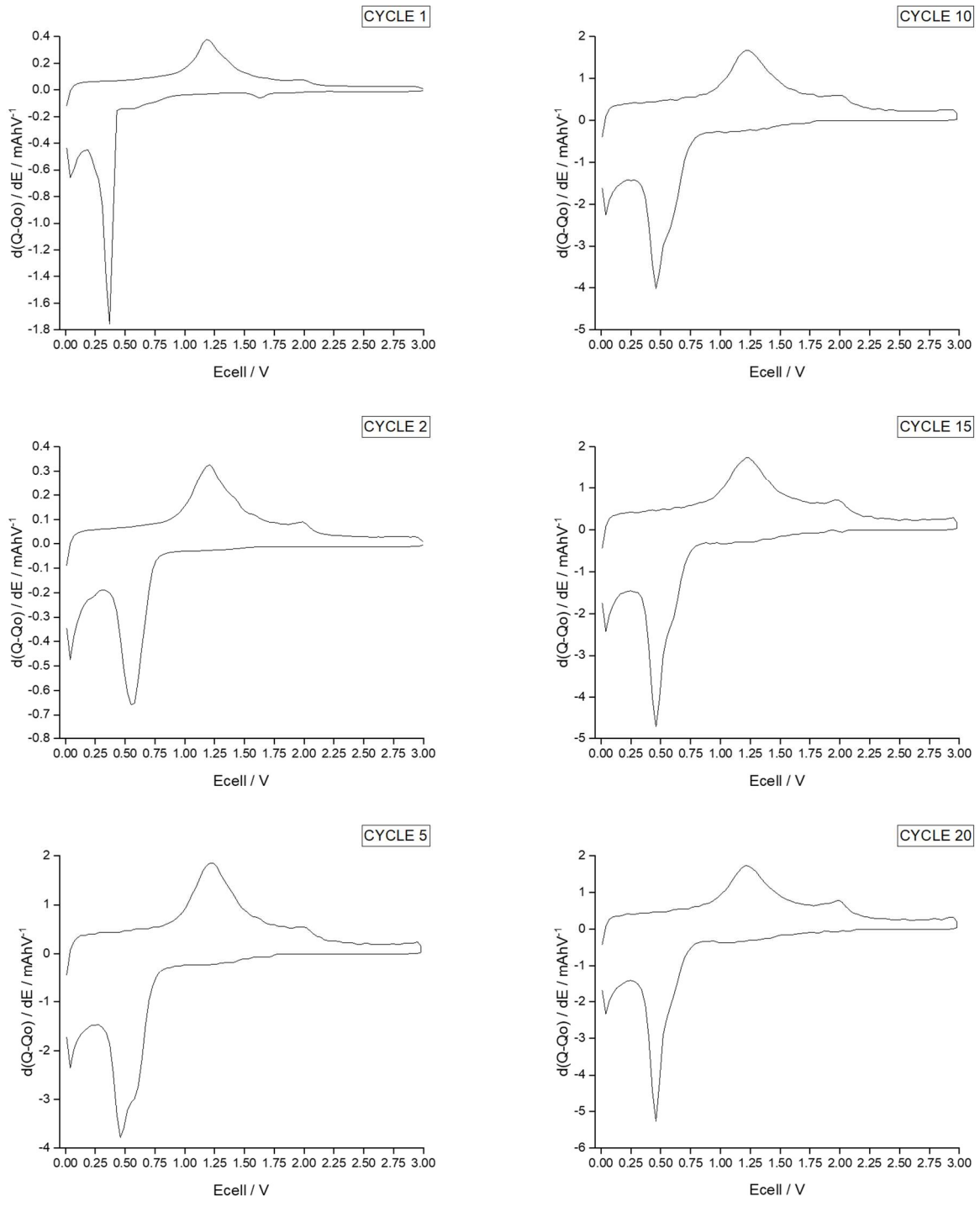


*Figure 5.26. Differential capacity plots for cycles 1 – 20 of the 600 °C / 4 hr sample.*

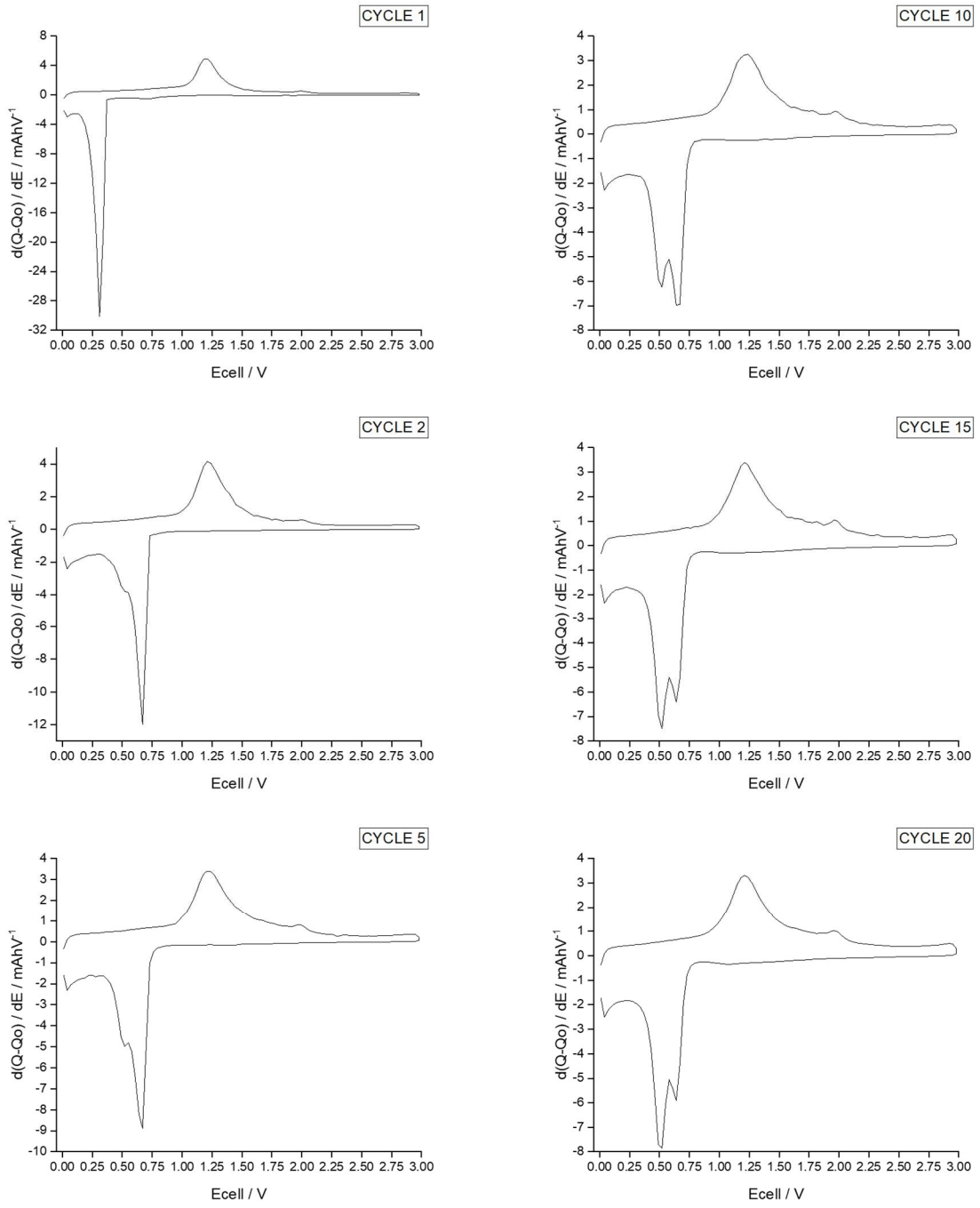


*Figure 5.27. Differential capacity plots for cycles 1 – 20 of the 1000 °C / 4 hr sample*

In a study by G. Nagaraju et al., the differential capacity analysis for their MOF-derived MnO@C composite was plotted between 1 and 5 cycles. The major reduction peak in the first cycle occurs at 0.28 V in G. Nagaraju et al.'s study, which is comparable to the values observed for discharge of the first cycle for Fisher, 600 °C/ 4 hr and 1000 °C/ 4 hr samples in Table 5.7, at 0.25, 0.38 and 0.3 V. For the oxidation of $Mn^0$ during charge, the oxidation peak for is observed at 1.25 V in their study, which is again comparable to the large 1.2 V peak observed for the pristine, 600 °C/ 4 hr and 1000 °C/ 4 hr samples. In the nanocomposites there is an extra redox peak at 2.0 V during charge for the two nanocomposites throughout cycling suggests that there is another redox-active process arising in these samples, which is also seen in G. Nagaraju et al.'s study. In their study, they ascribed this to an 'additional oxidation process' that provides increased capacity in subsequent cycles. Based on the fact that this peak is not seen for the Fisher sample, this extra redox peak can be ascribed to the presence of the carbon framework, which appears to have a high surface area by analysis of the TEM image for the 600 °C/ 4 hr sample, highlighted in Fig. 5.16.[81]

For the Fisher sample, the conversion reaction initially occurs at 0.25 V, but then increases to 0.7 V on the second cycle. In a study on MnO/C nanocomposites by J. Liu et al., the increased lithiation voltage is hypothesised to be due to enhanced kinetics from the pulverisation of the anode material after this first discharge.[77] In subsequent cycles this conversion reaction appears to occur at voltages between 0.5 – 0.52 V, indicating that after the first few cycles the SEI layer has formed adequately. The same trend is true for the 600 °C/ 4 hr half-cell: the conversion reaction initially occurs at 0.38 V. On the second discharge this voltage rises to 0.55 V, and from cycle

5 onwards this voltage stabilises at 0.45 V. In the 600 °C/ 4 hr half-cell, however, there appears to be slight broadening of the conversion peak between cycles 5 and 15 and a suspected shoulder peak at 0.6 V is identified, however by cycle 20 this peak sharpens to the original 0.45 V conversion peak.

In the 1000 °C/ 4 hr sample, the conversion reaction initially occurs at 0.3 V. On the second discharge this voltage rises to 0.6 V, and a shoulder peak appears to form at 0.52 V. By cycle 5 this shoulder is prominent. By cycle 10, the shoulder peak is very prominent at 0.5 V, though the original 0.6 V peak remains the strongest peak. On cycle 15 the peak at 0.5 V peak is stronger than the 0.6 V peak and by cycle 20 this peak 0.5 V has grown significantly. This extra redox peak during discharge is likely to come from the carbon composite framework. Though this carbon composite framework is present for the 600 °C/ 4 hr sample, its intrinsic structure and electrochemical activity will most likely differ for the carbonaceous material due to the difference in heating conditions.

### 5.5.2 Electrochemical comparisons of $_{nano}$MnO–C composites from pristine, QCR and EOL LMO sources

The general half-cell manufacturing procedure is outlined in Experimental 3.5.1. To compare the influence of Mn source on electrochemistry, pristine, QCR and EOL $LiMn_2O_4$ precursor materials were used to synthesised 600 °C/ 4 hr $_{nano}$MnO–C composites. These nanocomposites were mixed with carbon black and sodium carboxymethylcellulose (CMC) in an 80:10:10 ratio, respectively, and coated onto a copper film before cutting out electrodes to test in a Li-ion battery half-cell. Before

adding water to make the anode slurry, the active material and carbon black were ground together at 350 rpm for 30 minutes to ensure effective mixing had taken place. Once Li-ion half cells of these materials had been synthesised, they were cycled using galvanostatic cycling with potential limitation, which is the standard technique used for electrochemical analysis of batteries. These conversion anodes were cycled between 0.05 and 3 V vs $Li^+/Li$ for 15 cycles. All half-cells were cycled using constant current of 10 $mAg^{-1}$ for the first few formation cycles, followed by 50 $mAg^{-1}$ current applied for subsequent cycles.

Focussing on voltage-capacity plot for these three cells, shown in Fig. 5.28 – 5.30, the voltage in the first cycle rapidly drops to 0.38 V during discharge for all samples. This has been linked the decomposition of the electrolyte and subsequent formation of the solid electrolyte interphase, as observed for the other MnO samples in section 5.5.1. As seen for the cells in in section 5.5.1 , there is a voltage plateau corresponding to the lithiation process, which is indicative that the $Mn^{2+}$ within the oxide is being reduced to Mn during discharge (shown in the forward reaction in equation 1 in section 1.5.1) and a voltage drop from the plateau to 0.05 V at the end of discharge, which, again, is indicative of further Li insertion into the carbon framework, as observed in experiments on MnO—C composite materials by Y. Lin et al.[85] In the first charge a slope between 0.8 and 2.15 V for all the 600 °C/ 4 hr samples is indicative of the oxidation of metallic manganese to the divalent Mn which corresponds to the reverse reaction shown in equation 3.

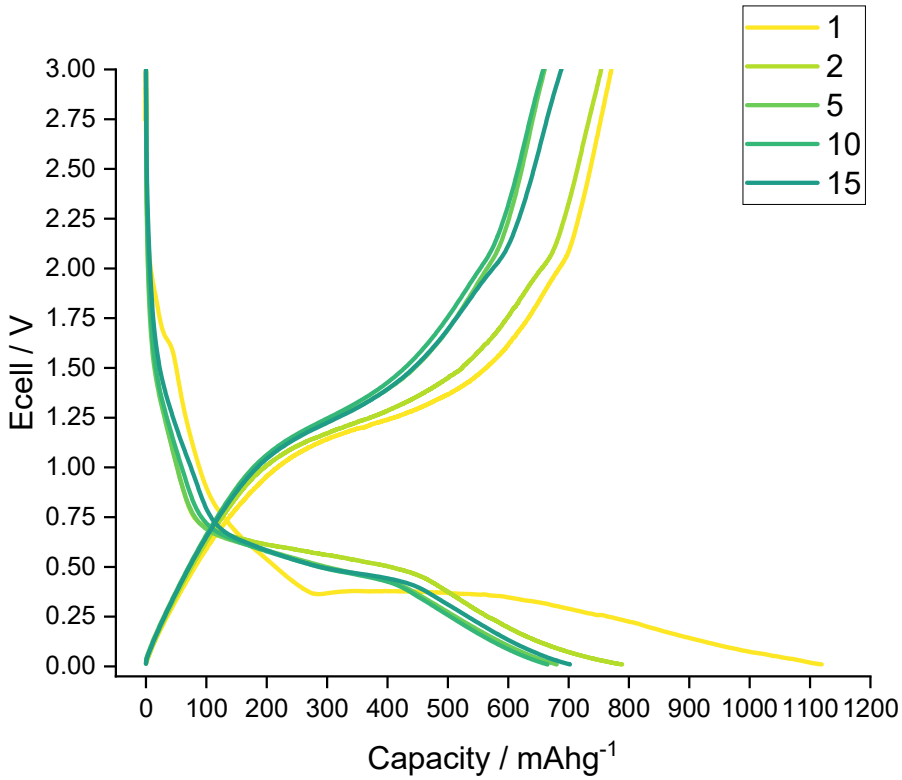


*Figure 5.29. Voltage-capacity curves for one of the pristine 600 °C / 4 hr $_{nano}$MnO—C composite half-cells.*

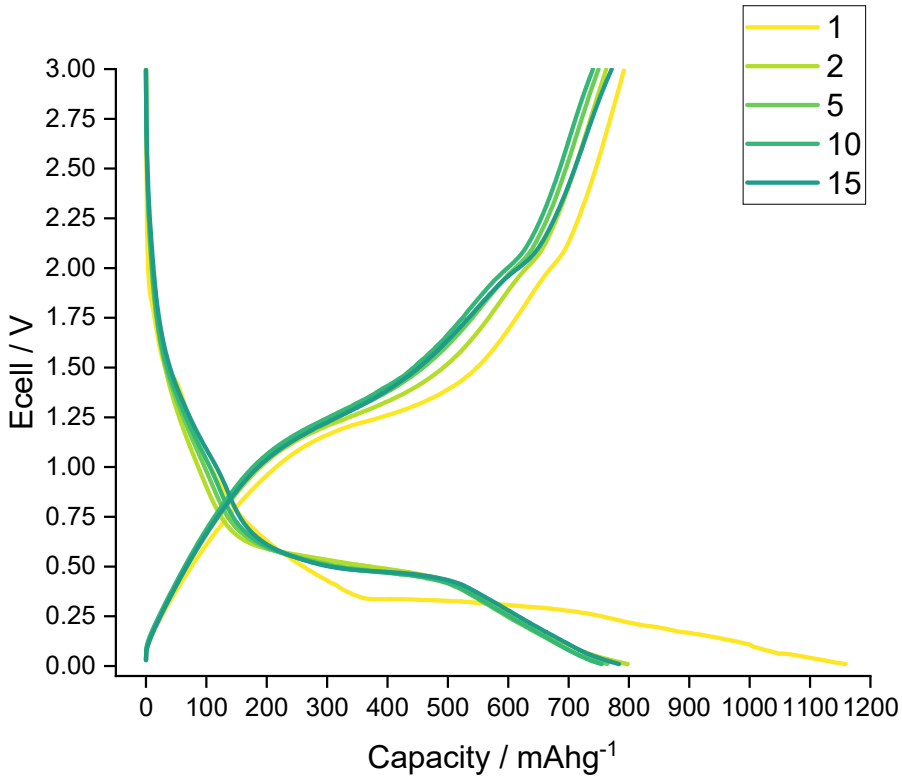


*Figure 5.28 Voltage-capacity curves for one of the QCR 600 °C / 4 hr $_{nano}$MnO—C composite half-cells*

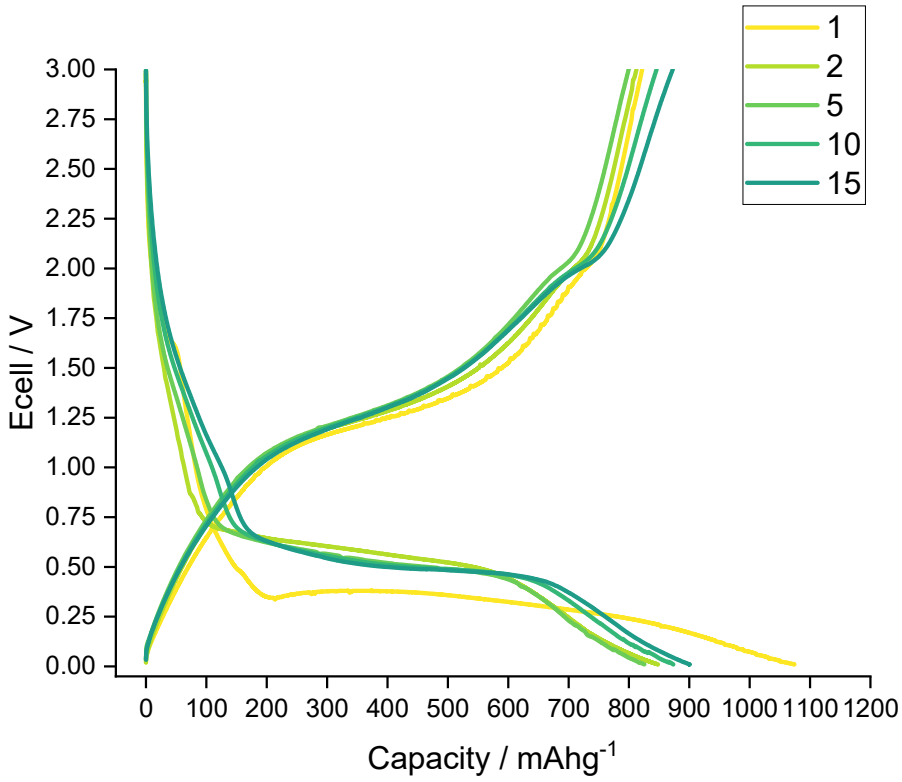


*Figure 5.30. Voltage-capacity curves for one of the EOL 600 °C / 4 hr $_{nano}$MnO—C composite half-cells*

The average first discharge/ charge capacities and coulombic efficiency of one of each of the half-cells are shown in table 5.8.

*Table 5.8. First discharge/charge capacities of each MnO sample with calculated coulombic efficiency.*

| Mn sample source | First discharge capacity ($mAhg^{-1}$) | First cycle irreversible capacity loss ($mAhg^{-1}$) | Coulombic efficiency (%) |
|---|---|---|---|
| **Pristine** | 1060 (±90) | 320 (±45) | 70 (±0.02) |
| **QCR** | 1145 (±14) | 362 (±5) | 68 (±0.0005) |

| | | | |
|---|---|---|---|
| **EOL** | 1101 (±37) | 256 (±9) | 77 (±0.01) |

It appears that the greatest first cycle capacity loss arises in the pristine sample, with negligible differences in coulombic efficiency being measured for the QCR and EOL samples. This is unexpected based on the differences in crystallite domain sizes and lattice parameters – it in fact suggests that contaminant ions observed in the leached samples may positively impact the first cycle coulombic efficiency observed in these samples. To understand the differences between the three half-cells further, their capacity fading behaviour was compared and displayed in Fig. 5.31. For the first discharge capacities of each sample the standard deviation error bar overlaps all renders the differences between them as statistically insignificant. In subsequent cycles, however, the capacity retention was the poorest for the pristine sample, followed by the QCR and finally the EOL sample. The average capacity for each sample after 15 cycles was 697 (±19), 777 (±12), and 916 (±37) $mAhg^{-1}$ which equates to 66 %, 68%, and 83 % of the original capacities exhibited for the pristine, QCR and EOL half-cells, respectively. In the pristine sample, the $_{nano}$MnO-C composites begin to increase in capacity after 8 cycles. For the QCR sample this fluctuates and for the EOL sample this capacity increase arises after 5 cycles. The retained capacity for the EOL half-cells is suggestive that the EOL sample had the highest degree of contamination, as hypothesised, which has significant impact in the first 15 cycles. The next stabilised material is the QCR sample, with an expected lower degree of contamination. The pristine and QCR samples have crystallite domain size and cell parameter values with no statistical difference, whereas for the EOL sample they differ. In all samples, the capacity increase was observed during

cycling, and was most evident for the EOL half-cells. As stated previously, it has been highlighted that one reason for the general increase in electrochemical capacity of MnO comes from extra oxidation of $Mn^{2+}$ ions during cycling. In a study investigating the capacity increase of MnO by H. Liu et al., it was highlighted that an increased oxidation of the divalent manganese in the structure is likely to impact structural stability because of the coordination number and ionic size changes of Mn in a higher oxidation state. In their experiments, they formed metal oxide – MnO composites to affect the oxidation of the Mn during cycling. There were many composites formed, two of which were Co, and Ni-MnO composites, which were two of the contaminant ions that were detected in the leached samples from the ICP-OES data identified in Appendix 10.6. In their study it was observed using EDS that the Ni and Co were dispersed in the form of $Co^0$ and $Ni^0$ metal amongst the nanoparticles. The electrochemical data for these composites shows a stable cycling behaviour out to 100 cycles since these elements inhibit oxidation of the divalent Mn. Additionally, it was deduced that these metals enhance the conductivity of the electrodes which leads to a greater capacity all while stabilising the system.[83] Though there is no evidence for the existence of the metallic contaminant phases in the XRD patterns of the $_{nano}$MnO─C composites in this Chapter the capacity trend and hypothesised degree of contamination for the leached samples aligns with the expected improvement observed for the electrochemical data of these samples.

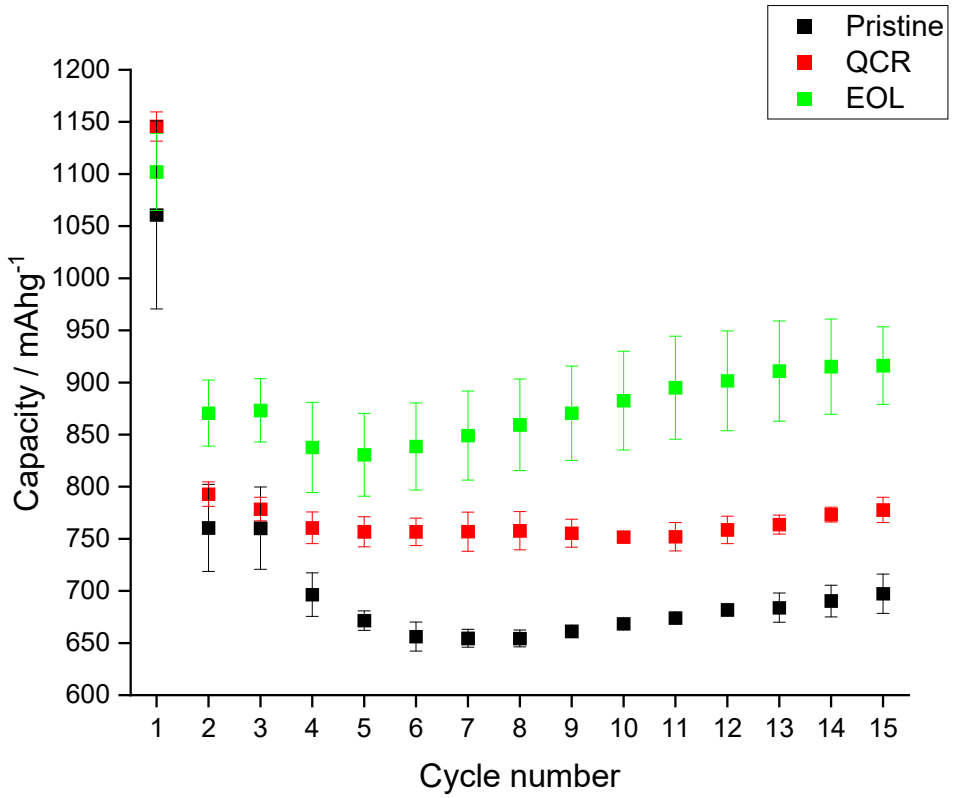


*Figure 5.31. Capacity versus cycle number plot comparing the capacity fade of pristine, QCR, and EOL 600 °C / 4 h $_{nano}$MnO—C composites*

As was calculated in section 5.5.1 the influence framework has influence on the capacity reached the voltage-capacity curves have been calculated as a function of voltage versus Li concentration. As the transfer of 2 $Li^+$ ions correspond to a theoretical capacity of 755 $mAhg^{-1}$, it is clear in all cases that this value is exceeded in the first discharge. For the pristine, QCR EOL half-cells the average Li concentration fell between 2.8 – 3.0 $Li^+$, as due to the overlap in standard error the differences between the samples were not statistically significant

It is expected that lithiation and delithiation is expected via transfer of 2 $Li^+$ ions during discharge/ charge. This value is only exceeded in the first 2 cycles for pristine half-cell. Only the EOL half-cell exceeds the theoretical Li uptake concentration value out to 15 cycles. Based on the previous findings that EOL sample has a higher degree of contamination, and as the EOL contaminants have been seen to affect the morphology of the Mn oxides synthesised in Chapter 3, it appears that contamination from the leaching process appears to enhance Li uptake within these half-cells. As is observed by the higher capacities reached at 15 cycles by the QCR and EOL materials.

To further understand the differences in the voltage curves and capacity fade and between the pristine, QCR and EOL nanocomposites, differential capacity analysis was used. Looking into differential capacity versus voltage phase transition behaviour enables redox activity to be distinguished that is less obvious in the plateaus in the complementary voltage-capacity data, and is useful to determine whether differences between the pristine, QCR and EOL samples could be attributed to redox/ capacitive processes.[191] One of each of the pristine, QCR and EOL nanocomposites were compared between cycles 1 and 15 and summarised in Table 5.9, and the differential capacity plots are shown in Figs. 5.32 – 5.34.

*Table 5.9 Differential capacity analysis comparisons for 600 °C / 4 hr MnO nanocomposites synthesised from pristine, QCR and EOL precursors*

| Cycle no. | Reaction | Pristine | QCR | EOL |
|---|---|---|---|---|

| | | | | |
|---|---|---|---|---|
| **C1** | **Discharge** | Peak at **0.38 V** shows conversion of MnO to metallic Mn. | Peak at **0.38 V** shows conversion of MnO to metallic Mn. | Peak at **0.38 V** shows conversion of MnO to metallic Mn. |
| | **Charge** | Two redox peaks between **0.8 and 2.15 V** | Two redox peaks between **0.8 and 2.15 V** | Two redox peaks between **0.8 and 2.15 V** |
| **C2** | **Discharge** | **0.55 V** conversion | **0.49 V** conversion | **0.55 V** conversion |
| | **Charge** | See C1 | See C1 | See C1 |
| **C5** | **Discharge** | **0.45 V** conversion (potential shoulder **at 0.6 V**) | **0.45 V** conversion | **0.45 V** conversion (potential shoulder **0.6 V**) |
| | **Charge** | See C1 | See C1 | See C1 |
| **C10** | **Discharge** | **0.45 V** conversion with potential shoulder **at 0.6 V** | **0.45 V** conversion | **0.48 V** conversion |
| | **Charge** | See C1 | See C1 | See C1 |
| **C15** | **Discharge** | **0.45 V** conversion with potential shoulder **at 0.6 V** | **0.45 V** conversion | **0.48 V** conversion |
| | **Charge** | See C1 | See C1 | See C1 |

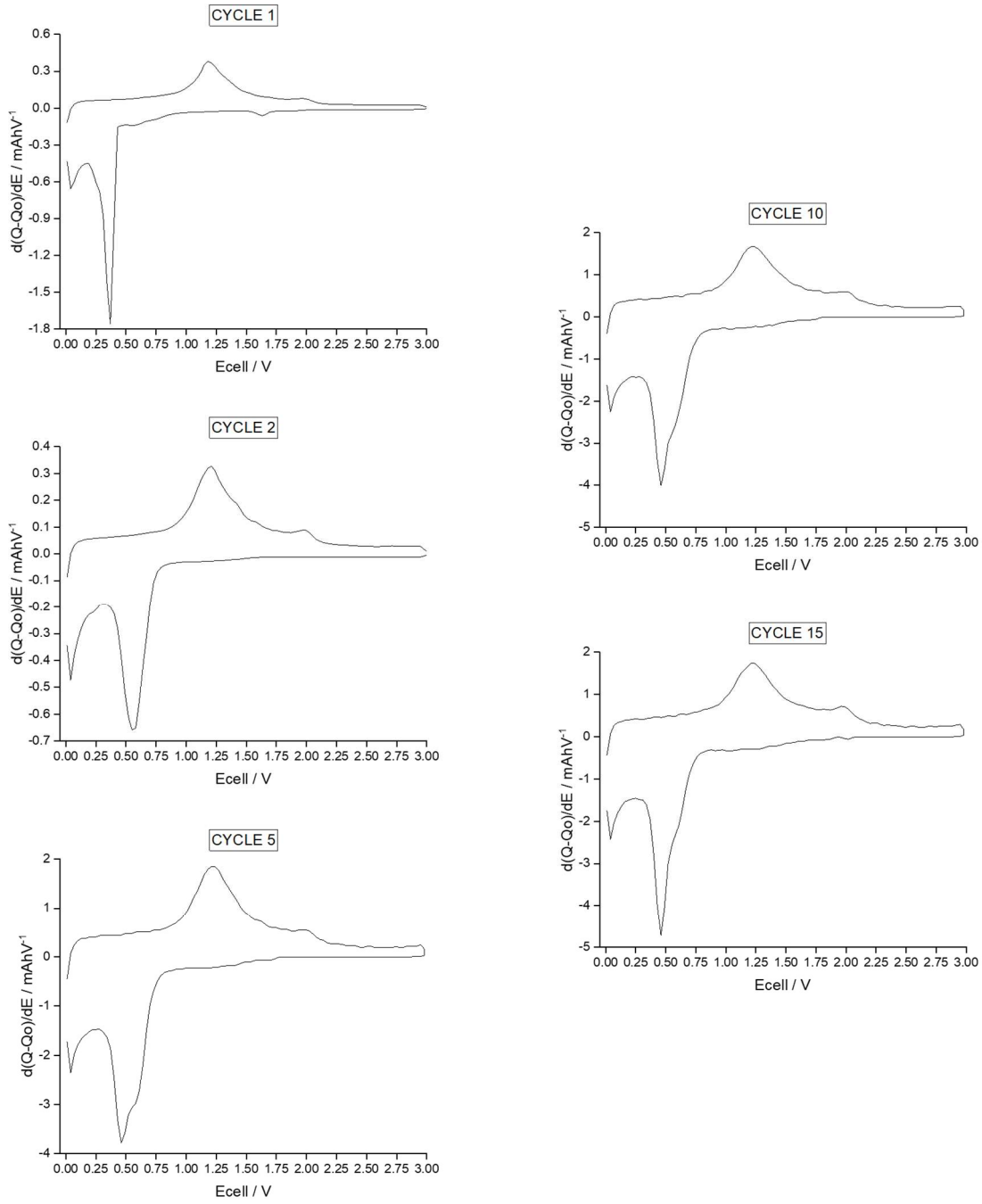


*Figure 5.32. Differential capacity plots for cycles 1 – 15 of the pristine 600 °C / 4 hr nanocomposite*

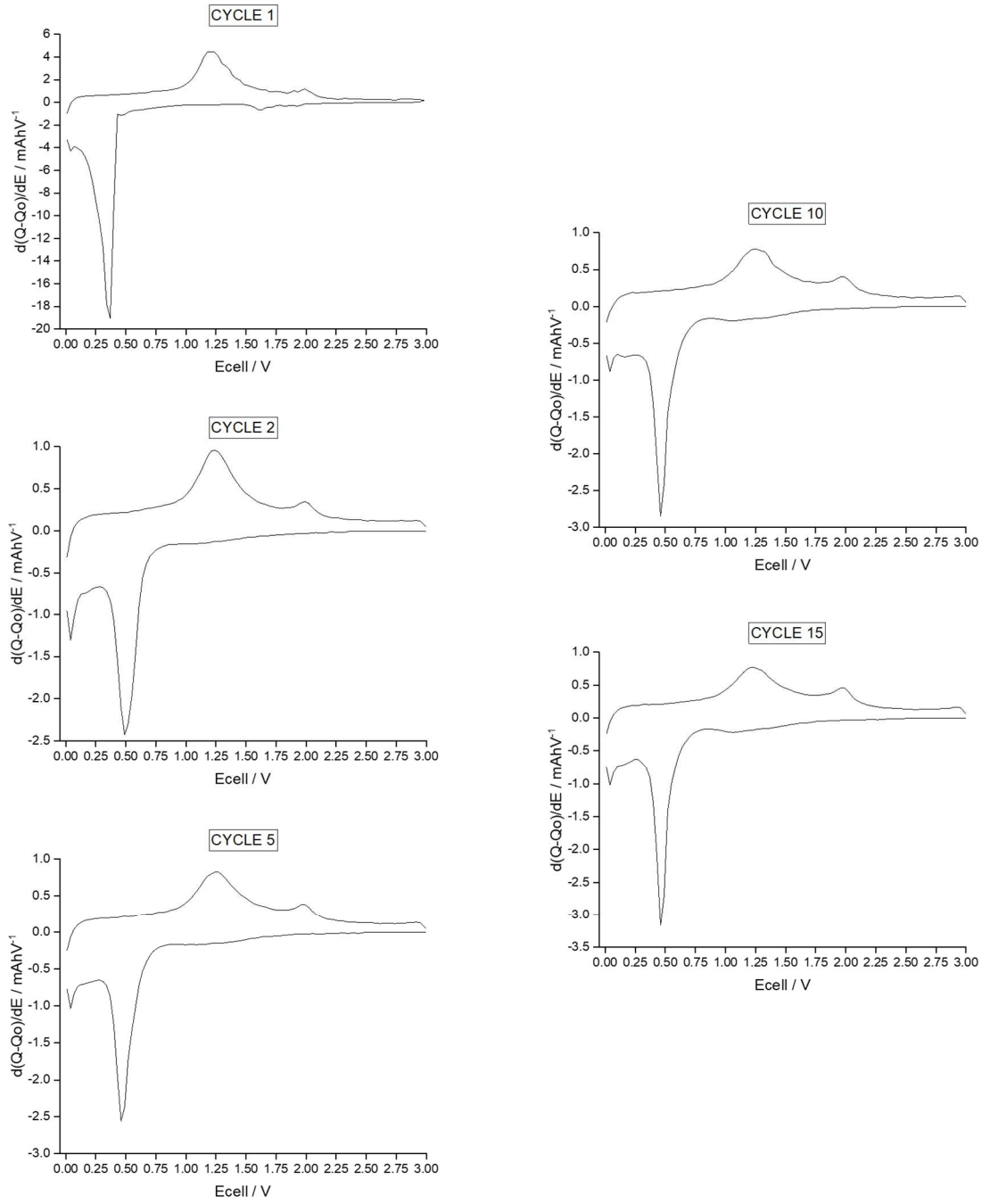


*Figure 5.33. Differential capacity plots for cycles 1 – 15 of the QCR 600 °C / 4 hr nanocomposite*

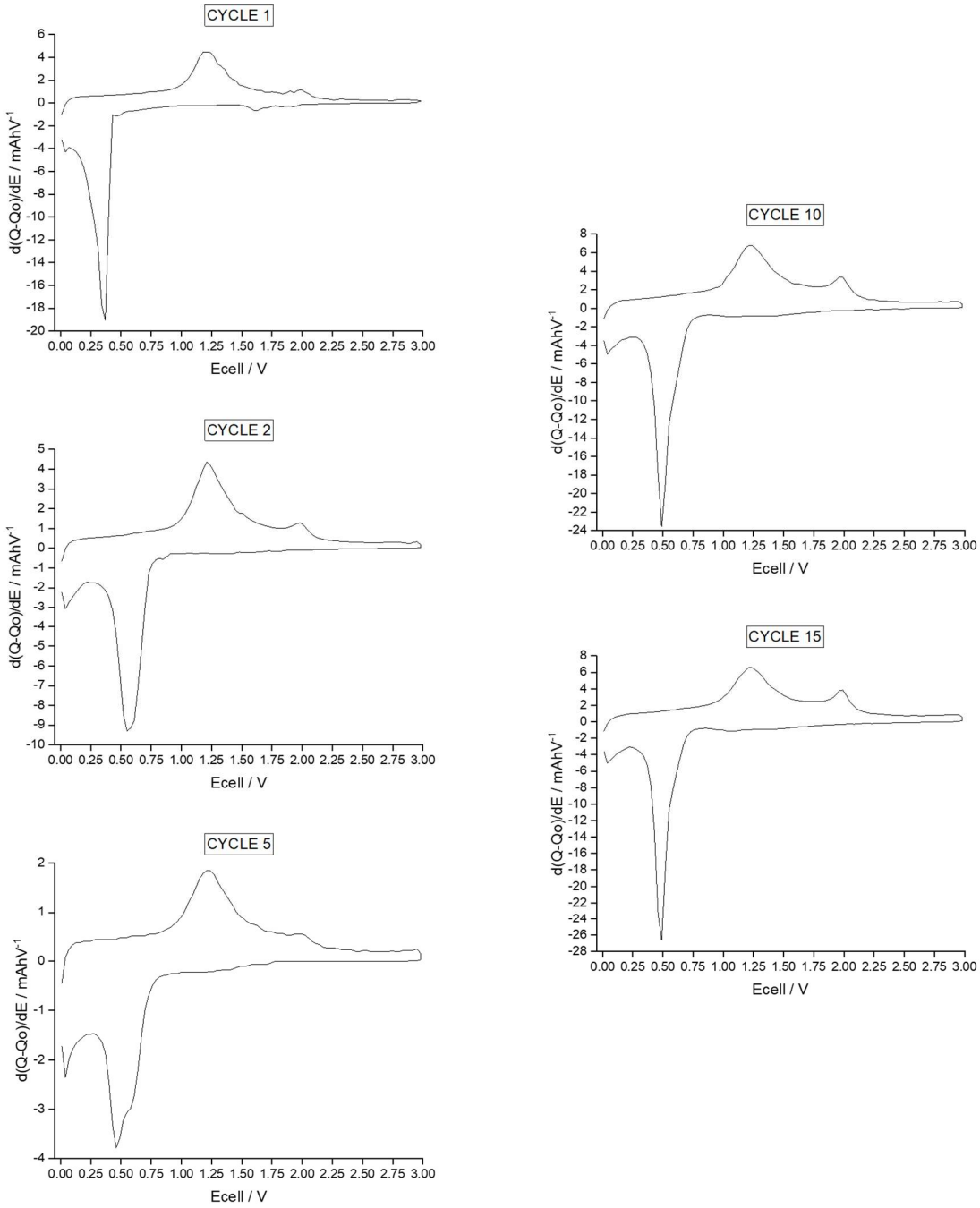


*Figure 5.34. Differential capacity plots for cycles 1 – 15 of the EOL 600 °C / 4 hr nanocomposite*

In all three $_{nano}$MnO─C half-cells, the redox activity in charge remains consistent between cycles 1- 15 across all cells, and in discharge there was a small amount of variability between the three half-cells. As was the case for the nanocomposites in the particle size experiments, in the charging process the first redox peak between 0.8 and 1.6 V remains the strongest peak and the peak between 1.6 and 2.2 V remains the least intense redox-active peak throughout, with the former peak corresponding to the $Mn^0 \rightarrow Mn^{2+}$ oxidation and the latter redox peak thought to correspond to redox activity from the carbonaceous matrix.

For all samples, the plateau in voltage corresponding to conversion initially occurs at 0.38 V, but then increases to 0.55 V for the pristine and EOL half-cells and 0.49 V for the QCR material on the second cycle. In cycle 5 this appears to reduce to 0.45 V in all cases, however the pristine and EOL conversion peaks appear to have a slight shouldering peak, as seen previously for the nanocomposites in section 3.4.2. at 0.6 V. By cycle 10, the shouldering peak at 0.6 V is only seen for the pristine sample, conversion peaks arise during discharge at 0.45 V for the pristine and QCR samples and at 0.48 V for the EOL one. The same trend is seen for the 15$^{th}$ cycle.

Focussing on the influence of Ni and Co contaminants in the nanocomposites, based on the expected influence of these metals H. Liu et al.'s metal─MnO composite study, it appears that the contaminants present in these leached samples do not impact the redox behaviour of Mn during oxidation in the half-cells, as the redox peaks during charge appear at the same voltage in all three samples.[83] These results suggest that any differences in capacity fading may not just be attributed to the redox behaviour of the samples, and another reason for the deviation may be due to the difference in crystallite domain size/ lattice parameters/ morphology of for the

samples, that were hypothesised to have been influenced by the degree of contamination, as observed for the Mn oxides generated in Chapter 4. Another reason for deviation in capacity fade between samples may be due to a capacitive process, such as the reversible formation of an activated polymeric gel. This activation and stabilisation of this polymeric gel may occur do a different degree depending on the nature of the anode active material causing a deviation in capacity fading behaviour between samples. [79,81,83]

## 5.6 Conclusions

The investigation outlined in this chapter has highlighted the upcycling opportunity for leached Mn-rich cathode material from first generation quality-control rejected and end-of-life pouch cells. The mechanochemical route for synthesis of these materials has proven to be a success as the simplistic ball milling step has demonstrated that complex solvothermal routes are not necessary to generate the desired MOF precursor, and moderate decomposition temperatures of 600°C/ 4hr provide the desired $_{nano}$MnO─C composite. With respect to the electrochemical behaviour of these materials, the synthesised $_{nano}$MnO─C composites provide anode materials with superior capacities compared to those reached for graphite, and superior capacity retention when compared to MnO material lacking in the carbon matrix. The average capacity for the pristine, QCR and EOL samples after 15 cycles was 697 (±19), 777 (±12), and 916 (±37) $mAhg^{-1}$ which equates to 66 %, 68%, and 83 % of the original capacities exhibited, respectively. This indicates that both the leached materials perform have enhanced capacity retention when compared to the pristine

case – with capacities exceeding that of the theoretical capacity for MnO (at 755 $mAhg^{-1}$) for both the leached samples after 15 cycles, particularly for the EOL materials. Furthermore, these nanocomposites exhibit electrochemical capacities that are more than double that of graphite (372 $mAhg^{-1}$) indicating that upcycling the redundant cathode materials into these $_{nano}$MnO─C conversion anodes provides an exciting opportunity to access high-capacity anode materials as alternatives to graphite in lithium-ion batteries.[73]

## 5.7 Future work

As the aim of this Chapter is to demonstrate how leached materials can be upcycled for novel anode applications, further electrochemical investigation into long-term capacity retention and comparison between the pristine and leached materials will be of great value. Testing the anode materials in a full cell setup would be of value to determine whether the capacity increase would be limited without the presence of excess lithium, as this has the potential to limit the capacitive formation of the polymeric gel during cycling. Furthermore, reducing the amount of energy required to generate the materials is preferable to emphasize this upcycling benefit. Developing a method for synthesis of the sacrificial Mn-MOF that requires less time ball milling time would be of interest to reduce the energy intensity of this synthesis. Quantification and detection of the contamination observed for these leached samples is also something of value to determine differences in electrochemical behaviour. Methods to determine this include EDX to see the distribution of contaminants across the surface and XAS to determine the oxidation state of the

metal cations involved in the nanocomposite structure, to give insights into how the contaminants are incorporated into the structure.

A more developed understanding into the carbon framework would be highly valuable, as this appears to contribute to the electrochemistry observed, based on the differences in differential capacity analysis observed between the Fisher MnO and the nanocomposites. The use of sacrificial MOF precursors provides a template for the decomposition product of the $_{nano}$MnO–C composites. As a result of this the nature of the carbon framework can be explored and manipulated, which is likely to have an impact on the composition of the product and the resulting electrochemical performance. Only terephthalic acid was explored as a MOF precursor material, whereas in the literature many acid precursors have been explored to manipulate the synthetic product – such as trimesic acid.[80] Generating an intermediate MOF product will enable understanding into how the carbon framework forms, which will then give insight into how the carbon framework impacts electrochemical performance, as it appears to contribute to the electrochemical performance of these materials.

Finally, to gain a better understanding into the formation of the $_{nano}$MnO–C composite, thermogravimetric analysis would be a good technique to probe the formation of this material over time. This has been explored by G. Nagaraju et al., where a Mn-based MOF was decomposed under nitrogen to observe the degradation products. Based on the terephthalic acid precursor used in the experiments within this chapter, it is expected that there would be weight losses due to removal of the aromatic organic components and from decomposition of the carbonaceous organic linkers into $CO_2$. The residual weight retention over a given temperature range would

also show the stability of the MnO nanocomposite, as was seen in Nagaraju et al.'s experiments – a 60% weight retention was seen up to 1000 °C.[81]

## 5.8 References (continued)


182 J. Hou, Y. Guo, Y. Zhang, J. Li, Y. Xu, Z. Fang, J. Yang and M. Wu, *Mater. Lett.*, 2022, **325**, 132761.

183 R. Das, P. Pachfule, R. Banerjee and P. Poddar, *Nanoscale*, 2012, **4**, 591–599.

184 G. Sylwia and B. Szcze, 2021, **46**, 109–124.

185 B. Karadeniz, A. J. Howarth, T. Stolar, T. Islamoglu, I. Dejanović, M. Tireli, M. C. Wasson, S.-Y. Moon, O. K. Farha, T. Friščić and Krunoslav Užarevi, *ACS Sustain. Chem. Eng.*, 2018, **6**, 15841–15849.

186 W. Liang, S. K. B. Ariff, W. Zhou, D. Jana, S. Z. F. Phua and Y. Zhao, *Asian Chem. Editor. Soc.*, 2020, **6**, 204–207.

187 N. Mironova-ulmane, A. Kuzmin, V. Skvortsova and G. Chikvaidze, *Acta Phys. Pol. A*, 2018, **133**, 1013–1016.

188 S. Radhakanth and R. Singhal, *Chem. Eng. Sci.*, 2023, **265**, 118224.

189 M. Faraji, Y. Yamini and N. Salehi, in *Magnetic Nanomaterials in Analytical Chemistry*, ed. T. M. Mazaher Ahmadi, Abbas Afkhami, Elsevier, 2021, pp. 49–50.

190 S. Wu, H. Liu, Z. Huang, H. Xu and W. Shen, *Appl. Catal. B Environ.*, 2022, **312**, 1–12.

191 Investigating battery aging using Differential Capacity Analysis (DCA), https://www.biologic.net/topics/investigating-battery-ageing-using-differential-

capacity-analysis-dca/#:~:text=Plotting the differential capacity dQ,degradation over long test cycles.

# 6 Extracting value from upcycled Mn-based material: studying Mn oxalate as a conversion anode for Li-ion battery applications

## 6.1 Table of Figures

## 6.2 Chapter introduction

In this Chapter, experimentation will focus on the electrochemical behaviour exhibited by Mn oxalate conversion anodes, and comparison will be made between three Mn oxalate samples which have been synthesised from pristine $LiMn_2O_4$ (LMO), and LMO that has been selectively leached from quality control rejected (QCR) and end-of-life (EOL) Nissan Leaf cathodes. Mn oxalate dihydrate characterisation comparisons were made in Chapter 4 using TGA-MS, ICP-OES, Raman, XRD, Rietveld refinement and SEM/EDX. Though literature studies have been used to explore the electrochemical behaviour of Mn oxalate conversion anodes, there have not been studies that manipulate the cycling voltage range to determine its effect on electrochemistry, nor have there been syntheses that use Mn precursors from recycled battery material. Furthermore, there is a lack of investigation into the in-situ structural changes that arise during the conversion reaction of Mn oxalate. The first aim of this Chapter is therefore to enhance fundamental understanding into the electrochemical behaviour of Mn oxalate anode through manipulation of galvanostatic cycling conditions, followed by structural insights of this material using in-situ pair distribution function analysis. The second aim is to determine whether the electrochemical performance for the leached material is comparable to that seen for the pristine material through comparisons between Mn oxalate generated from pristine LMO, and LMO from leached QCR and EOL battery scrap. These experiments will shed light on the electrochemical behaviour observed for these materials and indicate the success of upcycling of leached material into Mn oxalate for an anode application.

## 6.3 Methods

As outlined in section 4.3 of this thesis, reductive acidic leaching was used to reduce lithium manganese oxide spinel from the Nissan Leaf composite electrodes into solution. The cathode strip was shredded, and the current collector was removed so that $LiMn_2O_4$ (LMO) could be leached from the remaining active material using ascorbic acid. The leachate was then heated and ground to form LMO powder, the precursor for the interconversion reactions. To form Mn oxalate, LMO was added to a 1.25 M solution of oxalic acid in a precipitation reaction, the overview for this reaction scheme is displayed in Figure 6.1.

For the electrochemical analyses of these cells, the active material (AM) used was Mn oxalate (either pristine, QCR or EOL) which was combined with carbon black (CB) and sodium carboxymethylcellulose (CMC) in an 80:10:10 AM: CB: CMC ratio.

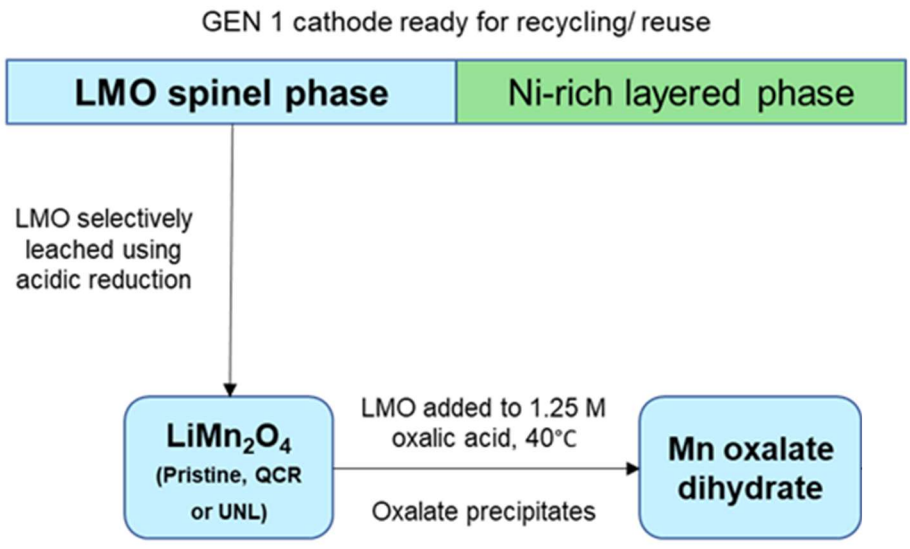


*Figure 6.1. Mn oxalate dihydrate synthetic scheme.*

This material was then cast onto copper foil and dried prior to Li-ion half-cell assembly in a vacuum oven. To samples were heated to remove the surface water within the Mn oxalate structure prior to assembly as guided by the dehydration temperature reported in the literature.[91,192] Half-cell manufacture is outlined in experimental section 3.5.1 of this thesis. For each Mn oxalate half-cell, voltage ranges and current rates were varied to understand the origin of any electrochemical behaviour. For in-situ experiments, the electrochemical data was collected at Diamond Lightsource on the I-15-1 dedicated XPDF beamline where three half-cells were assembled using the DRIX setup outlined in experimental section 3.3.3. The half-cells measured were a pristine Mn oxalate film, a film that had been cycled to 105 cycles in with a 2 V voltage limit (2 V max) and one that had been precycled to 105 cycles with a 3 V voltage limit (3 V max). As the DRIX cell required an active material anode layer that was at least 100 microns thick for detection in the x-ray beam, shown in Fig. 3.4. a free-standing electrode film (FSF) was synthesised. This meant that the active material film was cast without a copper foil current collector. To synthesise this film, an electrode slurry was mixed using sodium carboxymethyl cellulose binder (CMC), carbon black (CB) and the Mn oxalate active material (AM), as before, however the ratio of these materials within the slurry was 60: 20: 20 AM: CMC: CB to ensure the film had increased binder content to reduce its brittleness. This enhanced flexibility meant that the anode film could be synthesised without any copper foil support. To generate the FSF the slurry was cast onto a clean sheet of glass, that was transferred onto a hotplate in a fume hood to dry at 80 ° C for 2 hours. Further details on the precycling and assembly into the DRIX cell for these FSF half-cells are outlined in section 6.3.3.

## 6.4 Results and discussion

### 6.4.1 Voltage range investigations into Mn oxalate electrochemical behaviour using galvanostatic cycling and differential capacity analysis

Capacities much higher than the theoretical capacity have been reported for Mn oxalate in the literature, as stated in section 1.5.7, as well as an increase in capacity during cycling. Though some of the high capacity can be attributed to SEI formation in the first cycles, this does not rationalise the extensive capacity increase observed for these materials. In the past, the origin of this capacity increase has been assigned to the formation of a polymeric gel layer in early cycles that becomes activated in subsequent cycles. This being said, little investigation has been done into the conditions required to stimulate the capacity increase, as previous studies involving galvanostatic cycling of Mn oxalate half-cells are conducted with a voltage limit of 3 V.[72,91–94] Therefore, in this section, galvanostatic cycling comparisons are made between pristine Mn oxalate cycled up to a 2 V and 3 V cutoff, to determine whether this capacity increase is still observed in the reduced voltage range, providing deeper understanding into the conditions required for this capacity increase. Following on from this, differential capacity analysis is explored to measure the proportion of capacity coming from redox-active and capacitive contributions for these two systems over 100 cycles.

To compare the influence of voltage range on electrochemical behaviour, pristine Mn oxalate half-cells were synthesised. These half-cells were cycled using galvanostatic cycling with potential limitation, which is the standard technique used for electrochemical analysis of batteries. The selected voltage ranges were: 0.01 and 2

V and 0.05 and 3 V – now referred to as 2 V max and 3 V max, respectively. These cells were cycled in triplicate up to 100 cycles: with 30 $mAg^{-1}$ current applied for 4 formation cycles, followed by 150 $mAg^{-1}$ for subsequent cycles.

The voltage-capacity plots for one of each half-cell cycled up to 2 V and 3 V max for 1 to 100 cycles are shown in Fig. 6.2 and the first discharge capacities and coulombic efficiencies are depicted in Table 6.1. For both half-cells, displayed in Fig. 6.2, there was a rapid initial drop in voltage during the first discharge, corresponding to the decomposition of the electrolyte and subsequent formation of the solid electrolyte interphase, followed by a voltage plateau at around 0.55 V. The voltage plateau seen during first discharge corresponds to the forward conversion reaction of Mn oxalate whereby $Mn^{2+}$ is reduced to $Mn^{0}$ (shown in equation 4) and has been reported in the literature discussion outlined in section 1.5.7.[72,94] The voltage tail-off down to 0.01 and 0.05 V for 2 and 3 V max, respectively, has been reported to correspond to the formation of a gel layer on the surface of the anode, that gives the anode extra capacity and causes pseudo-capacitive behaviour.[72,92,94] In subsequent cycles for the 2 V max cell , this conversion plateau appears to decrease, whereas for the 3 V max cell this plateau remains in subsequent cycles, indicating that charging to the 3 V max voltage limit provides a reversible conversion product at the top of charge, that is not seen in the 2 V max cell. During charge in the first few cycles of the 2 V and 3 V max cells there is slope between 0.8 and 1.75 V. This is lost in subsequent cycles for the 2 V max cell but retained for the 3 V max cell. These coulombic efficiencies are extremely poor and have been assigned in the past to an irreversible to the formation of an amorphous product alongside the formation of the

SEI layer during this first discharge, which is a known flaw in conversion electrode materials.[72,92,94]

*Table 6.1 Average first discharge capacities and first cycle irreversible capacity loss of the 2 V and 3 V Mn oxalate half-cells with calculated coulombic efficiency.*

| **Voltage maximum** | **First discharge capacity ($mAhg^{-1}$)** | **First cycle irreversible capacity loss ($mAhg^{-1}$)** | **Coulombic efficiency (%)** |
|---|---|---|---|
| **2 V** | 1143 (±13) | 621 (±12) | 46 (±0.001) |
| **3 V** | 1037 (±53) | 536 (±42) | 48 (±0.01) |

The average first discharge capacity in both cases is much greater than the theoretical capacity of 375 $mAhg^{-1}$ for Mn oxalate, at 1143 (±13) $mAhg^{-1}$ for the 2 V max cell and 1037 (±53) $mAhg^{-1}$ for the 3 V max cell, which has been ascribed to the initial formation of an SEI layer, which causes the poor coulombic efficiency on the first charge, displayed in Table 6.1. These discharge capacities are of similar magnitude to those reported in studies prior, including those from Y. Yang et al. Y. Duan at al., Y. Jia et al., Y. Zhang et al., and Y. He et al. in section 1.5.7. [72,93,95,96] In all these studies, for the first cycle for each of these Mn oxalate half-cells, there was a huge first cycle irreversible capacity loss with first cycle coulombic efficiency as low as 29.4% in Y. Duan et al.'s study. This was hypothesised to be due a multitude of electrochemical characteristics, including the formation of $Li_2CO_4$ during discharge, radical volume changes from the active material pulverisation discharge during

cycling, and due to side reactions in this first cycle – namely the reaction of the electrolyte on the anode surface to form solid electrolyte interphase (SEI). To determine whether the Mn oxalate anode had formed an amorphous product in the first discharge, as hypothesised for pulverisation of conversion anode material, ex-situ XRD measurements were taken of three Mn oxalate half-cells that had been cycled versus Li / $Li^+$. The cells were disassembled in an Argon-filled glovebox and washed with DMC prior to drying under this inert atmosphere.

The three half-cells studied were as follows:

- An Mn oxalate half-cell that had been wetted for 16 hours but had not been cycled electrochemically.
- An Mn oxalate half-cell that had been discharged down to 0.01 V (after 16 hours wetting)
- An Mn oxalate half-cell that had completed one cycle to 3 V max (after 16 hours wetting).

The XRD results of this study are shown in Fig. 6.3. The products after the first discharge and after the first cycle are amorphous, supporting the notion that this crystalline-to-amorphous phase transition will have occurred during cycling contributing to the poor coulombic efficiency in the first cycle for the Mn oxalate anodes. Further structural insights of the conversion anode reaction during the first cycle are outlined in the PDF study in section 6.4.2, with the products of the conversion reaction being measured in-situ, further enhancing understanding of these materials.

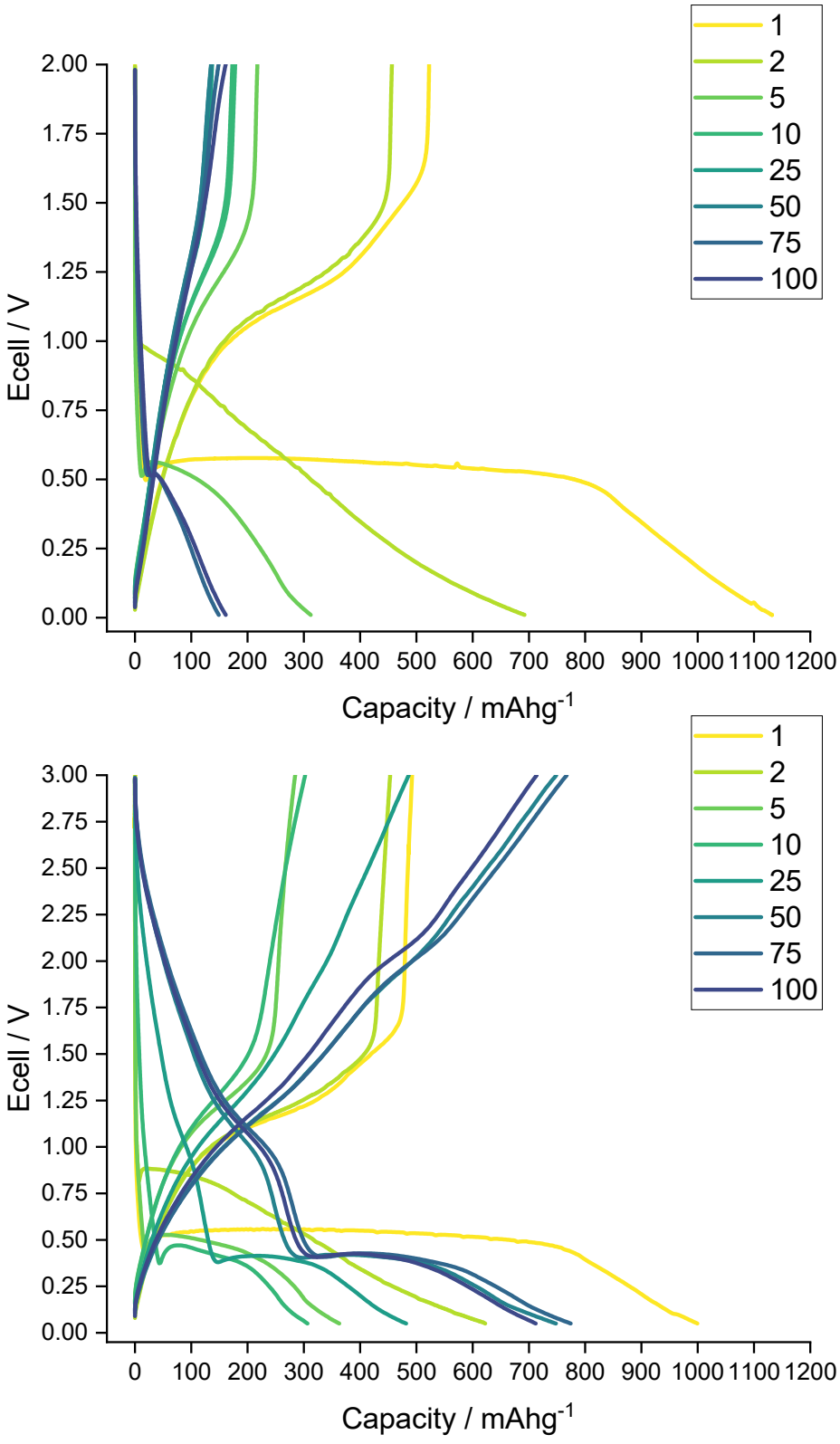


*Figure 6.2. Voltage-capacity curves showing the change in volage profile for pristine Mn oxalate between 1 – 100 cycles (2 V max: top, 3 V max: bottom)*

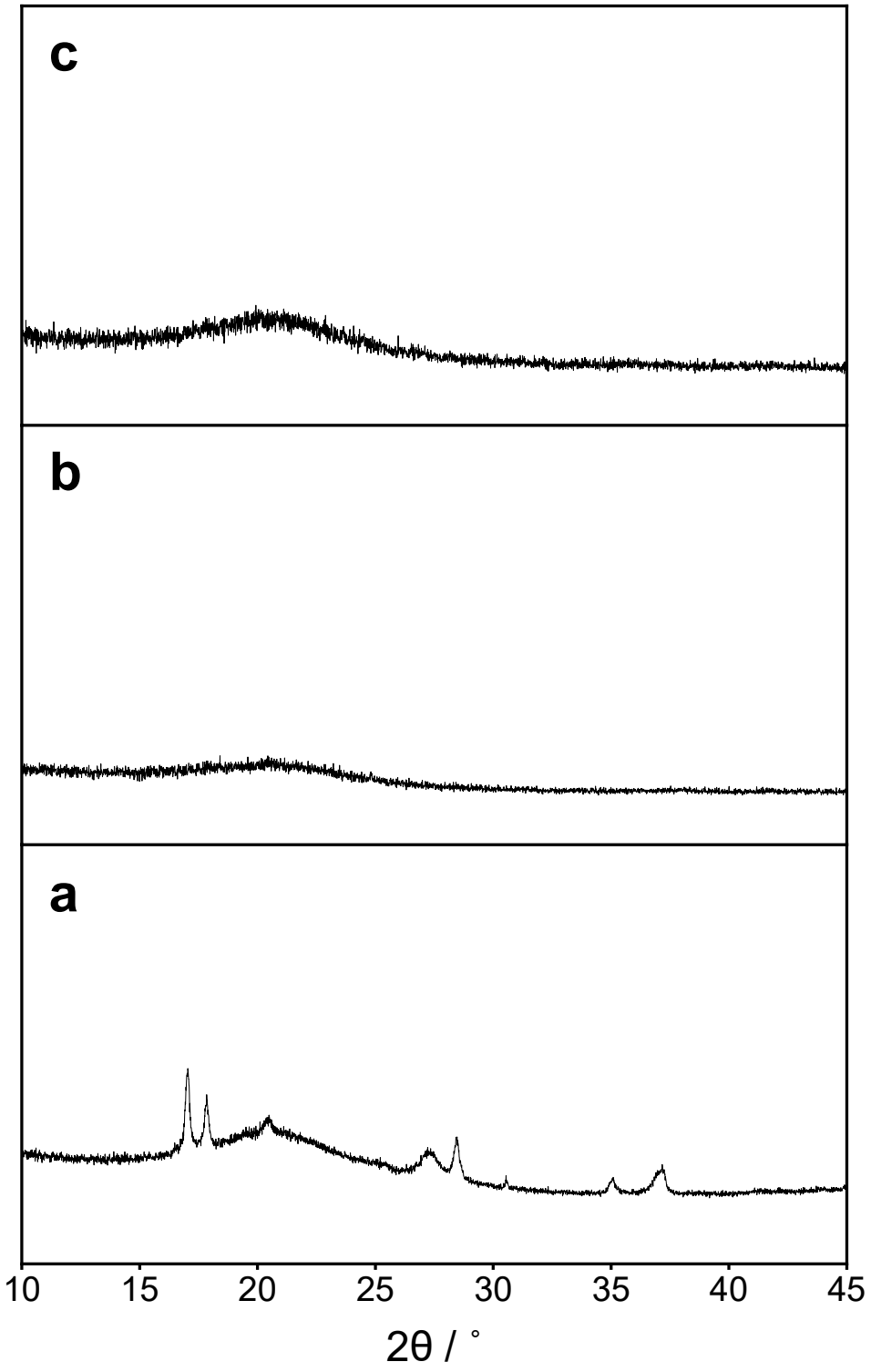


*Figure 6.3. Stacked XRD patterns showing 16 hour-wetted Mn oxalate anode (a), the anode after first discharge down to 0.01 V (b) and after one cycle (c).*

To see the effect on capacity of these materials cycled in different voltage ranges, the Mn oxalate half-cells were galvanostatically cycled in triplicate at each voltage limit, and the average capacity for each cycle was calculated and displayed in Fig. 6.4. There is a clear difference in capacity fading behaviour between these systems: the 2 V max cell has an extremely poor capacity retention compared to the 3 V case. Furthermore, the capacity does not continually decrease throughout cycling for each system but, in fact, begins to increase after a few cycles. In the case of the 2 V max cells, this arises after 40 cycles, and for the 3 V max cells this arises much sooner, after 10 cycles. By the $100^{th}$ cycle, the discharge capacity of the 2 V max cells averaged out at 160 $mAhg^{-1}$ (± 7 $mAhg^{-1}$) and for the 3 V max cells averaged out at 723 $mAhg^{-1}$ (± 8 $mAhg^{-1}$), at 14% and 70% of their first discharge capacity, respectively. This capacity recovery is remarkable, particularly as the capacity dropped as low as 133 $mAhg^{-1}$ (± 2 $mAhg^{-1}$) for the 2 V max cells and 308 $mAhg^{-1}$ (± 3 $mAhg^{-1}$) for the 3 V max cells. This gradual increase incapacity has been observed in the literature by an array of experimentalists, and they put this down to the irreversible formation of the polymeric gel film that grows within the first few cycles. This film has been hypothesised to grow and thicken in initial cycles – which causes a decrease in capacity in initial stages due to this side reaction product impeding lithium ion diffusion which inhibits the conversion reaction in the active material - however after several cycles this film becomes activated and its formation becomes reversible, which increases the resultant discharge capacity.[72,92,94] To gain more understanding into the difference in capacitive and faradaic contribution to the 2 V and 3 V max half-cell capacity behaviour, differential capacity analysis was used.

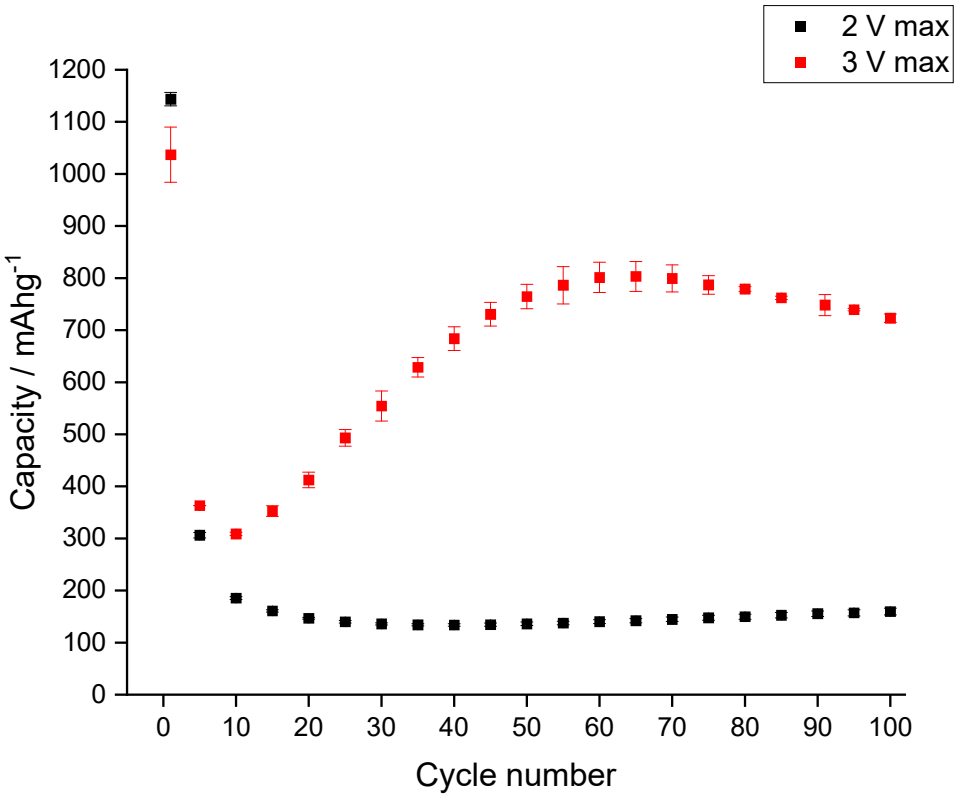


*Figure 6.4.Capacity versus cycle number plots for the 2 V max and 3 V max cells, with error bars marked on the average capacities observed across cells for in each case.*

The first discharge capacity exhibited by both cells exceeded the theoretical capacity of Mn oxalate. This, and the significant difference in electrochemical behaviour between cells cycled at 2 V and 3 V max, motivated extra investigation into the origin of these phenomena. By calculating differential capacity versus voltage phase transition behaviour that is less obvious in the plateaus in the complementary voltage-capacity curve – occurrences may be resolved using this technique, including a loss of Li inventory, electrolytic side reactions, crystal structure reordering, amongst others.[191] As differential capacity plots give rise to peaks at particular voltages corresponding to redox activity it is easy to observe when a system is cycling through

a Faradaic (redox) or a non-Faradaic (capacitive) process. Pseudo capacitance occurs in the absence of Faradaic behaviour can be observed in differential capacity plots as a square plot with no peaks that can be ascribed to redox behaviour.[193] Differential capacity plots are summarised in Table 6.2. and shown in Figs. 6.5 and 6.6 for the 1st, 2nd, 5th, 25, 50th, 75th and 100th cycle of one of each of the 2 V and 3 V max cells.

*Table 6.2. Differential capacity analysis comparisons for pristine Mn oxalate half cells cycled up to 2 V and 3 V max between 1 and 100 cycles.*

| Cycle no. | Reaction | 2 V max half-cell | 3 V max half-cell |
|---|---|---|---|
| **C1** | **Discharge** | Peak at **0.55 V** shows conversion of Mn ox to metallic Mn. | Peak at **0.55 V** shows conversion of Mn ox to metallic Mn. |
| | **Charge** | Two redox peaks between **0.80 and 1.75 V** | Two redox peaks between **0.80 and 1.75 V** |
| **C2** | **Discharge** | **0.90 V** conversion | **0.80 V** conversion |
| | **Charge** | See C1 | See C1 |
| **C5** | **Discharge** | **0.55 V** conversion | **0.50 V** conversion |
| | **Charge** | No redox activity observed | One redox peak between **1.0 and 1.4 V** |
| **C10** | **Discharge** | **0.55 V** conversion | **0.45 V** conversion |

| | | | |
|---|---|---|---|
| | **Charge** | See C5 | See C5 |
| **C25** | **Discharge** | **0.52 V** conversion | **0.40 V** conversion |
| | **Charge** | See C5 | See C5 |
| **C50** | **Discharge** | **0.52 V** conversion | **0.40 V** conversion |
| | **Charge** | See C5 | Two redox peaks between **0.75 and 2.25 V** |
| **C75** | **Discharge** | **0.50 V** conversion | **0.40 V** conversion |
| | **Charge** | See C5 | See C50 |
| **C100** | **Discharge** | **0.50 V** conversion | **0.40 V** conversion |
| | **Charge** | See C5 | See C50 |

In the first cycle, there is a sharp peak at approximately 0.55 V for both the 2 V and 3 V max cells which has been assigned to the conversion reaction of Mn oxalate in the first discharge (the forward reaction in equation 4), as seen in the voltage-capacity curves as the plateau at this voltage. In the charging of the first cycle of each half-cell, in both cases, there are two peaks corresponding to redox activity between 0.80 and 1.75 V. These are thought to correspond to the oxidation of the metallic manganese back into its divalent state. In the second cycle, the conversion peak is observed at approximately 0.90 and 0.80 V in the 2 V and 3 V max cells, respectively. This increased potential is unsurprising based on the pulverisation of the crystalline material which gives a higher surface area: volume ratio, meaning more Li is required to react in the second cycle. After these initial cycles the electrochemical behaviour appears to deviate between the 2 V and 3 V max cells. On cycle 5, the 2 V max cell loses a significant amount the redox capacity during (the capacity around ~ 0.55 V is

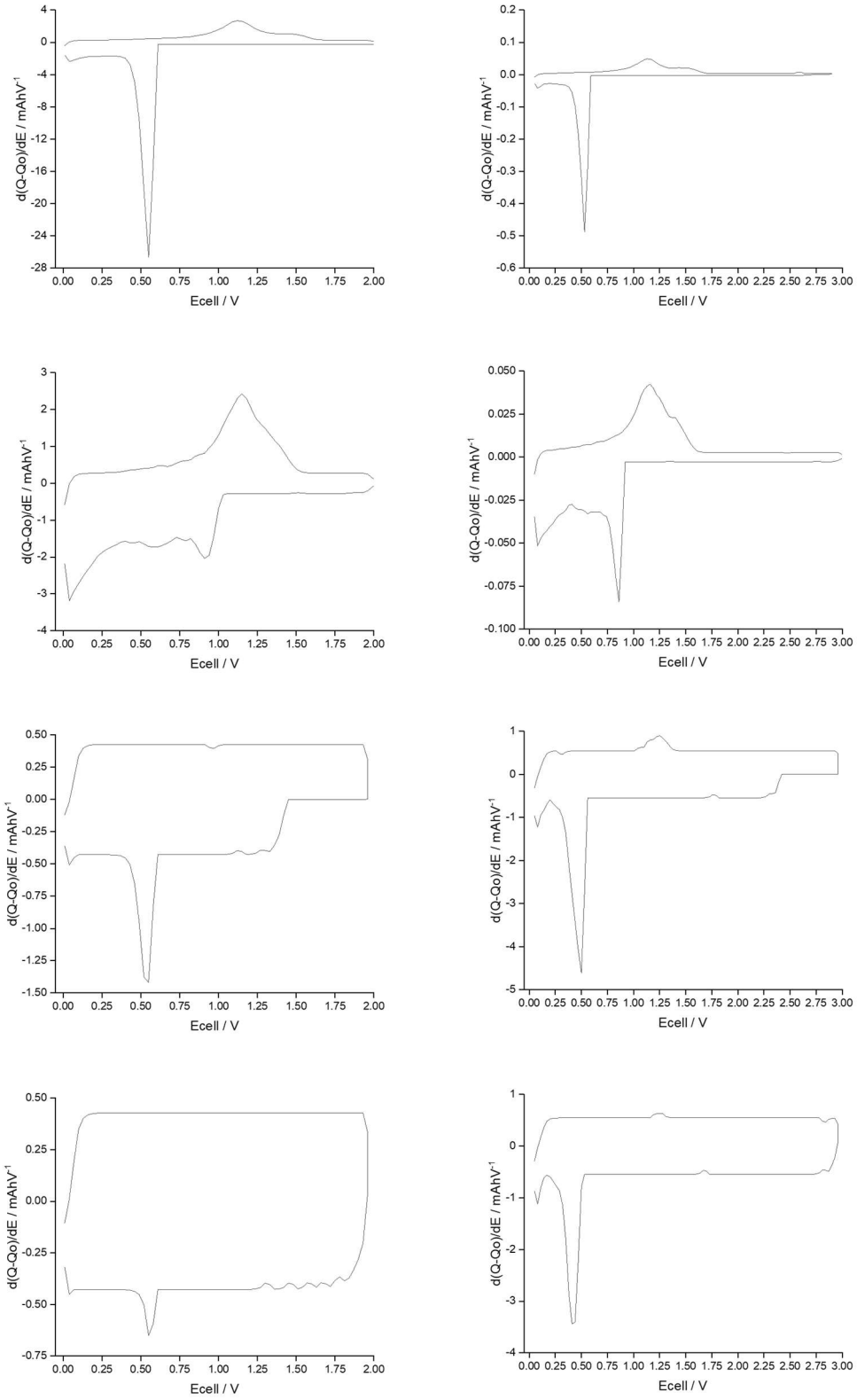


*Figure 6.5. Differential capacity plots showing the difference in redox activity between 2 V max (LHS) and 3 V max (RHS) Mn oxalate half-cells, with the 1st 2nd 5th and 10th cycles compared (top to bottom).*

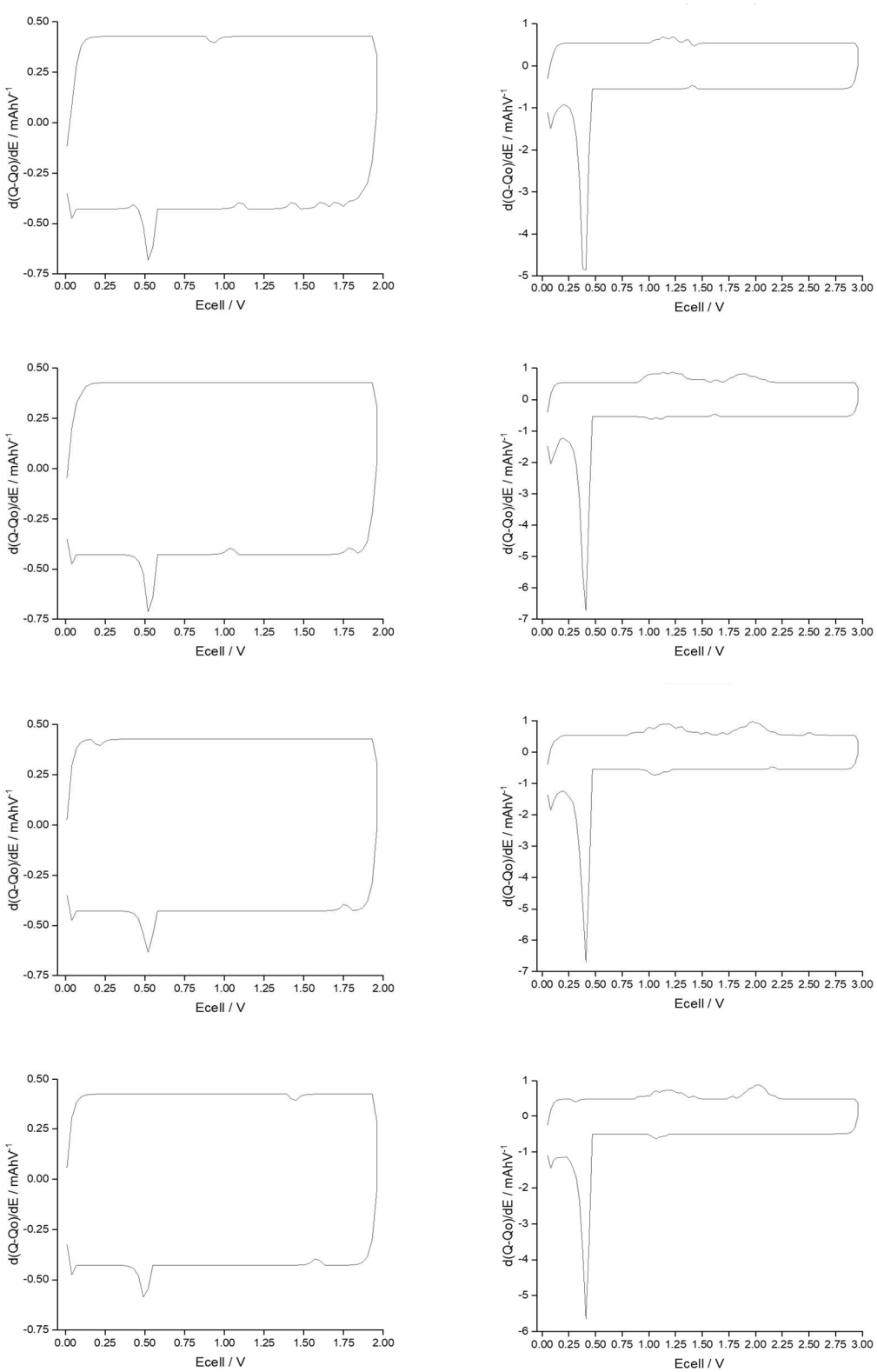


*Figure 6.6 Differential capacity plots showing the difference in redox activity between 2 V max (LHS) and 3 V max (RHS) Mn oxalate half-cells, with the 25th, 50th, 75th and 100th cycles compared (top to bottom).*

very small) whereas for the 3V max cell, not only does the capacity around 0.50 V remain significant, but the Mn redox appears to remain during charge where it is absent for the 2 V max cell. For the 2 V max cell in cycles 10, 25, 50, 75 and 100 this continues, and the square-shaped plots indicate the lack of redox-active behaviour in these systems. With respect to the observed capacity increase in the 2 V system after 40 cycles, the formation of a polymeric gel-like layer is likely to be the reasoning for this increase based on the differential capacity data. This gel layer will give rise to pseudocapacitive electrochemical activity, giving rise to no redox peaks in the differential capacity plot between cycles 5 and 100.[94] For cycle 5 in the 3 V max cell, only one redox peak is observed between 1.0 and 1.4 V in the charging process, which remains the same in cycles 10 and 25. By cycle 50, there are 2 redox peaks between 0.75 and 2.25 V, indicating that cycling past 2 V ensures more redox activity is accessed in the Mn oxalate cells. Considering the lack of redox activity in the 2 V half-cell compared to the 3 V half-cell after the second cycle, this could infer that there is a difference in local structure of the materials give rise to the enhanced 3 V max half-cell's redox activity, which will be investigated further using in-situ pair distribution function analysis section 6.4.2.

To quantify the difference in faradaic and capacitive contributions to the total capacity of these cells, the discharge and charge capacities were plotted as a function of their capacitive and redox contributions for one cell of each of the 2 V and 3 V max cycled cells illustrated in Fig. 6.7 (the marked voltage-capacity curves that were used to determine this qualitatively are shown in Appendices 10.7 and 10.8). From this data, the redox activity exhibited in the 3 V cells is much higher in both charge and discharge out to 100 cycles than for the 2 V cells. Furthermore, the redox capacity

was more prevalent for the discharge in both cells, whereas in the charge the capacitive behaviour was higher for the 2 V max voltage, but it fluctuated in the 3 V half-cell. Past 50 cycles, the redox behaviour dominated for the 3 V cell. The significant redox behaviour difference observed during charge for the 3 V cell compared to the 2 V cell may be due to the difference in structure for the half-cells – the 3 V cell appears to have a structure that contributes to redox activity whereas the 2 V cell appears to mainly have capacitive cycling out to 100 cycles – to further probe the anode products generated during cycling pair distribution function analysis (PDF) was used, outlined in section 4.3.3. Understanding whether there is any difference in conversion products of this material is an essential step in further understanding the electrochemical data deviations.

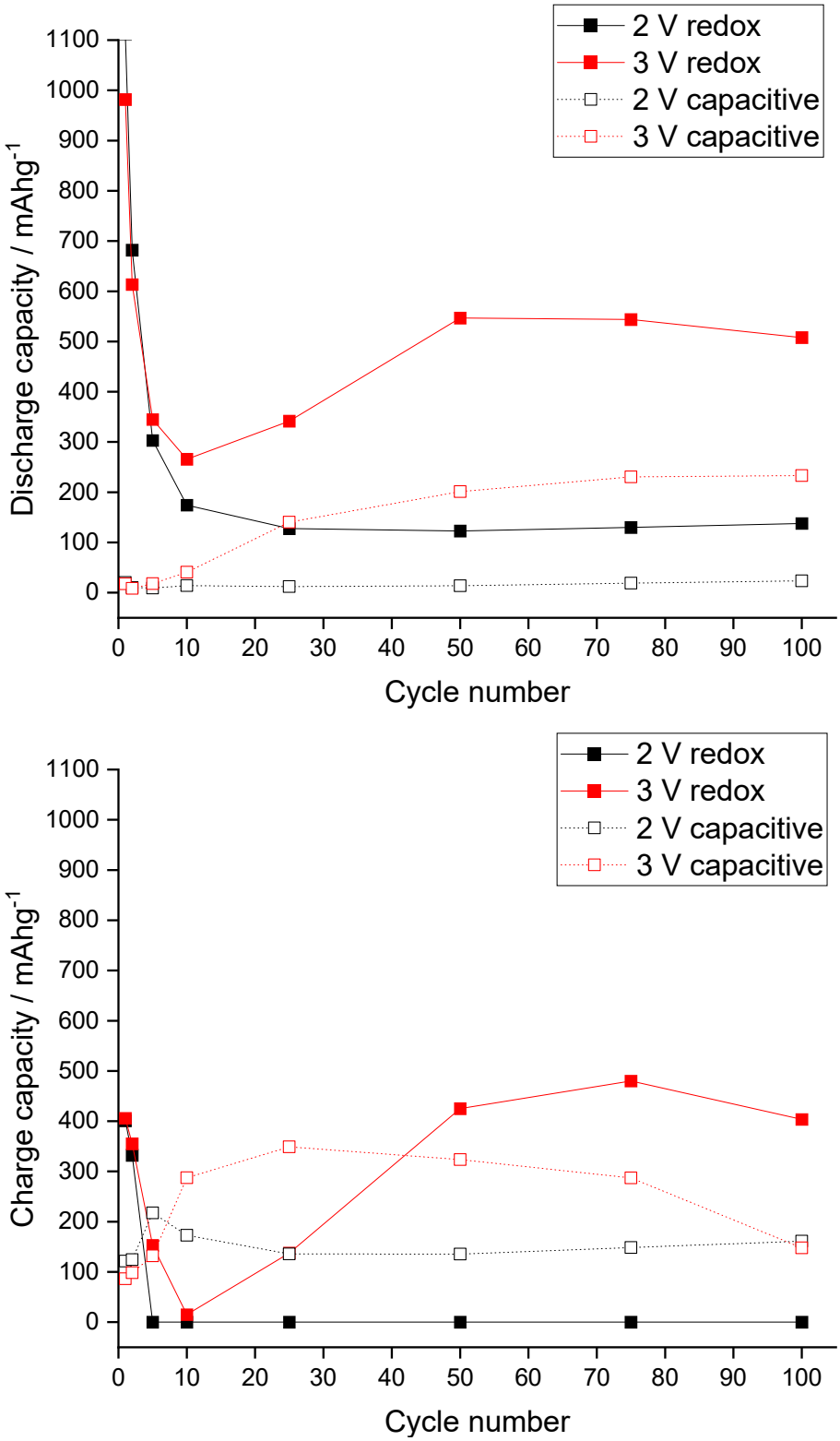


*Figure 6.7. Discharge (top) and charge (bottom) capacity versus cycle number plots showing the difference in capacitive and faradic contribution to the capacity for the 2 V and 3 V max half-cells.*

### 6.4.2 In-situ investigations into Mn oxalate electrochemical behaviour using pair distribution function (PDF) analysis

As stated in experimental section 3.4, pair distribution function (PDF) analysis enables users to study localised order within materials. This technique is necessary in this study as the conversion anode product after discharge is amorphous and does not give rise to sharp XRD peaks due to a lack of long-range order in the material. Not only has PDF been used to study these conversion anode products on an atomic scale, but the experiments were run in-situ, meaning that the electrochemical system could be studied in a contained environment and the conversion products were studied as they were generated. Though the conversion reaction of Mn oxalate has been explored extensively in the literature, the observation of the conversion reaction products using in-situ PDF has not been explored, presenting an opportunity for local structural determination within these materials.

As stated in the methods section in 6.3, the electrochemical data was collected at Diamond Lightsource on the I-15-1 dedicated XPDF beamline where three half-cells were assembled using the DRIX setup outlined in experimental section 3.3.3. The free-standing films were prepared as outlined in section 6.3. For the precycled material, 14 mm diameter discs of the FSF were then cut and transferred into an inert atmosphere glovebox for subsequent coin cell assembly in C2032-type coin cells, as outlined in experimental section 3.5.1. The cells were then cycled at 30 $mAg^{-1}$ for 4 formation cycles, followed by a 150 $mAg^{-1}$ current density for subsequent cycles. The capacity versus cycle number data for the precycled samples is shown in Fig. 6.8.

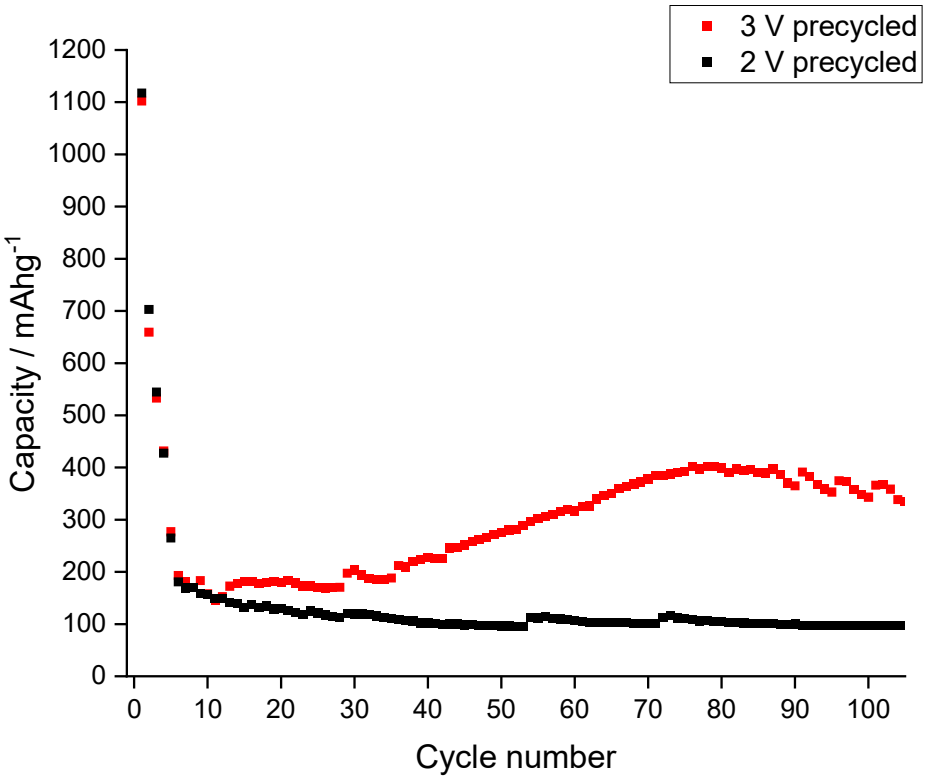


*Figure 6.8. Capacity versus cycle number plot for the 2 V and 3 V max free-standing film half-cells.*

As observed in Fig. 6.8, the capacity retention for the 2 V and 3 V max FSF half-cells was inferior to the 2 and 3 V max half-cells shown in Fig. 6.4, which is due to the absence of the copper current collector in the setup and the increased thickness of the anode film. The current collector not only supports the coating but enhances the electrical conductivity between the electrode and external circuits, and its absence here highlights the benefit of its presence.[194] Despite its less desirable capacity, the capacitive recovery for the 3 V FSF half-cell is superior to the 2 V case, meaning its analysis in a synchrotron x-ray beam will give information into the conversion product after the polymeric gel has formed. To extract the FSF post-cycling, the half-cells were disassembled in an Argon-filled glovebox, washed with dimethyl carbonate

(DMC, 99%) and dried within the glovebox. These films were then vacuum sealed in containers to be transported over to Diamond Light Source, where they were then placed directly into an inert Argon-filled glovebox prior to DRIX cell assembly. In the DRIX assembly, the cell was manufactured using a Li counter electrode, glass microfibre separators, and the free-standing Mn oxalate film that had been pre-cycled in the CR2032 half-cells. The composition/ concentration of the electrolyte used was (1.0 M LiPF6 EC:DEC = 50:50). The electrodes were stacked within a quartz capillary that had been stacked and compressed between two current collector rods which, in these experiments, were composed of stainless steel. The pristine Mn oxalate material half-cell was assembled using a FSF that had not been cycled, which had been dried in a vacuum oven prior to DRIX cell assembly. The pristine DRIX half-cell was cycled at 60 $mAg^{-1}$ for 1 cycle, whereas the 2 V and 3 V precycled half-cells were cycled at 45 and 30 $mAg^{-1}$, respectively. The precycled cells were both supposed to be cycled at 30 $mAg^{-1}$ to ensure as many PDF data points were measured as possible, as they take less time to reach their full capacity than the pristine cell in its first cycle. The reason the precycled cells were not both collected at 30 $mAg^{-1}$ was due to time constraints during beamtime experiments, meaning the current density used to cycle the 2 V precycled cell was increased to collect as many data points as possible in the given time. The PDF data points were collected approximately every hour.

The voltage-capacity data for a pristine sample cycled between 0.05 and 3 V is shown in Fig. 6.9 and the in-situ PDF measurements are marked on in colours corresponding to the PDF plot shown in Figs 6.10 and 6.12. The voltage was held at

3 V at the end of the first cycle to ensure the final data point was measured at the correct voltage.

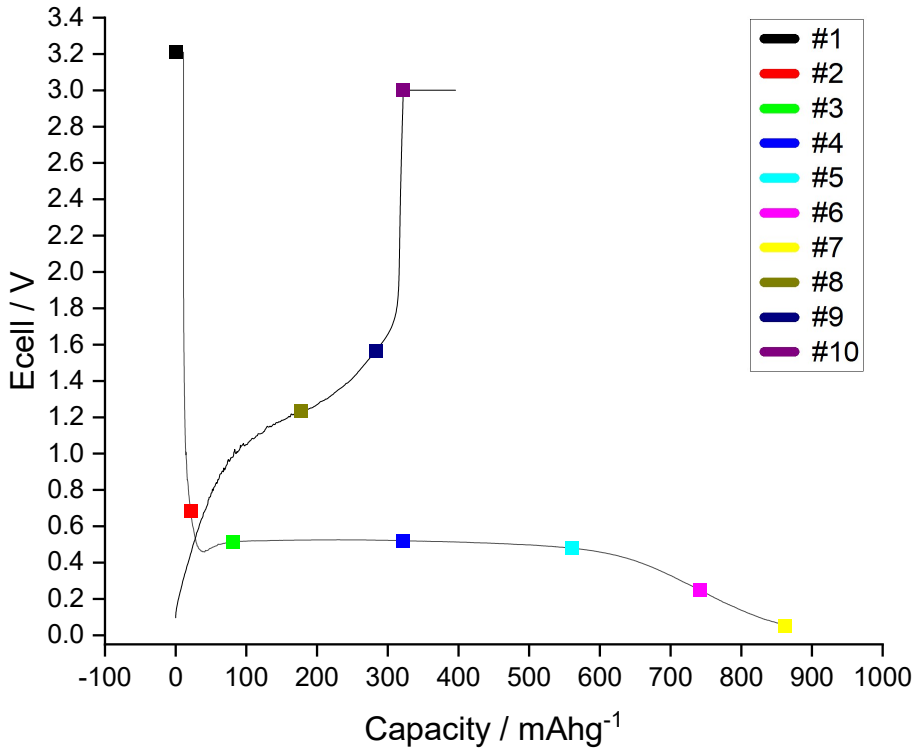


*Figure 6.9. Voltage-capacity data shown for the pristine sample cycled between 0.05 and 3 V at a current density of 60 $mAg^{-1}$ with data points marked during cycling for the PDF data collection.*

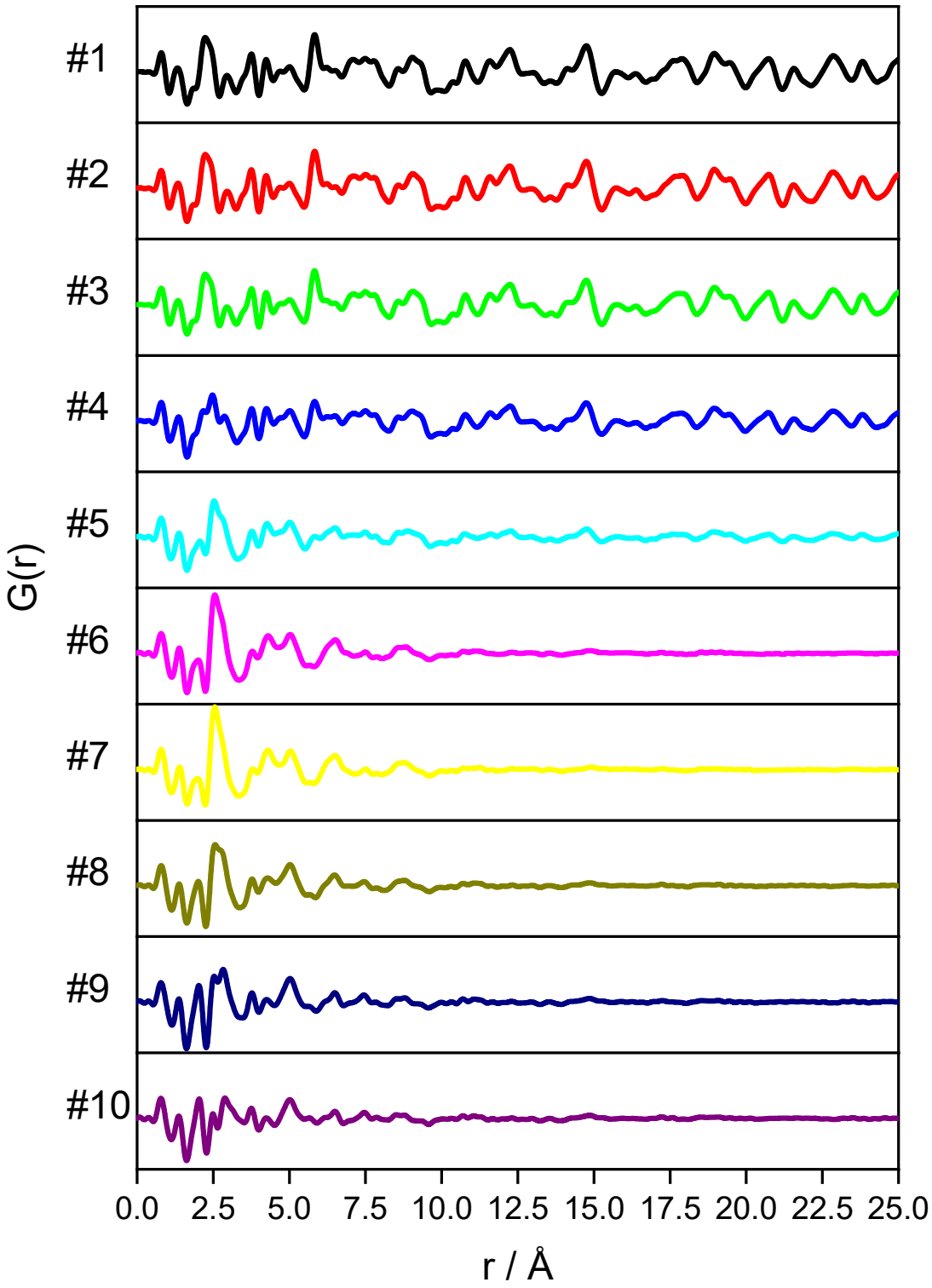


*Figure 6.10. In-situ pair distribution function data between 0 and 25 angstroms, showing the localised structural changes of the pristine sample cycled between 0.05 and 3 V at a current density of 60 $mAg^{-1}$. The colours correspond to the data points marked during cycling in Fig. 6.9.*

The first clear observation in the PDF data is the pulverisation of the active material during discharge in accordance with the ex-situ XRD data depicted in Fig. 6.3. Looking at the first PDF collected before cycling (PDF #1, in black) and moving through between data points to the end of discharge, marked in yellow (PDF #7), and onwards to the top of charge, marked in purple (PDF # 10) there are no distinguishable bond distances observed past 10 angstroms by the end of discharge, and past this point, indicating that the material pulverises to a nanomaterial as small as 1 nanometre. This indicates that the amorphous products after the first discharge and the first cycle support the notion that this crystalline-to-amorphous phase transition arises during cycling, contributing to the poor coulombic efficiency in the first cycle for the Mn oxalate anodes. This also aligns with the increased voltage required for on the second discharge for both the 2 V and 3 V half-cells in section 6.4.1.

The first PDF plots, depicted in black, red, and green, are overlaid in Fig. 6.11. The original crystalline structure remains intact during this portion of discharge, which is expected, since this is from preliminary discharging whereby the electrolyte decomposes, and subsequent formation of the solid electrolyte interphase occurs which will not initiate pulverisation of the crystalline electrode material. To determine the expected initial structure of the Mn oxalate within the half-cell, pristine Mn oxalate powder was heated to generate the dehydrated product, as was done prior to half-cell assembly. This dried Mn oxalate was then analysed using XRD, and the collected XRD pattern was used to calculate the structural details via Rietveld refinement. Based on the result, the dehydrated structure was defined as an orthorhombic Mn oxalate structure with space group Pmna, displayed in Fig. 6.12.

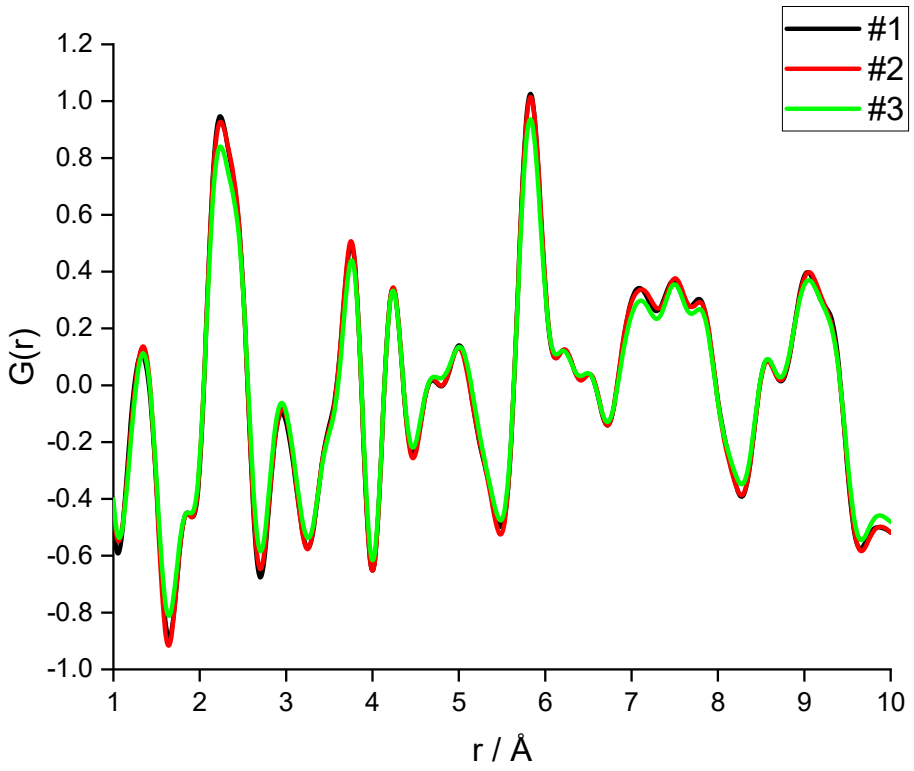


*Figure 6.11. . In-situ pair distribution function data between 1 and 10 angstroms, showing the localised structural changes of the pristine sample between PDFs #1 through to #3 at the beginning of the first discharge. The colours correspond to the data points marked during cycling in Fig. 6.10.*

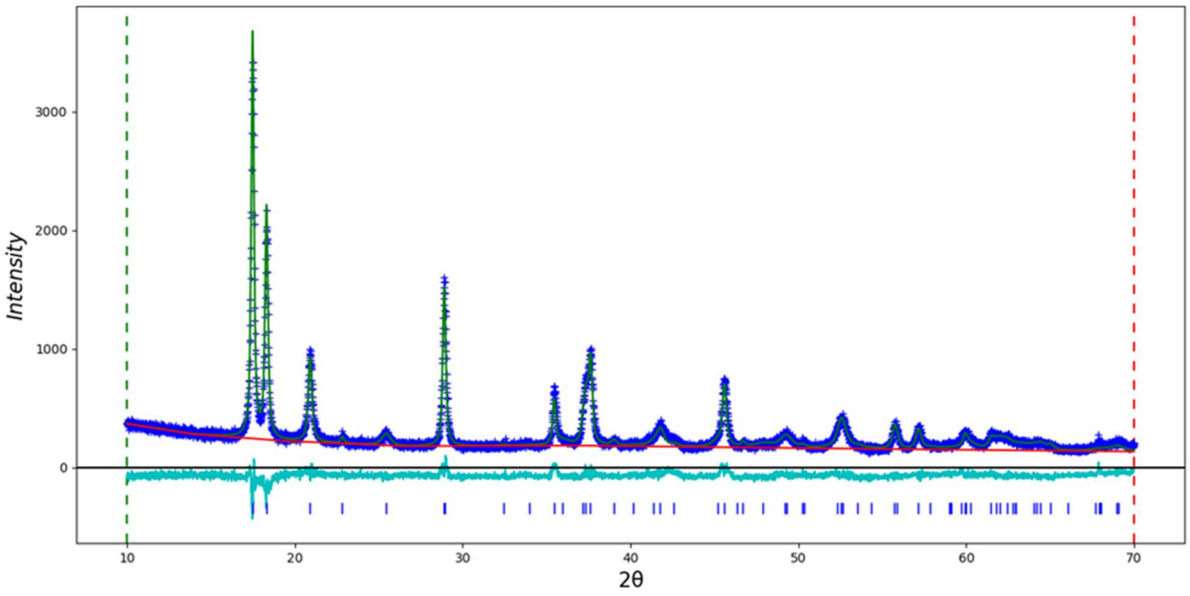


*Figure 6.12. Refined XRD pattern of a pristine Mn oxalate dihydrate that had been heated to remove hydrated water and refined to determine the structure, which was an orthorhombic γ-Mn oxalate with space group Pmna.*

The orthorhombic phase used to match expected bond distances for the pair distribution function to those observed in PDF #1 came from the Inorganic Crystal Structure Database (ICSD), from a study by A.N. Puzan et al.[192] The comparison between PDF #1 and the expected Mn-Mn, Mn-O, and Mn-C bond distances for the orthorhombic Mn oxalate sample with space group Pmna are displayed in Fig. 6.13.[195]

The PDF of the dehydrated orthorhombic structure correlates well to the observed in-situ data for PDFs #1 – #3, indicating that this Mn oxalate with space group Pmna is the crystalline starting material in the experiment. The dominant bond distances can be ascribed as follows:

- Mn─Mn bond distances: Peaks at 3.36, 3.79 Å, 5.85 Å, 7.02 Å , 7.47 Å, 7.88 Å 8.56 Å and 9.08 Å.
- Mn─O bond distances: Peaks at 2.28 Å, 4.28 Å, and 8.56 Å.
- Mn─C bond distances: Peaks at 3.02 Å, 4.62 Å, 5.24 Å, 6.23 Å, 7.02 Å, 7.88 Å and 8.56 Å.

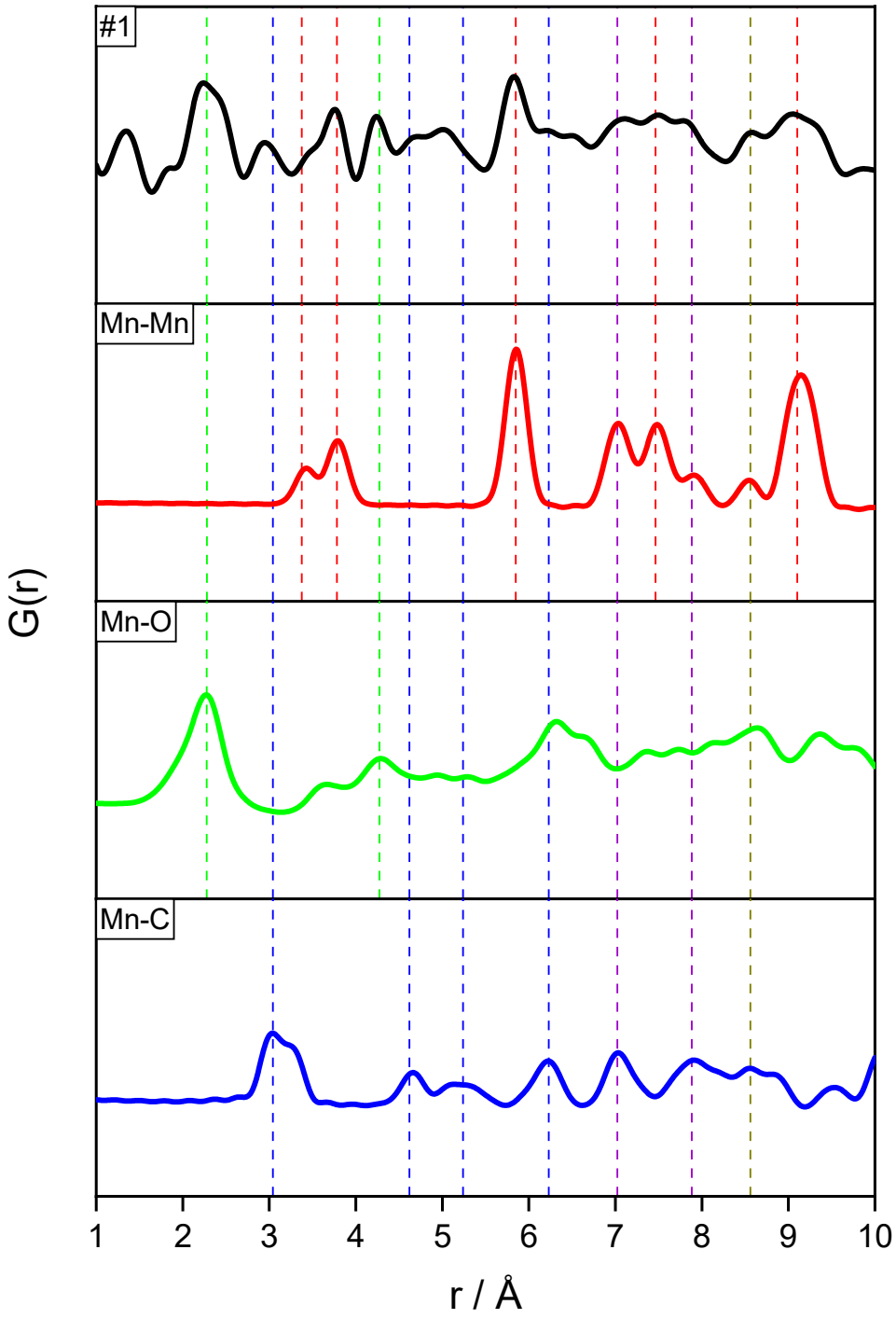


*Figure 6.13. PDF extraction comparing PDF #1 with PDF plots for individual bond interactions for dehydrated orthorhombic Mn oxalate with space group Pmna. Individual atom distances plotted to facilitate peak identification, with dotted lines used to match to peak intensities in red for Mn-Mn bond distances, green for Mn-O and blue for Mn-C. The purple line corresponds to both Mn-O and Mn-C, and the brown line for all three bonds.*

Once the discharge curve plateaus the conversion reaction begins, as observed in the PDF data between PDFs #3 – #7, along with the pulverisation and significant structural changes that occur. Based on literature discussion, it is expected that $Mn^{2+}$ within the Mn oxalate will be reduced to $Mn^0$ metal and the Li will react with the remaining oxalate to form Li oxalate, as outlined in equation 4.[72,94,95] To analyse whether this was the case, the PDF data for plots #3, #5, and #7 have been overlaid between 1 and 10 angstroms, shown in Fig. 6.14. To determine whether they Mn metal had formed, crystallographic information files (CIFs) were extracted from the Inorganic Crystal Structure Database (ICSD) and PDFs were extracted to determine the bond distances. Mn metal with space group $i\bar{4}3m$, known as α-manganese, from X. Hua et al.'s study was identified to correlate with the in-situ PDF data.[76] It appears from the overlaid PDFs that the Mn oxalate converts to metallic manganese, as expected in equation 4, during discharge, with decrease in intensity of key Mn oxalate peaks such as the peak at 2.28 Å corresponding to Mn—O, and the peaks at 7.02 Å, 7.88 Å and 8.56 Å corresponding to Mn—C bond distances, amongst many others. In PDF #7 at the end of discharge, the dominant bond distances observed are assigned to the Mn-Mn (from α-manganese) bond distances at 2.59 Å, 4.25 Å, 5.10 Å, 6.55 Å, 7.56 Å and 8.80 Å. The bond distance matching for this is shown in Fig. 6.15.

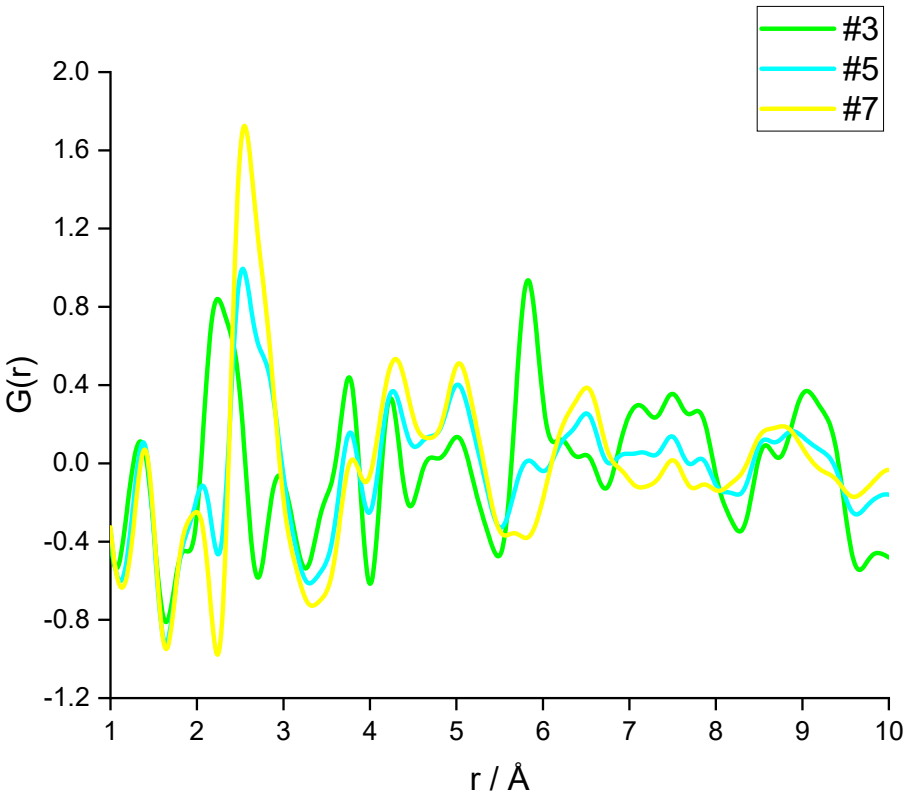


*Figure 6.14. In-situ pair distribution function data between 1 and 10 angstroms, showing the localised structural changes of the pristine sample during the conversion reaction in the first discharge. The colours correspond to the data points marked during cycling.*

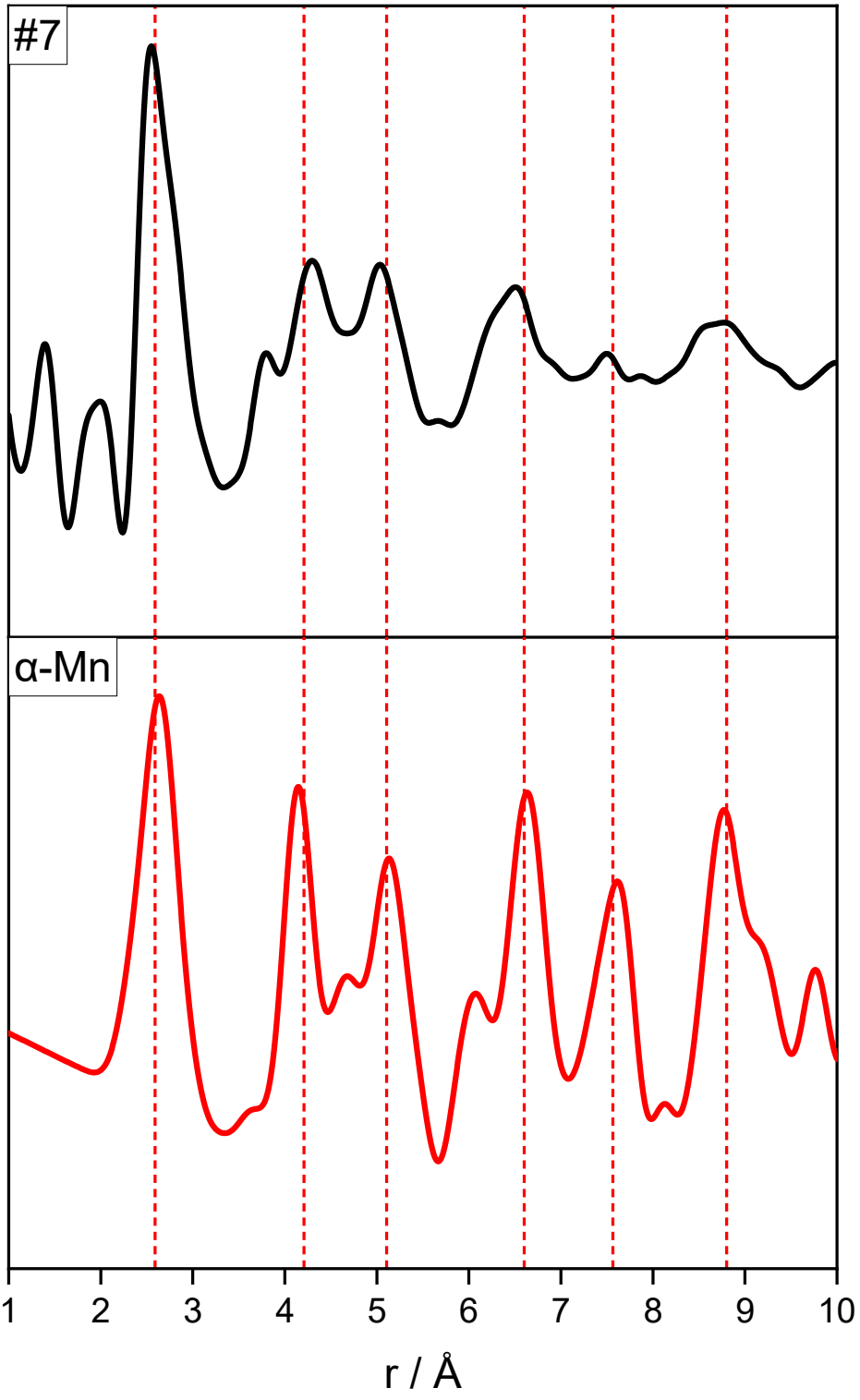


*Figure 6.15. PDF extraction comparing PDF #7 with PDF plots for individual bond interactions for α-Mn with space group $i\bar{4}3m$. Dotted lines used to match to peak intensities in red for Mn-Mn bond distances in the CIF file and the in-situ PDF data.*

Next, to analyse the changing local structure during charge, the PDF data for plots #7 - #10 were overlaid between 1 and 10 Å, shown in Fig. 6.16. It is clear from the PDF data that the Mn reacts during charge to form a new product which, based on the reversible conversion reaction explored in equation 4, was expected to be Mn oxalate from the oxidation of metallic manganese during charge. To determine whether orthorhombic Mn oxalate reformed at the end of charge, PDFs #1 and #10 were compared, displayed in Fig. 6.17. Some of the peaks observed after one cycle do not correspond to those for Mn oxalate, which is indicative that another product was formed after one cycle.

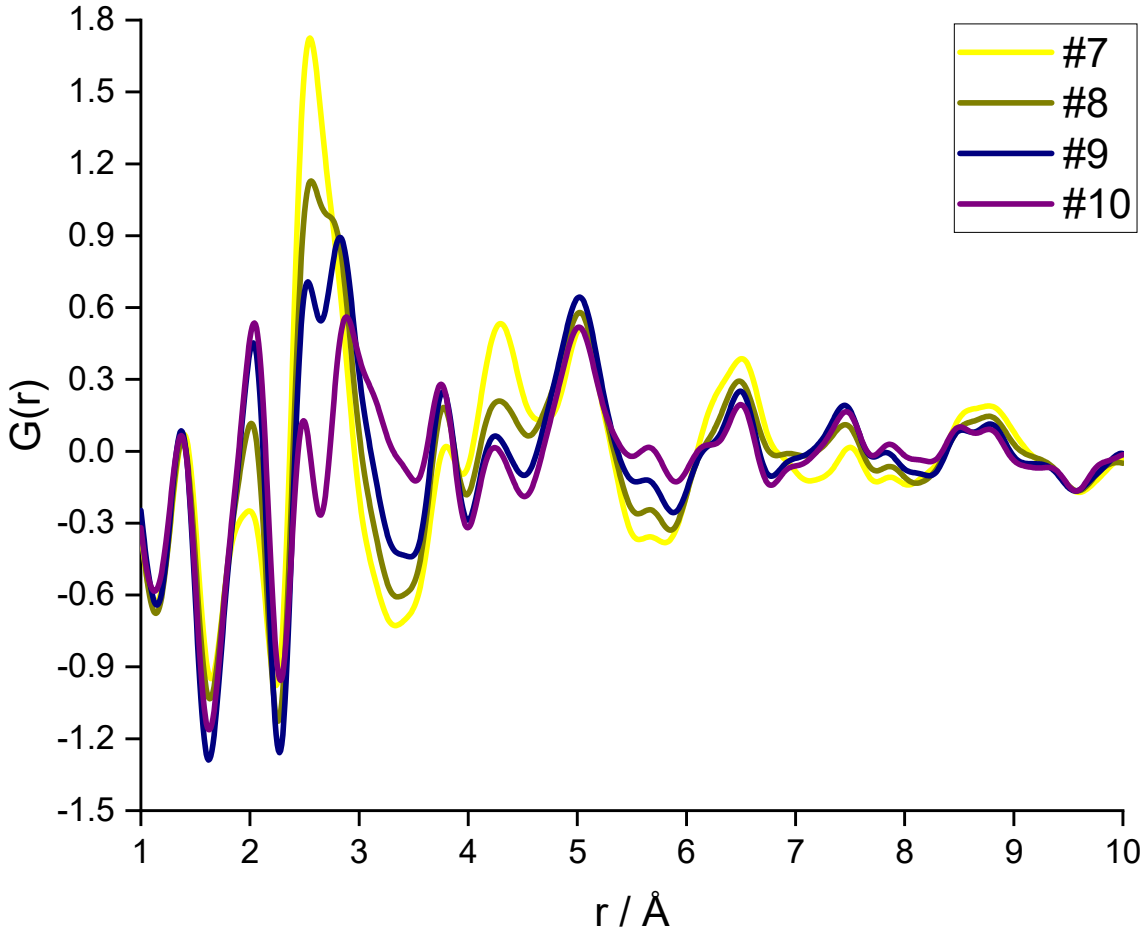


*Figure 6.16. In-situ pair distribution function data between 1.5 and 7 angstroms, showing the localised structural changes of the pristine sample during the conversion reaction for cycles #7 #9 and #10 in the first charge. The colours correspond to the data points marked during cycling in Fig. 6.9.*

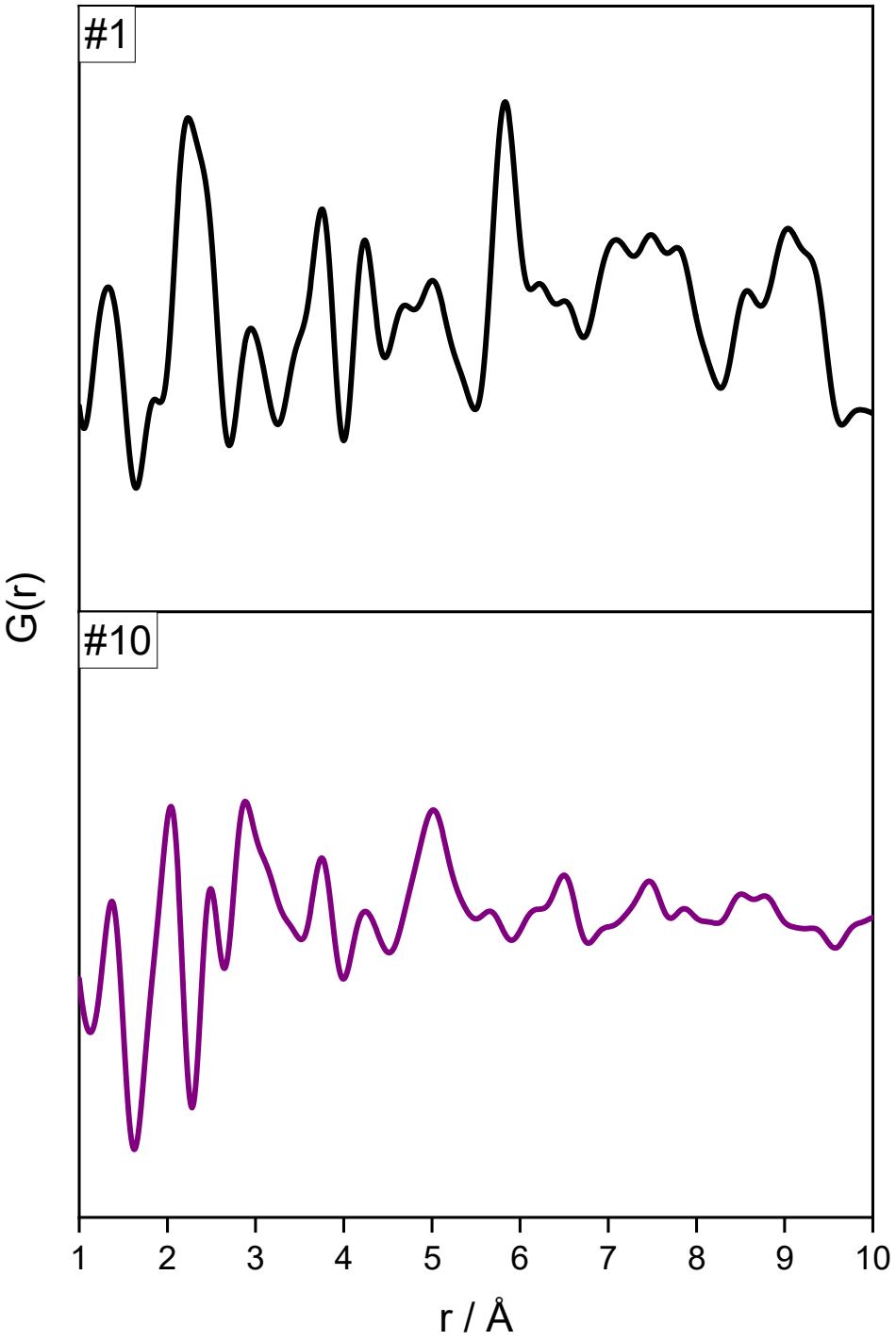


*Figure 6.17. In-situ pair distribution function data between 1 and 10 angstroms, showing the localised structural changes of the pristine sample for PDFs #1 and #10.*

To be specific, the Mn oxalate peaks that are not present in PDF #10 include:

- 2.28 Å, 7.02 Å and 8.56 Å corresponding to Mn-O
- 4.62 Å and 8.56 Å corresponding to Mn-C
- 5.85 Å and 7.02 8.56 Å and 9.08 Å corresponding to Mn-Mn

The fact that these bond distances are no longer present is indicative of a new structure formed at the end of the cycle, as that it appears that the Mn oxalate does not cycle reversibly to generate Mn oxalate at the end of each cycle, as is expected based on equation 4. One thing that is key to note is the difference in the charge value reached for the 3 V max half-cell and the pristine material cycled in the DRIX cell upon charge – in the 3 V max half-cell depicted in Fig. 6.2, the coin cell this material reached a charge capacity of 492 $mAhg^{-1}$, whereas the DRIX cell only reached 322 $mAhg^{-1}$, which is less than the theoretical capacity of Mn oxalate (375 $mAhg^{-1}$). This decreased capacity highlights that the full conversion reaction is not achieved by the end of this cycle in the DRIX cell. Based on this, it is expected that PDF #10 is a combination of two phases: the alpha-manganese conversion product that had not fully converted, and another Mn-based product. Focussing on X. Hua et al.'s study on reconversion chemistry of $Mn_3O_4$ in a Li-ion battery setup, it was observed that the α-Mn metal conversion product at the end of discharge for a $Mn_3O_4$ conversion anode did not reversibly convert to form the original Mn oxide but, in fact, the Mn metal formed at the end of discharge converted back to a new Mn oxide material, namely zincblende-structured MnO. As the Mn product at the end of discharge in this in-situ experiment was correlated to the same alpha-Mn metal phase with space group $i\bar{4}3m$, it was therefore hypothesised that the conversion

product at the end of charge would be a zincblende MnO phase with space group $F\bar{4}3m$.[76]

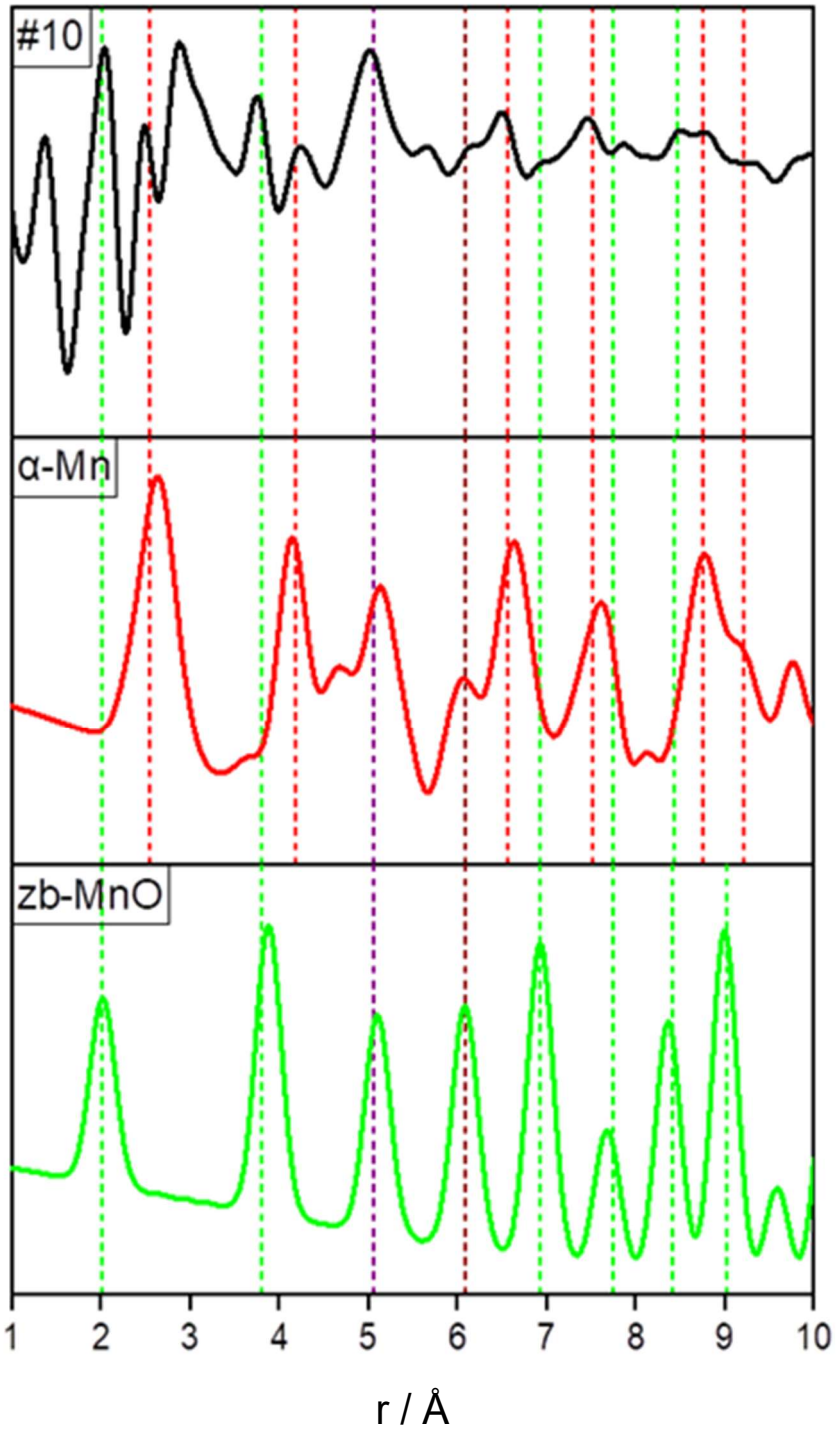


*Figure 6.18. PDF extraction comparing PDF #10 with PDF plots for alpha-Mn and zincblende MnO. Individual atom distances plotted to facilitate peak identification, with dotted lines used to match to peak intensities in red for alpha-Mn bond distances and green for zb-Mn-O The purple line corresponds to both alpha-Mn and zb-Mn-O.*

The CIF file for the zincblende structure was taken from a study by B. Thiodijo Sendja et al., and the lattice parameters for this unit cell were taken from those calculated in X. Hua et al.'s study. [76,196] Based on the peak matching between PDF #10 and the calculated PDFs, it appears that the calculated plots correlate to the structure of the material observed in PDF #10 considerably, indicating that both these phases are present at the end of charge. To determine whether this product at the end of the first cycle is retained throughout cycling, comparisons were made in Fig. 6.19:

- In Fig. 6.19a – comparison was made between the product at the end of charge (3 V) in the pristine sample's first cycle and the 3 V pre-cycled material at the beginning of discharge, (PDF # 21, plotted in Fig. 6.19), to determine whether the 3 V pre-cycled material had the same structure at the top of charge.
- In Fig. 6.19b – comparison was made between the material at the beginning of discharge for the 2 V pre-cycled material (PDF #11, plotted in Fig. 6.19) and 3 V pre-cycled material to determine whether the structure remained the same during pre-cycling to different voltage maxima.

Based on Fig 19a, though there were slight differences in peak intensities, the in-situ PDF data pre-cycled 3 V material has the same structure in PDF #21 as that of PDF #10, indicating it's the reversible cycling of this material throughout cycling at 3 V, as was projected in X. Hua et al.'s study for the zincblende material, further clarifying the likelihood that this MnO material had formed.[75] In Fig. 19b, the different structures indicate that the cycling the material to a higher voltage maximum gives a different reaction product during electrochemical cycling, giving rise to such a different

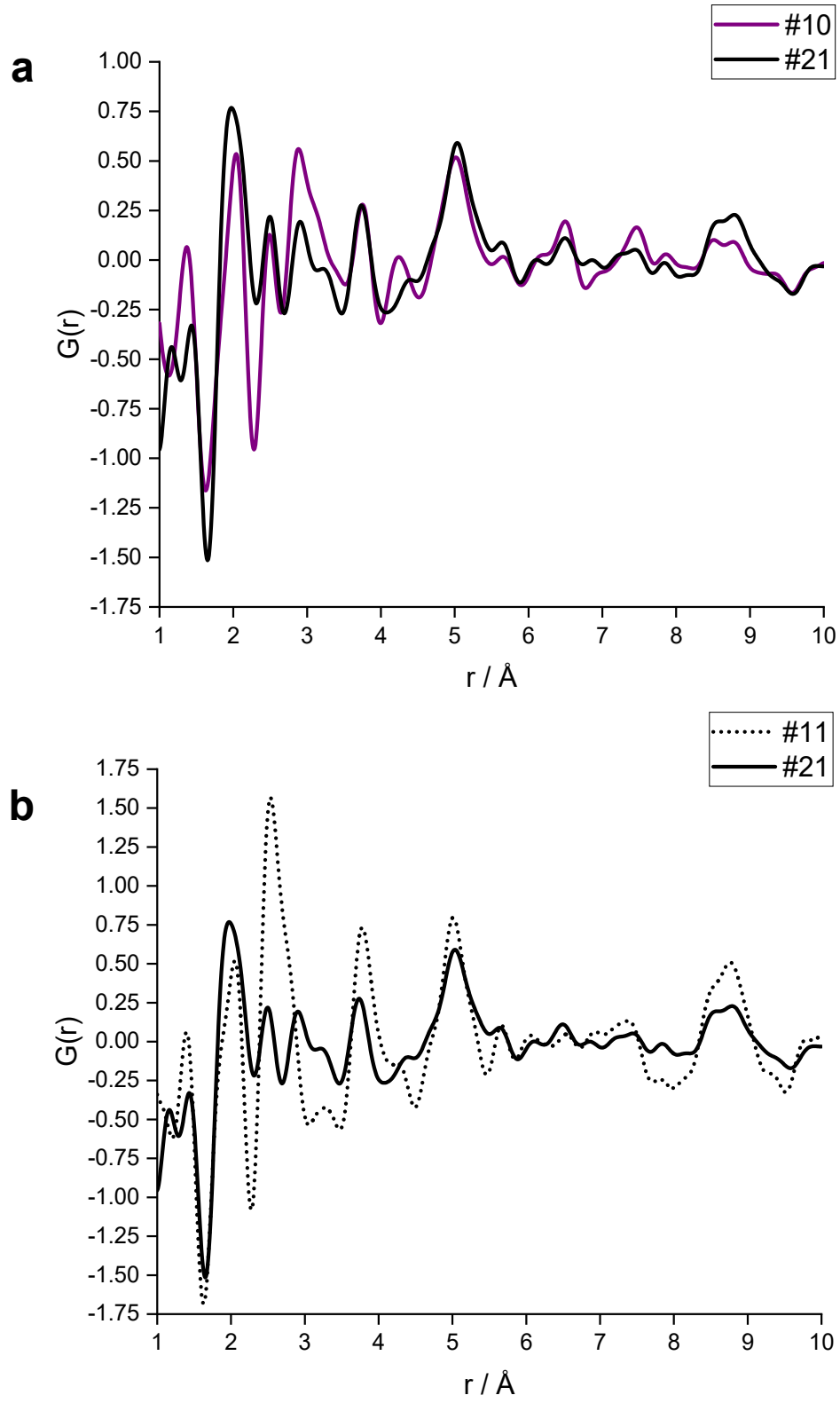


*Figure 6.19. Comparisons made between a) the product at the end of charge (3 V) for the pristine sample (#10) versus the pre-cycled material at the beginning of discharge (#21) and b) the 2 V and 3 V pre-cycled materials at the beginning of discharge (#10 and #11).*

electrochemical performance, as seen for the 2 V max and 3 V max cells in the first section.

PDF #9 is the final PDF measured in the pristine cell before the voltage exceeds the 2 V voltage limit, therefore this structure gives a good idea of the difference in the structure of the material in the first cycle at the end of charge for the 2 V cell versus the 3V pristine DRIX cell. The conversion product displayed in PDF #7 during charge gave rise to the same bond distances as that for PDF # 10, aside from the peak intensities corresponding to bond distances of 2.5 Å and 2.85 Å – this structure difference may be the key difference in the subsequent cycling performance for the 2 V and 3 V max cells. To investigate the electrochemical behaviour after 105 cycles further for the 2 V precycled electrode material, the in-situ PDF measurements were compared across the 106$^{th}$ cycle. The voltage-capacity data for this sample cycled between 0.01 and 2 V is shown in Fig. 6.20. The discharge capacity of 2 V precycled half-cell improved in the DRIX setup. The capacity at the end of pre-cycling was just under 100 mAhg$^{-1}$, whereas for the DRIX cell the capacity reached 350 mAhg$^{-1}$. One reason for this may be since the DRIX cell setup ensured a fresh supply of electrolyte was introduced into the system, and further side-reactions between Li and the electrolyte arose were facilitated during the discharge of the 2 V precycled material. Unfortunately, PDF data was only collected for the discharge and charge up to ~0.85 V, meaning the full charging process was not captured using in-situ PDF. The set of in-situ PDF measurements are marked on in colours corresponding to the electrochemical data are shown in the PDF plot in Fig. 6.21. As was observed for the pristine material after the initial discharge, there are very few distinct bond distances observed past 10 angstroms due to the pulverisation of the crystalline precursor

active material structure during the initial conversion reaction when the cell was precycled. To determine the structural changes observed during the 106$^{th}$ cycle, the PDFs measured during discharge were overlaid in Fig. 6.22, and those for charge were overlaid in Fig. 6.23.

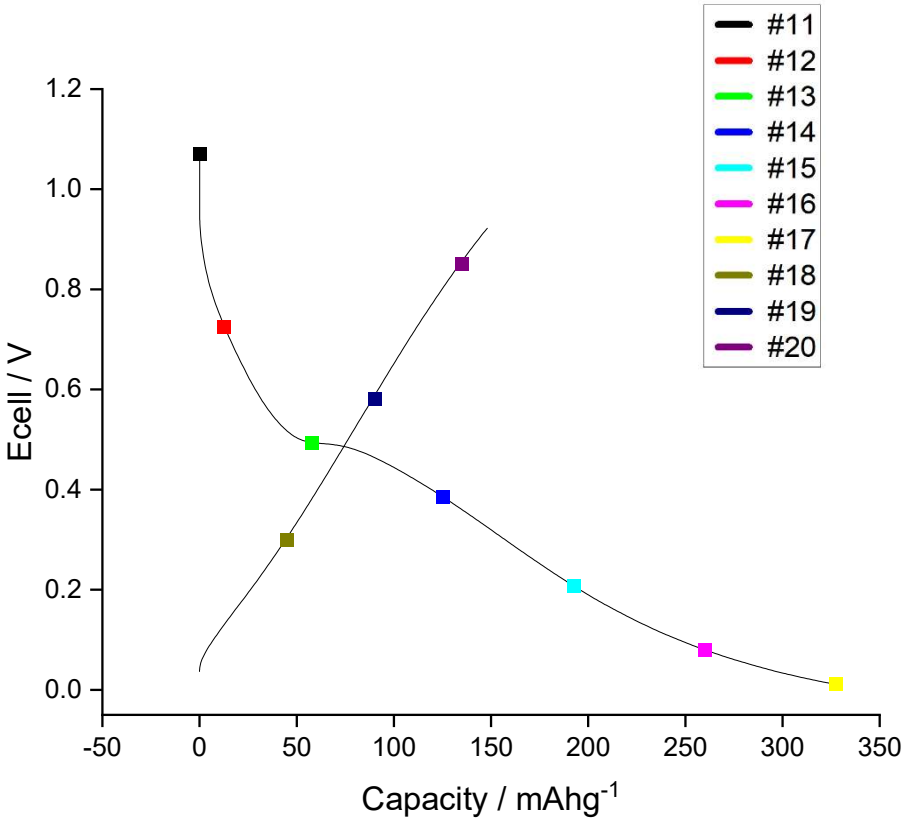


*Figure 6.20. Voltage-capacity data shown for the pristine sample cycled between 0.01 and 2 V at a current density of 45 mAg$^{-1}$ with data points marked during cycling for the PDF data collection.*

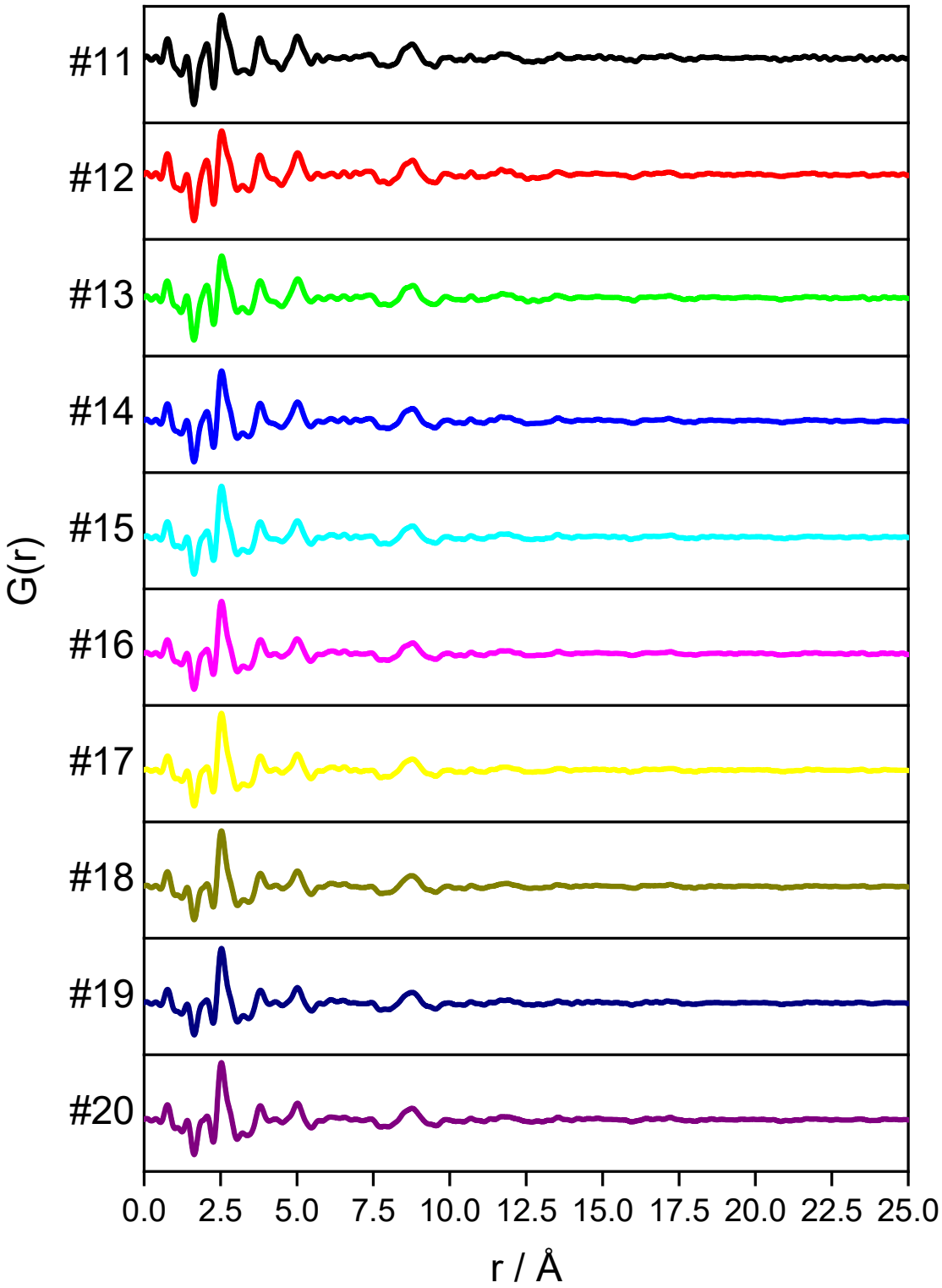


*Figure 6.21. In-situ pair distribution function data between 0 and 25 angstroms, showing the localised structural changes of the pristine sample cycled between 0.05 and 2 V at a current density of 45 $mAg^{-1}$. The colours correspond to the data points marked during cycling in Fig. 6.20.*

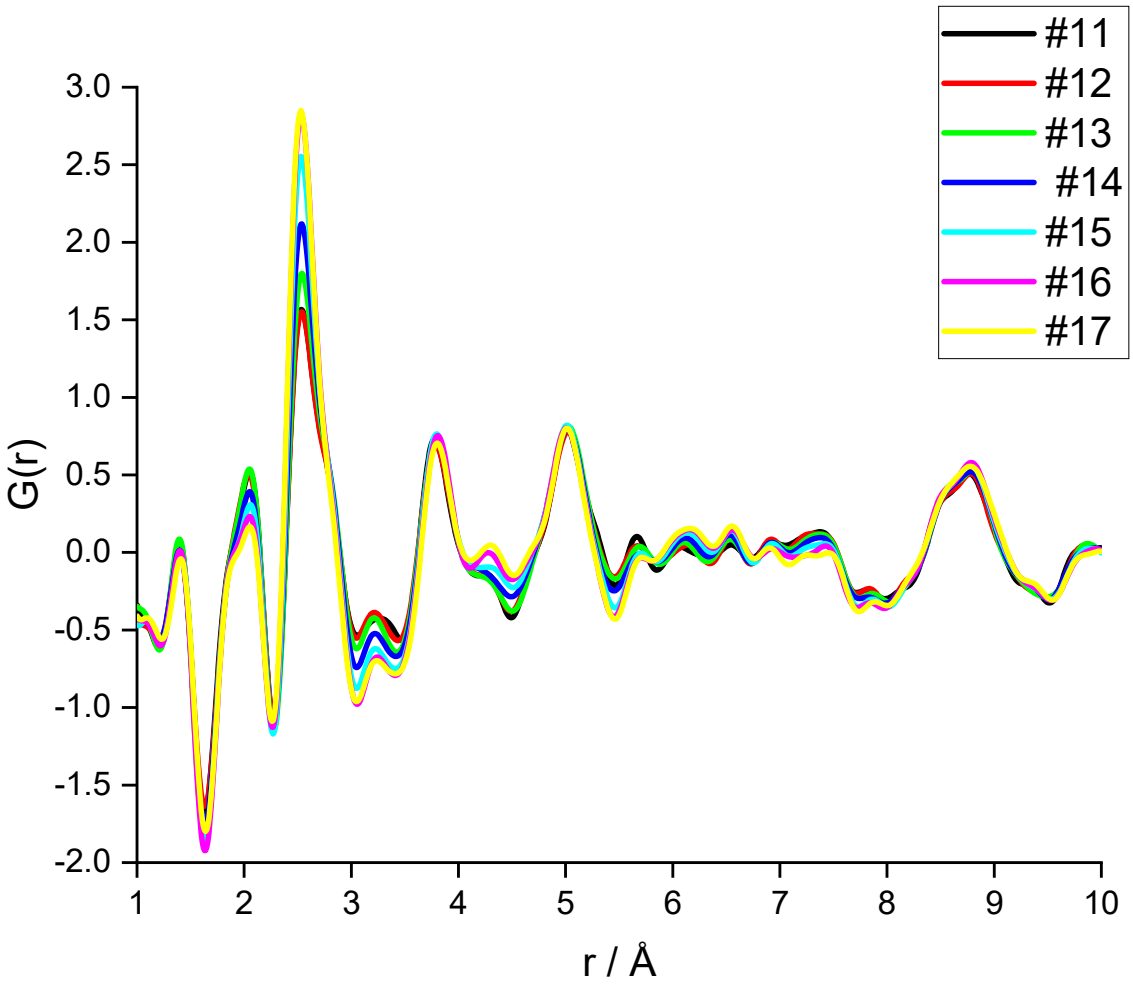


*Figure 6.22. In-situ pair distribution function data between 1 and 10 angstroms, showing the localised structural changes of the 2 V sample during the conversion reaction in the 106$^{th}$ discharge. The colours correspond to the data points marked during cycling.*

In the 106$^{th}$ discharge, there appeared to be some very minor structural changes for the 2 V pre-cycled cell. As the half-cell discharged the peak corresponding to a bond distance of 2.06 Å marginally decreased in intensity, as did the peaks at 3.22, 5.67, 6.90,7.41 7.85 Å. For the bond distance of 2.53, 4.32, 6.12 and 6.55 Å the peaks grew somewhat in intensity out to the end of discharge. The remaining peaks showed very little fluctuation in peak intensity. Overall, there appeared to be no substantial structural change indicating that the cell did not convert into a new material during discharge in this cycle. For the charging up to 0.85 V, there appeared to be no changes in the structure of the material, in there appeared to be no changes in the structure of the material, indicating that any structure changes that occur during charge did so past 0.85 V. To determine whether into the electrochemical behaviour after 105 cycles could be understood further for the 3 V precycled electrode material, the in-situ PDF measurements were measured for cycle 106. The voltage-capacity data for this sample cycled between 0.01 and 3 V is shown in Fig. 6.24, with the PDF plots marked labelled. The corresponding PDF plots are stacked in Fig 6.25. There are no significant bond distances past 10 Å,  as was the case for the 2 V precycled material, showing the pulverisation that arose in all cases during conversion of the crystalline Mn oxalate starting material. The capacity of 3 V precycled DRIX half-cell reached ~295 mAhg$^{-1}$ during discharge which was a little lower than the ~335 mAhg$^{-1}$ capacity reached at the end of pre-cycling in the half-cell setup. The reason for this decreased capacity may be due to the transfer of the free-standing film into the DRIX half-cell. It is possible that the removal of the FSF from its native electrochemical environment to have introduced artefacts (despite being removed in an inert atmosphere and transferred in a vacuum sealed container) during the time delay

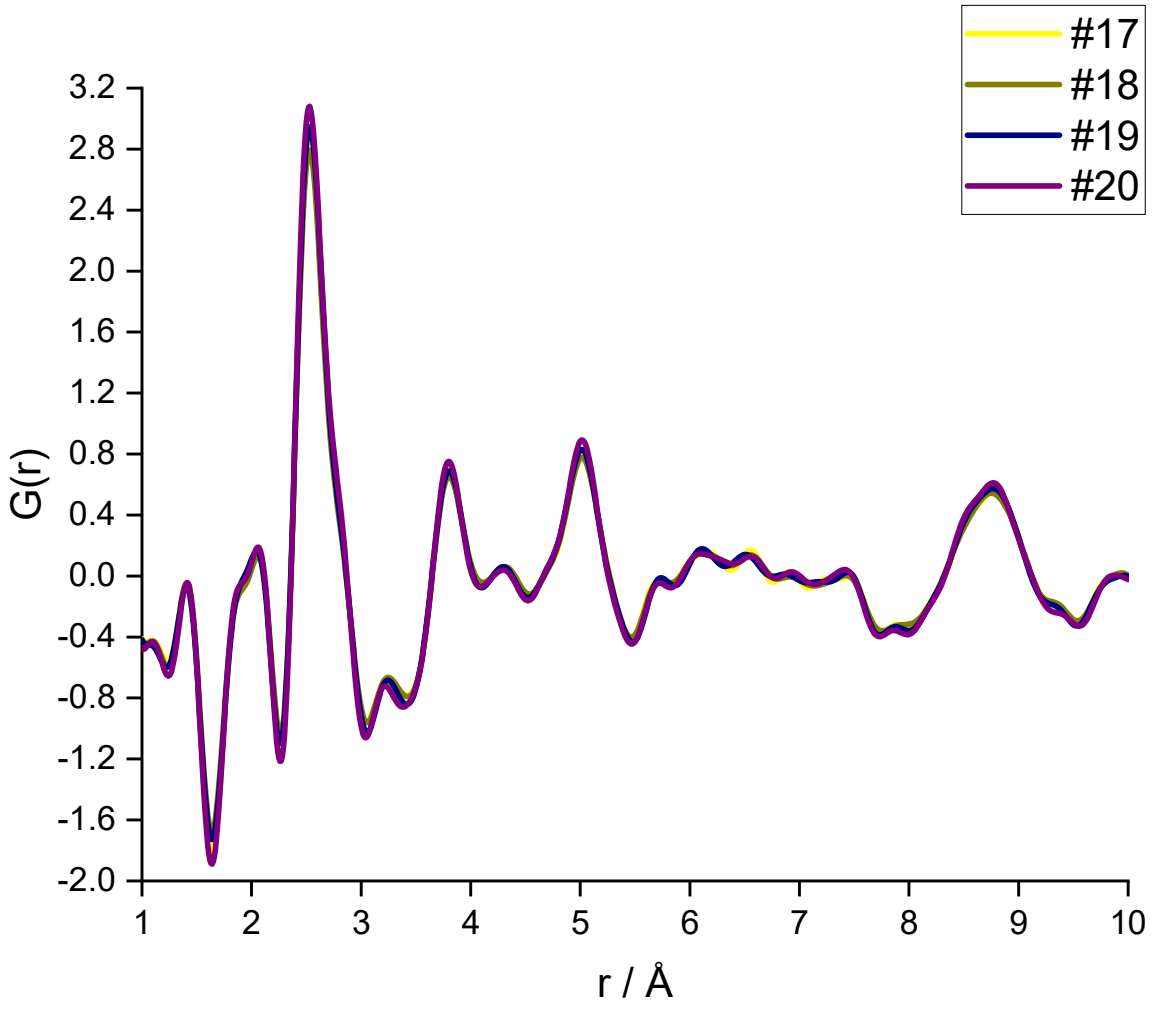


*Figure 6.23. In-situ pair distribution function data between 1 and 10 angstroms, showing the localised structural changes of the 2 V precycled sample during the conversion reaction during 106$^{th}$ charge. The colours correspond to the data points marked during cycling.*

between measurement of the 105$^{th}$ and 106$^{th}$ cycle. The capacity reached during charge is inherently poor for the 3 V precycled DRIX half-cell which indicates degradation from the FSF removal/ transfer.

To determine the structural changes observed during the 106$^{th}$ cycle for the 3 V precycled sample the PDFs measured during discharge and charge were overlaid and displayed in Fig. 6.26. In the 106$^{th}$ discharge, there appeared to be some very minor structural changes for the 3 V pre-cycled cell, with the most significant intensity changes arising for the unidentified peaks between 2.75 and 3.5 Å. In the charging data there was no structural change. These observations are likely due to the poor electrochemical performance of this material, whereby the capacity on charge reached less than 100 mAhg$^{-1}$.

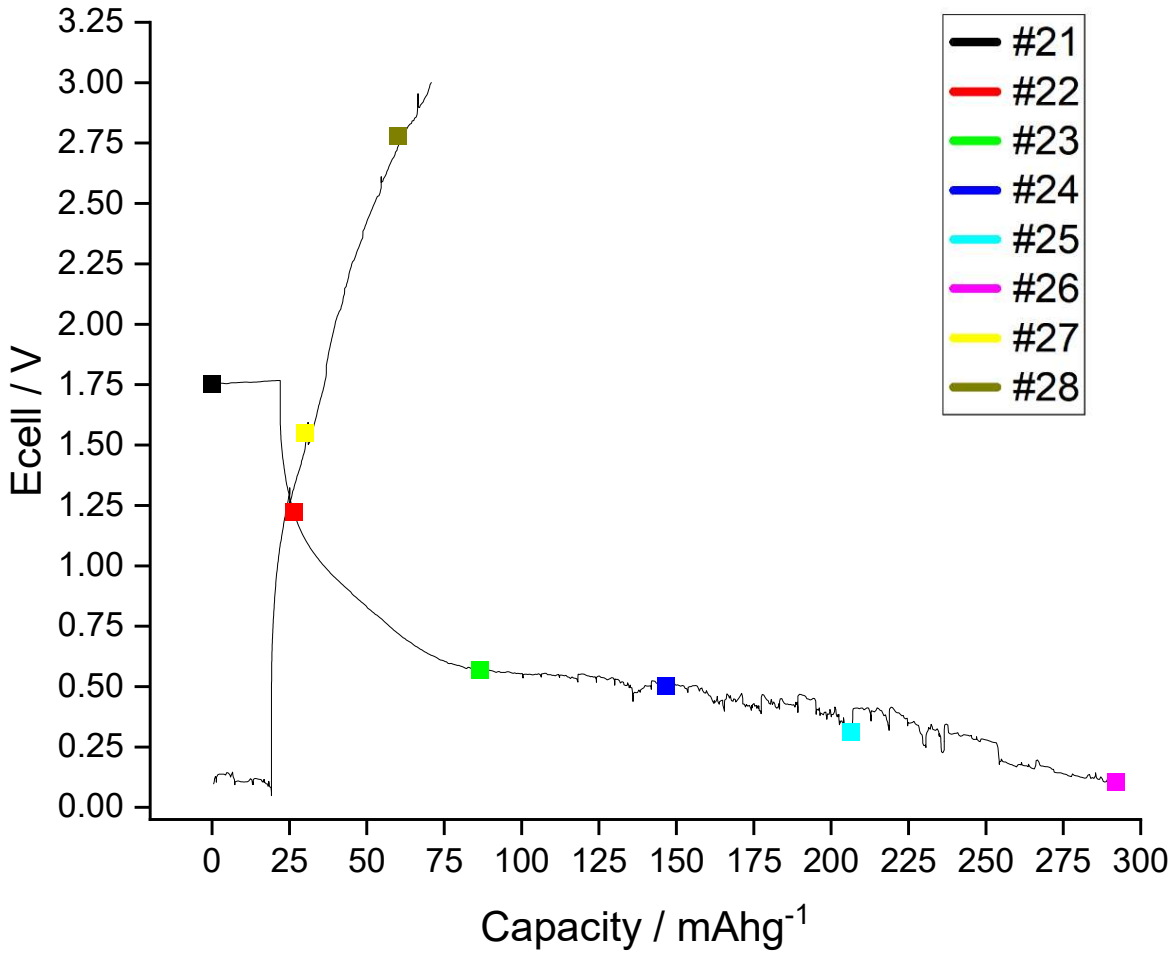


*Figure 6.24. Voltage-capacity data shown for the precycled sample cycled between 0.05 and 3 V at a current density of 30 $mAg^{-1}$ with data points marked during cycling for the PDF data collection.*

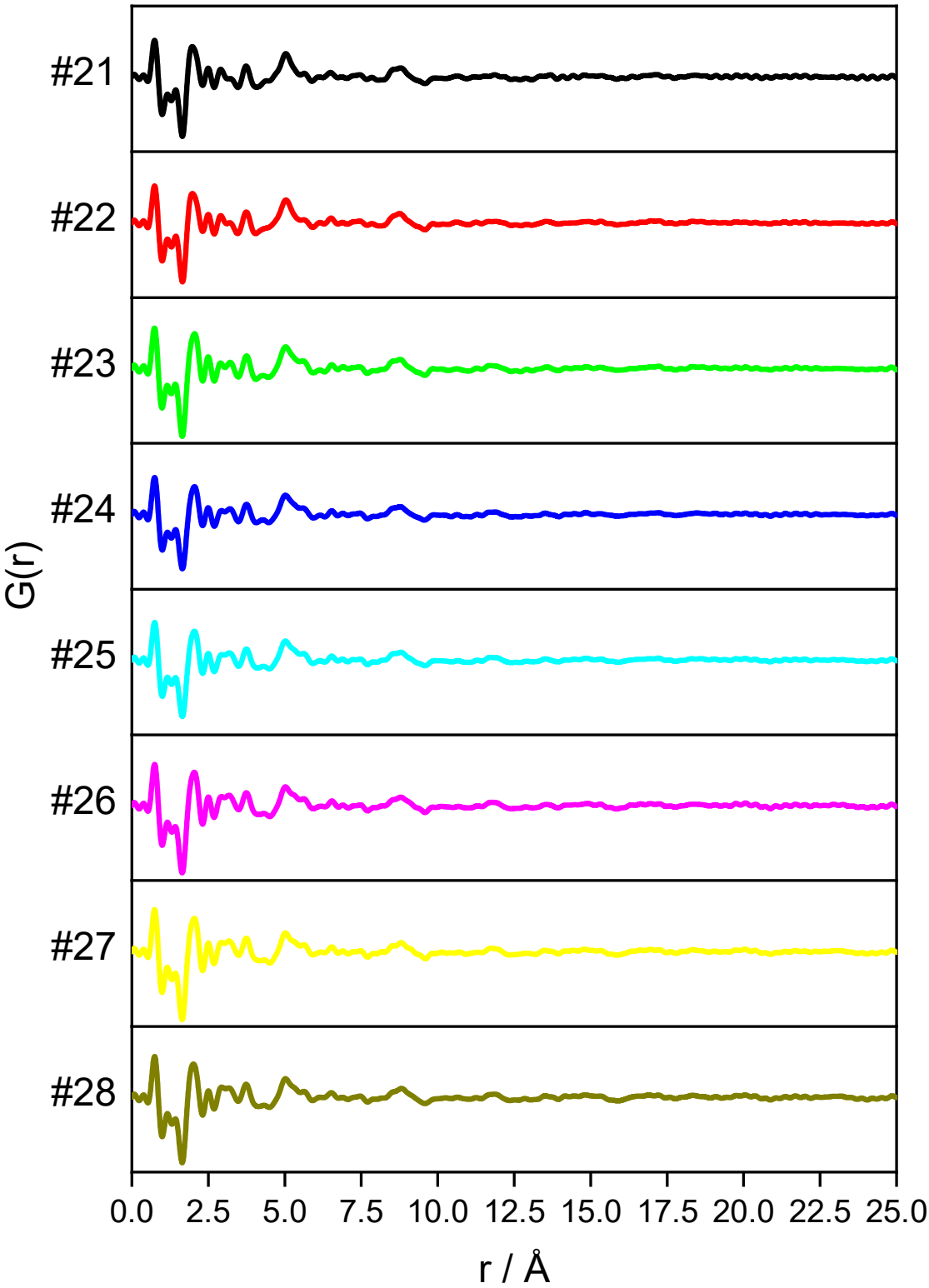


*Figure 6.25. In-situ pair distribution function data between 0 and 25 angstroms, showing the localised structural changes of the 3 V pre-cycled sample cycled between 0.05 and 3 V at a current density of 30 $mAg^{-1}$. The colours correspond to the data points marked*

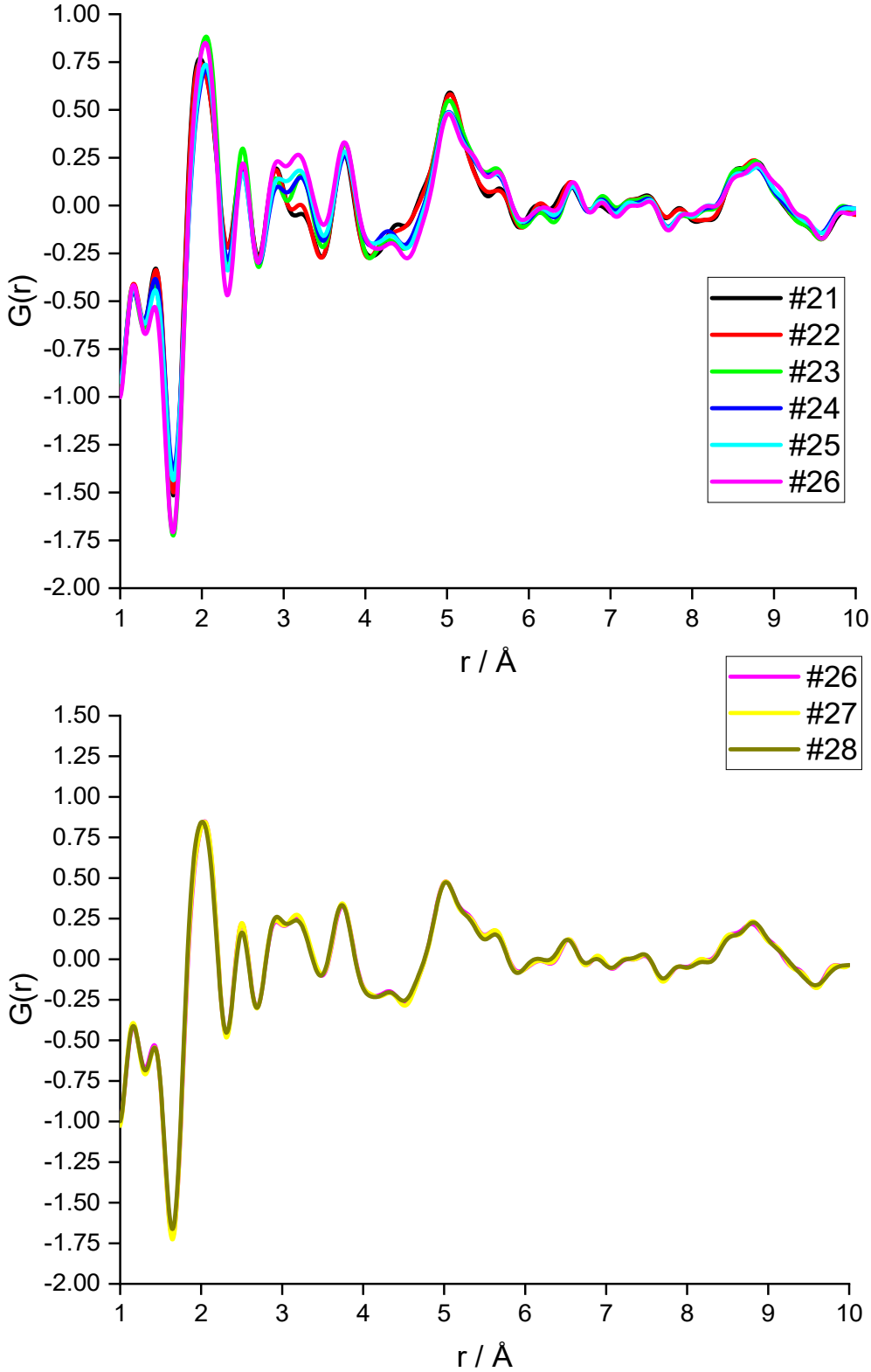


*Figure 6.26. In-situ PDF data between 1 and 10 Å, showing localised structural changes of the 3 V precycled sample during conversion in the 106$^{th}$ discharge (top) and charge (bottom). The colours correspond to the data points marked during cycling.*

When comparing the first cycle electrochemical data for the 3 V max cell to the in-situ PDF analysis, the structural information from the PDF patterns clearly reflects what is seen in the electrochemistry. Initial active material pulverisation occurs in the first discharge to form a metallic manganese product, with bond distances assigned to the Mn-Mn (α-Mn phase with space group $i\bar{4}3m$).[195] This pulverisation contributes to the large first cycle capacity loss seen for the Mn oxalates in the first discharge. The pulverisation also leads to higher surface area to volume ratio for the material, which means that a higher Li insertion voltage is required to electrochemically react with the material on subsequent cycles, as explored in the differential capacity study. In the subsequent charge, the Mn product appears to partially convert into a zincblende MnO phase with space group $F\bar{4}3m$, as observed for α-Mn in X. Hua et al.'s study.[75]

After 105 cycles, the structure of the material in the 2 V and 3 V precycled materials differs. For the 2 V half-cell the product does not resemble that of the material at the end of first discharge in the way that it does for the 3 V half-cell. This difference in structure between the 2 V and 3 V max cells highlights that the difference in capacity retention and redox activity is due to the deviation in structure of these materials when cycled at different voltage limits. The reversible growth of the polymeric gel must be complemented by the structure of the 3 V max material in longer-term cycling. During the 106$^{th}$ cycle in both cases, the structure of the material does not change significantly during charge, as is expected based on the capacitive behaviour that the 2 V max half-cell exhibits after 100 cycles in the differential capacity analysis. For the 3 V max cell, the electrochemical data was so poor that it is likely that this material did not react during charge in its 106$^{th}$ cycle so the redox activity was not observed.

### 6.4.3 Electrochemical comparisons of Mn oxalate synthesised from pristine, QCR and EOL LMO sources

Tackling waste from QCR and EOL lithium-ion batteries is an issue that has only become apparent in recent years, due to the high global uptake in electrification of the transport and energy storage sectors. Though the electrochemistry of Mn oxalate has been explored using an array of Mn sources, as outlined in section 1.5.7, there have not been any studies that use a Mn source from used QCR and EOL cathodes. In this section experiments will verify whether Mn oxalates generated from leached material exhibit comparable electrochemical performance to pristine material and whether these upcycled materials compare to Mn oxalates synthesised from other Mn sources within the literature. Comparisons between galvanostatic cycling of pristine, QCR and EOL Mn oxalates (at voltage limits of 2 V and 3 V) are made to determine the impact of Mn oxalate source on electrochemical behaviour out to 100 cycles. Mn oxalates explored in this section are synthesised from pristine (using an Alfa Aeser LMO), QCR and EOL LMO using the reaction scheme outlined in Fig. 6.1. The general cell manufacturing procedure is outlined in Experimental 3.5.1. To compare the influence of Mn oxalate precursor source on electrochemistry, each of pristine, QCR and EOL Mn oxalate samples were mixed with carbon black and sodium carboxymethylcellulose (CMC) in an 80:10:10 ratio, respectively, and coated copper film before cutting out electrodes to test in a Li-ion battery half-cell, using the same method as outlined for the pristine cells. Once Li-ion half cells of these materials had been synthesised, they were cycled using galvanostatic cycling with potential limitation. These conversion anodes were cycled between the two voltage ranges: 0.01 and 2 V and 0.05 and 3 V Li / $Li^+$– for 50 cycles each. They were cycled

at 30 $mAg^{-1}$ for 4 formation cycles, followed by 150 $mAg^{-1}$ current applied for subsequent cycles. The voltage-capacity plots for the first cycle for the pristine, QCR and EOL 2 V and 3 V (max voltage) samples are shown in Fig. 6.27 and the average first discharge capacities and coulombic efficiency is displayed in Table 6.3. For all cells there was an initial rapid drop in voltage during discharge, corresponding to the decomposition of the electrolyte and subsequent formation of the solid electrolyte interphase, followed by a voltage plateau. As stated previously, voltage plateau seen during first discharge corresponds to the forward conversion reaction of Mn oxalate (shown in equation 4), and the voltage tail-off down to 0.01 and 0.05 V for 2 and 3 V, respectively, has been reported to correspond to the formation of a gel layer on the surface of the anode, that gives the anode extra capacity and causes pseudo-capacitive behaviour.[72,92,94] To understand the amount of extra capacity added to these cells in their first discharge voltage versus $Li^+$ insertion graphs were plotted based on the theoretical amount of Li expected to react with the Mn oxalate precursor, whereby 2 $Li^+$ corresponds to 375 $mAhg^{-1}$ theoretical capacity. The Li concentration observed for the first cycle of the 2 V and 3 V max Mn oxalates from pristine, QCR and EOL precursors exhibited capacities that equated to the addition of between 5.25 – 6.25 x, which, at its highest, was over three times the amount of lithium expected for these samples (2 x) based on the theoretical calculation. Based on Mn oxalate doping studies by Duan at al. and Jia et al., these first cycle capacities and Coulombic efficiencies for the leached materials fall within expected values, all exceeding around 1000 $mAhg^{-1}$ for the first cycle discharge and coulombic efficiencies spanning between 46 and 50%.[93,95]

*Table 6.3. Average first discharge capacities and first cycle irreversible capacity loss of the pristine, QCR and EOL Mn oxalate half-cells with calculated coulombic efficiency.*

| Voltage maximum | First discharge capacity ($mAhg^{-1}$) | First cycle irreversible capacity loss ($mAhg^{-1}$) | Coulombic efficiency (%) |
|---|---|---|---|
| **2 V (Pristine)** | 1143 (±13) | 621 (±12) | 46 (±0.001) |
| **2 V (QCR)** | 1041 (±35) | 558 (±21) | 46 (±0.003) |
| **2 V (EOL)** | 1161 (±24) | 626 (±15) | 46 (±0.003) |
| **3 V (Pristine)** | 1037 (±53) | 536 (±42) | 48 (±0.01) |
| **3 V (QCR)** | 1081 (±46) | 567 (±5) | 48 (±0.002) |
| **3 V (EOL)** | 1066 (±22) | 533 (±19) | 50 (±0.01) |

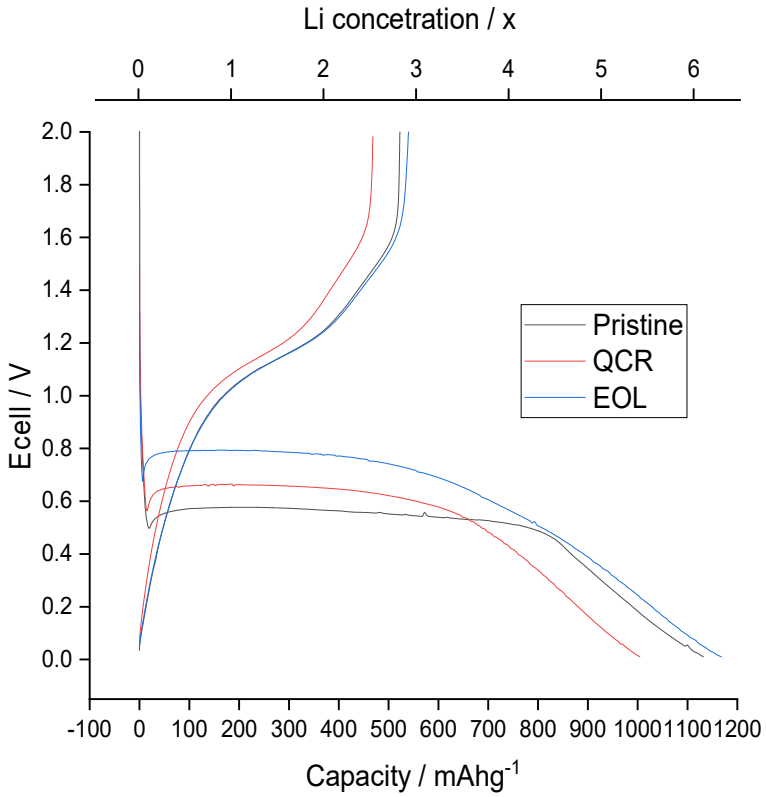


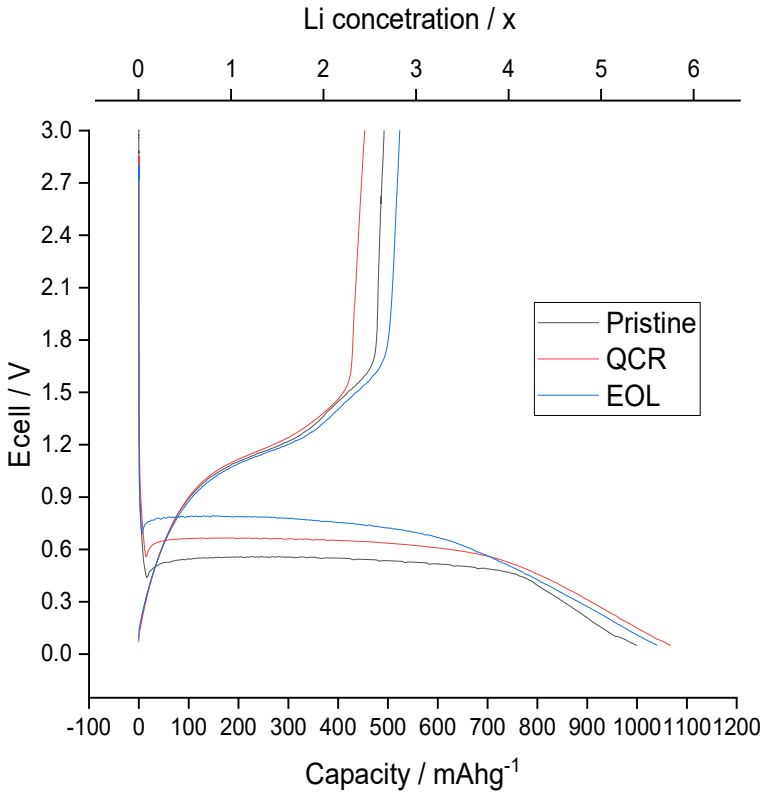


*Figure 6.27. Pristine QCR and EOL Ecel versus capacity plots for 2 V max (a) and 3 V max (b) first cycle, with Li concentration shown on a secondary x axis.*

To determine whether the Mn oxalate source had significant impact on electrochemical cycling behaviour, capacity fading was plotted in Fig. 6.28. As was observed for the pristine half-cells, the capacity fade was much more extreme for the 2 V max cells than for the 3 V max ones, with the pristine 2 V max sample exhibiting the poorest capacity recovery of the three half-cells. Looking only at the 2 V max cells it is evident that the most capacity recovery was observed for the EOL sample, followed by the QCR and then the pristine Mn oxalate. This trend aligns with a degree of contamination in these samples: EOL > QCR > pristine, shown in Table 4.3, which is suggestive that the contaminants may influence the capacitive increase in these systems. The 3 V max half-cells have a capacitive increase trend that follows the same trend within the first 30 cycles for these half-cells however the capacity then drops and stabilises in the opposite trend. Despite this drop in capacity retention for the leached materials, the capacity remains significantly higher than Mn oxalate's theoretical capacity in all cases. In Chapter 4, ICP-OES was used to highlight Ni and Co contamination in the interconverted Mn oxalates at low percentage masses (and copper/lithium contamination at even lower percentage masses). Ni and Co were expected from the layered phase, and Cu because of the over discharge of the QCR electrode during teardown. Though there are small amounts of Co and Cu contamination in the QCR material, the most significant contaminant throughout in the QCR and EOL Mn oxides is the Ni. Co contamination is significantly higher in the EOL material than for QCR. SEM data indicated the difference in morphology exhibited by the pristine, QCR and EOL Mn oxalate material. The polyhedral-like structure of the Mn oxalate became less apparent in the QCR / EOL samples, with the QCR sample exhibiting a smaller particle size distribution, and the EOL sample

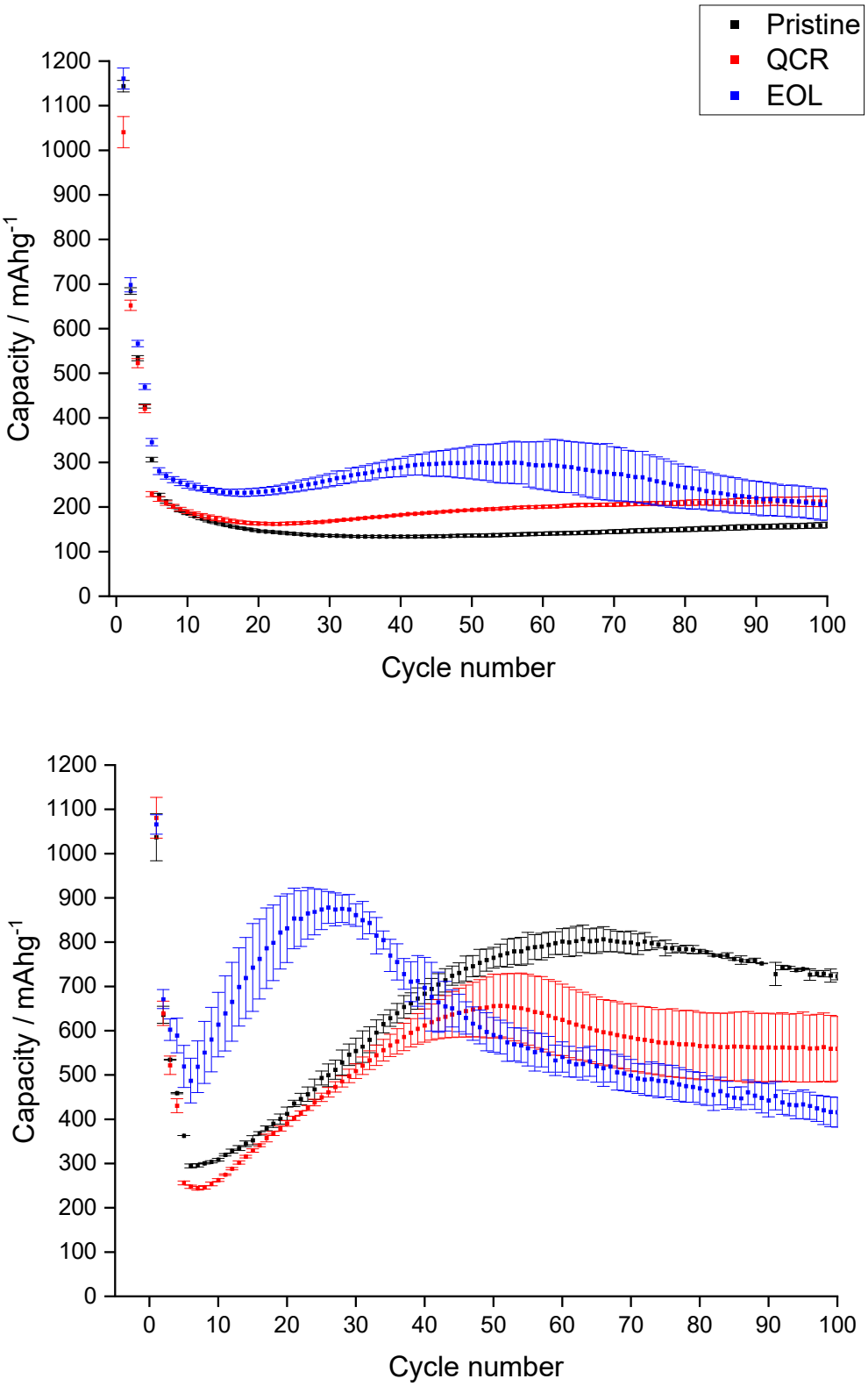


*Figure 6.28. Capacity versus cycle number plots for the pristine, QCR and EOL 2 V max (top) and 3 V max (bottom) cells.*

exhibiting the smallest particle size distribution of all the samples agglomeration. EOL Mn oxalate has the greatest resemblance to that of the Ni-doped Mn oxalate from a study by Y. Duan et al. The smaller average particle size is shown for the pristine sample therefore it is unsurprising that the differences in morphology are observed with deviations in electrochemistry. Manipulation of morphology of pure Mn oxalate has been used extensively in the literature to investigate and optimise performance of this conversion anode material. Methods outlined include solvothermal routes with optimisation of microwave-assisted reaction temperatures and use of a microchannel reactor to tailor particle morphology and size distribution.[72,96,97] In these investigations it has been identified that morphological manipulation has a profound impact on electrochemical performance. Furthermore, when considering the introduction of dopant ions into these systems, enhanced electrochemical performance has been observed and assigned to morphological influences as well as cooperative effects of the dopant ion and the manganese in the oxalate. In a study by Y. Duan et al. Mn oxalate doping was studied using Co, Ni, Cu and Zn (labelled as M) with stoichiometry $Mn_{0.5}M_{0.5}C_2O_4$. While the transition metal contaminants in the QCR and EOL Mn oxalates are in *much* lower quantities than this Y. Duan et al.'s findings give an insight on how these contaminant ions may impact cell cycling and differences in capacity fading observed in Fig. 6.28. Y. Duan et al. found that particle morphologies and structure of anode material dictates the electrochemical performance significantly. In their study the least effective rate performance came from Cu-doped Mn oxalate and the most came from the Ni-doped half-cells, which aligns with the Cu-doped sample having much the least desirable morphology and agglomeration of particles than the Ni-counterpart. In the SEM images of the Mn

oxalates in this discussion, shown in section 4.4.3, the average particle size of the samples follows the degree of contamination in the samples (pristine > QCR > EOL). In Y. Duan et al.'s study it was stated that the smaller the size of the active material particles gave rise to a larger specific surface area which is vital for enhancing electrochemical performance. Furthermore, the rod-like structure formed with Ni-doping provided greater electrode/electrolyte contact and diminished diffusion pathways for cycling while relieving volume expansion from the conversion reaction again optimising half-cell performance.[95] The electrochemical performance was therefore not only attributed to the enhanced kinetics of the electrode by the co-operative interaction of these metals with this mixed-metal system, but also due to the 1-D rod-like morphology of the generated active material. Such morphology was seen to enhance electron transport through the material which improves rate performance.[95] In a study by Y. Jia et al., iron-doping was used to manipulate the morphology of Mn oxalate material and investigation into the impact on electrochemistry was explored. Again, the enhanced electrochemical performance was attributed to cooperative effect between the two transition metals alongside the enhanced morphological characteristics that gave rise to an enhanced conductive network for lithium transport and storage.[93]

Comparing the first cycle voltage-capacity curves for the pristine, QCR and EOL samples at 2 V and 3 V, shown in Fig. 6.27, further highlights the differences between the samples during galvanostatic cycling. As the differences between 2 V and 3 V capacity curves have been explored in section 4.3.1, these comparisons focus on the differences between pristine, QCR and EOL Mn oxalate samples at the given voltage range (0.01 – 2 V or 0.05 – 3 V).

Firstly, the voltage plateau for the conversion reaction in the first discharge occurs at a higher voltage than for the pristine samples than for the QCR and EOL samples for both voltage ranges. In both the 2 V and the 3 V the pristine samples this plateau is observed at approximately 0.5 V, for the QCR samples this arises at ~0.625 V, and for the EOL samples this plateau is observed at ~0.75 V. As final clarification that the difference in voltage plateau seen for these samples was due to the contaminants, Mn oxalates were synthesised with the stoichiometric amounts of contaminants detected for QCR and EOL Mn in Chapter 4. As shown in Fig. 6.29, the QCR-doped and EOL-doped samples still followed the same trend as those seen in Fig. 6.27, indicating that these contaminants are likely to be the reason for the deviations in the conversion voltage plateau in the first discharge, and the SEM data indicates that the reason for this lies behind the varied morphology of these samples. Furthermore, the rod-like structure formed with Ni-doping provided greater electrode/electrolyte contact and diminished diffusion pathways for cycling while relieving volume expansion from the conversion reaction again optimising half-cell performance. [95]

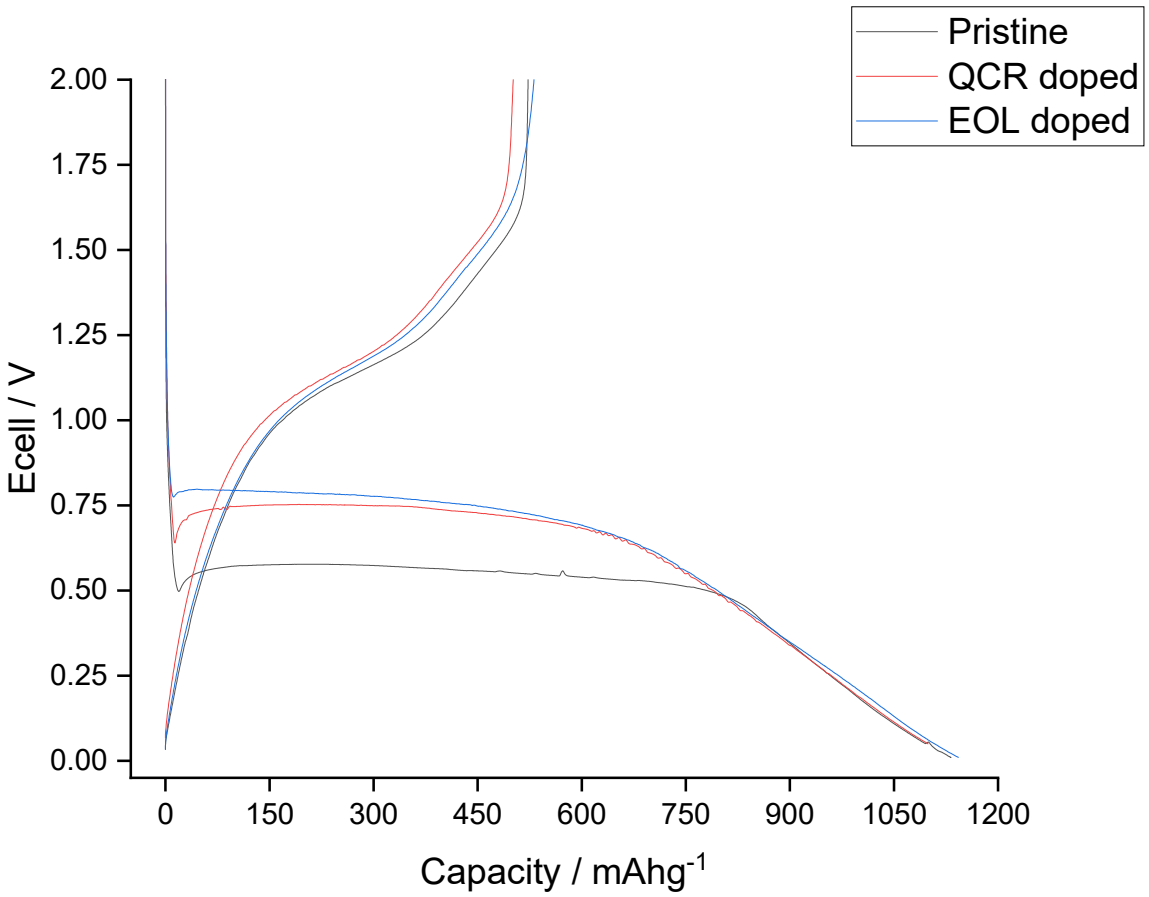


*Figure 6.29. Voltage-capacity curves showing first cycle (2 V max) of Mn oxalate cycling for pristine (black), QCR-doped (red), and EOL-doped (blue) material.*

## 6.5 Conclusions

The studies outlined in this Chapter have demonstrated that the widely reported Mn oxalate capacity increase arises due to the large voltage window that these half-cells are cycled within, with a 3 V maximum voltage. When the voltage limit is cut off at 2 V maximum, this has a profound effect on the electrochemical behaviour because of the accessed structures for these materials.

Looking specifically at the differential capacity analysis for these two scenarios, it is observed that any capacity increase observed for the 2 V max cell in the later cycles is due to capacitive contributions, which are likely to be because of the polymeric gel formation in the initial cycles. In the 3 V max half-cells, this be due to the redox active behaviour of this material and the polymeric gel formation combined. As it has been hypothesised in the literature, redox activity may not only be due to the Mn oxidation states expressed in the theoretical equation, but also due to higher Mn oxidation states, or even due to the reversible reaction of the C=O group in the anionic oxalate group.

As exhibited in the in-situ PDF data for all the studied oxalates, there is significant pulverisation of the anode material during first discharge, as expected, which leads to a significant first cycle irreversible capacity loss. After this initial capacity loss, it is observed that the capacity can be recovered significantly if the material is cycled up to 3 V in subsequent cycles, which is not so significant 2 V max half-cell. Based on the in-situ study, it has been confirmed that the conversion reaction outlined in equation 4 and in the literature is not representative of the in-situ scenario, as the product formed at the end of the first cycle does not match the structure of the initial

Mn oxalate material. This structure at the end of charge has in fact been identified to a zincblende-structured MnO with space group $F\bar{4}3m$, as determined in a study on X. Hua et al.'s study on reconversion chemistry Mn oxides.[76]

Furthermore, the deviation in electrochemical behaviour between 2 V and 3 V max can be attributed to the formation of a different structure during cycling between the two different voltage ranges. Following on from the in-situ investigation of Mn oxalate conversion anodes at different cycling conditions, this chapter has demonstrated that Mn oxalate conversion anode synthesis is successful using the interconversion of leached $LiMn_2O_4$ into Mn oxalate material, and that the voltage cutoff limits have the same capacity limitation effect on the Mn oxalate materials. After 100 cycles the capacity recovery of the 3 V max cycled half-cells remained as high as 725 – 750 $mAhg^{-1}$ for the pristine, 500 – 650 $mAhg^{-1}$ for the QCR and 400 – 475 $mAhg^{-1}$ for the EOL samples. Though the capacity retention after 100 cycles is lower with an increased degree of contamination, the capacity still outperforms the expected capacity based on the theoretical calculation, at 375 $mAhg^{-1}$, and of graphite, at 372 $mAhg^{-1}$, and it is suspected that tailoring the morphology of the leached Mn oxalate product will enhance the electrochemical properties of these materials, through enhanced electrode/electrolyte contact and diminished diffusion pathways for cycling while relieving volume expansion from the conversion reaction again optimising half-cell performance.

## 6.6 Future Work

In future work, the first experiments to be prioritised will involve further identification of the in-situ product at the end of the first cycle for the pristine half-cell. One method to do this would be to use a PDF refinement software, such as PDFgui. As the structural changes arise on a local scale, a few atoms can be used to identify the local structure of the material. Different phases can be refined against one another, and the refined parameters that are outputted include lattice parameters, atomic coordinates, and atomic displacement. This software would therefore enable the bond distances in the in-situ PDF data to be correlated to the in-situ products of the conversion reaction. Additionally, as explored in X. Hua et al.'s study, Metropolis Monte Carlo simulations could be utilised to understand the thermodynamic behaviour during cycling, which enables subsequent structural elucidation.[76197]

Another in-situ structural ID method would be to use in-situ XAS. By identifying this conversion product, as well as the product at the end of the first cycle in a 2 V max system, further conclusions can be made into the deviation in faradaic and capacitive behaviour for these systems. Using XAS the redox behaviour of the manganese could be measured in real-time, to determine the oxidation state of the conversion products during cycling – giving rise to further understanding of the capacity increase observed in the 2 V and 3 V max samples.

In-situ analysis of the first 5 cycles would be of great interest to probe how the material cycles from the product observed in the initial cycles where the SEI layer forms. Following on from this, long-term cycled cells with full electrochemical data would give further insights into the structural changes and resultant electrochemical

behaviour. To minimise the likelihood of unwanted artefacts in the precycled material, precycling the Mn oxalate in the DRIX half-cell setup to ensure the capacity increase took place in an airtight setup with no transfer interference prior to PDF measurement would be ideal, to ensure that there were no transfer issues introduced prior to PDF collection.

Another avenue of research would be investigation into the redox activity of the oxalate organic group in the high capacities achieved by the conversion anode using an array of techniques, including Raman, X-ray photoelectron spectroscopy and XRD, amongst many others, to determine whether there is any evidence for the anionic redox to half-cell capacity for these materials.[98,99] This could further explain the vast deviation from the theoretical capacity measured for the Mn oxalate half-cells.

In subsequent experiments, investigation into morphological composition of the Mn oxalate material would be of interest, as has been explored extensively in the literature due to its potential to enhance Li uptake and transport during the conversion reaction. One way to manipulate Mn oxalate morphology would be to use the leached LMO to generate a Mn acetate precursor material that could then be synthesised into a material with tailored morphology via a hydrothermal/ solvothermal setup via one of the synthetic routes outlined in the literature. Furthermore, nanostructured material could be synthesised by this method which would reduce the degree of pulverisation in the first few cycles, minimising first cycle irreversible capacity loss in the materials.[72,91–95,97]

To further clarify the influence of morphology on the conductivity of the Mn oxalates, electrochemical impedance spectroscopy would be of great value. The charge-transfer and surface layer resistance in the middle frequency range is related to the charge-transfer resistance ($R_{ct}$) are measurable using this technique. In particular, the charge transfer resistance indicates superior electronic transport throughout the active material when its value is lower, which has been denoted to come down to the intrinsic morphology of the material. Additionally, the electrode kinetics are enhanced with a decreasing charge transfer resistance value  which enhances rate performance of these materials.[93–95]

## 6.7 References (continued)


192 A. N. Puzan, V. N. Baumer and P. V. Mateychenko, *Acta Crystallogr.*, 2017, 911–916.

193 P. M. Biesheuvel, S. Porada and J. E. Dykstra, The difference between Faradaic and non-Faradaic electrode processes, https://arxiv.org/pdf/1809.02930.pdf, (accessed 24 January 2024).

194 J. Zhu, J. Feng and Z. Guo, *RSC Adv.*, 2014, **4**, 57671–57678.

195 Inorganic Crystal Structure Database (ICSD), https://www.psds.ac.uk/icsd, (accessed 1 March 2024).

196 B. T. Sendja, D. T. Kamgne, G. Aquilanti, L. Olivi and J. Rikkert, *Phys. B Phys. Condens. Matter*, 2018, **545**, 481–490.

197 H. S. Geddes, H. Blade, J. F. McCabe, L. P. Hughes and A. L. Goodwin, *Chem. Commun.*, 2019, **55**, 13346–13349.

# 7 Closing discussion

In the introduction, it was outlined that the electrification of the portables, transport and ESS sectors is set to skyrocket in the next decade, which means that lithium-ion battery demand is set to do so too.[103] These batteries contain an array of valuable materials, and once these batteries reach the end of their usable lifetime there will be a great opportunity for materials extraction from lithium-ion battery scrap. It was also outlined that current commercialised battery recycling infrastructure relies on pyro and hydrometallurgical routes; however, these routes have their shortcomings, and diversifying the recycling practices implemented will enable further value to be derived from battery scrap material. [36–39,41] It has been highlighted here that one mode of battery recycling methodologies that has not been extensively utilised is upcycling, which enables derivation of increased value from lower worth waste materials. Prior studies on upcycling have been focussed around NMC upcycling, by taking low-Ni NMC chemistries and upcycling this material into a more 'current' Ni' rich form.[52,53] What is key to note, is that little focus has been placed on recycling of other early generation chemistries that will be prevalent in the waste stream, but lesser used in the current battery sector, such as the material LMO. LMO was utilised in the first-generation Nissan Leaf pouch cells in a mixed cathode phase, and this means that it will be prevalent in the preliminary EOL battery waste stream.

To derive value from upcycling this LMO phase, it was established that alternative anode chemistries are a valuable avenue to explore. With respect to the most commercialised anode material, graphite, which is well-understood and routinely used – there are concerns surrounding its circularity in the lithium-ion battery supply

chain, largely surrounding questions over the economic value for extracting the material. [60,61]

To address the lack of upcycling of redundant LMO material, and to provide upcycling products of this redundant cathode material into novel anode materials to contend with graphite, experiments outlined in this thesis have demonstrated the capabilities available for selective extraction and upcycling of LMO material into Mn-based products. Though there has been extensive research into recycling of spent battery materials in the literature, very little research has been done on upcycling electrodes and, notably, on upcycling of spent LMO cathode material. Exploring routes to extract this dated cathode material and exploring methodologies to showcase the potential of the derived Mn-based materials from outmoded LMO cathodes has been studied extensively in this thesis.

In Chapter 4, the aims were to explore the effectiveness of interconversion of this material into Mn oxalate, $Mn_2O_3$ and $Mn_3O_4$ through structural comparison to their pristine counterparts to verify whether this was the case. Experiments outlined in Chapter 4 have highlighted the efficacy of a selective leaching process for the extraction of LMO from spent cathode material and the effectiveness of interconversion of this material into Mn oxalate, $Mn_2O_3$ and $Mn_3O_4$. The LMO, Mn oxalate, $Mn_2O_3$ and $Mn_3O_4$ formed with structure $Fd\bar{3}m$, C12/c1, Pcab and $I4_1/amd$ respectively, across the pristine and leached QCR and EOL samples in all cases, indicating that any degree of contamination from the leached material was minimal and did not compromise the material structure. Through ICP-OES analysis it was observed that the contamination in the interconverted products came from the layered phase (Ni and Co contamination) in both EOL and QCR samples, with further

Cu contamination the case of the QCR samples, due to the over discharging of the cathode material prior to disassembly. These variations aligned with the lattice parameters calculated from the refined XRD patterns of all the interconverted samples, with unit cell contraction and lattice parameter shrinkage observed for the most-part in the leached samples. SEM-EDX data highlighted the variation in morphology between these samples, which was of benefit for subsequent experiments on the interconverted Mn oxalate testing undertaken in Chapter 6.

In Chapter 5, the first aim was to first derive a simple mechanochemical route to manufacture a $_{nano}$MnO-C composite material, whereby Mn oxalate dihydrate could be utilised as a precursor. The nanocomposite had been reported to provide a respectable electrochemical performance when cycled as a conversion anode material, and so was an obvious upcycling product for the LMO material when considering materials to rival graphite. [79–83]

By developing a simplistic process for manufacturing these nanocomposites through mechanochemistry, utilisation of leached Mn-rich cathode material from first generation quality-control rejected and end-of-life pouch cells could then be applied to this synthetic route, as it had been demonstrated in Chapter 4 that LMO material was routinely upcycled into Mn oxalate. As stated in Chapter 5, the simplistic mechanochemical route for synthesis of these was successful in generating the desired $_{nano}$MnO-C composite for subsequent electrochemical analysis, and optimisation experiments provided the correct heating temperature to provide the most effective electrochemical performance, which came to a 600 °C/ 4h temperature / hold time. The second aim of this chapter was to demonstrate the value of the leached materials in the nanocomposite form and provide evidence that these were

effective conversion anode materials. The average capacities exhibited for the pristine, QCR and EOL samples after 15 cycles were 697 (±19), 777 (±12), and 916 (±37) $mAhg^{-1}$ which equates to 66 %, 68%, and 83 % of the original capacities exhibited, respectively. This indicates that both the leached materials have enhanced capacity retention when compared to the pristine case – with capacities exceeding that of the theoretical capacity for MnO (at 755 $mAhg^{-1}$) for both the leached samples after 15 cycles, particularly for the EOL materials. Furthermore, these nanocomposites exhibit electrochemical capacities that are more than double that of graphite (372 $mAhg^{-1}$) indicating that upcycling the redundant cathode materials into these $_{nano}$MnO-C conversion anodes has demonstrated the success in upcycling this redundant LMO material into high-capacity anode materials as an alternative to graphite.

In Chapter 6, the first aim was to develop understanding into the electrochemical behaviour of Mn oxalate conversion anodes through manipulation of the cycling voltage range, not only to determine its effect on electrochemistry but also on the structure of the Mn oxalate during cell runtime, using in-situ pair distribution function (PDF) analysis. One of the first features demonstrated in this analysis is that the Mn oxalate capacity increase was facilitated by the large cycling voltage window with 3 V maximum voltage. When the voltage limit was cut off at 2 V maximum, this has a profound effect on the electrochemical behaviour because of the accessed structures for these materials. By the $100^{th}$ cycle, the discharge capacity of the 2 V max cells averaged out at 160 $mAhg^{-1}$ (± 7 $mAhg^{-1}$) and for the 3 V max cells averaged out at 723 $mAhg^{-1}$ (± 8 $mAhg^{-1}$), at 14% and 70% of their first discharge capacity, respectively, indicating the effect of the 3 V maximum voltage on capacity retention.

What's more is that there was capacity recovery in both cases – in the 2 V cell the capacity dropped as low as 133 $mAhg^{-1}$ (± 2 $mAhg^{-1}$) for the 2 V max cells and 308 $mAhg^{-1}$ (± 3 $mAhg^{-1}$) for the 3 V max cells. To shed light on this, the differential capacity analysis was analysed for these two scenarios, and it was shown that any capacity increase observed for the 2 V max cell in the later cycles looks to come from capacitive contributions, which are likely to be because of the polymeric gel formation in the initial cycles. In the 3 V max half-cells, this be due to the redox active behaviour of this material and the polymeric gel formation combined. As it has been hypothesised in the literature, redox activity may not only be due to the Mn oxidation states expressed in the theoretical equation, but also due to higher Mn oxidation states, or even due to the reversible reaction of the C═O group in the anionic oxalate group. In the in-situ structural study of the Mn oxalate materials through PDF analysis, the electrochemical behaviour was interpreted further. The pulverization the electrode during the first cycle was confirmed during first discharge, it was also shown that the conversion reaction outlined in equation 4 and in the literature is not representative of the in-situ scenario, as the product formed at the end of the first cycle does not match the structure of the initial Mn oxalate material on the short-range scale. This structure at the end of charge has been hypothesised to match with a zincblende-structured MnO with space group $F\bar{4}3m$, although the poor electrochemistry meant that only part of the anode material converted into this phase, and subsequent PDF experiments and refinements would be necessary to obtain all the structural information of the phase at the end of discharge. The reconversion of α-Mn to zincblende MnO was observed in a study on X. Hua et al.'s, whereby the reconversion chemistry of $Mn_3O_4$ was shown to never return to this starting material,

as was deduced from this Mn oxalate study.[76] This revelation not only provides more understanding into the electrochemical behaviour of this material but provides more opportunity for subsequent determination of conversion products in subsequent cycles, as unfortunately the resolved electrochemical data of the precycled materials outlined in this thesis were relatively poor which meant structural conversion was minimal. In the 2 V and 3 V precycled materials for PDF study, their structures differed greatly, and the 3 V max system reflected the material present at the end of the first charge in the PDF analysis, whereas the 2 V max system did not. This further gives explanation for the deviation in electrochemical behaviour between 2 V and 3 V max cells, due to the structural deviation during cycling between the two different voltage ranges. Following on from the structural experiments, the second aim of this Chapter was to determine whether the electrochemical performance for the leached material was comparable to that seen for the pristine material through comparisons between Mn oxalate generated from pristine LMO, and LMO from leached QCR and EOL battery scrap. These experiments proved to be highly successful in upcycling the interconverted $LiMn_2O_4$ into Mn oxalate material. After 100 cycles the capacity recovery of the 3 V max cycled half-cells remained as high as 725 – 750 $mAhg^{-1}$ for the pristine, 500 – 650 $mAhg^{-1}$ for the QCR and 400 – 475 $mAhg^{-1}$ for the EOL sample. Though the capacity retention after 100 cycles was lower with an increased degree of contamination from the leached samples, the capacity still outperforms the expected capacity based on the theoretical calculation, at 375 $mAhg^{-1}$, and of graphite, at 372 $mAhg^{-1}$, and it is suspected that tailoring the morphology of the Mn oxalate product will aid the electrochemical properties of these materials.

# 8 Conclusions

The investigations outlined within this thesis has showcased the upcycling potential of LMO from QCR and EOL battery scrap. An into Mn-based materials through an array of experiments. In Chapter 4, through selective extraction of $LiMn_2O_4$ from quality control-rejected and end-of-life battery Nissan Leaf cathodes, it has been demonstrated that this material can not only be extracted but it can also be interconverted into an array of new Mn-based products with the same crystal structure as their pristine counterpart. With respect to the crystal structures: $LiMn_2O_4$ formed a cubic close-packed spinel structure with space group $Fd\bar{3}m$, α'-Mn oxalate dihydrate formed with space group C12/c1, $Mn_2O_3$ with space group Pcab, and $Mn_3O_4$ with space group I41/amd. These results highlighted that LMO can be leached and interconverted into an array of Mn-based products with minimal contamination, and that this minor contamination does not impact the formation of the crystalline material with the desired space group based on their comparison to the pristine case. In Chapter 5, the anode upcycling opportunity for leached Mn-rich material from first generation quality-control rejected and end-of-life cathode was realised. A mechanochemical route involving one ball milling step followed by moderate decomposition temperatures hold times of 600°C/ 4 hr provide the desired $_{nano}$MnO-C composite, demonstrating that complex solvothermal routes are not necessary to generate these materials. With respect to the electrochemical behaviour of these leached materials, average capacity for the pristine, QCR and EOL samples after 15 cycles was 697 (±19), 777 (±12), and 916 (±37) $mAhg^{-1}$ which equates to 66 %, 68%, and 83 % of the original capacities exhibited, respectively. This highlights the

enhanced capacity retention when compared to the pristine case – and indicates that upcycling redundant cathode materials into these $_{nano}$MnO-C conversion anodes provides an exciting opportunity to access high-capacity anode materials as alternatives to graphite in lithium-ion batteries.

In Chapter 6, it was demonstrated that Mn oxalate conversion anode synthesis is successful using the interconversion of leached $LiMn_2O_4$ into Mn oxalate material, and that the voltage cutoff limits limit the achievable capacity retention for the conversion anodes. Additionally, in-situ structural studies identified that the conversion product at the end of the first cycle was not Mn oxalate, opposing the reported reversible conversion reaction reported extensively in the literature. The product at the end of discharge was, in fact, correlated to a zincblende-MnO phase, which was still resolvable in subsequent cycles for the 3 V max precycled half-cell indicating the reversibility of this MnO phase after the initial cycle. For the leached samples, after 100 cycles the capacity recovery of the 3 V max cycled half-cells remained as high as 725 – 750 $mAhg^{-1}$ for the pristine, 500 – 650 $mAhg^{-1}$ for the QCR and 400 – 475 $mAhg^{-1}$ for the EOL samples. Though the capacity retention after 100 cycles is lower with an increased degree of contamination, the capacity still outperforms the expected capacity based on the theoretical calculation, at 375 $mAhg^{-1}$, therefore it is suspected that tailoring the morphology of the Mn oxalate product will enhance the electrochemical properties of these materials.

In conclusion, it can be rationalised that there is significant value for upcycling LMO from leached cathode material. Not only are the contaminants from this leaching process present in minor quantities, but when leached material is interconverted into materials for conversion anode applications, the morphological variation has a

profound influence on the electrochemical performance, providing exciting potential for these materials.

# 9 Future Work

An assortment of subsequent experiments have been outlined at the end of each Chapter to continue experimentation on these systems, therefore, in this summary, further experiments that can be applied across investigations are outlined here.

Firstly, PDF studies on the cycling behaviour of both conversion anode materials would be of great value, to see how the local order of these materials compares in initial and subsequent cycles. If the Mn oxalate discharges to form this zincblende MnO structure in the first cycle and reversibly converts through this material in subsequent cycles, it will be of interest to determine how the structural changes within this system compare to that of a $_{nano}$MnO-C composite. In such experiments, PDF refinement will be utilised to enhance the identification of the in-situ products detected using this method, with software such as PDFgui and thermodynamic calculations such as Metropolis Monte Carlo simulations for subsequent structural elucidation.[76197]

For the conversion anode experiments, further electrochemical investigation into long-term capacity retention and comparison between the pristine and leached materials will be of great value. Additionally, removing the excess Li that comes from the Li counter electrode by testing the the anode materials in a full cell setup would be of value to determine how the capacity increase of these anodes is affected, as the limitation of this Li source is likely to diminish the extensive capacity increase observed due to the loss of Li inventory during side-reactions to form the SEI layer and polymeric gel. The comparison of electrochemical behaviour between the half-cells and in a full cell experiment, combined with an in-situ XAS study to monitor the

Mn oxidation state in real time would give in-depth evidence into the redox-activated behaviour of the Mn-based electrodes during cycling. capacitive formation of the polymeric gel during cycling.

Finally, to gain more structural understanding of the leached material structure, one method to determine the site at which the contaminant ions dope into the interconverted materials could be through x-ray absorption spectroscopy (XAS). This enables quantification of the average oxidation state of the manganese ions within the pristine /QCR / EOL materials using the occupation of the d-orbitals within the Mn atoms to determine the oxidation state.[71] Not only could XAS be utilised ex-situ to determine the oxidation state of the Mn in the interconverted products, but it could also be used in-situ, to identify the conversion products observed during conversion when utilised in conversion anode applications. The redox behaviour of the manganese could be measured in real-time, to determine the oxidation state of the conversion products during cycling – giving evidence for the extra oxidation of manganese with the capacity increase hypothesised after many cycles for both the MnO and Mn oxalate anodes.

# 10 Appendix

## 10.1 EDX analysis of pristine samples

### 10.1.1 $LiMn_2O_4$

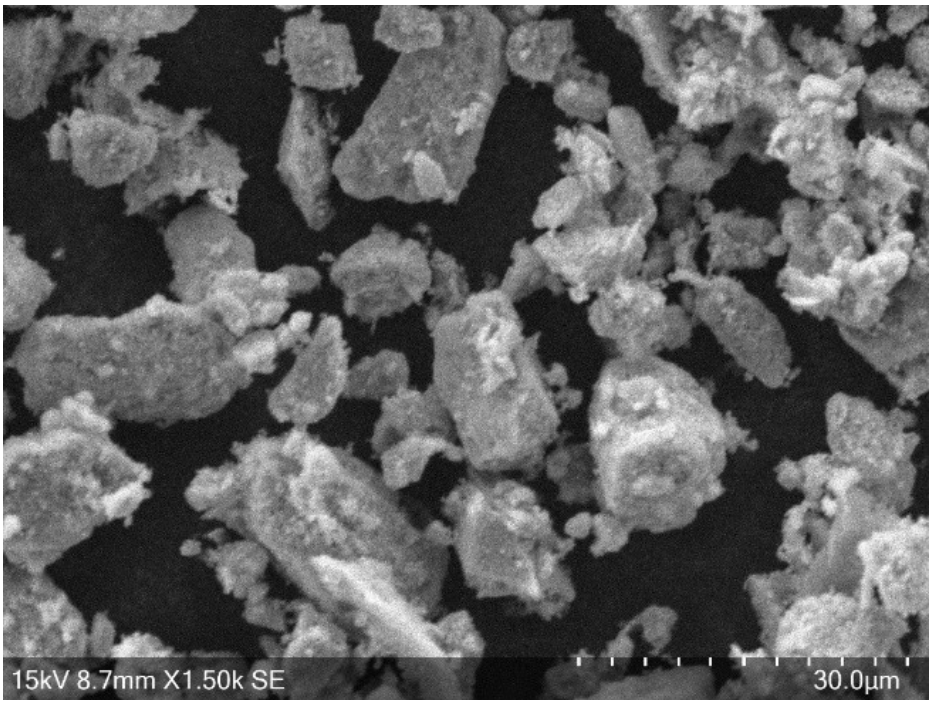


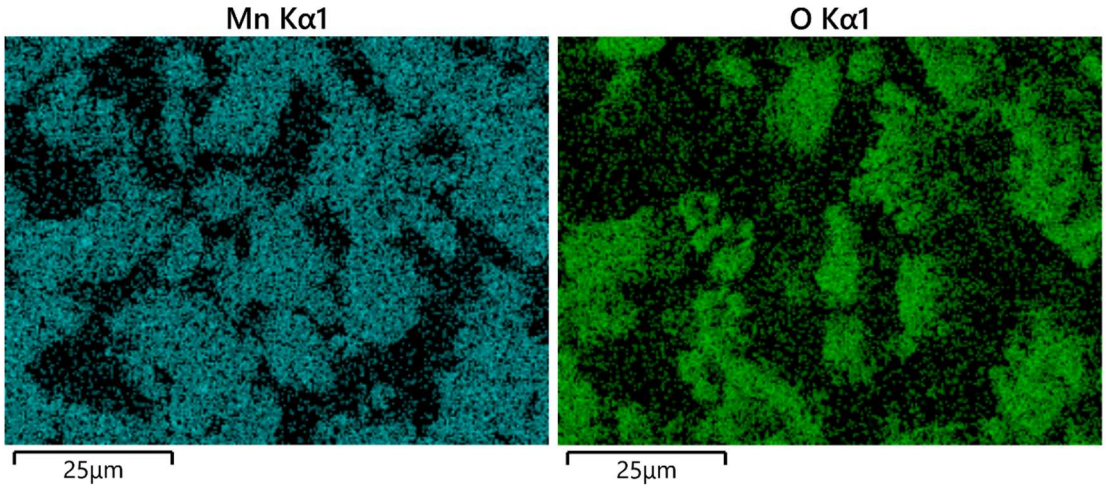

## 10.1.2 Mn oxalate dihydrate

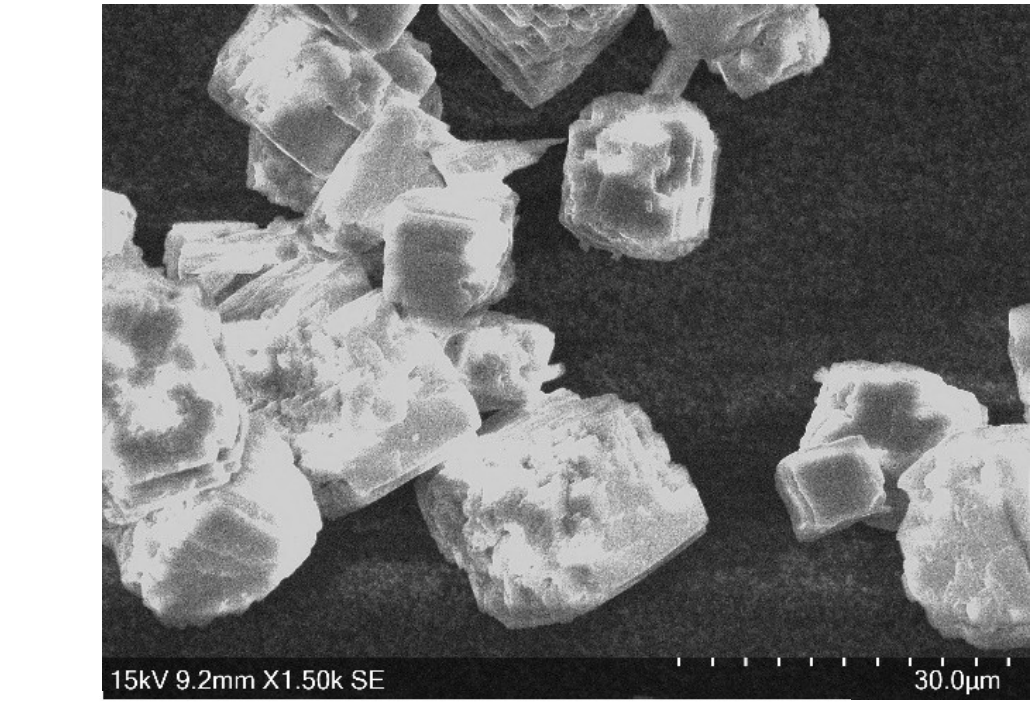


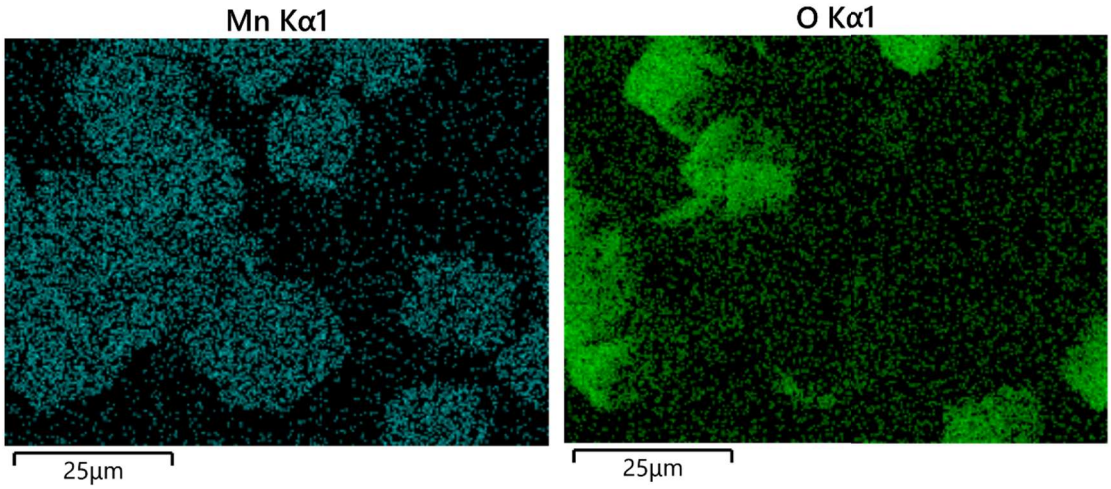


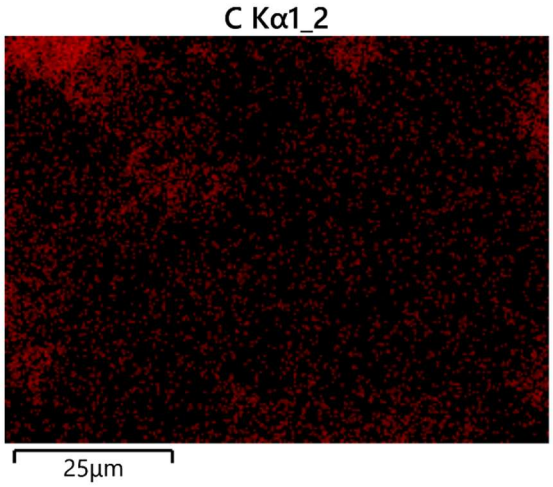

### 10.1.3 $Mn_2O_3$

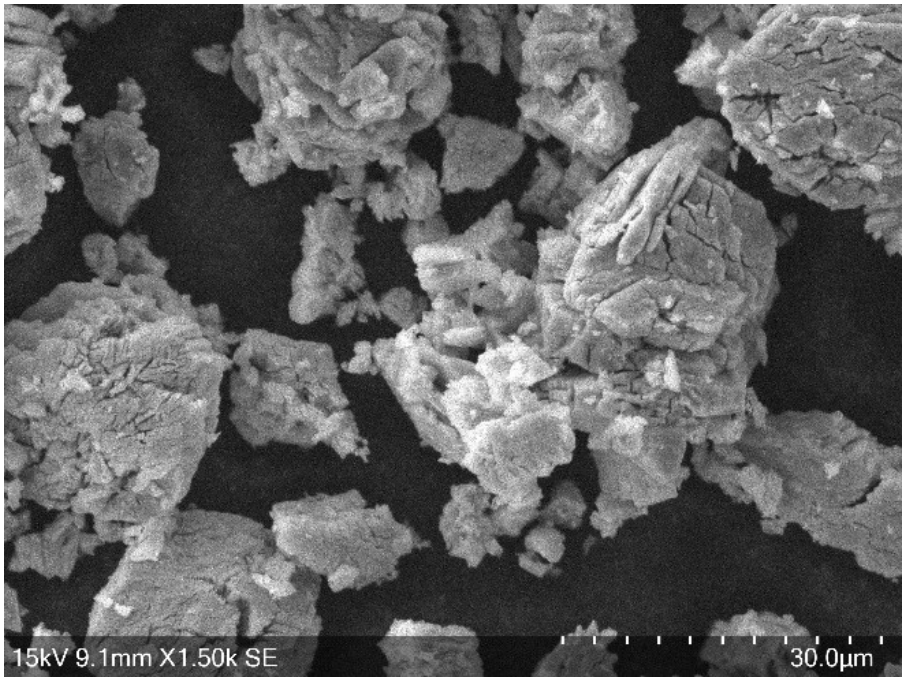


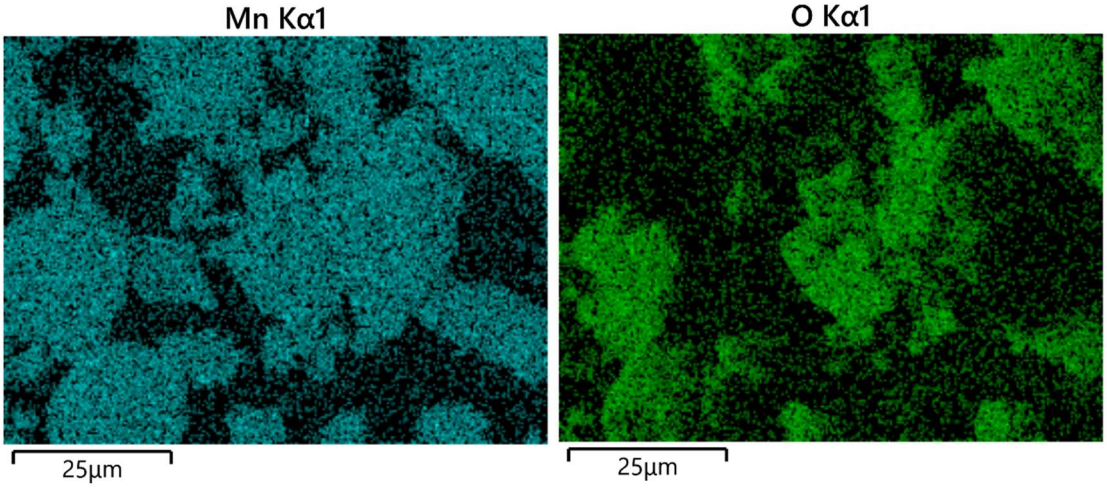

## 10.1.4 $Mn_3O_4$


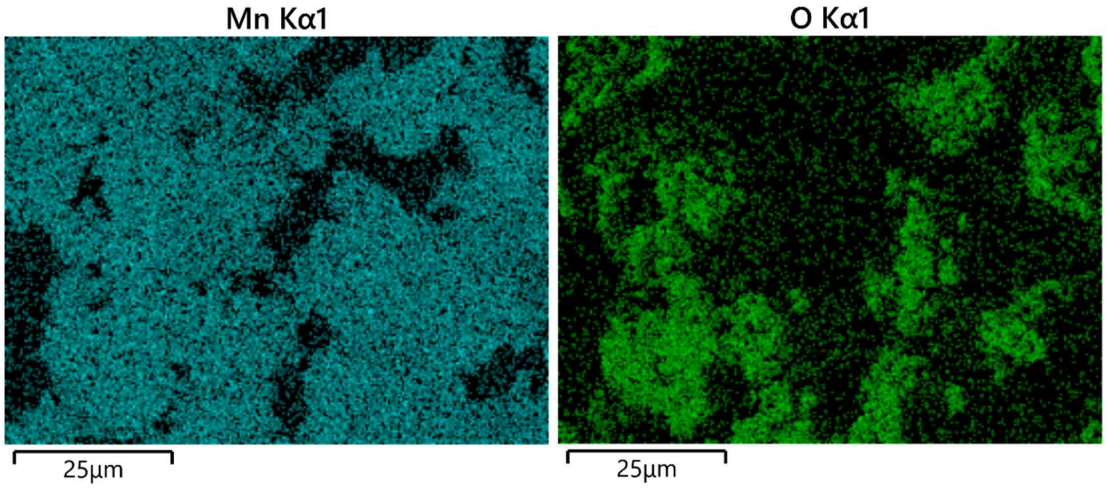

## 10.2 EDX analysis of QCR-leached samples

### 10.2.1 $LiMn_2O_4$

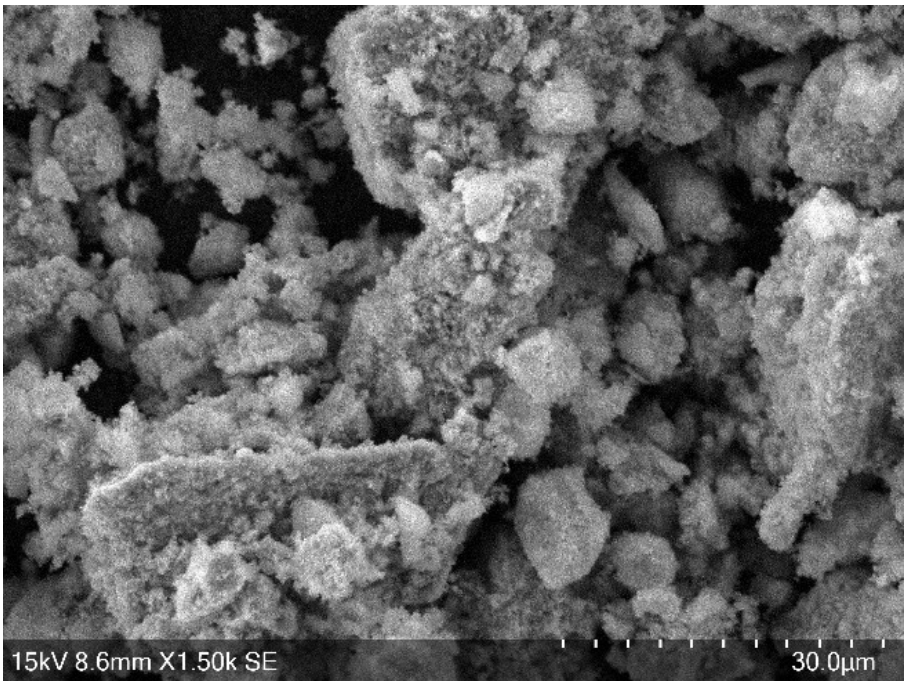


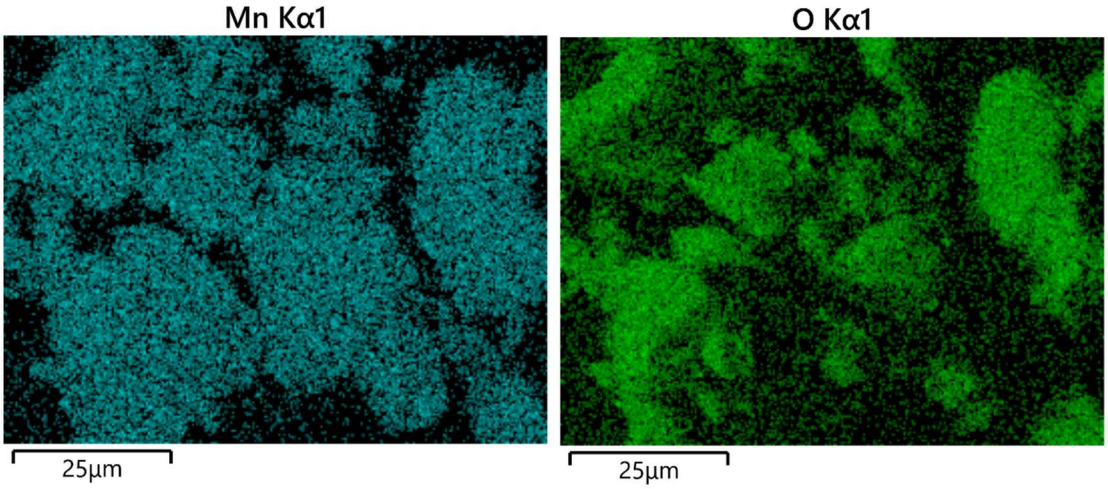

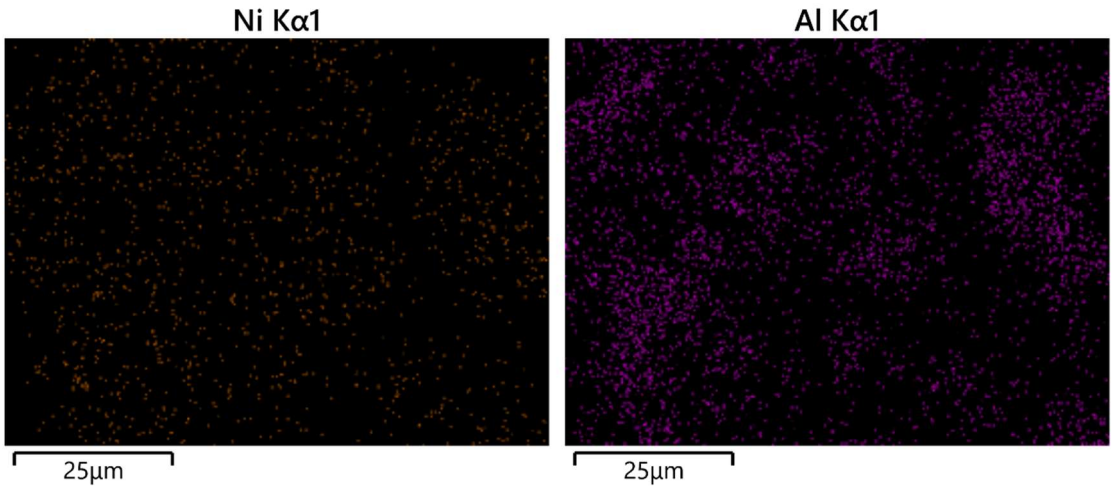
Ni Kα1
Al Kα1
25µm
25µm

## 10.2.2 Mn oxalate dihydrate

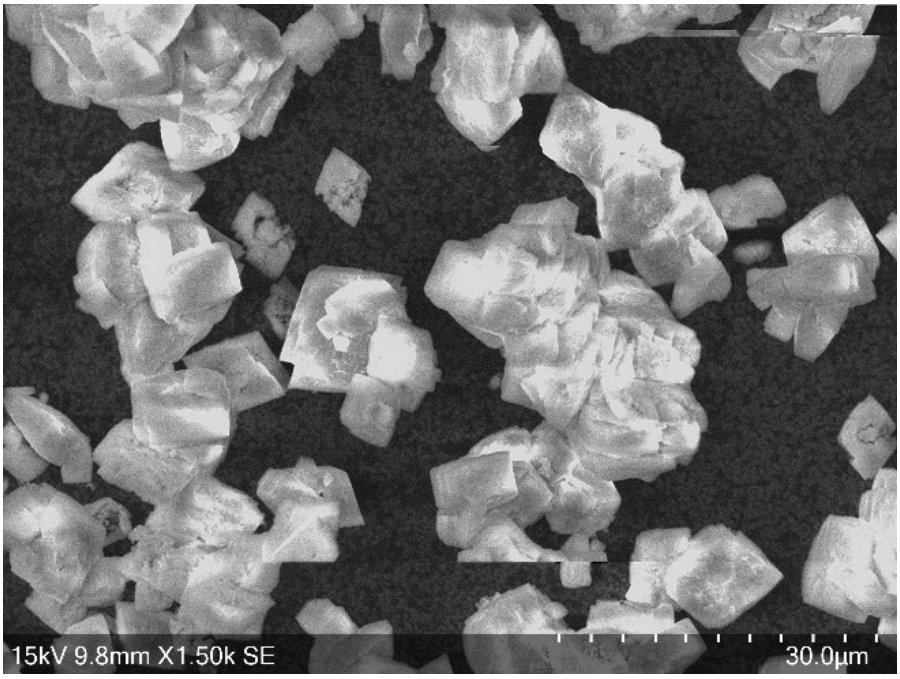


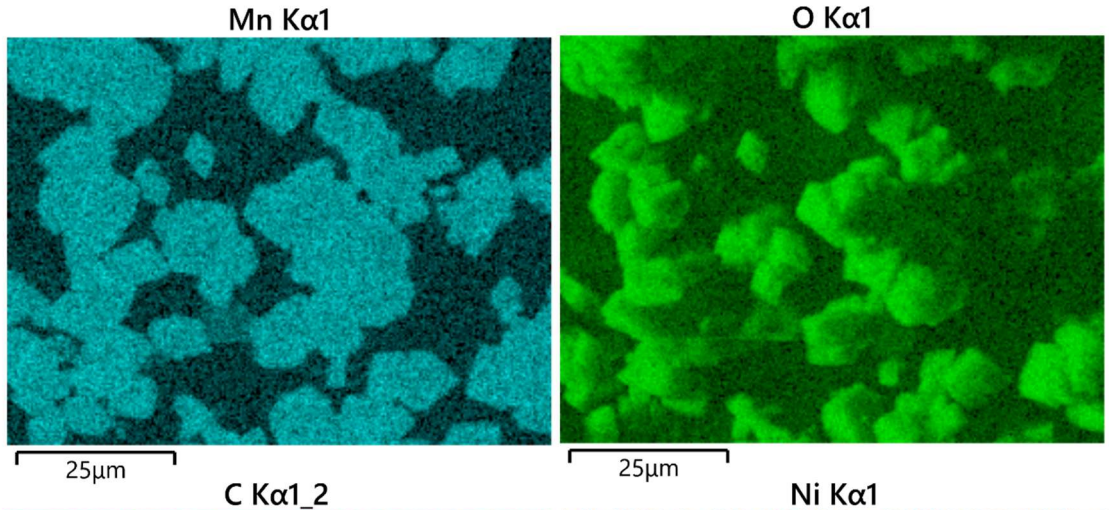


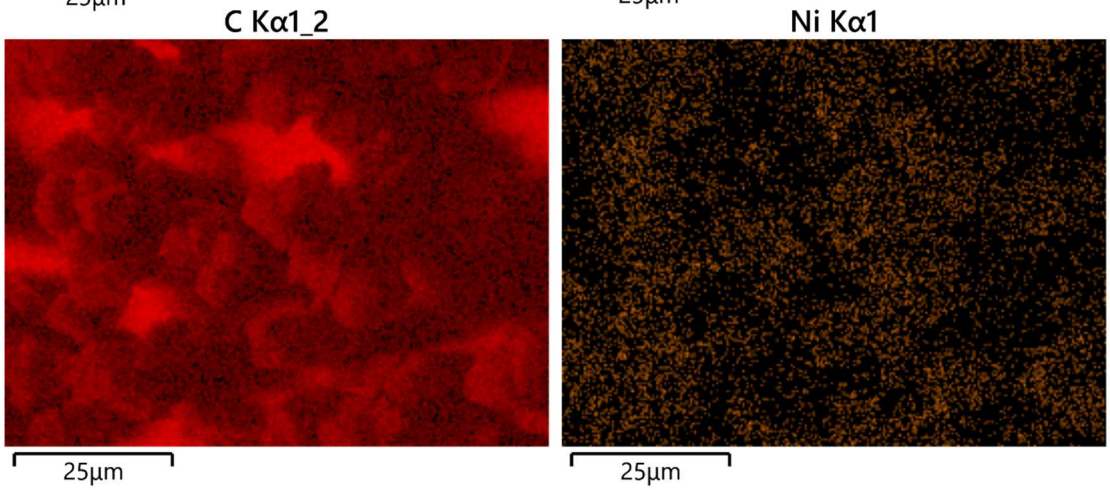

## 10.2.3 $Mn_2O_3$

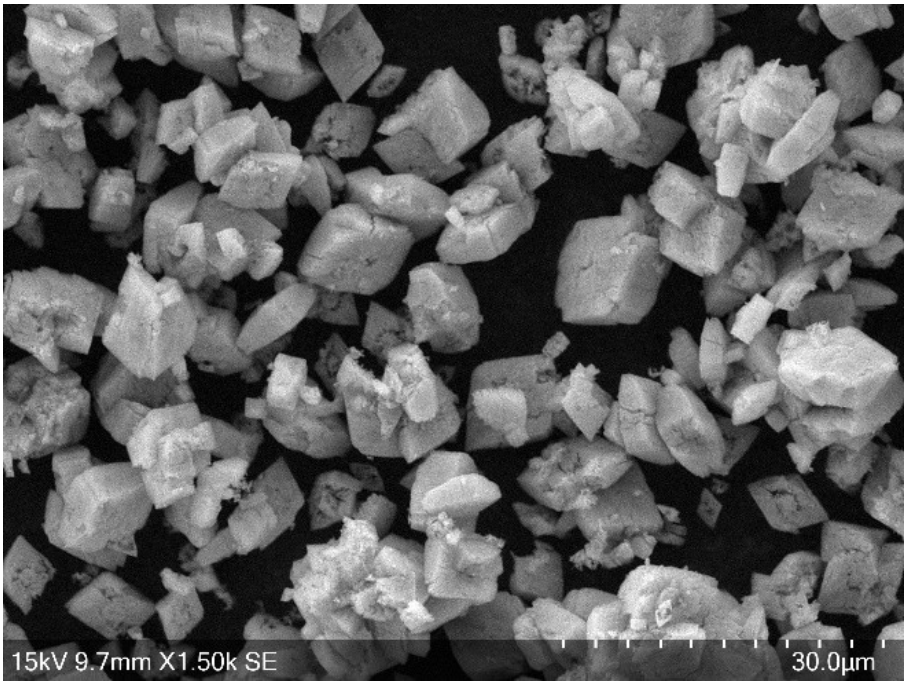


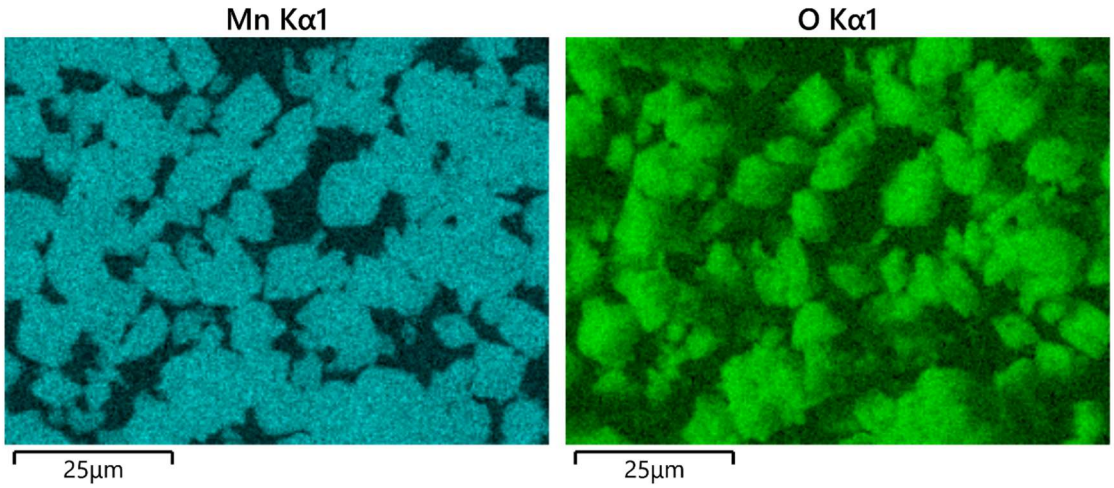


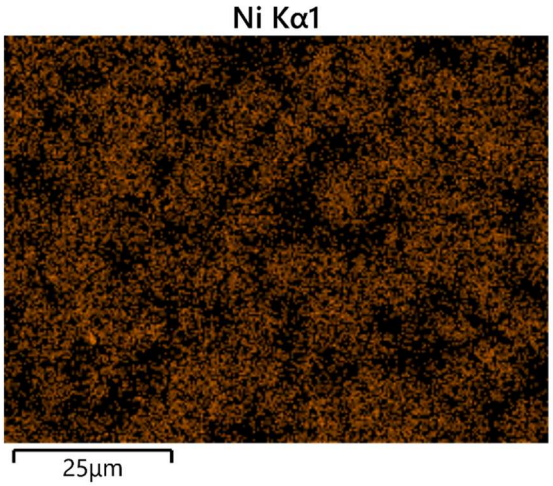

## 10.2.4 $Mn_3O_4$

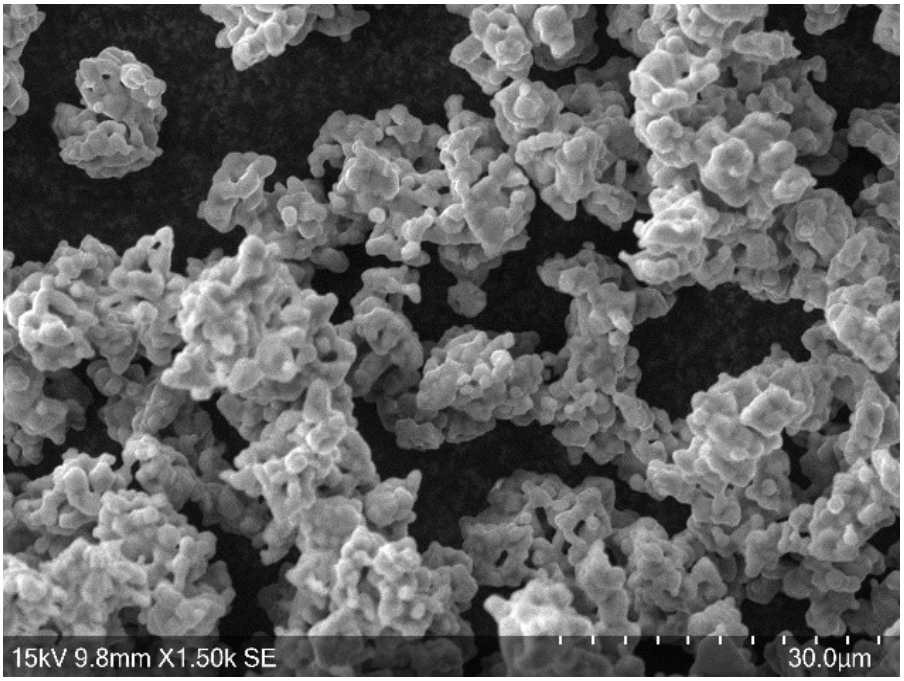


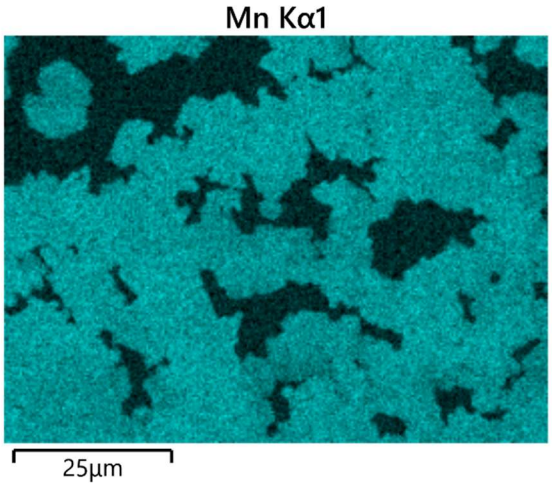


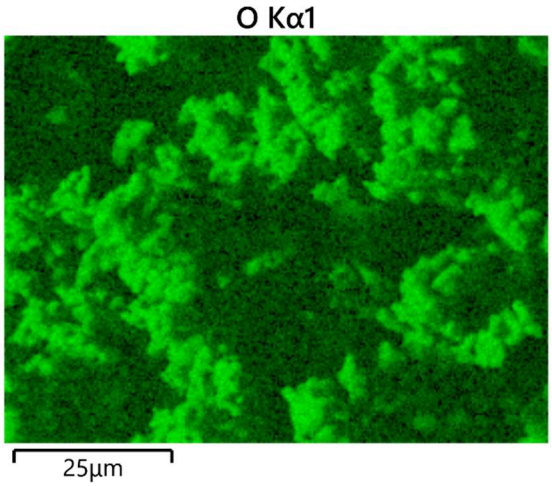


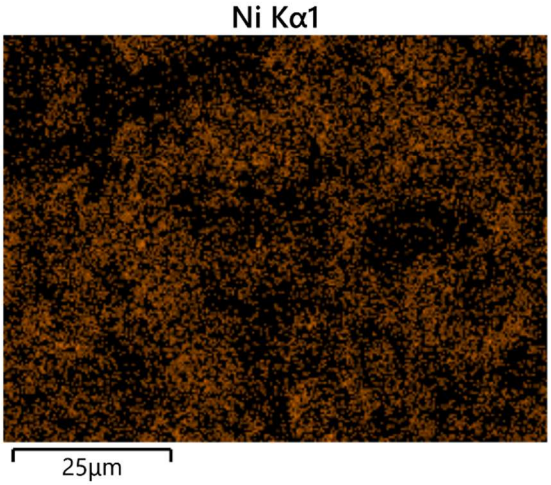

## 10.3 EDX analysis of EOL-leached sample

### 10.3.1 $LiMn_2O_4$

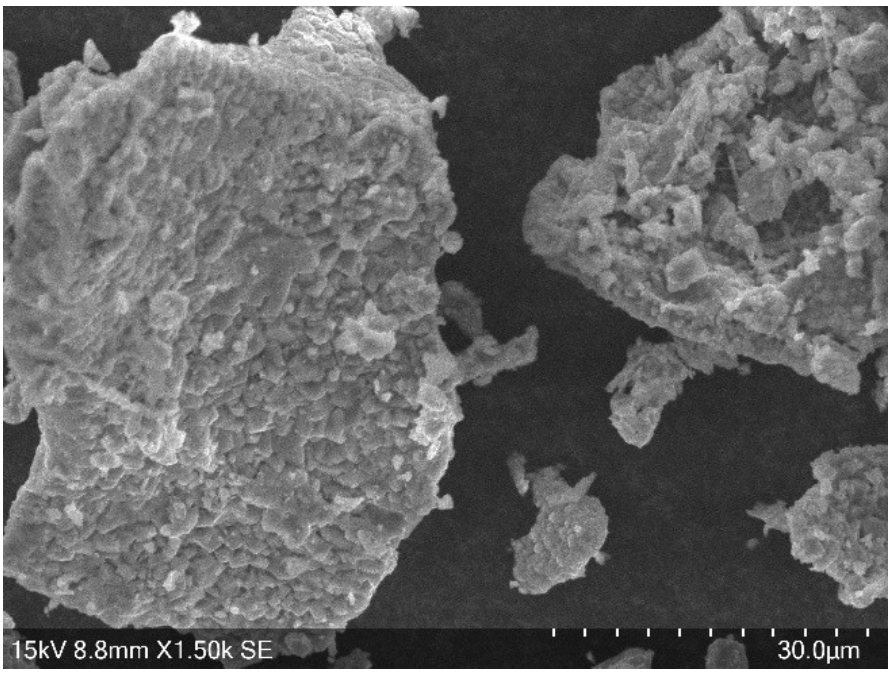


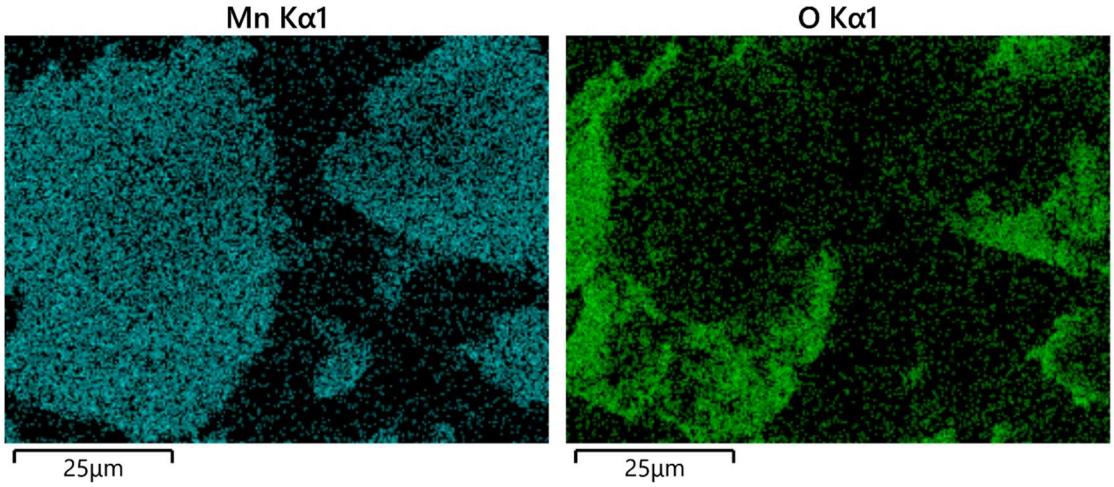

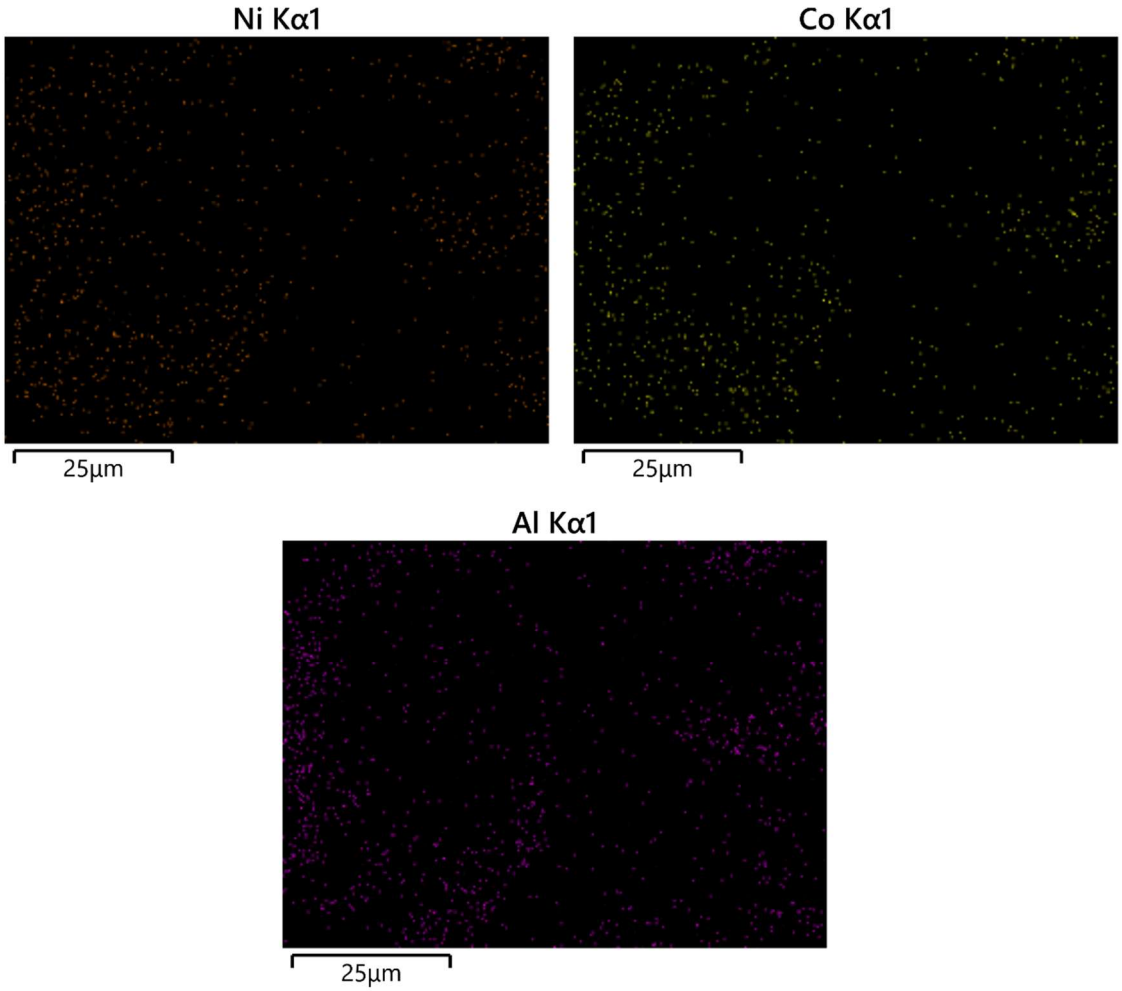
Ni Kα1
25µm
Co Kα1
25µm
Al Kα1
25µm

## 10.3.2 Mn oxalate dihydrate

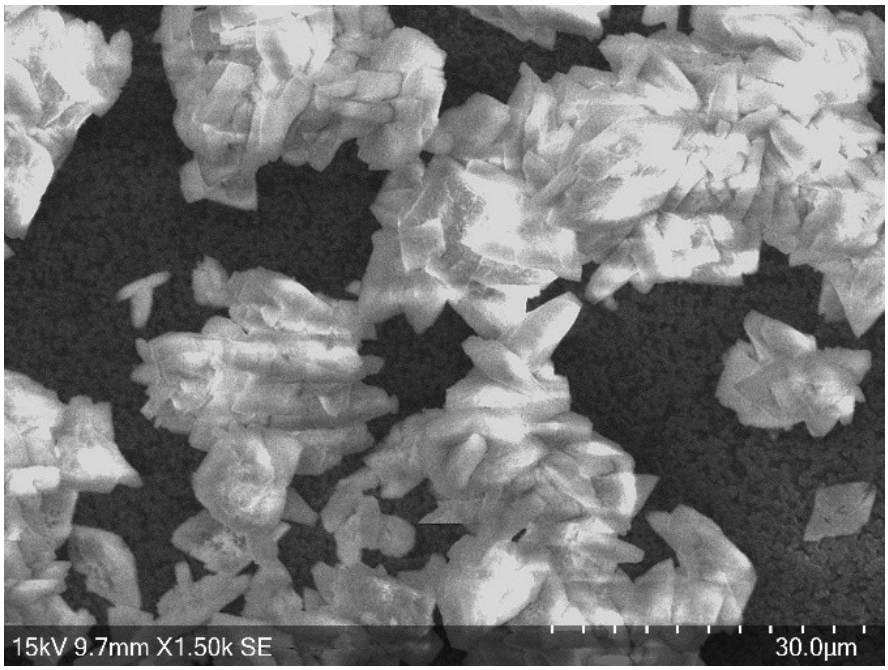


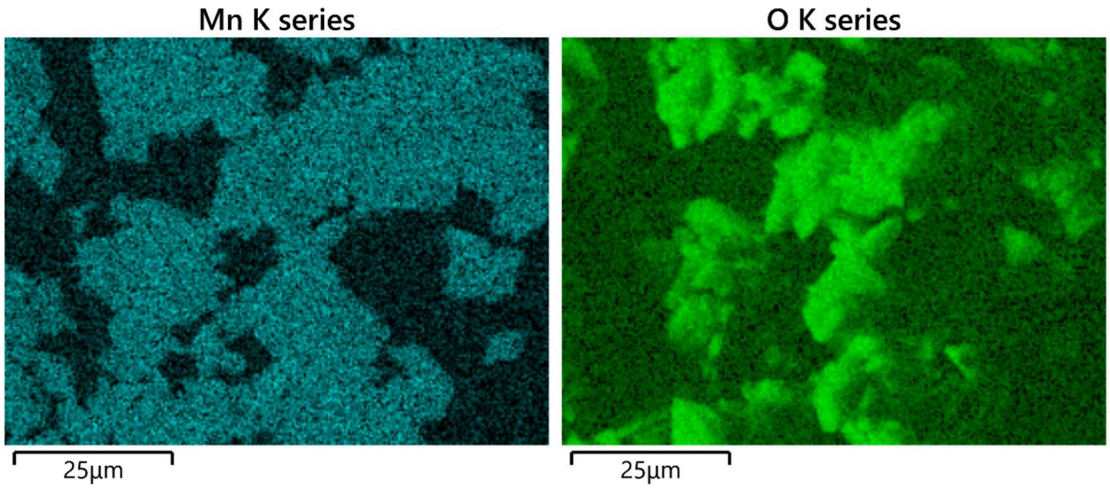

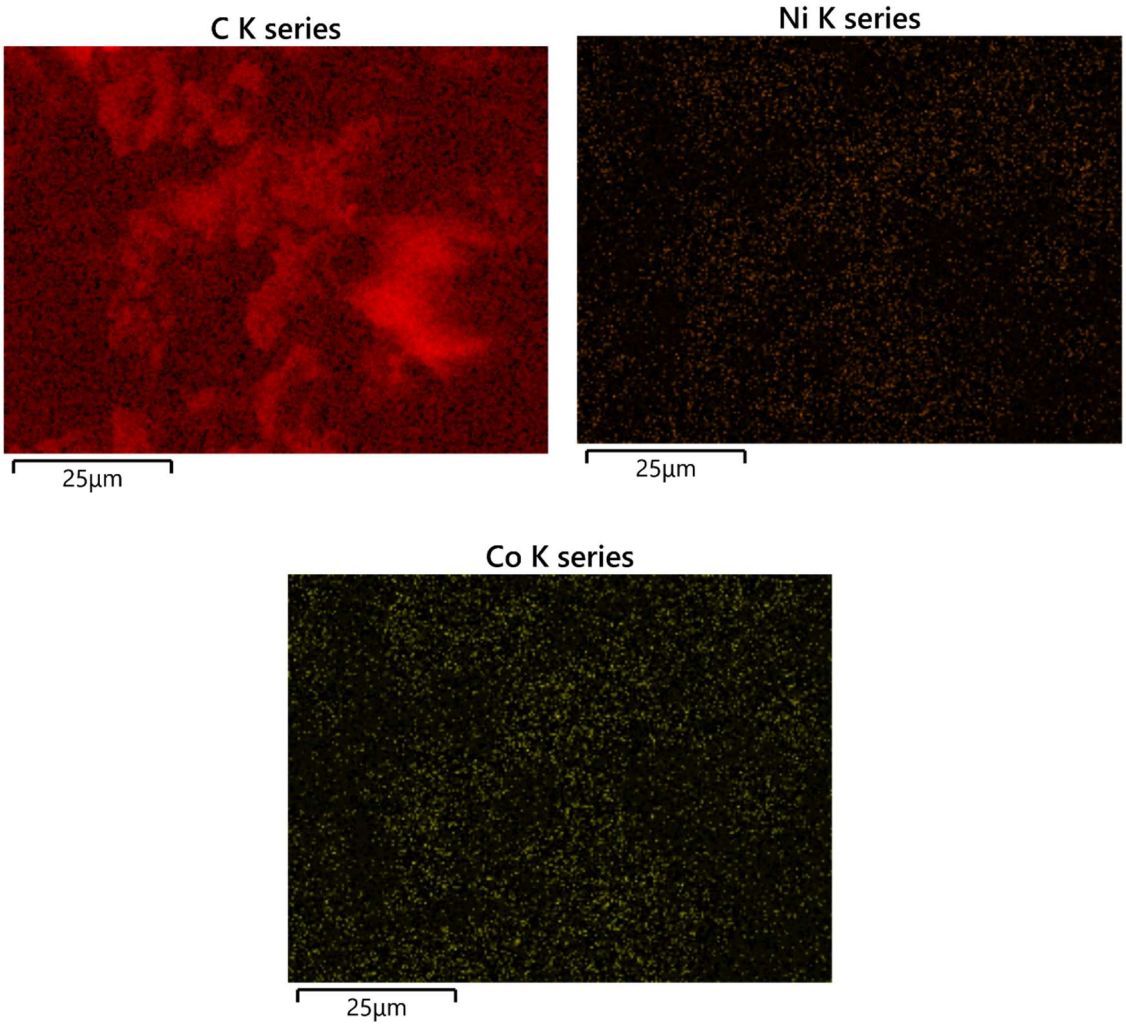
C K series
25µm
Ni K series
25µm
Co K series
25µm

### 10.3.3 $Mn_2O_3$

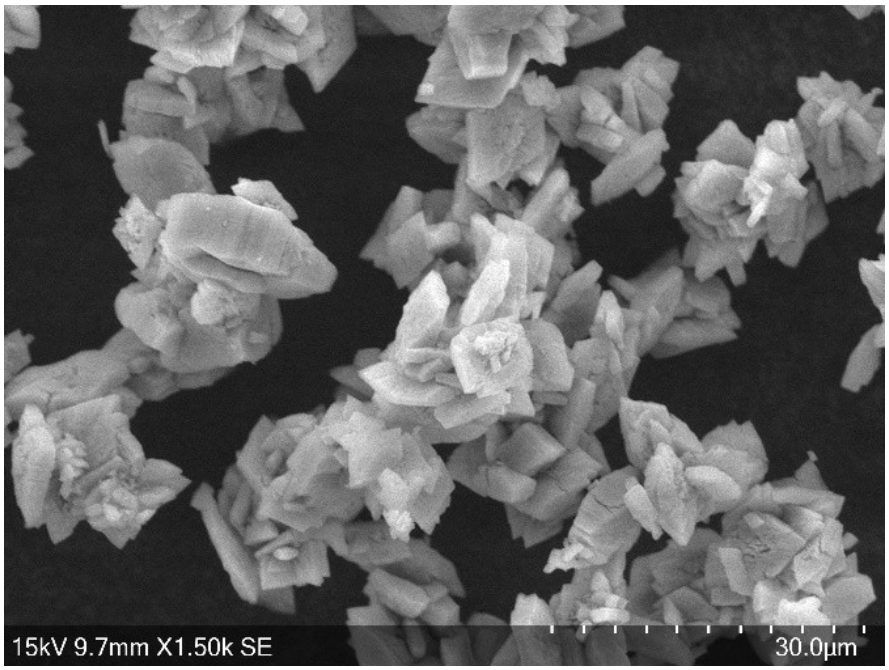
15kV 9.7mm X1.50k SE
30.0µm

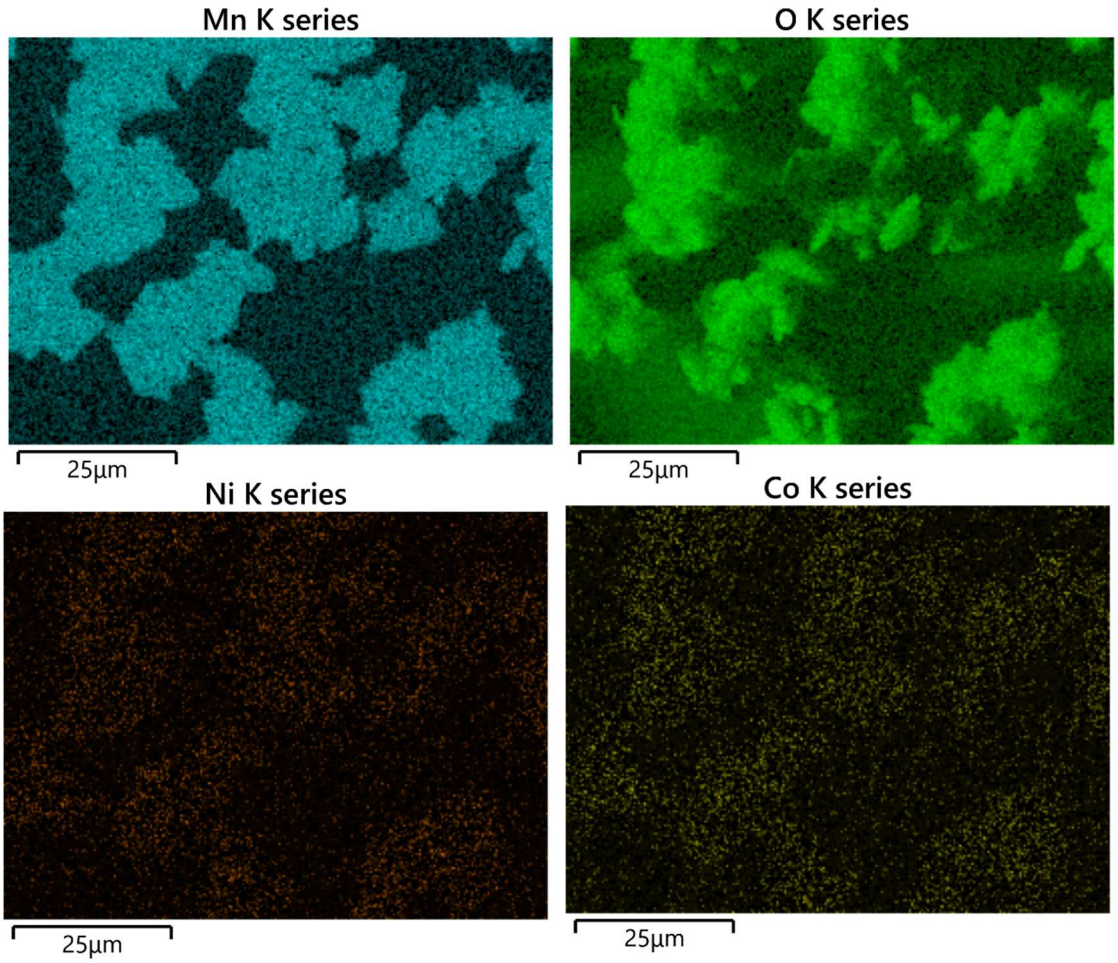
Mn K series
O K series
25µm
25µm
Ni K series
Co K series
25µm
25µm

## 10.3.4 $Mn_3O_4$

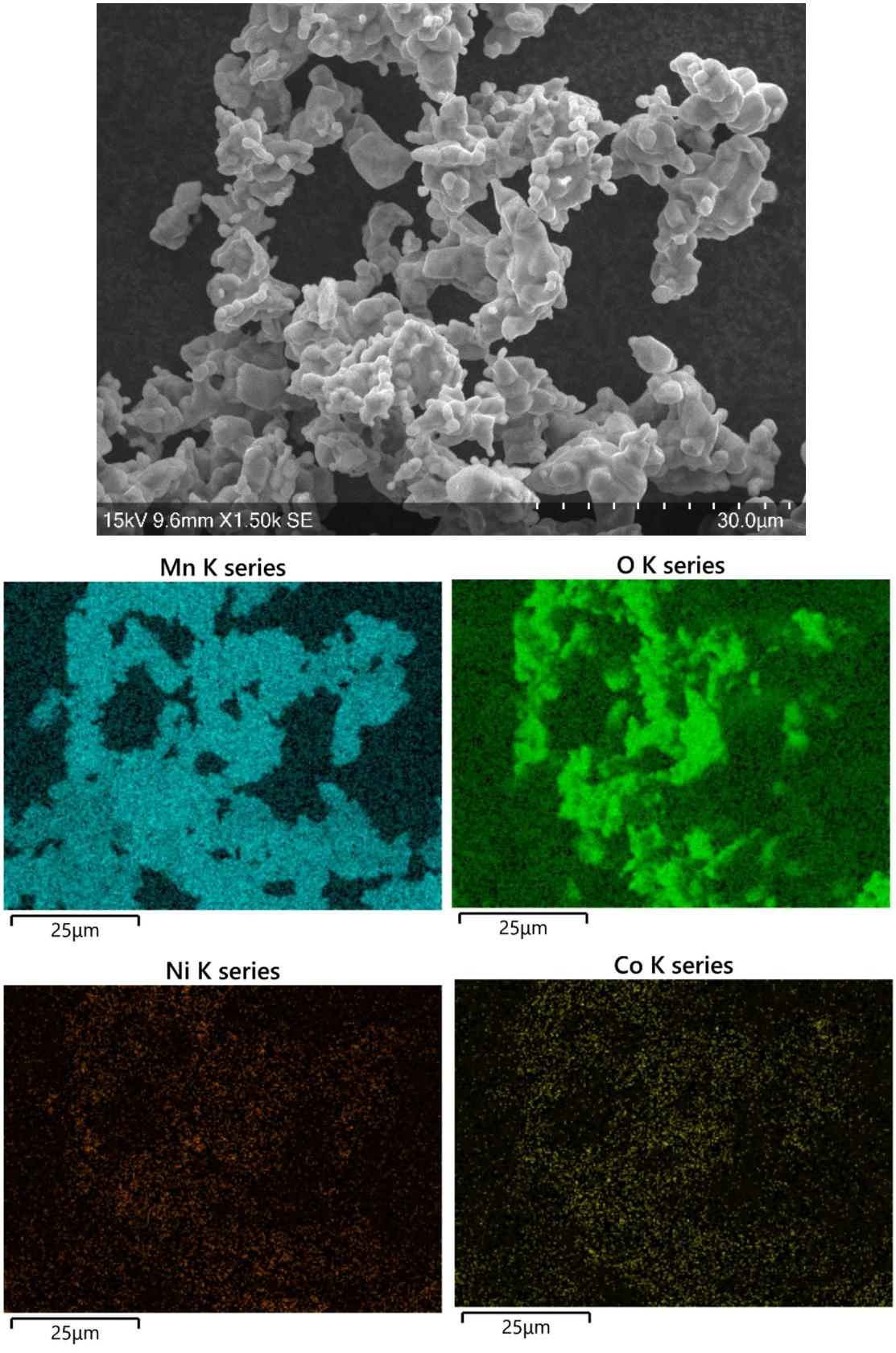
15kV 9.6mm X1.50k SE
30.0µm
Mn K series
25µm
O K series
25µm
Ni K series
25µm
Co K series
25µm

## 10.4 EDX analysis of pristine 600 °C/ 4h $_{nano}$MnO–C composite

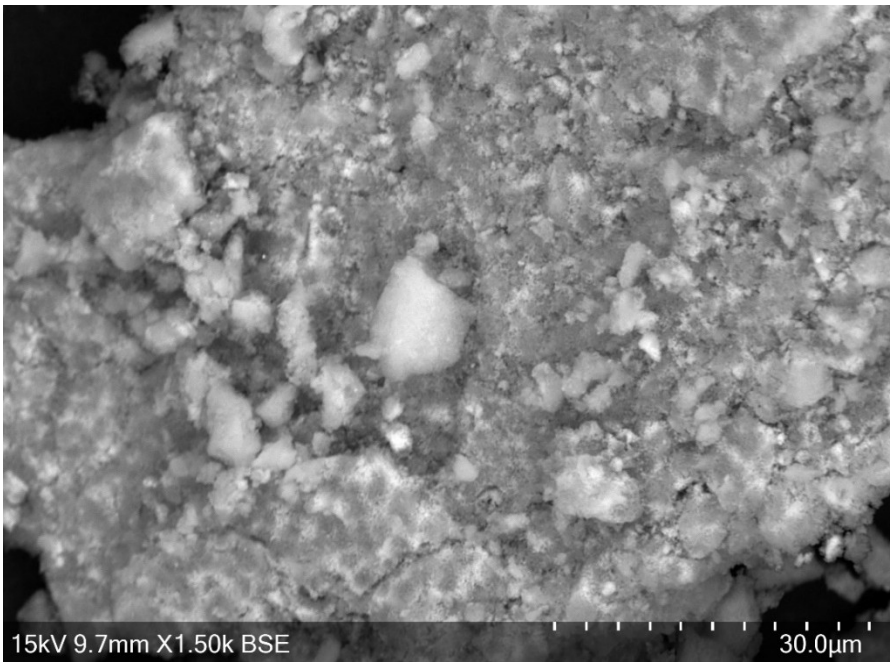


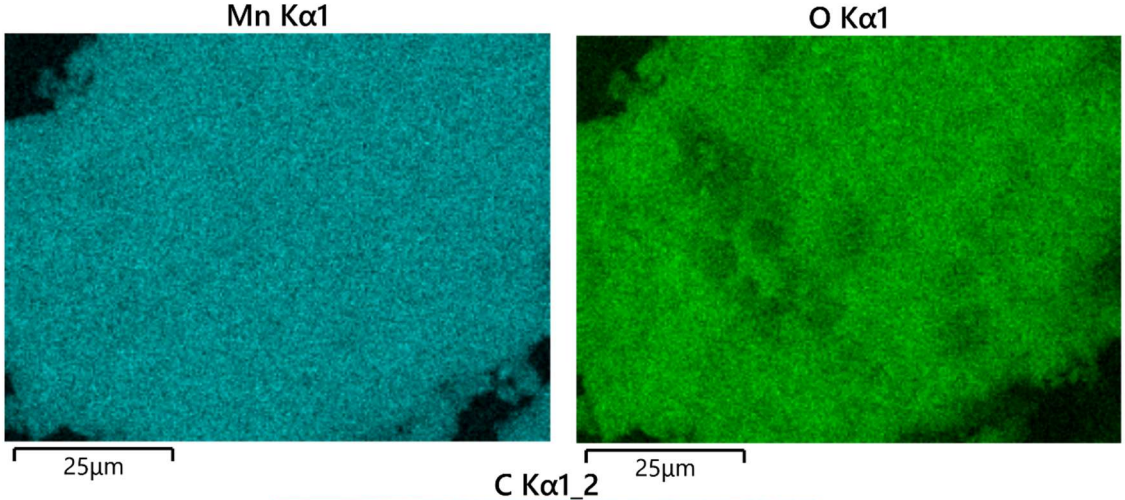


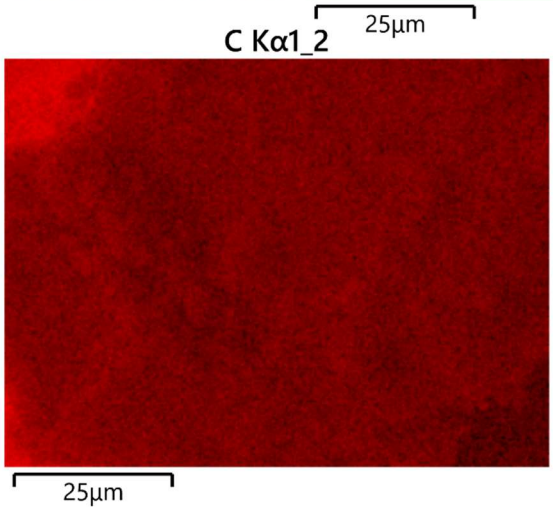

## 10.5 EDX analysis of ascorbic acid treated 600 °C/ 4h $_{nano}$MnO–C composite

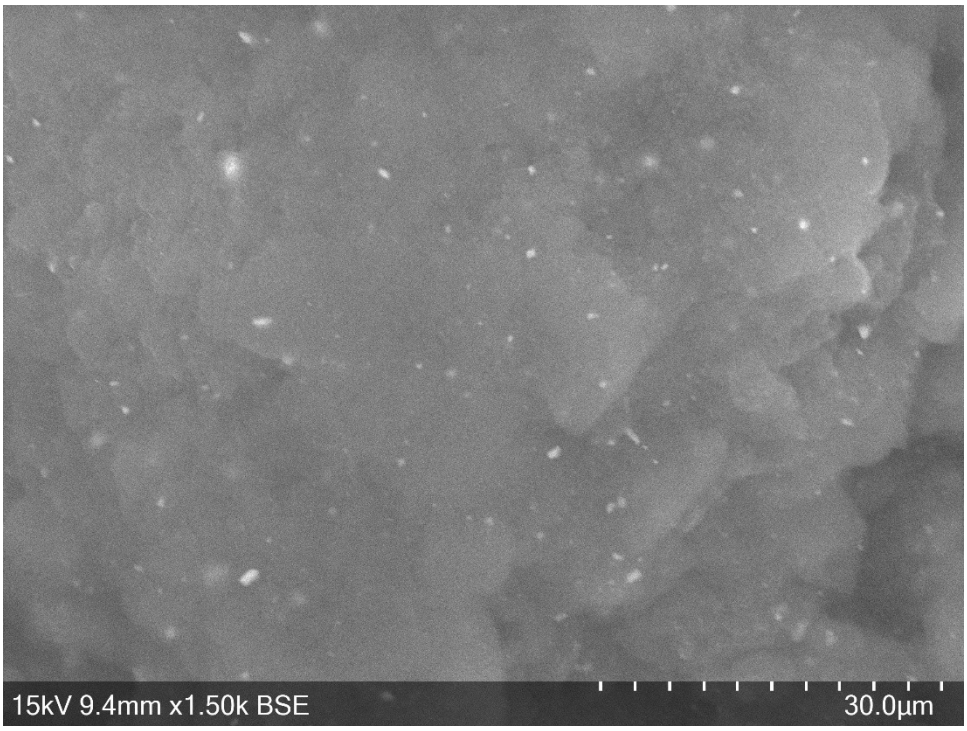


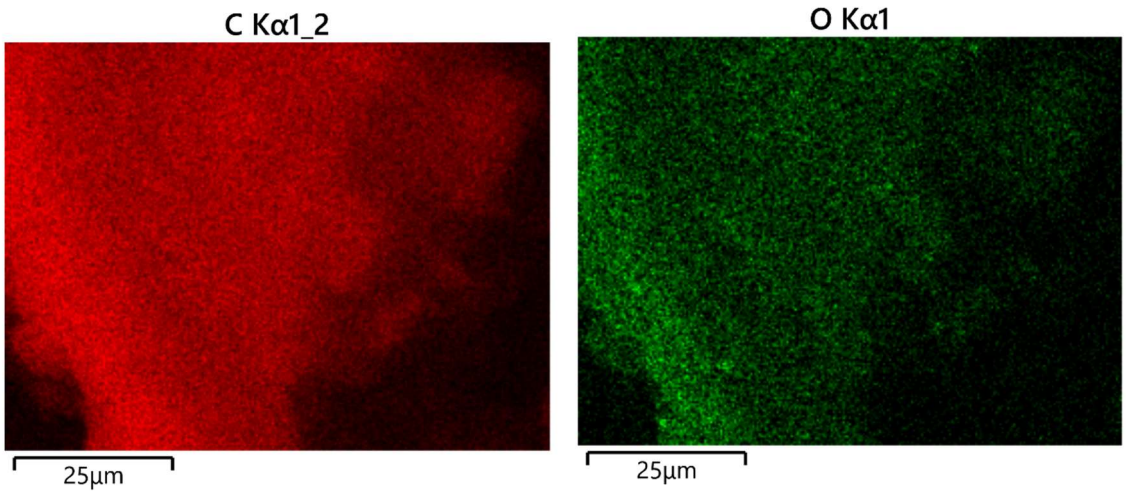

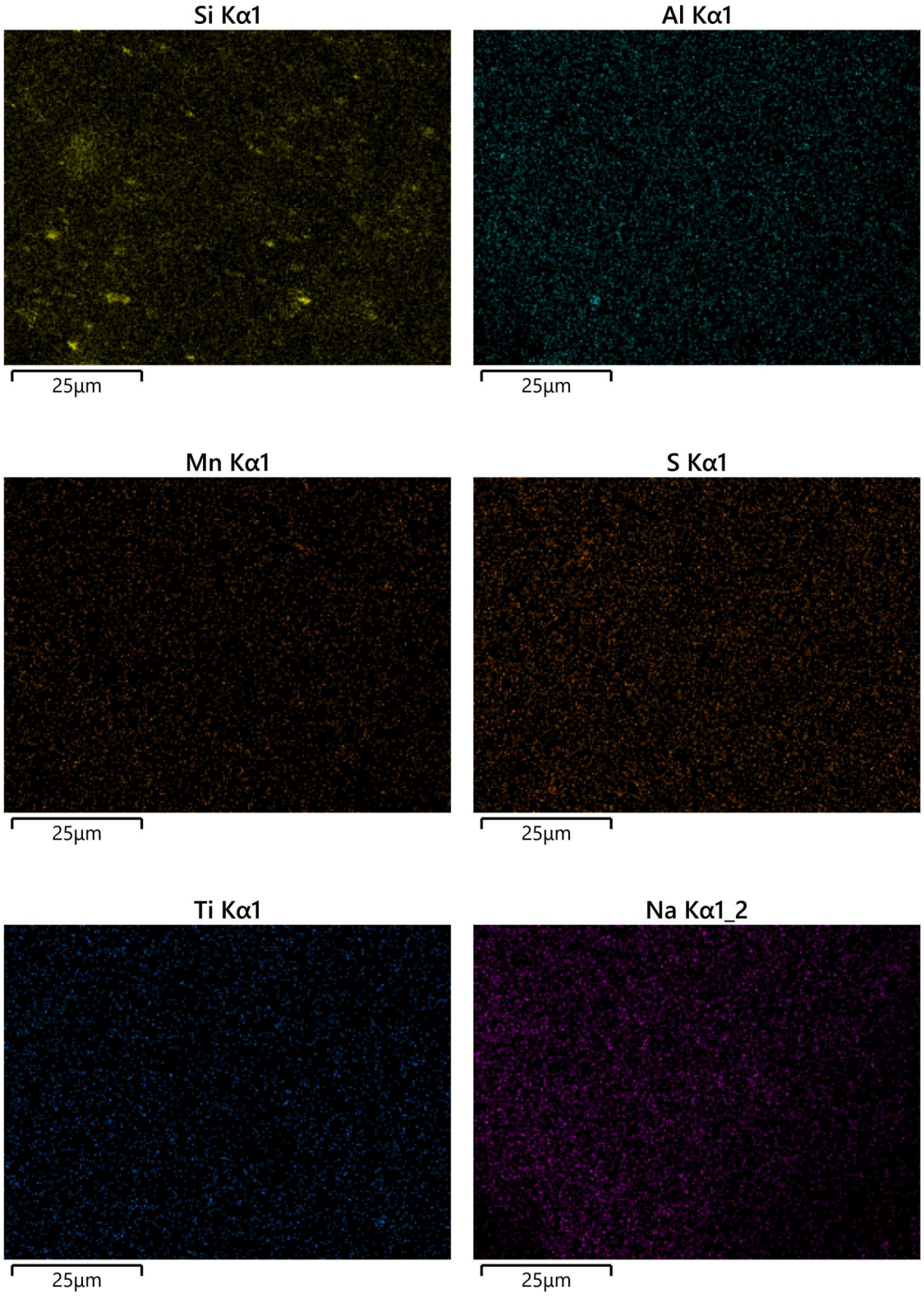
Si Kα1
25µm
Al Kα1
25µm
Mn Kα1
25µm
S Kα1
25µm
Ti Kα1
25µm
Na Kα1_2
25µm

# 10.6 ICP-OES analysis of pristine, QCR and EOL $_{nano}$MnO–C composites

*Appendix 10.6. Unquantified confirmation of the presence of contamination in the pristine (P-$_{nano}$MnO-C), QCR (Q-$_{nano}$MnO-C) and EOL (E-$_{nano}$MnO-C) samples.*

| Sample | Present in MnO sample (< 0.01 % by mass) | | | | | |
|---|---|---|---|---|---|---|
| | Li | Mn | Ni | Co | Al | Cu |
| **P-$_{nano}$MnO-C** | N | Y | N | N | N | N |
| **Q- $_{nano}$MnO-C** | Y | Y | Y | Y | Y | N |
| **E- $_{nano}$MnO-C** | Y | Y | Y | Y | N | N |

# 10.7 Quantified Faradaic and non-Faradaic behaviour of 2 V max Mn oxalate half-cell between cycle 1 and 100

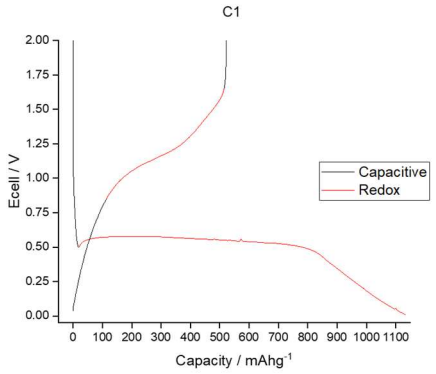


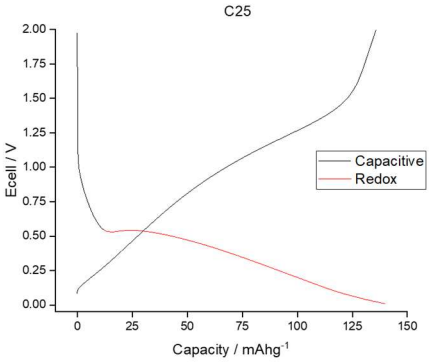


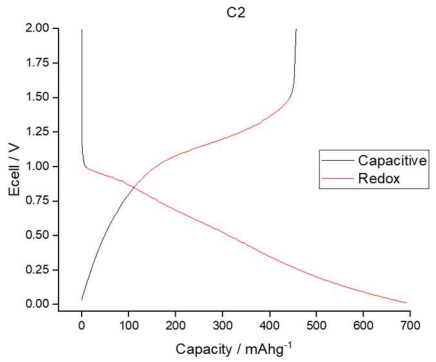


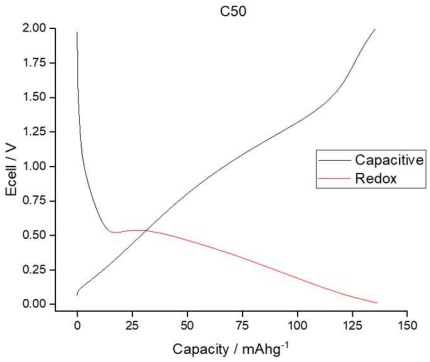


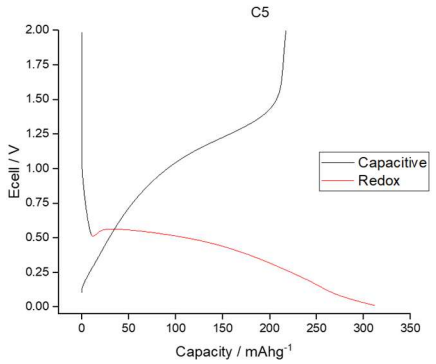


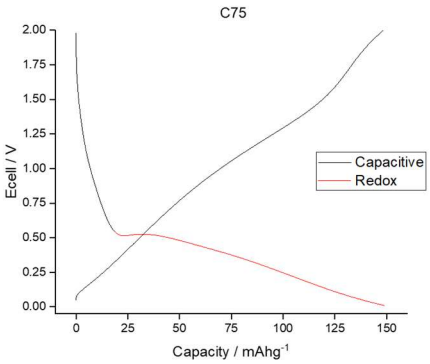


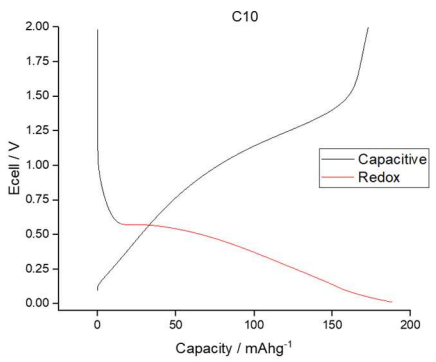


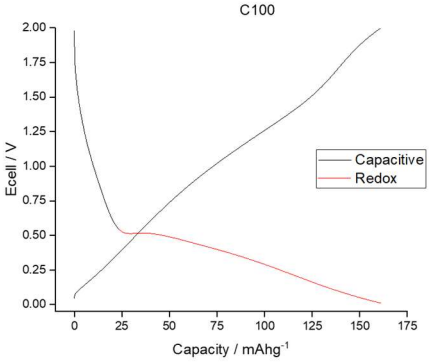

# 10.8 Quantified Faradaic and non-Faradaic behaviour of 3 V max Mn oxalate half-cell between cycle 1 and 100